EVALUATING AND AUGMENTING FUEL-SAVING BENEFITS OBTAINED IN AIRCRAFT FORMATION FLIGHT

by

WENDY AWELE OKOLO

Presented to the Faculty of the Graduate School of
The University of Texas at Arlington in Partial Fulfillment
of the Requirements
for the Degree of

DOCTOR OF PHILOSOPHY

THE UNIVERSITY OF TEXAS AT ARLINGTON

May 2015

ACKNOWLEDGEMENTS

I thank my Father in Heaven and dedicate this dissertation to Him. Without Him, none of this would have been possible.

To my family, I thank you for loving, supporting, and encouraging me to believe I could achieve anything I wanted. I am truly grateful to you all for being patient with me especially this past year as I got closer to the end. I could not have done any of this without you and I thank and love you all.

To my advisor Atilla Dogan, you have been a great teacher, a wonderful mentor, a true inspiration, and more importantly, a friend. Your guidance, support, and patience over the past few years, which motivated me in so many ways, has finally culminated in this dissertation. I appreciate all that you have done.

To my sponsor, William Blake, at the Air Force Research Laboratory, I am fully indebted to you for being a mentor and a guide throughout my graduate studies, especially during the three summers I spent at Wright-Patterson Air Force Base. I thank you for all your support.

To my dissertation committee, Kent Lawrence, Chaoqun Liu, Kamesh Subbarao, Donald Wilson, I thank you for your time and for providing valuable insight and recommendations regarding this dissertation.

To the University of Texas at Arlington, especially the Mechanical and Aerospace Engineering Department, for rewarding my every milestone and spurring me to even greater heights, I thank you.

May 6, 2015

ABSTRACT

EVALUATING AND AUGMENTING FUEL-SAVING BENEFITS OBTAINED IN AIRCRAFT FORMATION FLIGHT

WENDY AWELE OKOLO, Ph.D.

The University of Texas at Arlington, 2015

Supervising Professor: Atilla Dogan

When an aircraft flies, it generates wake vortices, which induce a non-uniform wind distribution in its wake. A trail aircraft, placed in the wake of a lead's aircraft vortices experiences this non-uniform wind distribution with varying directions and magnitudes, depending on the location within the wake. It has been demonstrated that there is a "sweet spot" within the wake of a leader in which a trail can experience upwash which leads to reduced drag. Through this mechanism, aircraft can save significant amounts of fuel by flying at the sweet spot of the lead aircraft's wake.

This dissertation provides two metrics of obtaining the sweet spot and evaluating the benefits to the trail aircraft at the sweet spot: a static and a dynamic study. The static study, similar to wind tunnel tests in which aircraft are statically placed in formation without trimming, investigates the induced aerodynamic forces and moments on the trail aircraft as it varies its position within the wake of the lead aircraft, and assigns the relative location of maximum lift-to-drag ratio as the static sweet spot. The dynamic study, similar to flight tests which account for trim, analyzes the control surface deflection and thrusts for the trail aircraft as it varies its

position within the lead's wake and assigns the location of minimum thrust as the dynamic sweet spot.

The static and dynamic analyses are applied to aircraft formations with different relative sizes and varying configurations of trail aircraft such as a flying-wing and a conventional aircraft. Results indicate that sweet spot locations and associated benefits are dependent on the weight of the leader and the relative sizes of the aircraft pair in the formation. This dissertation then augments the fuel-savings by investigating alternate lateral trimming methods to reduce the need for drag-inducing control effector deflections required at the static sweet spot. Internal fuel transfer and differential thrusting are employed to increase the thrust saved at the static sweet spot, making it comparable to the dynamic sweet spot.

Formation simulations of extended durations are also studied to understand the impact of significant weight variations in the leader on the formation benefits. In long-duration flights, the lead and trail aircraft weights decrease due to fuel burn. Since the upwash generated by the leader decreases with lift and weight as fuel is burned, the magnitudes of the non-uniform wind induced and thus benefits for the trail decrease. This decrease is investigated for a 6.5-hour formation simulation. Although there is a reduction in the benefits with time, the overall benefits of flying in formation is significant enough to motivate formations of such long durations.

Finally, the feasibility of formation flying is also considered from a perspective of comfort levels for passengers or aircrew in the trail aircraft. Using international standards for likely reactions of a person subjected to discomforts characterized by vibrations, it is shown that there is no additional detrimental degradation of comfort levels for a person onboard a trail aircraft in formation as compared to a solo flight.

TABLE OF CONTENTS

ACKNOWLEDGEMENTS iii

ABSTRACT iv

LIST OF ILLUSTRATIONS xi

LIST OF TABLES xvii

1. INTRODUCTION 1

1.1 Motivation 1

1.2 Literature Review 2

1.2.1 Formation Benefit Quantification 2

1.2.2 Sweet Spot Determination 3

1.2.3 Alternate Trimming Techniques 5

1.2.4 Aircraft Ride Quality 6

1.3 Problem Statement 9

1.4 Original Contributions 9

2. AIRCRAFT SIMULATION DEVELOPMENT 13

2.1 EQ-II Aircraft 14

2.1.1 Aerodynamic Model 15

2.1.2 Engine Configuration 28

2.1.3 Fuel Tank Configuration 29

2.1.4 Actuator Dynamics 32

2.2 Trail KC-135R Aircraft 33

2.2.1 Aerodynamic Model 33

2.2.2 Engine Configuration 41

2.2.3 Fuel Tank Configuration 43
2.2.4 Actuator Dynamics 43
2.3 Lead KC-135R Aircraft 45
2.3.1 Aerodynamic Model 45
2.3.2 Engine Configuration 47
2.3.3 Fuel Tank Configuration 47
2.3.4 Actuator Dynamics 48
2.4 Equations of Motion 48
2.4.1 Trail Aircraft 49
2.4.2 Lead Aircraft 54
2.5 Control Design 55
2.5.1 Trajectory-Tracking Control Design for Trail 55
2.5.2 VHRCAH Control Design for Lead 68
2.6 Non-uniform Wind Effect Modeling 70
2.6.1 Description 70
2.6.2 Validation 72
3. SWEET SPOT EVALUATION 77
3.1 Configuration 77
3.2 Analysis 78
4. KC-135R - EQ-II FORMATION 81
4.1 Static Study 82
4.1.1 Large EQ-II Variant behind KC-135R of Nominal Weight . . . 82
4.1.2 Large EQ-II Variant behind Heavy KC-135R 87
4.1.3 Small EQ-II Variant behind KC-135R of Nominal Weight . . . 87
4.2 Dynamic Study 90
4.2.1 Large EQ-II Variant behind KC-135R of Nominal Weight . . . 90

4.2.2 Large EQ-II Variant behind Heavy KC-135R 94
4.2.3 Small EQ-II Variant behind KC-135R of Nominal Weight . . . 96
4.3 Comparison of Results of EQ-II Static and Dynamic Study 98
5. ALTERNATE LATERAL TRIMMING METHODS 103
5.1 Configuration 104
5.2 Effect of Rotational Wind in Trim 104
5.3 Fuel Transfer and Differential Thrust Analysis 108
6. KC-135R - KC-135R FORMATION 114
6.1 Static Study 115
6.1.1 KC-135R Trailing KC-135R of Nominal Weight 115
6.1.2 KC-135R Trailing Heavy KC-135R 116
6.2 Dynamic Study 119
6.2.1 KC-135R Trailing KC-135R of Nominal Weight 120
6.2.2 KC-135R Trailing Heavy KC-135R 123
6.3 Comparison of Static and Dynamic Results for KC-135R Pair 125
7. SCALED KC-135R TRAILING KC-135R 127
7.1 Trail Aircraft Re-Sizing 127
7.1.1 Dimensional Scaling 128
7.1.2 Dynamic Scaling 130
7.2 Static Simulation Results 132
7.2.1 Large KC-135R Trail 132
7.2.2 Small KC-135R Trail 136
7.3 Dynamic Simulation Results 137
7.3.1 Large KC-135R Trail 137
7.3.2 Small KC-135R Trail 140
7.4 Discussion and Comparison of Results with Prior EQ-II Variants . . . 141

8. FORMATION FLIGHT OF EXTENDED DURATION 146
8.1 Simulation Modification 147
8.2 Full Mission Set-Up 148
8.3 Comparisons without Atmospheric Turbulence 153
8.4 Comparisons in the Presence of Atmospheric Turbulence 155
8.5 Impact of Turbulence on the Formation Benefits 158
9. RIDE QUALITY ANALYSIS 161
9.1 Methods 162
9.1.1 Evaluating Comfort Levels using ISO Standards 162
9.1.2 Analysis Procedure 165
9.2 KC-135R Trail 168
9.2.1 Accelerations at the CM_E 170
9.2.2 Accelerations Offset from the CM_E 176
9.3 Large EQ-II Trail 179
10. CONCLUSIONS AND A GUIDE TO FUTURE WORK 182
10.1 Evaluating Benefits: Static versus Dynamic Sweet Spot 185
10.1.1 Notable Results 185
10.1.2 Future Work 185
10.2 Aircraft Sizes 186
10.2.1 Notable Results 186
10.2.2 Future Work 186
10.3 Augmentation of Benefits using Alternate Trimming 187
10.3.1 Notable Results 187
10.3.2 Future Work 187
10.4 Long-Duration Formations 188
10.4.1 Notable Results 188

10.4.2 Future Work 188
10.5 Ride Quality Analysis 190
10.5.1 Notable Results 190
10.5.2 Future Work 190
Appendix
A. EQ-II AERODYNAMIC MODEL DATA 192
B. KC-135R AERODYNAMIC MODEL DATA 211
REFERENCES 225
BIOGRAPHICAL STATEMENT 235

LIST OF ILLUSTRATIONS

Figure Page

Figure 2.1 Drawing of EQ-II Model 14

Figure 2.2 C_D vs. δ_{ar} 23

Figure 2.3 C_D vs. δ_{er} 23

Figure 2.4 C_L vs. α 25

Figure 2.5 $C_{\mathcal{M}}$ vs. α 27

Figure 2.6 Engine model for aircraft models 29

Figure 2.7 Fuel Tank Shape 30

Figure 2.8 Motion of CM of Fuel in XYZ Directions 31

Figure 2.9 Top and Side View of CM of Fuel 32

Figure 2.10 Digital DatCom representation 34

Figure 2.11 Drag Coefficient versus angle-of-attack 37

Figure 2.12 Drag Coefficient versus side slip 38

Figure 2.13 Lift Coefficient versus angle-of-attack 39

Figure 2.14 Pitching Moment Coefficient versus angle-of-attack 41

Figure 2.15 Components of the Thrust Vector 42

Figure 2.16 Fuel Tank Locations for Trail KC-135R 44

Figure 2.17 Top View Fuel Tank Model 44

Figure 2.18 Front View Fuel Tank Model 45

Figure 2.19 KC-135R Configuration for CFD Runs 73

Figure 2.20 Aerodynamic Force Coefficients in Lateral Sweep 74

Figure 2.21 Aerodynamic Moment Coefficients in Lateral Sweep 74

Figure 2.22 Aerodynamic Force Coefficients in Vertical Sweep 75
Figure 2.23 Aerodynamic Moment Coefficients in Vertical Sweep 76
Figure 3.1 Depiction of Grid used in Static and Dynamic Simulations . . . 79
Figure 4.1 Lift to Drag Ratio of Large EQ-II 83
Figure 4.2 Aerodynamic Rolling Moment of Large EQ-II 84
Figure 4.3 Aerodynamic Yawing Moment of Large EQ-II 85
Figure 4.4 Aerodynamic Pitching Moment of Large EQ-II 85
Figure 4.5 Side Force Coefficient of Large EQ-II 86
Figure 4.6 Lift to Drag Ratio of Large EQ-II: Heavy KC-135R 88
Figure 4.7 Aerodynamic Roll Moment of Large EQ-II: Heavy KC-135R . . 88
Figure 4.8 Lift to Drag Ratio of Small EQ-II 89
Figure 4.9 Aerodynamic Rolling Moment of Small EQ-II 89
Figure 4.10 Simulation Stop Parameter of Large EQ-II 91
Figure 4.11 Thrust Increase of Large EQ-II 91
Figure 4.12 Aileron Deflection of Large EQ-II 92
Figure 4.13 Elevator Deflection of Large EQ-II 93
Figure 4.14 Rudder Deflection of Large EQ-II 94
Figure 4.15 Thrust Increase of Large EQ-II: Heavy Leader 95
Figure 4.16 Aileron Deflection of Large EQ-II: Heavy Leader 95
Figure 4.17 Thrust Increase of Small EQ-II 97
Figure 4.18 Aileron Deflection of Small EQ-II 97
Figure 4.19 Depiction of Wingtip Overlap Parameters 99
Figure 4.20 Sweet Spot Locations showing Zero Roll: EQ-II 100
Figure 5.1 Induced Wind 106
Figure 5.2 Control Variables Wind 107
Figure 5.3 Mass and CM of Fuel Tanks 110

Figure 5.4 Control Variables 111
Figure 6.1 Lift to Drag Ratio of KC-135R 116
Figure 6.2 Aerodynamic Rolling Moment of KC-135R 116
Figure 6.3 Aerodynamic Pitching Moment of KC-135R 117
Figure 6.4 Aerodynamic Yawing Moment of KC-135R 117
Figure 6.5 Side Force Coefficient of KC-135R 118
Figure 6.6 Lift to Drag Ratio of KC-135R: Heavy Leader 118
Figure 6.7 Aerodynamic Roll Moment of KC-135R: Heavy Leader 119
Figure 6.8 Simulation Stop Parameter of KC-135R 120
Figure 6.9 Thrust Increase of KC-135R 121
Figure 6.10 Aileron Deflections of KC-135R 121
Figure 6.11 Elevator Deflections of KC-135R 122
Figure 6.12 Rudder Deflections of KC-135R 122
Figure 6.13 Thrust Increase of KC-135R: Heavy Leader 124
Figure 6.14 Aileron Deflections of KC-135R: Heavy Leader 124
Figure 7.1 Scaled Aircraft Comparison 132
Figure 7.2 Lift to Drag Ratio of Large KC-135R 133
Figure 7.3 Aerodynamic Rolling Moment of Large KC-135R 134
Figure 7.4 Aerodynamic Yawing Moment of Large KC-135R 134
Figure 7.5 Aerodynamic Pitching Moment of Large KC-135R 135
Figure 7.6 Lift to Drag Ratio of Small KC-135R 136
Figure 7.7 Aerodynamic Rolling Moment of Small KC-135R 137
Figure 7.8 Simulation Stop Parameter of Large KC-135R 138
Figure 7.9 Thrust Increase of Large KC-135R 138
Figure 7.10 Aileron Deflection of Large KC-135R 139
Figure 7.11 Elevator Deflection of Large KC-135R 140

Figure 7.12 Rudder Deflection of Large KC-135R 141
Figure 7.13 Thrust Increase of Small KC-135R 142
Figure 7.14 Aileron Deflection of Small KC-135R 142
Figure 7.15 Sweet Spot Locations showing Zero Roll: Scaled KC-135R . . . 144
Figure 8.1 Fuel Tank Numbering for Trail KC-135R 149
Figure 8.2 Fuel Flow and Amount in Each Tank for Trail KC-135R 150
Figure 8.3 Lift Coefficients for Lead KC-135R 151
Figure 8.4 Induced Wind Components on Trail KC-135R 152
Figure 8.5 Fuel Burn Rate for Trail KC-135R 154
Figure 8.6 Fuel Saved for Trail KC-135R 156
Figure 8.7 Induced Wind Components with Turbulence 157
Figure 8.8 Trajectory of Trail in Turbulence 158
Figure 8.9 Turbulent Fuel Burn Rate for Trail KC-135R 159
Figure 8.10 Fuel Saved for Trail KC-135R in Turbulent Flight 160
Figure 8.11 Fuel Burned in Turbulent vs. Turbulence-Free Flight 160
Figure 9.1 Axis System for ISO 2631 163
Figure 9.2 Effective Wind Components for Trail 169
Figure 9.3 Linear and Angular Accelerations for Trail KC-135R 171
Figure 9.4 Acceleration PSD Estimates for Cases 1 and 2 172
Figure 9.5 Acceleration PSD Estimates for Cases 3 and 4 174
Figure 9.6 Acceleration PSD Estimates for Cases 4 and 5 175
Figure 9.7 Acceleration PSD Estimates: Locations Offset from CM_E . . . 177
Figure 9.8 Acceleration PSD Estimates for Cases 6 and 7 181
Figure A.1 C_D vs. α 193
Figure A.2 C_D (Pitching Moment) vs. α 194
Figure A.3 C_D vs. δ_r 194

Figure A.4 C_S vs. α 196
Figure A.5 C_S (Rolling Moment) vs. α 196
Figure A.6 C_S (Yawing Moment) vs. α 197
Figure A.7 C_S vs. δ_r 197
Figure A.8 C_S vs. δ_{ar} 197
Figure A.9 C_S vs. δ_{er} 198
Figure A.10 C_L (Pitching Moment) vs. α 199
Figure A.11 C_L vs. δ_r 199
Figure A.12 C_L vs. δ_{ar} 200
Figure A.13 C_L vs. δ_{er} 200
Figure A.14 $C_{\mathcal{L}}$ vs. α 201
Figure A.15 $C_{\mathcal{L}}$ (Rolling Moment) vs. α 201
Figure A.16 $C_{\mathcal{L}}$ (Yawing Moment) vs. α 202
Figure A.17 $C_{\mathcal{L}}$ vs. δ_{al} 202
Figure A.18 $C_{\mathcal{L}}$ vs. δ_{ar} 202
Figure A.19 $C_{\mathcal{L}}$ vs. δ_{el} 203
Figure A.20 $C_{\mathcal{L}}$ vs. δ_{er} 203
Figure A.21 $C_{\mathcal{M}}$ (Pitching Moment) vs. α 205
Figure A.22 $C_{\mathcal{M}}$ vs. δ_{al} 205
Figure A.23 $C_{\mathcal{M}}$ vs. δ_{ar} 206
Figure A.24 $C_{\mathcal{M}}$ vs. δ_{el} 206
Figure A.25 $C_{\mathcal{M}}$ vs. δ_{er} 206
Figure A.26 $C_{\mathcal{M}}$ vs. δ_b 207
Figure A.27 $C_{\mathcal{N}}$ (Rolling Moment) vs. α 208
Figure A.28 $C_{\mathcal{N}}$ (Yawing Moment) vs. α 208
Figure A.29 $C_{\mathcal{N}}$ vs. δ_r 209

Figure A.30 $C_{\mathcal{N}}$ vs. δ_{ar} 209
Figure A.31 $C_{\mathcal{N}}$ vs. δ_{er} 209
Figure B.1 $\boldsymbol{f}_{\boldsymbol{C}_{D_{\delta_e}}}$ vs. δ_e 212
Figure B.2 $\boldsymbol{f}_{\boldsymbol{C}_{D_{\delta_a}}}$ vs. δ_a 213
Figure B.3 $\boldsymbol{f}_{\boldsymbol{C}_{D_{\delta_r}}}$ vs. δ_r 213
Figure B.4 $\boldsymbol{C}_{L_{\dot{\alpha}}}$ vs. α 214
Figure B.5 $\boldsymbol{f}_{\boldsymbol{C}_{L_{\delta_e}}}$ vs. δ_e 214
Figure B.6 $\boldsymbol{C}_{S_{p1}}$ vs. α 215
Figure B.7 $\boldsymbol{f}_{\boldsymbol{C}_{S_{\delta_r}}}$ vs. δ_r 215
Figure B.8 $\boldsymbol{C}_{\mathcal{L}_{\beta 1}}$ vs. α 216
Figure B.9 $\boldsymbol{C}_{\mathcal{L}_{p1}}$ vs. α 216
Figure B.10 $\boldsymbol{C}_{\mathcal{L}_{r1}}$ vs. α 218
Figure B.11 $\boldsymbol{f}_{\boldsymbol{C}_{\mathcal{L}_{\delta_a}}}$ vs. δ_a 218
Figure B.12 $\boldsymbol{f}_{\boldsymbol{C}_{\mathcal{L}_{\delta_r}}}$ vs. δ_r 219
Figure B.13 $\boldsymbol{C}_{\mathcal{M}_{\dot{\alpha}}}$ vs. α 220
Figure B.14 $\boldsymbol{f}_{\boldsymbol{C}_{\mathcal{M}_{\delta_e}}}$ vs. δ_e 220
Figure B.15 $\boldsymbol{C}_{\mathcal{N}_{p1}}$ vs. α 222
Figure B.16 $\boldsymbol{C}_{\mathcal{N}_{r1}}$ vs. α 222
Figure B.17 $\boldsymbol{f}_{\boldsymbol{C}_{\mathcal{N}_{\delta_a}}}$ vs. δ_a 223
Figure B.18 $\boldsymbol{f}_{\boldsymbol{C}_{\mathcal{N}_{\delta_r}}}$ vs. δ_r 223

LIST OF TABLES

Table		Page
Table 2.1	Comparison of HASC02 Predictions and Wind Tunnel Data	16
Table 2.2	Geometric Parameters for EQ-II	21
Table 2.3	Geometric Parameters for KC-135R	35
Table 2.4	Nominal Conditions by Turn rate and Airspeed	67
Table 4.1	Aircraft Formation Pairs	81
Table 4.2	Summary of Static and Dynamic Results for EQ-II	102
Table 5.1	Thrust Comparison	108
Table 5.2	Thrust Comparison with Alternative Trim	113
Table 5.3	Thrust Comparison with Alternative Trim: Heavy Leader	113
Table 6.1	KC-135R - KC-135R Aircraft Formation Studies	115
Table 6.2	Summary of Static and Dynamic Results for Trail KC-135R	125
Table 7.1	Aircraft Wingspan	128
Table 7.2	Summary of Static and Dynamic Results for Scaled KC-135R	143
Table 9.1	ISO Vibration Total Values and Comfort Levels	164
Table 9.2	Ride Quality Cases for Trail KC-135R	168
Table 9.3	Passenger Locations within Trail	176
Table 9.4	Vibration Values at Different Locations	178
Table 9.5	Ride Quality Cases for Large EQ-II	180
Table A.1	Drag Coefficient Parameters	195
Table A.2	Side Force Coefficient Parameters	198
Table A.3	Lift Coefficient Parameters	200

Table A.4 Rolling Moment Coefficient Parameters 204
Table A.5 Pitching Moment Coefficient Parameters 207
Table A.6 Yawing Moment Coefficient Parameters 210
Table B.1 Drag Coefficient Parameters 217
Table B.2 Lift Coefficient Parameters 217
Table B.3 Side Force Coefficient Parameters 217
Table B.4 Rolling Moment Coefficient Parameters 219
Table B.5 Pitching Moment Coefficient Parameters 221
Table B.6 Yawing Moment Coefficient Parameters 224

CHAPTER 1

INTRODUCTION

1.1 Motivation

Nature has shown that birds fly in a vee formation during migration. In theory, this results in an increase in the range capability of each bird in the formation [1, 2, 3]. The formation leads to a reduction in drag experienced by the birds due to the wingtip vortices generated by the preceding birds. The birds intuitively know the region of the localized upwash that requires less thrust and enables them to fly longer. This improvement in aerodynamic performance has led researchers to investigate how aircraft can fly in formation and obtain similar aerodynamic benefits which lead to drag reduction and fuel savings.

Like birds, aircraft flight generates wake vortices that induce non-uniform wind field in their wake. A trailing aircraft, flying in the wake of the lead aircraft, can experience induced wind components and gradients with various magnitudes and directions depending on the location within the induced non-uniform wind field. The non-uniform wind field can be beneficial or detrimental to the trail aircraft and it has been demonstrated [4, 5, 6, 7] that there is a "sweet spot" within the wake of the leader aircraft where the follower aircraft experiences upwash, which leads to reduced drag. The reduced drag translates to a reduction in thrust and thus fuel saving, proving the rational for formation flight. Through this mechanism, when aircraft fly in formation, they can save significant amounts of fuel by flying at the "sweet spot" of the lead aircraft's wake.

1.2 Literature Review

This section is focused on summarizing the prior studies pertaining to formation flight and this research. The relevant research studies related to the quantification of the benefits of formation flight are presented and compared. In addition, overviews are presented of unconventional trimming methods to increase the benefits of flying in formation, such as moving mass actuation and differential thrusting. This is done to assess the feasibility of employing these methods in this study to improve the existing formation benefits. A literature review on ride quality from the perspective of flying in formation is then presented.

1.2.1 Formation Benefit Quantification

The implication of the improved aerodynamic performance of the trail aircraft has motivated a number of studies on formation flight by the industry, academia, and the government [8, 9, 10, 11] with different methods of quantifying the formation benefits. The Air Force Research Laboratory (AFRL), for instance, has a renewed interest in formation flight as a new initiative pertaining to fuel efficiency. Former Air Force Chief Scientist, Dr. Werner J.A. Dahm, is reported [12] stating "You can have aircraft flying separated along the trailing vortex at a greater distance than some might assume – even in vertical separation – and still get fuel efficiency benefits while addressing safety and other concerns about this type of flying". To this effect, a number of wind tunnel, computer simulation, and flight test measurements have been done to ascertain the feasibility and quantify the benefits of formation flight.

The earliest quantitative flight test measurements were done in the late 20th century by Hummel using Dornier-28 aircraft [8]. Knowing apriori that the location of maximum aileron deflection is close to the position for maximum drag reduction, they used a peak-seeking controller to find the location of maximum aileron deflection,

where they obtained significant power reduction. More recently, NASA, within the Autonomous Formation Flight Program, conducted formation flight tests of two F/A-18 aircraft at different Mach numbers and altitudes [9, 13]. The tests indicated significant drag reductions over 20% and fuel savings over 18% [13] for the trail aircraft when placed with wingtip overlap from 10 - 20% wingspan with respect to the lead aircraft. A study by the Air Force Institute of Technology (AFIT) looked at the impact of trimming the aircraft on the location of the sweet spot [11]. This earlier assessment of T-38 formation flight by AFIT discovered that when the effect of aileron deflection was considered, the sweet spot moved inboard by 0.04 spans compared to the untrimmed case. Although the T-38 study ignored pitch and yaw trim, the actual aircraft will have to be trimmed with the elevator for pitch moments and the rudder for yaw moments. These studies suggest that the formation flight benefits can be quantified in different ways including thrust/fuel savings and drag reduction. These methods of quantification are not necessarily one to one and it is important to understand the reasons for the disparities between them.

1.2.2 Sweet Spot Determination

In this dissertation, it is assumed that the sweet spot can be obtained online during flight. Thus, the focus is on maintaining that sweet spot using a trajectory-tracking controller to position the trail aircraft relative to the leader at the sweet spot. In practice, the location of the sweet spot first has to be determined in flight using a control algorithm to steer the trail aircraft in the direction of the sweet spot which could be quantified using thrust or fuel flow reductions, drag reductions, or maximum aileron deflections. This falls under the umbrella of extremum-seeking (peak-seeking) control, which involves on-line optimization to find a maximum or minimum of a certain function. This control technique has made a resurgence in

the last few decades in various fields such as fluid flow, combustion, and biomedical systems [14].

In the area of formation flight, peak-seeking has been used in conjunction with non-linear estimation techniques such as, Kalman and Particle Filters, to determine the characteristics of the property to be minimized or maximized in order to find the sweet spot. One of the earliest extremum-seeking applications to formation flight was done by Hummel, in which he utilized a discrete-time peak-seeking algorithm to find the location of maximum aileron deflection in the lateral direction and maximum induced upwash in the vertical direction of a trail Dornier Do-28 aircraft in formation with another [8]. More recently, Chicka et al [15] derived a peak-seeking controller to find the location of maximum induced rolling moment on the trail aircraft, assuming that the rolling moment can be effectively measured and the location of maximum induced rolling moment corresponds to the location of maximum induced lift. That study ignored changes in the lift distribution resulting from control deflections. Similarly, researchers Binetti [16] and Ryan [17] utilized the Kalman Filter to estimate the gradients (and Hessian in the case of Ryan [17]) of their performance functions optimizing pitch angle and induced drag coefficient respectively. Binetti et al [16] did not consider trim drag in determining the location of minimum pitch angle for their trailing Lockheed C-5 aircraft and assume that this static location of minimum pitch angle is the optimum position for formation flight for the pair of C-5 aircraft. Ryan et al [17] employed the induced drag coefficient map considering trimming. Although this technique considers trim effect, static maps are first created and the algorithm is not an online extremum-seeking technique. The different metrics used to guide the peak-seeking controllers to the sweet spot reiterate the differences that exist in the literature for quantifying the benefits of formation.

1.2.3 Alternate Trimming Techniques

Studies such as Hummel's, discovered that the induced aerodynamic moments on the trail aircraft, at the sweet spot, result in the need for deflections of the aileron and rudder with "moderate sized" adverse drag-inducing effects [8]. When the trail aircraft is placed at the sweet spot of the lead aircraft, the trail experiences lower drag but at the same time experiences induced aerodynamic moments [18]. Thus, to trim the aircraft under the effect of the induced moments, its control effectors need to be trimmed with such deflections that they may induce additional drag, which reduces the benefits of fuel efficiency. For example, ailerons and rudder are trimmed in non-zero deflections, which increase the aircraft drag [18]. Thus, if alternate methods of trimming the aircraft can be found to reduce/eliminate the need for the control surfaces, then equivalent or possibly higher fuel savings could be obtained at the sweet spot.

One alternate trimming method is moving-mass actuation to affect the aircraft dynamics. It has been shown that variations in the mass and inertia distribution of a system [19, 20, 21, 22, 23] have an effect on its dynamics and could be used as a method of control for a vehicle [24, 25, 26, 27]. The Concorde supersonic transport redistributed fuel during flight to trim [28, 29, 30] and that approach is closely related to unconventional trimming technique utilized in this dissertation. In the Concorde, the weight distribution and thus the center of mass is changed by pumping fuel from the forward trim tanks to the rear trim tanks and vice versa to compensate for the change in the center of lift from the wings.

Another alternate trimming technique is employing differential thrust to generate moments to trim. The advent of research into utilization of differential thrusting to trim in case of control surface failure was preceded by a NASA Dryden Research Center development of a Propulsion-Controlled Aircraft system (PCA)[31]. This sys-

tem was evaluated in simulations and actual flight to assess the feasibility of differential thrusting as an emergency replacement to control damaged aircraft [32]. Their studies indicated that the PCA system works and is able to provide enough control authority for a "survivable landing" [32]. Commercial jetliner pilots have utilized differential thrusting to provide additional flight control authority in the roll and yaw [33] as evidenced by a United Airlines flight in which there was control surface failure on the McDonnell Douglas DC-10 aircraft. Asymmetric thrusting of the engines on the wing was then used to stabilize and control the aircraft [34]. One disadvantage of this technique is that engine dynamics is usually slower than the actuator dynamics and is one of the reasons differential thrusting is used as a last resort to trim. In the case of formation flight, the lag in the engine response is not of concern as it is not an emergency control situation but a mechanism for reducing the trim drag in a steady-state cruise flight.

1.2.4 Aircraft Ride Quality

Ride quality is a measure of the comfort levels for an individual located in a vehicle as it is subjected to vibrations, accelerations, and adverse atmospheric effects such as turbulence. It is typically desired that a quantitative measure of comfort levels be obtained as opposed to simply qualifying the comfort levels as "steady", "unsteady", "smooth", or "turbulent." A passenger's health, physiology, and psychological attitude [35] can influence the quantification of ride quality, making the determination of ride quality a subjective endeavor. Since human perception of comfort is subjective and depends on a host of factors, some attempts are made to incorporate the subjective human biases into the assessment of ride quality [35, 36, 37]. These attempts stress the importance of accounting for passenger-dependent factors

in addition to environmental conditions such as wind and turbulence, in determining the highly non-linear subjective assessment of ride quality.

Another approach is to eliminate the human biases to provide an objective quantitative measure of a qualitative quantity. The International Organization for Standardization (ISO) outlines a guide (ISO 2631-1) which can be used to provide an assessment of human comfort levels during exposures to whole-body vibration based on frequency-weighted accelerations [38]. This standard is an extension of von Gierke's studies [39, 40] on human tolerance to vibration frequencies and amplitudes and expands upon the importance of vibration characteristics of frequency and amplitude on human endurance limits.

The principal advantage of the ISO 2631-1 standard is that it provides an objective characterization of the vibration environment with respect to its effect on a human. ISO 2631-1, though far-reaching in its applicability, can not be used in all ride assessment analyses such as when the acceleration frequencies under consideration are significantly higher than the 80 Hz upper ISO 2631-1 limit or when the accelerations tend to be impulsive and can not be analyzed spectrally as is the case with marine vehicles [41]. For aircraft applications, ISO 2631-1 standard has been utilized successfully in various studies for a number of environmental conditions which fall under the envelope of its usage.

Regarding formation flight, there have only been a few mentions of passenger comfort in formation. NASA Dryden during a preliminary flight test of C-17 aircraft formation [42] noted crew comments on the ride quality of the trail aircraft when attempting to maintain certain positions relative to the lead. The crew noted where the ride was smooth in some locations and in others, the ride was "very unsteady." Additional input was provided by the flight test engineer who noted the pilot's re-

actions during the ride and reported "rougher ride quality-buffeting" where the crew also felt the unsteadiness of the ride.

More recently, the AFRL in conjunction with Boeing researchers conducted a full endurance mission of a C-17 aircraft pair formation from Edwards Air Force Base, California to Joint Base Pearl Harbor-Hickam, Hawaii and back. During this flight test, they demonstrated "in-flight rendezvous, day and night operations, and flew several hours in each direction" [43]. One important aspect of this mission was to understand how the formation impacted the aircrew workload and minimal workload with satisfactory ride quality was qualitatively reported by the aircrew.

Michael et al [44] investigated ride quality as an analysis metric of an autonomous formation flight system. String stability, a measure of how errors propagate along a stream of interconnected systems, was analyzed. The formation was allowed to have string instability which implies that position errors increasingly propagate from one aircraft to the next. ISO 2631-1 was employed to translate the vehicle accelerations to a measure of pilot comfort. They reported that the ride quality was a surprisingly significant factor in assessing string stability and constraining the autonomous formation flight system to certain gain-sets for development and flight testing.

A quantitative assessment of passenger comfort in formation flight was done by Bizinos [45] using a two-aircraft formation. A simplified aerodynamic model of the two aircraft in the formation was employed assuming ideal control and no compensatory control inputs by the pilot or autopilot. Bizinos employed varying turbulence intensity levels and obtained the acceleration responses of the trail aircraft which were then converted to passenger comfort levels using the ISO 2631-1 Standard. These passenger comfort levels were compared to comfort levels for an aircraft flying solo under these

same turbulent conditions and it was observed that there was an increase in passenger discomfort at the optimum drag location for the trail aircraft.

1.3 Problem Statement

This dissertation aims to provide a holistic approach to the formation flight endeavor. Specifically, the aim is to formulate the problem considering the benefits of flying different aircraft configurations in formation, accounting for the effect of trim, trail aircraft size, and lead aircraft weight on the formation benefits, exploring the feasibility of increasing the savings currently obtained by flying in formation, and determining the performance of formation from the perspective of ride quality.

1.4 Original Contributions

There are different methods of studying aircraft formation flight. With such variations in analysis, there is no consistent uniform metric with which to quantify the benefits of flying in formation. For this reason, this dissertation establishes two methods to determine the sweet spot for different pairs of aircraft: a static and dynamic analysis. The static analysis does not account for trimming and assigns the sweet spot as the relative location for the trail aircraft in which the lift to drag ratio is the highest. The dynamic analysis, similar to an actual flight in which trimming is performed assigns the sweet spot where the thrust required for the trail aircraft is the least.

This dissertation also answers the question of whether the sweet spot determined from the static study changes once the trimming of the aircraft is considered in the dynamic simulation. As in the AFIT study of the T-38 formation [11], trim-

ming needs to be considered. In this research, pitch, roll, and yaw are accounted for unlike the T-38 study which did not account for pitch and yaw trim.

It is also not clear which sweet spot, static or dynamic, poses the best benefits for formation. It is shown that at the static sweet spot, the induced aerodynamic moments require that the control effectors of the trailing aircraft be trimmed with such deflections that they may induce additional drag, which will reduce the benefits of fuel efficiency for certain trail aircraft configurations. The ailerons and rudder, for instance, are trimmed in non-zero deflections, which increase the aircraft drag [7]. This dissertation shows which sweet spot is the most advantageous for which aircraft pair.

An additional contribution in this dissertation is in the aircraft type utilized in the formations. Most prior studies of formation flight such as those done by Hummel and NASA used (i) homogenous configurations in which the lead and trail aircraft are identical and (ii) relatively conventional aircraft pairs with fuselage and tail configurations. In this research a conventional pair of KC-135R tanker aircraft is utilized as well as a heterogenous aircraft pair. For the heterogenous formation, a conventional KC-135R tanker is used as the lead aircraft while an unconventional flying-wing EQ-II aircraft model is utilized as the trail aircraft. Two variants of the EQ-II are studied in this dissertation, a large and small variant.

In addition, it is unknown how changes in the mass of the lead aircraft in the formation affect the location of the sweet spot and the associated benefits of flying in formation. There is a dependence of the vortex strength of an aircraft on its weight. Thus, as the lead aircraft weight changes in flight, the strength of the vortices it generates will also vary. This may impact the results of the formation analysis and corresponding benefits. Studies are presented which show the effect of a change in lead aircraft weight on the aerodynamics and thrust-saving benefits for the trail aircraft.

Based on the fact that the results of the formation study and associated benefits are dependent on the weight of the lead aircraft, a formation of long-duration is studied as an original contribution to this field. Formation flights of long duration, representative of transatlantic missions, are simulated to provide realistic assessments of the benefits of flying a mission in formation as the weights of the lead and trail aircraft decrease due to fuel burn, not just at a point in time in which the weights are constant.

Also, the effect of variations in the size of the trail aircraft have not been studied. A prior numerical analysis by Thien et al [46] investigated the effects of the lead aircraft's position and shape on the aerodynamic performance of the formation. Specifically, the shape, wing position, incidence angle, aspect ratio, dihedral, and taper ratio of the lead aircraft were varied and the effect on the lift, drag, and pitching moments of the trail aircraft were studied using a simple wing model. In that study, only the geometrical aspect of the lead aircraft was varied. This dissertation examines the effect of using different sized trail aircraft for the formations.

Furthermore, this research improves the fuel savings for the trail aircraft in formation by reducing the drag-inducing control effector deflections at the sweet spot. This is done by employing unconventional methods of trimming such as differential thrusting and internal fuel transfer to move the center of gravity of the aircraft and generate moments to trim. These techniques have been previously utilized to generate moments to trim an aircraft in fields other than formation flight. Combining these two methods has the capability of increasing the fuel savings obtained in formation flight. It is demonstrated in this dissertation that moving the center of mass with fuel transfer between fuel tanks and utilizing differential thrusting enables trimming the aircraft with minimal deflection of control effectors.

Finally, this dissertation assesses the quality of flight as a passenger or aircrew member is seated within the trail aircraft during a formation. This quantitative analysis incorporates a principal factor of closing the loop and factoring in control responses to the environmental conditions. Bizinos [45], who studied passenger comfort in the trail aircraft for various turbulence cases, performed an open-loop study with no control algorithm which prevented the simulation of non-zero perturbed state variables. In this research, the effect of the controller on the closed-loop system is accounted for in the ride quality determination using the ISO 2631-1 guidelines.

CHAPTER 2

AIRCRAFT SIMULATION DEVELOPMENT

This chapter presents the details of the simulation developed for the formation flight study with regards to the aircraft types and models, control design, and aerodynamic effect from the lead on the trail. The present work uses previously developed equations of motion for a lead tanker aircraft and a trail aircraft undergoing aerial refueling that include time-varying mass and inertia due to fuel transfer and the non-uniform wind effect from the tanker [47]. The equations were implemented in an integrated MATLAB/Simulink-based environment with feedback controllers for the lead tanker aircraft to hold speed, altitude, and commanded yaw rate, and for the trail (receiver) aircraft to maintain a trajectory relative to the lead.

The simulation environment is developed in a modular structure such that a new aircraft can easily be introduced into the simulation. Results of the simulation were verified using flight test data from the 2004 Automated Aerial Refueling program and the simulations are based on realistic flight data. Thus, the simulation can accurately reproduce test flight conditions for any pair of aircraft in terms of wind and turbulence exposure and relative motion, as well as other state variables such as altitude and airspeed. Overviews of the aircraft equations of motion, aerodynamic models, non-uniform wind effect modeling, and the control design for the lead and trail aircraft, are presented in this chapter with additional details provided in the Appendices.

2.1 EQ-II Aircraft

The Equivalent Model-II (EQ-II) is a fictional vehicle initially created in support of the USAF Automated Aerial Refueling (AAR) program, which developed the technologies and components necessary to provide in-flight refueling of air vehicles [48]. The aircraft was created to represent the performance and maneuvering characteristics of a long range, high subsonic cruise, low observable, tailless bomber. It was developed using conceptual design methods for planform geometry and sizing, vortex lattice methods for aerodynamic estimations, and historical data based non-dimensional radius of gyration calculations for inertia properties [49]. The EQ-II has two variants, a small and large, with wingspans of 34 m and 51 m, respectively. Although the two variants have identical aerodynamic properties, they have different mass/inertia properties and different engine characteristics.

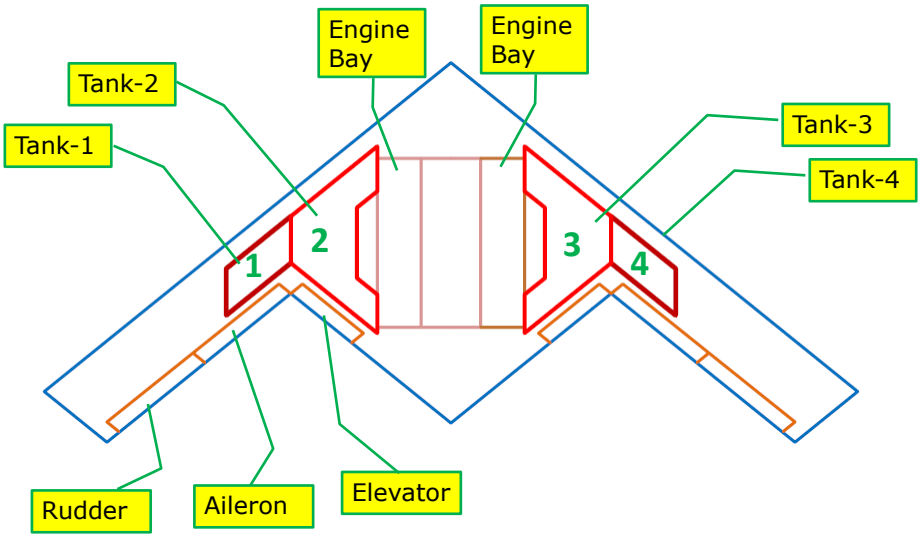

Figure 2.1. Drawing of EQ-II Model [49].

A schematic of the fuel tank and control surfaces of the EQ-II is given in Fig. 2.1. Both large and small variants of the EQ-II have six control surfaces; namely, the left clamshell (δ_{rl}), right clamshell (δ_{rr}), left outboard elevon (δ_{al}), right outboard elevon (δ_{ar}), left inboard elevon (δ_{el}) and right inboard elevon (δ_{el}). Independent control surfaces are designed for pitch, roll, yaw, and deceleration use. Pitch control can be attained with the inboard elevons while the outboard elevons can be used as ailerons for roll control. Yaw control may be attained by utilizing the clamshell surfaces on each of the wings. Using the clamshells on both sides provides the function of a speed brake. Multiple surfaces may be commanded together for additional effectiveness if required. Also the EQ-II has multiple engines which can be independently controlled to generate differential thrust for additional yaw control. The EQ-II model is derived from an Equivalent Model (EQ-I) aircraft which was developed to enable the creation of a simulation model for automated aerial refueling of unmanned aerial vehicles. Additional details of the EQ-I model can be obtained in Reference [50].

An aerodynamic model for the EQ-II aircraft is developed for implementation in an integrated simulation environment for aerial refueling and formation flight. This model was employed in simulations as a receiver to simulate its effects on the tanker aircraft and vice versa during aerial refueling operations. For formation flight, the aircraft model is employed in simulations as a trail aircraft to study the fuel-saving benefits it obtains as it flies in formation with a leader.

2.1.1 Aerodynamic Model for EQ-II

This section shows the procedure of estimating the aerodynamic force and moment coefficients using polynomial functions which can be implemented in a simulation environment and used to investigate the response of the EQ-II aircraft in a variety of flight conditions.

Table 2.1. Comparison of HASC02 Predictions and Wind Tunnel Data

Parameter	HASC02	N-9M	XB-35
C_{L_α} (1/rad)	4.53	4.58	4.39
$C_{\mathcal{M}_\alpha}$ (1/rad)	-0.18	-0.26	-0.22
$k(dC_D/dC_L{}^2)$	0.043		0.051
$C_{L_{\delta_e}}$ (1/rad)	0.79	0.74	0.74
$C_{\mathcal{M}_{\delta_e}}$ (1/rad)	-0.28	-0.23	-0.26
$C_{\mathcal{M}_q}$ (1/rad)	-1.40		-1.56

The aerodynamic coefficient data of the Equivalent Model II (EQ-II) aircraft and damping derivative data were estimated using vortex lattice methods with empirical corrections for the EQ-II configuration as described in Section 2.1.1.1. Control surface effectiveness of the EQ-II which utilizes clamshells and elevons for pitch, roll, and yaw control, was also estimated using the same methods. Section 2.1.1.2 presents the aerodynamic force and moment coefficients in the form of polynomial expressions fitted into these data points.

2.1.1.1 Computational Tools

The majority of the aerodynamic database was obtained from the vortex lattice code HASC02, which is an updated version of the NASA code HASC95 [51], and supplemented with CFD data. The CFD runs were done using a thick airfoil and a flat airfoil. HASC does not consider thickness or airfoil volume thus, it is acceptable to use the CFD airfoil data to confirm the trends and magnitudes of the aerodynamic force and moment coefficients estimated from the HASC02 data.

HASC02 predictions are first compared with wind tunnel data for vintage flying wing configurations [52, 53] as shown in Table 2.1. Both sets of data are with the propellers removed. The HASC02 results compare very well with the test data.

The HASC02 grid for the EQ-II was generated manually based on the design given in the specification for the large EQ-II variant which is also referred to as the Equivalent Model III (EQ-III) [48]. The wing was modeled as a flat plate. HASC02 does not include viscous effects so corrections to the database were made in several areas. Zero-lift drag at cruise was estimated at 0.010. This value is somewhat high compared to typical flying wing wind tunnel data, but was chosen to account for propulsion installation effects and excrescences present on full scale aircraft but absent on most wind tunnel models. The elevators and ailerons were modeled by HASC02. However, their effectiveness was reduced for large deflections using factors obtained from the USAF Datcom [54]. For example, for a 30 degree deflection of the outboard elevons, the effectiveness is reduced by 35%. Profile drag for the conventional trailing edge devices was also taken from the Datcom. The clamshell type drag rudders were modeled using an empirical database that has been assembled at the Air Force Research Laboratory (AFRL) [55]. This database shows that at low angles of attack, a clamshell control generates a force which is effectively perpendicular to the hingeline of the surface and is a function of the deflection angle only. From the sweep of the hingeline, this force is divided into body axis axial force and side force components, which are then resolved into a yawing moment based on the respective moment arms.

One of the design goals for the EQ-II was neutral stability in pitch and yaw. This was satisfied by placing the nominal center of gravity at the aerodynamic center predicted by HASC02, and zeroing the yawing moment variation with sideslip. A complete tabular listing of the aerodynamic database is given in the EQ-III model specification report [48].

2.1.1.2 Modeling Aerodynamic Coefficients

The basic aerodynamic coefficient data (C_N, C_A, C_Y) in the body-fixed frame and damping derivative data were estimated using vortex lattice methods with empirical corrections for the Equivalent Model-II configuration, as described above. From the HASC02 code, the aerodynamic force components in the body frame are obtained. In the implementation of the aerodynamic model, the components in the wind frame, i.e., drag, side force, and lift coefficients, are preferred. To compute the components in the wind frame from the components in the body frame, the rotation matrix from the wind frame to body frame, in terms of the angle of attack and side slip, is used, which leads to

$$C_L = -\sin(\alpha)C_A + \cos(\alpha)C_N \tag{2.1}$$

$$C_D = \cos(\alpha)\cos(\beta)C_A - \sin(\beta)C_Y + \sin(\alpha)\cos(\beta)C_N \tag{2.2}$$

$$C_S = -\cos(\alpha)\sin(\beta)C_A - \cos(\beta)C_Y - \sin(\alpha)\sin(\beta)C_N \tag{2.3}$$

where the values of angle of attack, α, were [-6, -4, -2, 0, 2, 4, 6, 8, 10, 12] and the values of sideslip, β, were [-15, -10, -5, 0, 5, 10, 15].

The aerodynamic coefficients could be organized as look-up tables which could then be used directly in simulations. Instead, representations of the aerodynamic data are obtained by assuming polynomial functions. The coefficients of the polynomials are computed by employing the LSE (Least Squares Estimation) method. This functional approach is preferred to the look-up tables because functional (polynomial) representation is easier to implement in simulation and more suitable for linearization as the linearization requires the partial derivatives of the aerodynamic coefficients. The orders of the polynomials are determined based on the LSE error comparison. The order of a polynomial is increased only when the LSE error is significantly reduced compared to the polynomial of lower order. For certain coefficients, the range

of the data points are divided into two parts (mostly as negative and positive ranges) and two separate polynomial fits are carried out. This is done when a very high order would be required to cover the whole range with a single polynomial. This is the approach taken in developing the aerodynamic model for all aircraft utilized in this dissertation.

To derive the functional representations of the aerodynamic force and moment coefficients, polynomial approximations were obtained through curve fitting to derive the dependencies of the coefficients on each of the independent variables (angles of attack and sideslip, pitch, roll and yaw rates, and the control effector deflections) separately. In some instances, the force or moment coefficients exhibit dependency on both the angle of attack and sideslip. To capture this additional dependency, the coefficients of a polynomial function were first estimated for each value of α (or β). Then, each of the estimated coefficients was used as the dependent variable in new polynomial functions with α (or β) being the independent variable of the functions. Finally, the coefficients from all functions were then combined to derive the final functional representation of the aerodynamic coefficient.

For example to determine the relationship between C_D and α, a polynomial function was approximated for the drag dependence on angle of attack. The coefficients of this function were estimated multiple times, once for each value of β

$$C_D = \eta_2 \alpha^2 + \eta_1 \alpha + \eta_0 \tag{2.4}$$

The estimated coefficients, η_i, were then used as the dependent variables in a new function,

$$\eta_i = \lambda_2 \beta^2 + \lambda_1 \beta + \lambda_0, \tag{2.5}$$

where the λ are the coefficients estimated for this polynomial. Thus, the final model is

$$C_D = \eta_2(\beta)\alpha^2 + \eta_1(\beta)\alpha + \eta_0(\beta) \tag{2.6}$$

This polynomial representation allows the relationship between C_D and α to change relative to the value of β, thus capturing the dependence on both the angle of attack and the sideslip angle. For easy referencing in this dissertation, the coefficients of the independent variables are labeled using a combination of the independent variables and their respective orders. For instance, $\mathbf{C}_{F_{\alpha 2}}$ is the "F" aerodynamic coefficient of the α variable to the second order. The superscript in the coefficient, if there is one, identifies the second variable on which the coefficient has an additional dependency. Thus, $\mathbf{C}^{\beta 2}_{F_{\alpha 2}}$ is the coefficient of the β^2 variable in the $C_{F_{\alpha 2}}$ expression. Control surface effectiveness was estimated using the same methods as the aerodynamic force and moment coefficients, however the value of β was zero for all cases of α.

Sections 2.1.1.3 and 2.1.1.4 contain the expressions for the force and moment coefficients, respectively. These equations were derived using the model as explained in Eqs. (2.4) - (2.6). Each force or moment coefficient equation have a set of graphs that are a visual representation of the relationships depicted in the equation. For brevity, a few of these graphs are presented in Sections 2.1.1.3 and 2.1.1.4 while the others are given in Appendix A. The square markers that are on each graph represent the data obtained from HASC02 that was used to estimate the model coefficients. The solid lines and other non-square figures represent the fitted line for the given variable.

Table 2.2. Geometric Parameters for EQ-II

Parameter	Small EQ-II	Large EQ-II
S_R (m^2)	176.79	397.81
b (m)	33.89	50.84
c (m)	7.08	10.62

2.1.1.3 Force Coefficients

The aerodynamic forces are given by the following standard expressions

$$D = \frac{1}{2}\rho V^2 S_R C_D, \tag{2.7}$$

$$S = \frac{1}{2}\rho V^2 S_R C_S, \tag{2.8}$$

$$L = \frac{1}{2}\rho V^2 S_R C_L, \tag{2.9}$$

where S_R is the surface area of the EQ-II and ρ is the ambient air density. The geometric properties of the large and small variants of the EQ-II aircraft used in the aerodynamics are given in Table 2.2.

The aerodynamic drag coefficient is

$$\begin{aligned} C_D = {} & \mathbf{C}_{D_{\alpha 2}}(\beta)\alpha^2 + \mathbf{C}_{D_{\alpha 1}}(\beta)\alpha + \mathbf{C}_{D_{\alpha 0}}(\beta) \quad + \mathbf{C}_{D_q}(\alpha)(\frac{l}{2V})q + \mathbf{C}_{D_{\delta_{r1}}}(\alpha)(\delta_{rl} + \delta_{rr}) \\ & + \mathbf{f}_{C_{D_{\delta_a}}}(\delta_{al}) + \mathbf{f}_{C_{D_{\delta_a}}}(\delta_{ar}) + \mathbf{f}_{C_{D_{\delta_e}}}(\delta_{el}) + \mathbf{f}_{C_{D_{\delta_e}}}(\delta_{er}) \end{aligned} \tag{2.10}$$

where

$$\mathbf{C}_{D_{\alpha 2}} = C_{D_{\alpha 2}}^{\beta 2}\beta^2 + C_{D_{\alpha 2}}^{\beta 1}\beta + C_{D_{\alpha 2}}^{\beta 0} \tag{2.11}$$

$$\mathbf{C}_{D_{\alpha 1}} = C_{D_{\alpha 1}}^{\beta 2}\beta^2 + C_{D_{\alpha 1}}^{\beta 1}\beta + C_{D_{\alpha 1}}^{\beta 0} \tag{2.12}$$

$$\mathbf{C}_{D_{\alpha 0}} = C_{D_{\alpha 0}}^{\beta 2}\beta^2 + C_{D_{\alpha 0}}^{\beta 1}\beta + C_{D_{\alpha 0}}^{\beta 0} \tag{2.13}$$

$$\mathbf{C}_{D_q} = C_{D_q}^{\alpha 1}\alpha + C_{D_q}^{\alpha 0} \tag{2.14}$$

$$\mathbf{C}_{D_{\delta_{r1}}} = C_{D_{\delta_{r1}}}^{\alpha 2}\alpha^2 + C_{D_{\delta_{r1}}}^{\alpha 1}\alpha + C_{D_{\delta_{r1}}}^{\alpha 0} \tag{2.15}$$

$$\mathbf{f}_{\mathbf{C}_{D_{\delta_a}}}(\delta_a) = \begin{cases} \mathbf{C}_{D_{\delta_{a2_p}}}\delta_a^2 + \mathbf{C}_{D_{\delta_{a1_p}}}\delta_a & \delta_a \geq 0 \\ 0 & \delta_a = 0 \\ \mathbf{C}_{D_{\delta_{a3_n}}}\delta_a^3 + \mathbf{C}_{D_{\delta_{a2_n}}}\delta_a^2 + \mathbf{C}_{D_{\delta_{a1_n}}}\delta_a & \delta_a \leq 0 \end{cases} \tag{2.16}$$

$$\mathbf{f}_{\mathbf{C}_{D_{\delta_e}}}(\delta_e) = \begin{cases} \mathbf{C}_{D_{\delta_{e2_p}}}\delta_e^2 + \mathbf{C}_{D_{\delta_{e1_p}}}\delta_e & \delta_e \geq 0 \\ 0 & \delta_e = 0 \\ \mathbf{C}_{D_{\delta_{e3_n}}}\delta_e^3 + \mathbf{C}_{D_{\delta_{e2_n}}}\delta_e^2 + \mathbf{C}_{D_{\delta_{e1_n}}}\delta_e & \delta_e \leq 0 \end{cases} \tag{2.17}$$

and

$$\mathbf{C}_{D_{\delta_{a2_p}}} = C^{\alpha 2}_{D_{\delta_{a2_p}}}\alpha^2 + C^{\alpha 1}_{D_{\delta_{a2_p}}}\alpha + C^{\alpha 0}_{D_{\delta_{a2_p}}} \tag{2.18}$$

$$\mathbf{C}_{D_{\delta_{a1_p}}} = C^{\alpha 2}_{D_{\delta_{a1_p}}}\alpha^2 + C^{\alpha 1}_{D_{\delta_{a1_p}}}\alpha + C^{\alpha 0}_{D_{\delta_{a1_p}}} \tag{2.19}$$

$$\mathbf{C}_{D_{\delta_{a3_n}}} = C^{\alpha 2}_{D_{\delta_{a3_n}}}\alpha^2 + C^{\alpha 1}_{D_{\delta_{a3_n}}}\alpha + C^{\alpha 0}_{D_{\delta_{a3_n}}} \tag{2.20}$$

$$\mathbf{C}_{D_{\delta_{a2_n}}} = C^{\alpha 2}_{D_{\delta_{a2_n}}}\alpha^2 + C^{\alpha 1}_{D_{\delta_{a2_n}}}\alpha + C^{\alpha 0}_{D_{\delta_{a2_n}}} \tag{2.21}$$

$$\mathbf{C}_{D_{\delta_{a1_n}}} = C^{\alpha 2}_{D_{\delta_{a1_n}}}\alpha^2 + C^{\alpha 1}_{D_{\delta_{a1_n}}}\alpha + C^{\alpha 0}_{D_{\delta_{a1_n}}} \tag{2.22}$$

$$\mathbf{C}_{D_{\delta_{e2_p}}} = C^{\alpha 2}_{D_{\delta_{e2_p}}}\alpha^2 + C^{\alpha 1}_{D_{\delta_{e2_p}}}\alpha + C^{\alpha 0}_{D_{\delta_{e2_p}}} \tag{2.23}$$

$$\mathbf{C}_{D_{\delta_{e1_p}}} = C^{\alpha 2}_{D_{\delta_{e1_p}}}\alpha^2 + C^{\alpha 1}_{D_{\delta_{e1_p}}}\alpha + C^{\alpha 0}_{D_{\delta_{e1_p}}} \tag{2.24}$$

$$\mathbf{C}_{D_{\delta_{e3_n}}} = C^{\alpha 2}_{D_{\delta_{e3_p}}}\alpha^2 + C^{\alpha 1}_{D_{\delta_{e3_p}}}\alpha + C^{\alpha 0}_{D_{\delta_{e3_p}}} \tag{2.25}$$

$$\mathbf{C}_{D_{\delta_{e2_n}}} = C^{\alpha 2}_{D_{\delta_{e2_p}}}\alpha^2 + C^{\alpha 1}_{D_{\delta_{e2_p}}}\alpha + C^{\alpha 0}_{D_{\delta_{e2_p}}} \tag{2.26}$$

$$\mathbf{C}_{D_{\delta_{e1_n}}} = C^{\alpha 2}_{D_{\delta_{e1_p}}}\alpha^2 + C^{\alpha 1}_{D_{\delta_{e1_p}}}\alpha + C^{\alpha 0}_{D_{\delta_{e1_p}}} \tag{2.27}$$

The numerical values of these coefficients and all others presented in this Section are given in Appendix A. Most noteably, due to the nature of the data, the relationship between C_D and δ_{al}, δ_{ar}, δ_{el}, and δ_{er} is modeled using two separate polynomials where positive deflections are modeled using a second-order polynomial and negative deflections are modeled using a third-order polynomial. Zero deflection angles result in no contribution to C_D. A graphical depiction of the dependence of C_D on the right aileron and right elevator is given in Figs. 2.2 and 2.3 respectively.

For the sake of brevity, the dependence of the drag coefficient on the left aileron and left elevator deflections are omitted as they are similar to the right control surfaces depicted in Fig. 2.2 and 2.3 respectively. Additional plots are given in Appendix A. Furthermore, C_D is independent of both roll rate, p, and yaw rate, r.

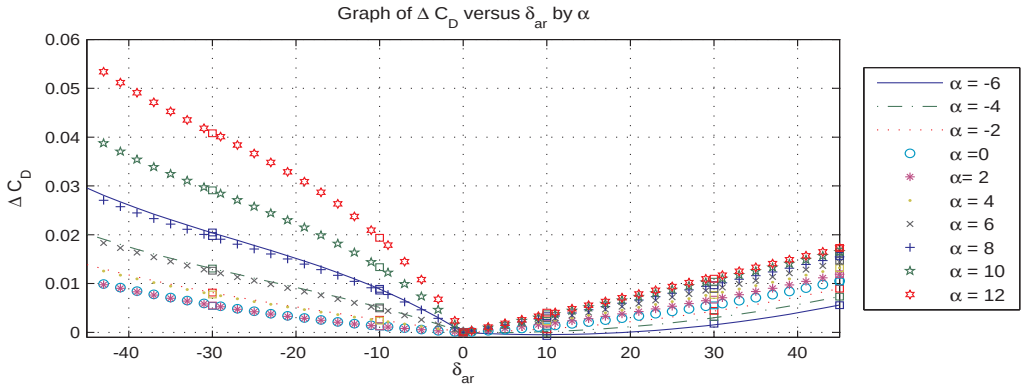

Figure 2.2. C_D vs. δ_{ar}.

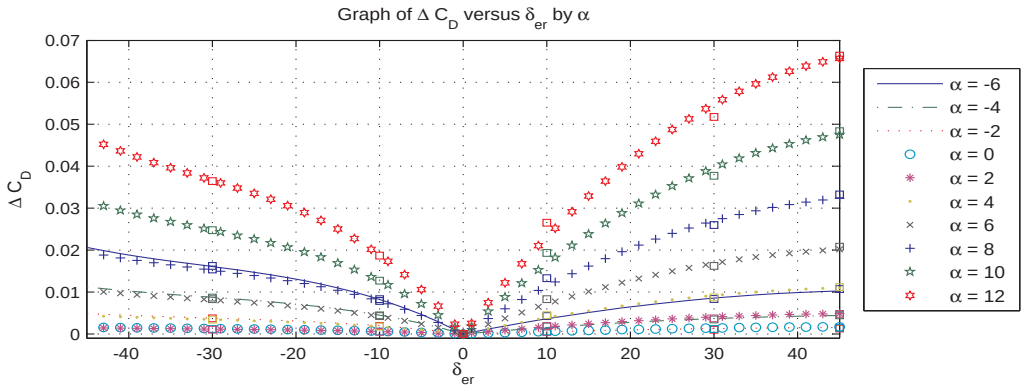

Figure 2.3. C_D vs. δ_{er}.

Similarly, the aerodynamic side force coefficient is

$$\begin{aligned} C_S &= \mathbf{C}_{S_{\alpha 2}}(\beta)\alpha^2 + \mathbf{C}_{S_{\alpha 1}}(\beta)\alpha + \mathbf{C}_{S_{\alpha 0}}(\beta) + \mathbf{C}_{S_p}(\alpha)(\frac{b}{2V})p + \mathbf{C}_{S_r}(\alpha)(\frac{b}{2V})r \\ &+ C_{S_{\delta_{r1}}}(\delta_{rl} - \delta_{rr}) + \mathbf{C}_{S_{\delta_{a3}}}(\alpha)(\delta_{al}^3 - \delta_{ar}^3) + \mathbf{C}_{S_{\delta_{a2}}}(\alpha)(\delta_{al}^2 - \delta_{ar}^2) \\ &+ \mathbf{C}_{S_{\delta_{a1}}}(\alpha)(\delta_{al} - \delta_{ar}) + \mathbf{C}_{S_{\delta_{e3}}}(\alpha)(\delta_{el}^3 - \delta_{er}^3) \\ &+ \mathbf{C}_{S_{\delta_{e2}}}(\alpha)(\delta_{el}^2 - \delta_{er}^2) + \mathbf{C}_{S_{\delta_{e1}}}(\alpha)(\delta_{el} - \delta_{er}) \end{aligned} \tag{2.28}$$

where the coefficient $C_{S_{\delta_{r1}}}$ is a constant and all other coefficients are as follows;

$$\mathbf{C}_{S_{\alpha 2}} = C_{S_{\alpha 2}}^{\beta 1}\beta + C_{S_{\alpha 2}}^{\beta 0} \tag{2.29}$$

$$\mathbf{C}_{S_{\alpha 1}} = C_{S_{\alpha 1}}^{\beta 1}\beta + C_{S_{\alpha 1}}^{\beta 0} \tag{2.30}$$

$$\mathbf{C}_{S_{\alpha 0}} = C_{S_{\alpha 0}}^{\beta 1}\beta + C_{S_{\alpha 0}}^{\beta 0} \tag{2.31}$$

$$\mathbf{C}_{S_p} = C_{S_p}^{\alpha 1}\alpha + C_{S_p}^{\alpha 0} \tag{2.32}$$

$$\mathbf{C}_{S_r} = C_{S_r}^{\alpha 1}\alpha + C_{S_r}^{\alpha 0} \tag{2.33}$$

$$\mathbf{C}_{S_{\delta_{a3}}} = C_{S_{\delta_{a3}}}^{\alpha 1}\alpha + C_{S_{\delta_{a3}}}^{\alpha 0} \tag{2.34}$$

$$\mathbf{C}_{S_{\delta_{a2}}} = C_{S_{\delta_{a2}}}^{\alpha 1}\alpha + C_{S_{\delta_{a2}}}^{\alpha 0} \tag{2.35}$$

$$\mathbf{C}_{S_{\delta_{a1}}} = C_{S_{\delta_{a1}}}^{\alpha 1}\alpha + C_{S_{\delta_{a1}}}^{\alpha 0} \tag{2.36}$$

$$\mathbf{C}_{S_{\delta_{e3}}} = C_{S_{\delta_{e3}}}^{\alpha 1}\alpha + C_{S_{\delta_{e3}}}^{\alpha 0} \tag{2.37}$$

$$\mathbf{C}_{S_{\delta_{e2}}} = C_{S_{\delta_{e2}}}^{\alpha 1}\alpha + C_{S_{\delta_{e2}}}^{\alpha 0} \tag{2.38}$$

$$\mathbf{C}_{S_{\delta_{e1}}} = C_{S_{\delta_{e1}}}^{\alpha 1}\alpha + C_{S_{\delta_{e1}}}^{\alpha 0} \tag{2.39}$$

Graphical representations of some of the relationships depicted in Eq. (2.28) are shown in Appendix A for conciseness. Moreover, C_S is independent of pitch rate, q.

The aerodynamic lift coefficient is

$$
\begin{aligned}
C_L &= \mathbf{C}_{L_{\alpha 1}}(\beta)\alpha + \mathbf{C}_{L_{\alpha 0}}(\beta) + \mathbf{C}_{L_q}(\alpha)(\frac{l}{2V})q + \mathbf{C}_{L_{\delta_{r1}}}(\alpha)(\delta_{rl} + \delta_{rr}) \\
&+ C_{L_{\delta_{a3}}}(\delta_{al}^3 + \delta_{ar}^3) + C_{L_{\delta_{a2}}}(\delta_{al}^2 + \delta_{ar}^2) + C_{L_{\delta_{a1}}}(\delta_{al} + \delta_{ar}) \\
&+ C_{L_{\delta_{e3}}}(\delta_{el}^3 + \delta_{er}^3) + C_{L_{\delta_{e2}}}(\delta_{el}^2 + \delta_{er}^2) + C_{L_{\delta_{e1}}}(\delta_{el} + \delta_{er}) \qquad (2.40)
\end{aligned}
$$

where all the coefficients are constants except for $\mathbf{C}_{L_{\alpha 1}}$, $\mathbf{C}_{L_{\alpha 0}}$, $\mathbf{C}_{L_q}$, and $\mathbf{C}_{L_{\delta_{r1}}}$ which are given below:

$$
\begin{aligned}
\mathbf{C}_{L_{\alpha 1}} &= C_{L_{\alpha 1}}^{\beta 2}\beta^2 + C_{L_{\alpha 1}}^{\beta 1}\beta + C_{L_{\alpha 1}}^{\beta 0} \qquad (2.41) \\
\mathbf{C}_{L_{\alpha 0}} &= C_{L_{\alpha 0}}^{\beta 2}\beta^2 + C_{L_{\alpha 0}}^{\beta 1}\beta + C_{L_{\alpha 0}}^{\beta 0} \qquad (2.42) \\
\mathbf{C}_{L_q} &= C_{L_q}^{\alpha 2}\alpha^2 + C_{L_q}^{\alpha 1}\alpha + C_{L_q}^{\alpha 0} \qquad (2.43) \\
\mathbf{C}_{L_{\delta_{r1}}} &= C_{L_{\delta_{r1}}}^{\alpha 1}\alpha + C_{L_{\delta_{r1}}}^{\alpha 0} \qquad (2.44)
\end{aligned}
$$

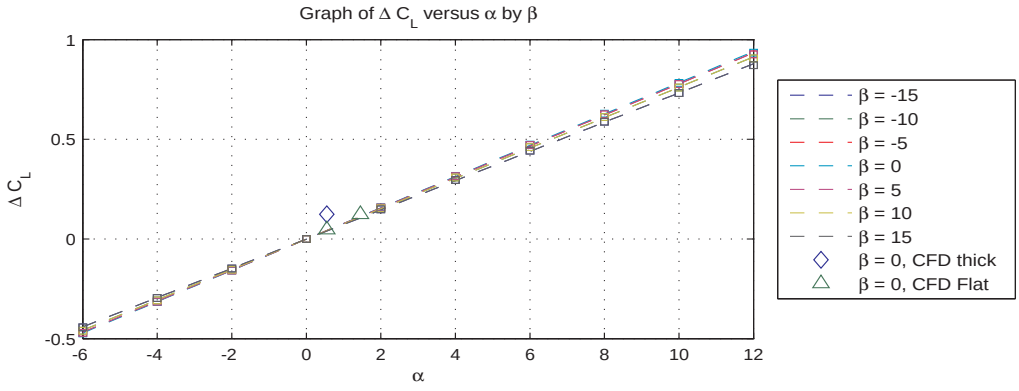

Figure 2.4. C_L vs. α.

Figure 2.4 depicts the lift coefficient dependence on angle of attack at various angles of sideslip. Fig. 2.4 presents a comparison between the HASC (Vortex Lattice Code) and CFD data. The CFD flat airfoil data for the lift variation with angle of attack lies on the HASC curve, thus, no modification is required if the flat airfoil

data is used as a benchmark for validating the lift coefficient dependence on angle of attack. The flat C_L is independent of p and r.

2.1.1.4 Moment Coefficients

The aerodynamic moments are given by the following standard expressions

$$\mathcal{L} = \frac{1}{2}\rho V^2 S_R b C_{\mathcal{L}}, \tag{2.45}$$

$$\mathcal{M} = \frac{1}{2}\rho V^2 S_R c C_{\mathcal{M}}, \tag{2.46}$$

$$\mathcal{N} = \frac{1}{2}\rho V^2 S_R b C_{\mathcal{N}}. \tag{2.47}$$

The aerodynamic rolling moment coefficient is

$$\begin{aligned} C_{\mathcal{L}} = & \mathbf{C}_{\mathcal{L}_{\alpha 1}}(\beta)\alpha + \mathbf{C}_{\mathcal{L}_{\alpha 0}}(\beta) + \mathbf{C}_{\mathcal{L}_p}(\alpha)(\frac{b}{2V})p + \mathbf{C}_{\mathcal{L}_r}(\alpha)(\frac{b}{2V})r \\ & + C_{\mathcal{L}_{\delta_{a3}}}(\delta_{al}^3 - \delta_{ar}^3) + C_{\mathcal{L}_{\delta_{a2}}}(\delta_{al}^2 - \delta_{ar}^2) \\ & + C_{\mathcal{L}_{\delta_{a1}}}(\delta_{al} - \delta_{ar}) + C_{\mathcal{L}_{\delta_{e3}}}(\delta_{el}^3 - \delta_{er}^3) \\ & + C_{\mathcal{L}_{\delta_{e2}}}(\delta_{el}^2 - \delta_{er}^2) + C_{\mathcal{L}_{\delta_{e1}}}(\delta_{el} - \delta_{er}) \end{aligned} \tag{2.48}$$

where all the coefficients are constants except $\mathbf{C}_{\mathcal{L}_{\alpha 1}}$, $\mathbf{C}_{\mathcal{L}_{\alpha 0}}$, $\mathbf{C}_{\mathcal{L}_p}$, and $\mathbf{C}_{\mathcal{L}_r}$;

$$\mathbf{C}_{\mathcal{L}_{\alpha 1}} = C_{\mathcal{L}_{\alpha 1}}^{\beta 1}\beta + C_{\mathcal{L}_{\alpha 1}}^{\beta 0} \tag{2.49}$$

$$\mathbf{C}_{\mathcal{L}_{\alpha 0}} = C_{\mathcal{L}_{\alpha 0}}^{\beta 1}\beta + C_{\mathcal{L}_{\alpha 0}}^{\beta 0} \tag{2.50}$$

$$\mathbf{C}_{\mathcal{L}_p} = C_{\mathcal{L}_p}^{\alpha 1}\alpha + C_{\mathcal{L}_p}^{\alpha 0} \tag{2.51}$$

$$\mathbf{C}_{\mathcal{L}_r} = C_{\mathcal{L}_r}^{\alpha 1}\alpha + C_{\mathcal{L}_r}^{\alpha 0} \tag{2.52}$$

A graphical representation of the relationships depicted in Eq. (2.48) are given in Appendix A. $C_{\mathcal{L}}$ is independent of q.

The aerodynamic pitching moment coefficient is

$$\begin{aligned} C_{\mathcal{M}} &= C_{\mathcal{M}_{\alpha 1}}\alpha + C_{\mathcal{M}_{\alpha 0}} + \mathbf{C}_{\mathcal{M}_q}(\alpha)(\frac{l}{2V})q \\ &+ C_{\mathcal{M}_{\delta_{a3}}}(\delta_{al}^3 + \delta_{ar}^3) + C_{\mathcal{M}_{\delta_{a2}}}(\delta_{al}^2 + \delta_{ar}^2) \\ &+ C_{\mathcal{M}_{\delta_{a1}}}(\delta_{al} + \delta_{ar}) + C_{\mathcal{M}_{\delta_{e3}}}(\delta_{el}^3 + \delta_{er}^3) \\ &+ C_{\mathcal{M}_{\delta_{e2}}}(\delta_{el}^2 + \delta_{er}^2) + C_{\mathcal{M}_{\delta_{e1}}}(\delta_{el} + \delta_{er}) \end{aligned}$$

where all the coefficients are constants except

$$\mathbf{C}_{\mathcal{M}_q} = C_{\mathcal{M}_q}^{\alpha 3}\alpha^3 + C_{\mathcal{M}_q}^{\alpha 2}\alpha^2 + C_{\mathcal{M}_q}^{\alpha 1}\alpha + C_{\mathcal{M}_q}^{\alpha 0} \tag{2.53}$$

Figure 2.5 shows a comparison between the HASC vortex lattice code and CFD thick and flat airfoil data. Unlike the lift coefficient HASC results which coincided with the CFD flat data, the pitching moment coefficient variation with angle of attack was modified to match the CFD flat data. The initial pitching moment model based on HASC was independent of angle of attack. The modification based on CFD creates a dependence of the pitching moment on the angle of attack as seen in Eq. (2.53).

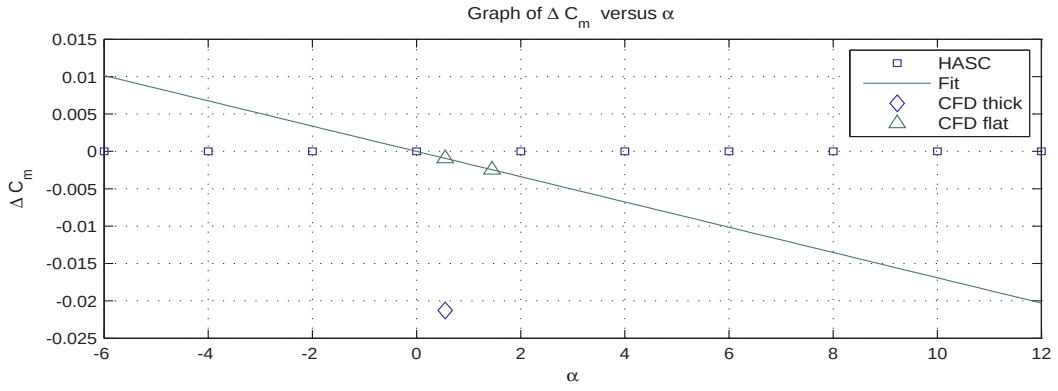

Figure 2.5. $C_{\mathcal{M}}$ vs. α.

The yawing moment coefficient is

$$\begin{aligned} C_{\mathcal{N}} &= \mathbf{C}_{\mathcal{N}_p}(\alpha)(\frac{b}{2V})p + \mathbf{C}_{\mathcal{N}_r}(\alpha)(\frac{b}{2V})r + C_{\mathcal{N}_{\delta_{r1}}}\delta_r \\ &+ \mathbf{C}_{\mathcal{N}_{\delta_{a2}}}(\alpha)(\delta_{al}^2 - \delta_{ar}^2) + \mathbf{C}_{\mathcal{N}_{\delta_{a1}}}(\alpha)(\delta_{al} - \delta_{ar}) \\ &+ \mathbf{C}_{\mathcal{N}_{\delta_{e3}}}(\alpha)(\delta_{el}^3 - \delta_{er}^3) + \mathbf{C}_{\mathcal{N}_{\delta_{e2}}}(\alpha)(\delta_{el}^2 - \delta_{er}^2) \\ &+ \mathbf{C}_{\mathcal{N}_{\delta_{e1}}}(\alpha)(\delta_{el} - \delta_{er}) \end{aligned} \tag{2.54}$$

where all the coefficients are constants except $\mathbf{C}_{\mathcal{N}_p}$, $\mathbf{C}_{\mathcal{N}_r}$, $\mathbf{C}_{\mathcal{N}_{\delta_{a2}}}$, $\mathbf{C}_{\mathcal{N}_{\delta_{a1}}}$, $\mathbf{C}_{\mathcal{N}_{\delta_{e3}}}$, $\mathbf{C}_{\mathcal{N}_{\delta_{e2}}}$, $\mathbf{C}_{\mathcal{N}_{\delta_{e1}}}$

$$\mathbf{C}_{\mathcal{N}_p} = C_{\mathcal{N}_p}^{\alpha 1}\alpha + C_{\mathcal{N}_p}^{\alpha 0} \tag{2.55}$$

$$\mathbf{C}_{\mathcal{N}_r} = C_{\mathcal{N}_r}^{\alpha 1}\alpha + C_{\mathcal{N}_r}^{\alpha 0} \tag{2.56}$$

$$\mathbf{C}_{\mathcal{N}_{\delta_{a2}}} = C_{\mathcal{N}_{\delta_{a2}}}^{\alpha 1}\alpha + C_{\mathcal{N}_{\delta_{a2}}}^{\alpha 0} \tag{2.57}$$

$$\mathbf{C}_{\mathcal{N}_{\delta_{a1}}} = C_{\mathcal{N}_{\delta_{a1}}}^{\alpha 1}\alpha + C_{\mathcal{N}_{\delta_{a1}}}^{\alpha 0} \tag{2.58}$$

$$\mathbf{C}_{\mathcal{N}_{\delta_{e3}}} = C_{\mathcal{N}_{\delta_{e3}}}^{\alpha 1}\alpha + C_{\mathcal{N}_{\delta_{e3}}}^{\alpha 0} \tag{2.59}$$

$$\mathbf{C}_{\mathcal{N}_{\delta_{e2}}} = C_{\mathcal{N}_{\delta_{e2}}}^{\alpha 1}\alpha + C_{\mathcal{N}_{\delta_{e2}}}^{\alpha 0} \tag{2.60}$$

$$\mathbf{C}_{\mathcal{N}_{\delta_{e1}}} = C_{\mathcal{N}_{\delta_{e1}}}^{\alpha 1}\alpha + C_{\mathcal{N}_{\delta_{e1}}}^{\alpha 0} \tag{2.61}$$

Appendix A contains these yawing moment dependence figures. $C_{\mathcal{N}}$ is independent of q.

2.1.2 Engine Configuration for EQ-II

The engines of the EQ-II aircraft are modeled as seen in Fig. 2.6. These engines generate thrust in the x-y plane along the x-axis of the body frame. This implies that with differential thrusting, the engines can generate only yawing moments.

$$M_P = \sum_{j=1}^{n/2} \Big\{ [0\ 0\ 1]^T \rho_{E_{Y_j}} (T_{L_j} - T_{R_j}) \Big\} \tag{2.62}$$

Eq. (2.62) formulates the moment generated by the engine thrusts of the EQ-II aircraft. Given the number of engines as n, $\rho_{E_{Y_j}}$ is the distance of the j^{th} pair of engines to the origin of the body frame along the y-axis. T_{L_j} and T_{R_j} are the magnitudes of the thrust from the left and right engines of the j^{th} pair. This expression clearly shows that differential thrust will generate yawing moment.

2.1.3 Fuel Tank Configuration for EQ-II

For all trail aircraft in this dissertation, a fuel tank subsystem is created in the simulation that models the fuel flow which may be transferred between fuel tanks, burned by the engines, or transferred into the aircraft as in the case of aerial refueling. As a result of the fuel flow, the mass and inertia properties of the trail aircraft vary with time and this variation is explicitly accounted for in the equations of motion outlined in Section 2.4.1. In the case of formation flight, this dissertation utilizes internal fuel transfer between fuel tanks as an alternate moment generation mechanism, as discussed in Chapter 1, necessitating modeling the dynamic effect of the fuel transfer process. In addition, for a formation of significant duration, fuel consumption plays an important role and the effect of fuel burn from individual fuel tanks requires the fuel subsystem incorporation to model the dynamic effect.

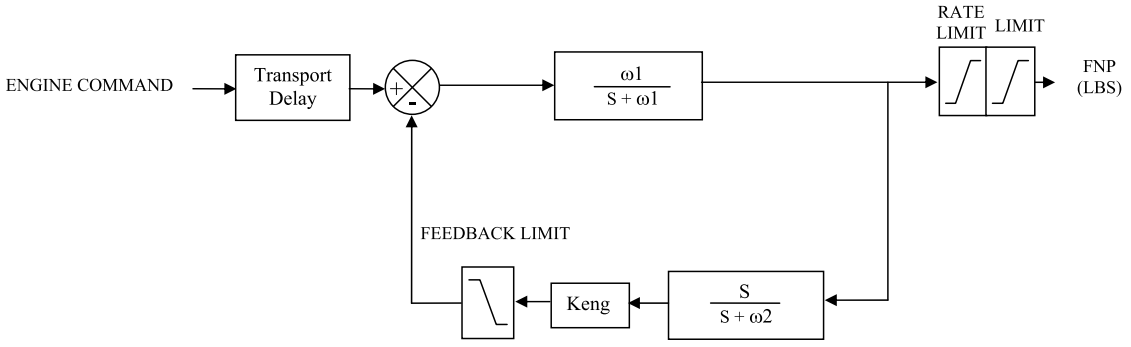

Figure 2.6. Engine model for aircraft models [56, 57].

The EQ-II has four fuel tanks, as shown in Fig. 2.1, labeled as Tanks 1, 2, 3 and 4. Figure 2.7 depicts a three dimensional view of the inner and outer fuel tanks on one side of the EQ-II model. Tanks 1 and 4 are outer fuel tanks with the shape of a parallelepiped; Tanks 2 and 3 are inner fuel tanks and of the shape of a prismoid with another prismoid carved out to make space for the landing gear bay. The inner fuel tanks are asymmetric with respect to the x and y axis. With all fuel tanks completely full, the fuel contributes 40 percent of the total aircraft weight. The fuel capacity of each inner tank contributes 15 percent of the weight, while the capacity of the smaller outer tank is 5 percent of the weight. Therefore, the inner fuel tanks hold three times more fuel than the outer fuel tanks 1 and 4.

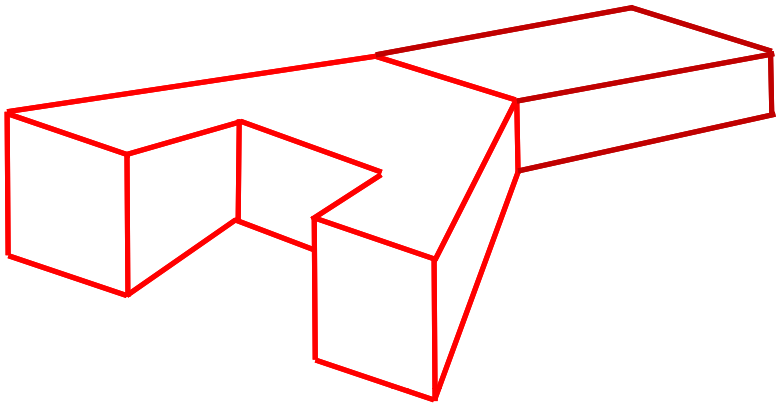

Figure 2.7. Fuel Tank Shape.

With fuel consumption and during internal fuel transfer between fuel tanks, the amount and the CM of the fuel in each fuel tank changes, which in turn changes the mass, CM, and thus inertia configuration of the aircraft. A centroid formulation algorithm is developed for the EQ-II in Reference [58] to calculate the position of the center of mass of the fuel in the fuel tanks as a function of fuel amount during the fuel transfer and/or fuel burn process. This algorithm also determines the first and

second derivatives of the position as a function of fuel amount and the amount of fuel flow in or out of the fuel tank. The outputs of this algorithm are directly fed into the equations of motion to model the dynamic effect of the fuel transfer between fuel tanks as the equations of motion, described in Section 2.4.1, include terms with fuel mass, the position, and the derivative of the position of the fuel CM in each fuel tank.

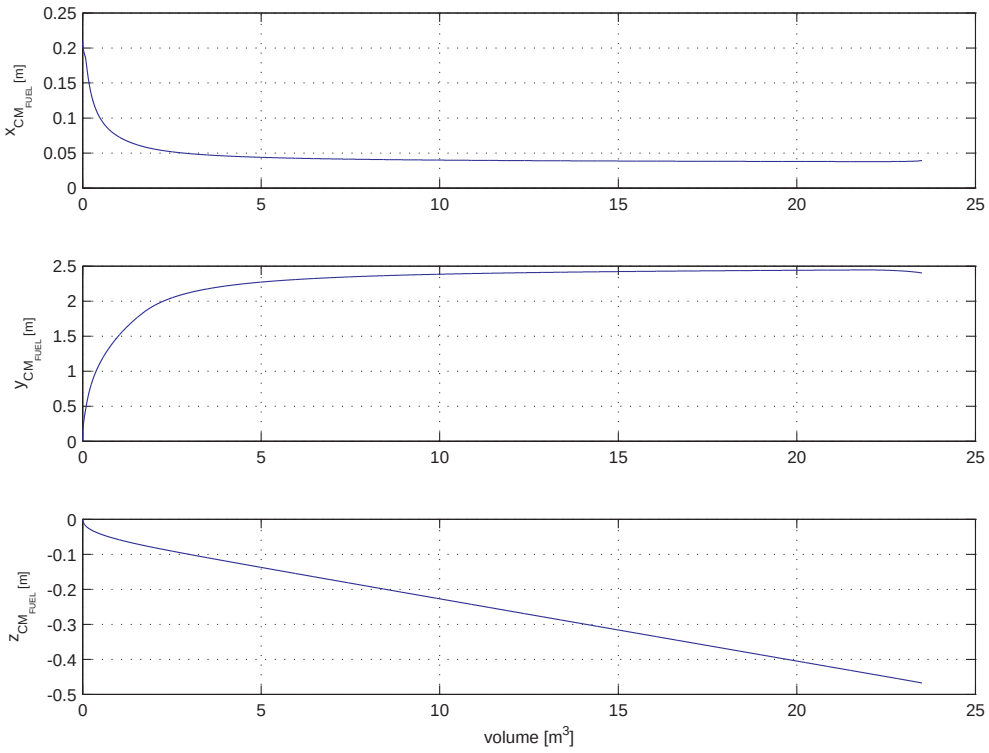

Figure 2.8. Movement of Center of Mass of Fuel in X, Y, and Z Directions.

The centroid formulation, implemented in the integrated MATLAB/Simulink-based environment, calculates the position of the center of gravity of the fuel in the fuel tanks as a function of fuel amount during the fuel transfer process. A sample case is simulated and the results are demonstrated in Figs. 2.8 and 2.9. Fig. 2.8 shows how the CG changes in the three directions as a function of fuel volume in the inner fuel tanks. Due to the geometry of the inner fuel tanks, the CM of the fuel in

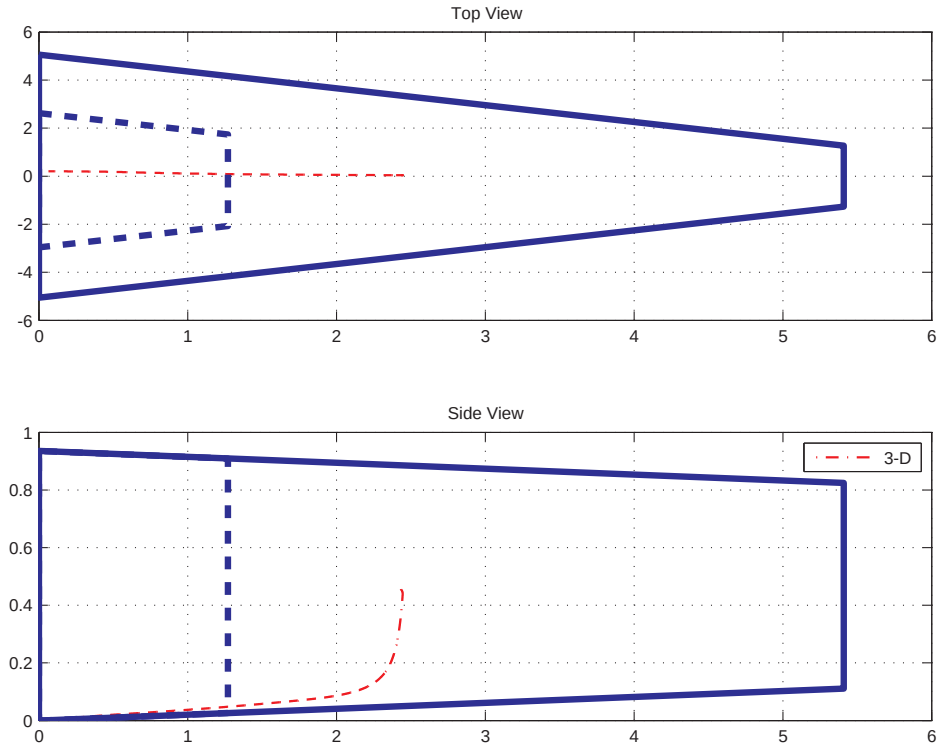

Figure 2.9. Views of Movement of Center of Mass of Fuel in Tanks.

tanks 2 and 3 moves in all three directions as the amount of fuel changes as shown in Figs. 2.8. Fig. 2.9 shows the trajectory of the CG movement as the fuel volume goes from zero to the full capacity. The CM of the fuel in the outer fuel tanks moves only up or down as the amount of fuel changes due to the simple geometry of the outer tanks.

2.1.4 Actuator Dynamics for EQ-II

Only actuator saturation and rate limit effects are considered for the EQ-II aircraft. The deflection ranges for the outboard elevons (ailerons) are (-30 deg, 30 deg), inboard elevons (elevators) are (-30 deg, 30 deg), and clamshells (rudder) are (0 deg, 60 deg). All three control surfaces have rate limits of $\pm$ 60 deg/s.

2.2 Trail KC-135R Aircraft

The KC-135R is a conventional Stratotanker aircraft with a fuselage and tail used primarily to provide aerial refueling support for long range fighters and bombers like the EQ-II aircraft. The KC-135R was created by modifying the KC-135A tanker to improve fuel consumption, emissions, and noise levels. The KC-135R is an integral part of the U.S.A.F KC-X tanker fleet with the newest addition being the KC-46 that is similar in configuration and larger in size than the KC-135R. In addition, the KC-135R is similar in design to commercial aircraft such as the Boeing 777, making it a prime candidate for the formation studies presented in this dissertation to show the formation benefits from a military or commercial perspective. This dissertation uses two different models for the KC-135R: a simple model for the lead KC-135R and a more detailed model for the trail KC-135R. The details of the model for the lead KC-135R are given in Section 2.3.

2.2.1 Aerodynamic Model for Trail KC-135R

2.2.1.1 Computational Tools

The aerodynamic model of the KC-135R tanker aircraft is developed based on Digital DatCom [59] data and supplemented with CFD results. These supplemental CFD results are for the lead KC-135R which, for the purposes of this dissertation, is modeled using a different and simpler aerodynamic model that differs from the trail KC-135R discussed in this section. The Digital DatCom representation of the vehicle is shown in Fig. 2.10.

For the present analysis, drag due to the aileron and rudder are required. Digital DatCom only provides roll and yaw due to aileron deflection. The aileron drag was calculated by treating the ailerons as symmetrically deflected flaps and using the drag

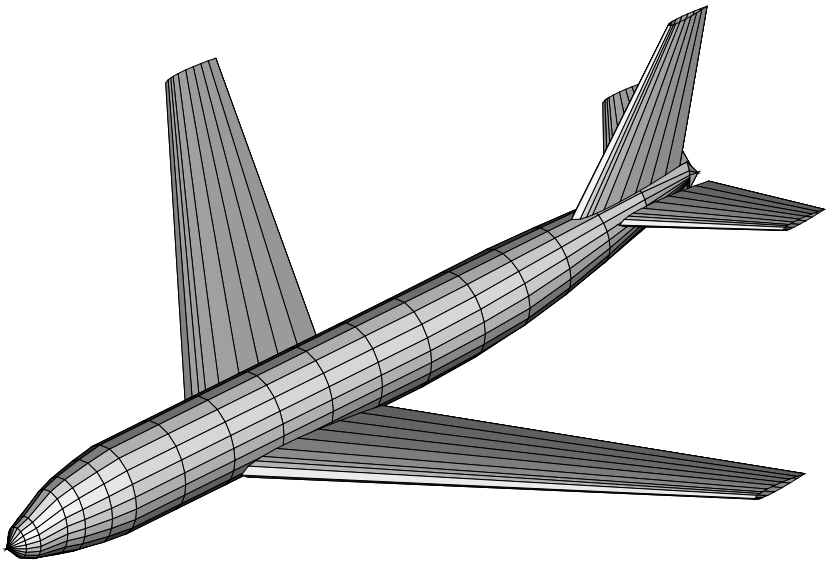

Figure 2.10. Digital DatCom representation of KC-135R.

from the DatCom flap method. Digital DatCom does not include any methods for rudders. This was overcome by rotating the vertical tail by 90 degrees and modeling it as a wing, with the rudders as wing flaps. Using this procedure, the lift, pitching moment and drag obtained for a flap correspond to the side force, yawing moment and drag of the rudder. These must be divided by two since this process models two wing panels and flaps while there is only one vertical tail and rudder. The rolling moment is obtained by changing the flaps to ailerons, and deflecting a single aileron. In both cases, the results need to be corrected to use the actual wing area and wing span as reference quantities for force and moment non-dimensionalization. To avoid using a spurious result as the Digital DatCom method for directional stability of a wing-body-horizontal-vertical tail configuration is sometimes inaccurate, a configuration buildup was run and the body-vertical tail result was used for directional stability.

Two sources of flight test data for configurations very similar to the KC-135R were found, one for a Boeing 707-200 [60] and one for a KC-135A [61]. The stability

Table 2.3. Geometric Parameters for KC-135R

Parameter	Value
S_R (m^2)	226.03
b (m)	39.88
c (m)	6.14

derivatives from these sources compared very favorably to the Digital DatCom results. The data obtained from Digital DatCom are then fitted with polynomials using a Least Squares method as in the case of the EQ-II. The final expressions for the aerodynamic force and moment coefficients and the comparisons with the Digital DatCom are presented in the following sections. These expressions may be followed by a set of graphs which are visual representations of the relationships between the aerodynamic coefficients and their dependent variables. The star markers on each graph represent the Digital DatCom data that was used to model the coefficients while the solid lines represent the fitted line for each variable. For brevity, additional figures and the values for each coefficient are given in Appendix B.

2.2.1.2 Force Coefficients

The aerodynamic forces are given by the following standard expressions

$$\boldsymbol{D} = \frac{1}{2}\rho V^2 \mathcal{S} \boldsymbol{C_D} \tag{2.63}$$

$$\boldsymbol{S} = \frac{1}{2}\rho V^2 \mathcal{S} \boldsymbol{C_S} \tag{2.64}$$

$$\boldsymbol{L} = \frac{1}{2}\rho V^2 \mathcal{S} \boldsymbol{C_L} \tag{2.65}$$

where $\mathcal{S}$ is the reference area and ρ is the ambient air density. The geometric properties of the KC-135R aircraft used in the aerodynamics are given in Table 2.3.

The drag coefficient is

$$\boldsymbol{C_D}\left(\beta,\alpha,\delta_a,\delta_e,\delta_r\right)=\boldsymbol{f_{C_{D_\alpha}}}\left(\alpha\right)+\boldsymbol{f_{C_{D_\beta}}}\left(\beta\right)+\boldsymbol{f_{C_{D_{\delta_a}}}}\left(\delta_a\right)+\boldsymbol{f_{C_{D_{\delta_e}}}}\left(\delta_e\right)+\boldsymbol{f_{C_{D_{\delta_r}}}}\left(\delta_r\right) \tag{2.66}$$

where

$$\boldsymbol{f_{C_{D_\alpha}}}\left(\alpha\right)=C_{D_{\alpha 6}}\alpha^6+C_{D_{\alpha 5}}\alpha^5+C_{D_{\alpha 4}}\alpha^4+C_{D_{\alpha 3}}\alpha^3+C_{D_{\alpha 2}}\alpha^2+C_{D_{\alpha 1}}\alpha+C_{D_{\alpha 0}}$$

$$\boldsymbol{f_{C_{D_\beta}}}\left(\beta\right)=C_{D_{\beta 2}}\beta^2+C_{D_{\beta 1}}\beta+C_{D_{\beta 0}}$$

$$\boldsymbol{f_{C_{D_{\delta_a}}}}\left(\delta_a\right)=\begin{cases} C_{D_{\delta_{a4_n}}}\delta_a^4+C_{D_{\delta_{a3_n}}}\delta_a^3+C_{D_{\delta_{a2_n}}}\delta_a^2+C_{D_{\delta_{a1_n}}}\delta_a+C_{D_{\delta_{a0_n}}} & ,\delta_a<0 \\ 0 & ,\delta_a=0 \\ C_{D_{\delta_{a4_p}}}\delta_a^4+C_{D_{\delta_{a3_p}}}\delta_a^3+C_{D_{\delta_{a2_p}}}\delta_a^2+C_{D_{\delta_{a1_p}}}\delta_a+C_{D_{\delta_{a0_p}}} & ,\delta_a>0 \end{cases}$$

$$\boldsymbol{f_{C_{D_{\delta_e}}}}\left(\delta_e\right)=\begin{cases} C_{D_{\delta_{e5_n}}}\delta_e^5+C_{D_{\delta_{e4_n}}}\delta_e^4+C_{D_{\delta_{e3_n}}}\delta_e^3+C_{D_{\delta_{e2_n}}}\delta_e^2+C_{D_{\delta_{e1_n}}}\delta_e+C_{D_{\delta_{e0_n}}} & ,\delta_e<0 \\ 0 & ,\delta_e=0 \\ C_{D_{\delta_{e3_p}}}\delta_e^3+C_{D_{\delta_{e2_p}}}\delta_e^2+C_{D_{\delta_{e1_p}}}\delta_e+C_{D_{\delta_{e0_p}}} & ,\delta_e>0 \end{cases}$$

$$\boldsymbol{f_{C_{D_{\delta_r}}}}\left(\delta_r\right)=\begin{cases} C_{D_{\delta_{r5_n}}}\delta_r^5+C_{D_{\delta_{r4_n}}}\delta_r^4+C_{D_{\delta_{r3_n}}}\delta_r^3+C_{D_{\delta_{r2_n}}}\delta_r^2+C_{D_{\delta_{r1_n}}}\delta_r+C_{D_{\delta_{r0_n}}} & ,\delta_r<0 \\ 0 & ,\delta_r=0 \\ C_{D_{\delta_{r5_p}}}\delta_r^5+C_{D_{\delta_{r4_p}}}\delta_r^4+C_{D_{\delta_{r3_p}}}\delta_r^3+C_{D_{\delta_{r2_p}}}\delta_r^2+C_{D_{\delta_{r1_p}}}\delta_r+C_{D_{\delta_{r0_p}}} & ,\delta_r>0 \end{cases}$$

The numerical values of these coefficients and all others presented in this Section are given in Appendix B. Figures 2.11 and 2.12 depict the dependence of the drag coefficient on the angle of attack and sideslip angle, respectively. Fig. 2.11 shows the drag coefficient dependence on angle of attack based on Digital DatCom and based on CFD. Two data points for $\boldsymbol{C}_{D_\alpha}$, 0.0156 and 0.0189 were obtained from the CFD results of the lead KC-135R at angles of attack of 0.5 and 1.2 degrees respectively. A few pseudo data points were then added to these and fitted with a 6th order polynomial fit. This was done to generate a curve close to the DatCom but containing the two CFD data points. Thus, in the polynomial expression for the drag

coefficient the CFD modification was done only to the $\boldsymbol{f}_{\boldsymbol{C}_{D_\alpha}}$ expression, changing it from a 5th order polynomial given to a 6th order polynomial.

Furthermore, note from Fig. 2.12 that the second order polynomial fit is performed only based on $\beta = \{-1, 0, 1\}$ degrees. This is because only the slope data is given from the Digital DatCom and thus the C_{D_β} values are not actual data points. Figures depicting additional drag dependencies are provided in Appendix B.

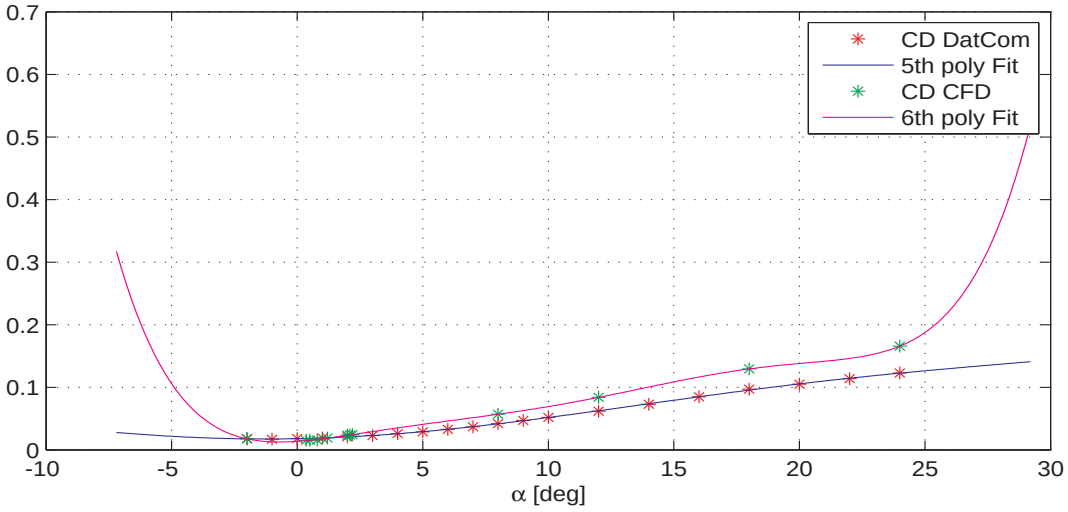

Figure 2.11. $\boldsymbol{f}_{\boldsymbol{C}_{D_\alpha}}$ (Drag Coefficient) versus α (angle-of-attack).

The lift coefficient is

$$\boldsymbol{C_L}(V, \alpha, \dot{\alpha}, q, \delta_e) = \boldsymbol{f}_{\boldsymbol{C}_{L_\alpha}}(\alpha) + C_{L_{q1}}\left[\frac{\bar{c}}{2V}\right] q + \boldsymbol{C}_{L_{\dot{\alpha}}}(\alpha)\left[\frac{\bar{c}}{2V}\right]\dot{\alpha} + \boldsymbol{f}_{\boldsymbol{C}_{L_{\delta_e}}}(\delta_e) \quad (2.67)$$

where

$$\boldsymbol{f}_{\boldsymbol{C}_{L_\alpha}}(\alpha) = C_{L_{\alpha 2}}\alpha^2 + C_{L_{\alpha 1}}\alpha + C_{L_{\alpha 0}}$$

$$\boldsymbol{C}_{L_{\dot{\alpha}}}(\alpha) = C^{\alpha 6}_{L_{\dot{\alpha}1}}\alpha^6 + C^{\alpha 5}_{L_{\dot{\alpha}1}}\alpha^5 + C^{\alpha 4}_{L_{\dot{\alpha}1}}\alpha^4 + C^{\alpha 3}_{L_{\dot{\alpha}1}}\alpha^3 + C^{\alpha 2}_{L_{\dot{\alpha}1}}\alpha^2 + C^{\alpha 1}_{L_{\dot{\alpha}1}}\alpha + C^{\alpha 0}_{L}$$

$$\boldsymbol{f}_{\boldsymbol{C}_{L_{\delta_e}}}(\delta_e) = C_{L_{\delta_{e4}}}\delta_e^4 + C_{L_{\delta_{e3}}}\delta_e^3 + C_{L_{\delta_{e2}}}\delta_e^2 + C_{L_{\delta_{e1}}}\delta_e + C_{L_{\delta_{e0}}}$$

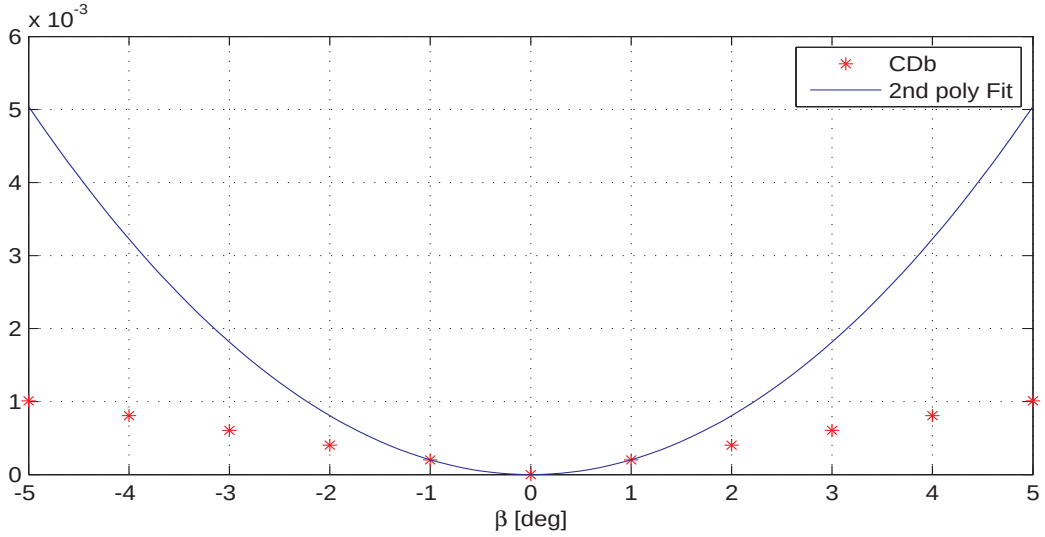

Figure 2.12. $\boldsymbol{f}_{\boldsymbol{C}_{D_\beta}}$ (Drag Coefficient) versus β (side slip angle).

The lift coefficient dependency on angle of attack is depicted in Fig. 2.13. As in the drag coefficient dependency on angle of attack, the lift coefficient dependency on angle of attack was modified based on two data points generated by CFD results. At angles of attack of 0.5 and 1.2 degrees, the lift coefficient of the lead KC-135R is 0.3391 and 0.4089 respectively. Additional points were inserted to the data points and a 2nd order polynomial fit was used to fit these points. Fig. 2.13 shows the lift coefficient dependency on angle of attack using Digital DatCom and CFD. The modification in the lift coefficient expression is seen in the $\boldsymbol{f}_{\boldsymbol{C}_{L_\alpha}}$ which changes from a 3rd order to a 2nd order polynomial.

The side force coefficient is given as

$$\boldsymbol{C_S}(V,\beta,\alpha,p,\delta_r) = C_{S_{\beta 1}}\,\beta + \boldsymbol{C}_{S_{p1}}(\alpha)\left[\frac{b}{2V}\right]p + \boldsymbol{f}_{\boldsymbol{C}_{S_{\delta r}}}(\delta_r) \tag{2.68}$$

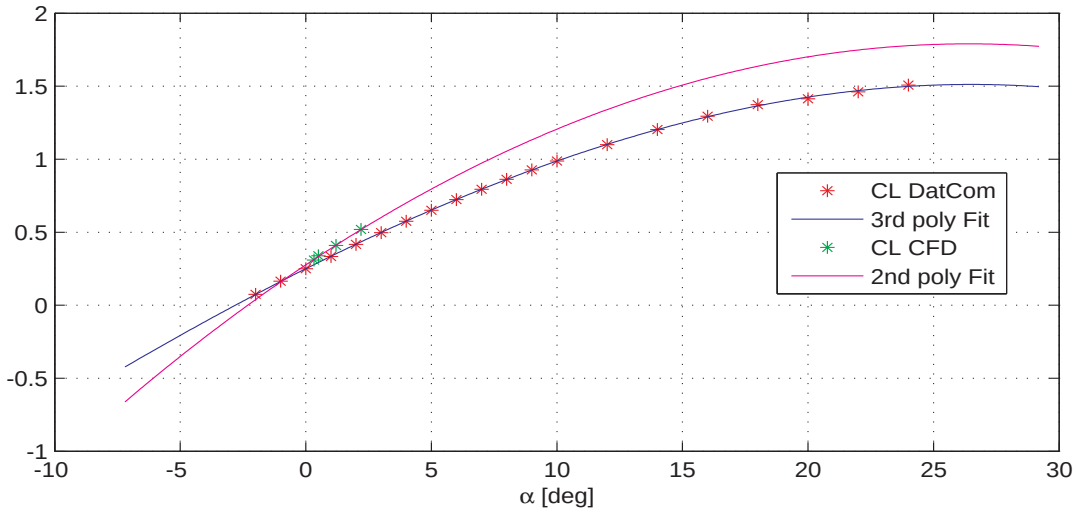

Figure 2.13. $\boldsymbol{f}_{\boldsymbol{C}_{L_\alpha}}$ (Lift Coefficient) versus α (angle-of-attack).

where

$$\boldsymbol{C}_{S_{p1}}(\alpha) = C_{S_{p1}}^{\alpha 3}\alpha^3 + C_{S_{p1}}^{\alpha 2}\alpha^2 + C_{S_{p1}}^{\alpha 1}\alpha + C_{S_{p1}}^{\alpha 0}$$

$$\boldsymbol{f}_{\boldsymbol{C}_{S_{\delta_r}}}(\delta_r) = C_{S_{\delta_{r3}}}\delta_r^3 + C_{S_{\delta_{r2}}}\delta_r^2 + C_{S_{\delta_{r1}}}\delta_r + C_{S_{\delta_{r0}}}$$

2.2.1.3 Moment Coefficients

The aerodynamic moments are given by the following standard expressions

$$\mathcal{L} = \frac{1}{2}\rho V^2 \mathcal{S}\, b\, \boldsymbol{C}_{\mathcal{L}}, \tag{2.69}$$

$$\mathcal{M} = \frac{1}{2}\rho V^2 \mathcal{S}\, \bar{c}\, \boldsymbol{C}_{\mathcal{M}}, \tag{2.70}$$

$$\mathcal{N} = \frac{1}{2}\rho V^2 \mathcal{S}\, b\, \boldsymbol{C}_{\mathcal{N}}. \tag{2.71}$$

where b is the wing span and $\bar{c}$ is the mean chord length.

The rolling moment coefficient is

$$\begin{aligned}\boldsymbol{C}_{\mathcal{L}}(V,\beta,\alpha,p,r,\delta_a,\delta_r) = {} & \boldsymbol{C}_{\mathcal{L}_{\beta 1}}(\alpha)\,\beta + \boldsymbol{C}_{\mathcal{L}_{p1}}(\alpha)\left[\frac{b}{2V}\right]p + \boldsymbol{C}_{\mathcal{L}_{r1}}(\alpha)\left[\frac{b}{2V}\right]r \\ & + \boldsymbol{f}_{\boldsymbol{C}_{\mathcal{L}_{\delta_a}}}(\delta_a) + \boldsymbol{f}_{\boldsymbol{C}_{\mathcal{L}_{\delta_r}}}(\delta_r)\end{aligned} \tag{2.72}$$

where

$$\boldsymbol{C}_{\mathcal{L}_{\beta 1}}(\alpha)=C_{\mathcal{L}_{\beta 1}}^{\alpha 6}\alpha^6+C_{\mathcal{L}_{\beta 1}}^{\alpha 5}\alpha^5+C_{\mathcal{L}_{\beta 1}}^{\alpha 4}\alpha^4+C_{\mathcal{L}_{\beta 1}}^{\alpha 3}\alpha^3+C_{\mathcal{L}_{\beta 1}}^{\alpha 2}\alpha^2+C_{\mathcal{L}_{\beta 1}}^{\alpha 1}\alpha+C_{\mathcal{L}_{\beta 1}}^{\alpha 0}$$

$$\boldsymbol{C}_{\mathcal{L}_{p1}}(\alpha)=C_{\mathcal{L}_{p1}}^{\alpha 6}\alpha^6+C_{\mathcal{L}_{p1}}^{\alpha 5}\alpha^5+C_{\mathcal{L}_{p1}}^{\alpha 4}\alpha^4+C_{\mathcal{L}_{p1}}^{\alpha 3}\alpha^3+C_{\mathcal{L}_{p1}}^{\alpha 2}\alpha^2+C_{\mathcal{L}_{p1}}^{\alpha 1}\alpha+C_{\mathcal{L}_{p1}}^{\alpha 0}$$

$$\boldsymbol{C}_{\mathcal{L}_{r1}}(\alpha)=C_{\mathcal{L}_{r1}}^{\alpha 6}\alpha^6+C_{\mathcal{L}_{r1}}^{\alpha 5}\alpha^5+C_{\mathcal{L}_{r1}}^{\alpha 4}\alpha^4+C_{\mathcal{L}_{r1}}^{\alpha 3}\alpha^3+C_{\mathcal{L}_{r1}}^{\alpha 2}\alpha^2+C_{\mathcal{L}_{r1}}^{\alpha 1}\alpha+C_{\mathcal{L}_{r1}}^{\alpha 0}$$

$$\boldsymbol{f}_{\boldsymbol{C}_{\mathcal{L}_{\delta_a}}}(\delta_a)=C_{\mathcal{L}_{\delta_{a3}}}\delta_a^3+C_{\mathcal{L}_{\delta_{a2}}}\delta_a^2+C_{\mathcal{L}_{\delta_{a1}}}\delta_a+C_{\mathcal{L}_{\delta_{a0}}}$$

$$\boldsymbol{f}_{\boldsymbol{C}_{\mathcal{L}_{\delta_r}}}(\delta_r)=C_{\mathcal{L}_{\delta_{r3}}}\delta_r^3+C_{\mathcal{L}_{\delta_{r2}}}\delta_r^2+C_{\mathcal{L}_{\delta_{r1}}}\delta_r+C_{\mathcal{L}_{\delta_{r0}}}$$

Appendix B contains depictions of the roll moment coefficient dependencies as well as the values of the coefficients.

The pitching moment coefficient is

$$\boldsymbol{C}_{\boldsymbol{\mathcal{M}}}(V,\alpha,\dot{\alpha},q,\delta_e)=\boldsymbol{f}_{\boldsymbol{C}_{\mathcal{M}_\alpha}}(\alpha)+C_{\mathcal{M}_{q1}}\left[\frac{\bar{c}}{2V}\right]q+\boldsymbol{C}_{\mathcal{M}_{\dot{\alpha}}}(\alpha)\left[\frac{\bar{c}}{2V}\right]\dot{\alpha}+\boldsymbol{f}_{\boldsymbol{C}_{\mathcal{M}_{\delta_e}}}(\delta_e) \quad (2.73)$$

where

$$\boldsymbol{f}_{\boldsymbol{C}_{\mathcal{M}_\alpha}}(\alpha)=C_{\mathcal{M}_{\alpha 3}}\alpha^3+C_{\mathcal{M}_{\alpha 2}}\alpha^2+C_{\mathcal{M}_{\alpha 1}}\alpha+C_{\mathcal{M}_{\alpha 0}}$$

$$\boldsymbol{C}_{\mathcal{M}_{\dot{\alpha}}}(\alpha)=C_{\mathcal{M}_{\dot{\alpha}1}}^{\alpha 6}\alpha^6+C_{\mathcal{M}_{\dot{\alpha}1}}^{\alpha 5}\alpha^5+C_{\mathcal{M}_{\dot{\alpha}1}}^{\alpha 4}\alpha^4+C_{\mathcal{M}_{\dot{\alpha}1}}^{\alpha 3}\alpha^3+C_{\mathcal{M}_{\dot{\alpha}1}}^{\alpha 2}\alpha^2+C_{\mathcal{M}_{\dot{\alpha}1}}^{\alpha 1}\alpha+C_{\mathcal{M}}^{\alpha 0}$$

$$\boldsymbol{f}_{\boldsymbol{C}_{\mathcal{M}_{\delta_e}}}(\delta_e)=C_{\mathcal{M}_{\delta_{e4}}}\delta_e^4+C_{\mathcal{M}_{\delta_{e3}}}\delta_e^3+C_{\mathcal{M}_{\delta_{e2}}}\delta_e^2+C_{\mathcal{M}_{\delta_{e1}}}\delta_e+C_{\mathcal{M}_{\delta_{e0}}}$$

Figure 2.14 shows the dependency of the pitching moment coefficient on angle of attack based on Digital DatCom and CFD results. Two data points for the pitching moment coefficient were obtained from the CFD results of the lead KC-135R aircraft. At angles of attack of 0.5 and 1.2 degrees, the pitching moment coefficients based on CFD are -0.027 and -0.033 respectively. With additional data points added to these two, a 3rd order polynomial fit is done and the results are shown on the same plot as the DatCom results depicted in Fig. 2.14.

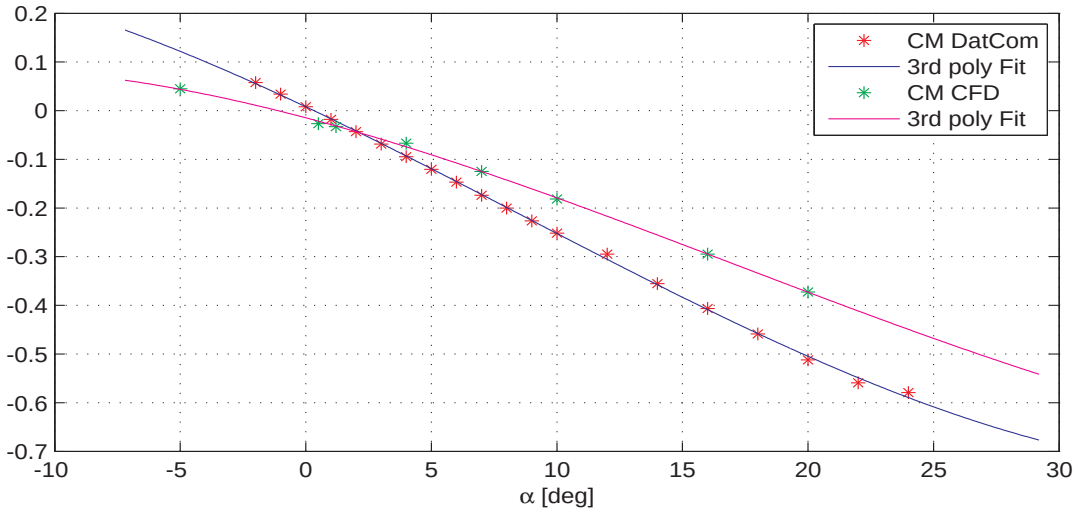

Figure 2.14. $\boldsymbol{f}_{\boldsymbol{C}_{\mathcal{M}_\alpha}}$ (Pitching Moment Coefficient) versus α (angle-of-attack).

The yawing moment coefficient is

$$\begin{aligned}\boldsymbol{C}_{\mathcal{N}}(V,\beta,\alpha,p,r,\delta_a,\delta_r) &= C_{\mathcal{N}_{\beta 1}}\beta + \boldsymbol{C}_{\mathcal{N}_{p1}}(\alpha)\left[\frac{b}{2V}\right]p + \boldsymbol{C}_{\mathcal{N}_{r1}}(\alpha)\left[\frac{b}{2V}\right]r \\ &\quad + \boldsymbol{f}_{\boldsymbol{C}_{\mathcal{N}_{\delta_a}}}(\delta_a) + \boldsymbol{f}_{\boldsymbol{C}_{\mathcal{N}_{\delta_r}}}(\delta_r) \qquad (2.74)\end{aligned}$$

where

$$\boldsymbol{C}_{\mathcal{N}_{p1}}(\alpha) = C^{\alpha 4}_{\mathcal{N}_{p1}}\alpha^4 + C^{\alpha 3}_{\mathcal{L}_{p1}}\alpha^3 + C^{\alpha 2}_{\mathcal{N}_{p1}}\alpha^2 + C^{\alpha 1}_{\mathcal{L}_{p1}}\alpha + C^{\alpha 0}_{\mathcal{N}_{p1}}$$

$$\boldsymbol{C}_{\mathcal{N}_{r1}}(\alpha) = C^{\alpha 4}_{\mathcal{N}_{r1}}\alpha^4 + C^{\alpha 3}_{\mathcal{N}_{r1}}\alpha^3 + C^{\alpha 2}_{\mathcal{N}_{r1}}\alpha^2 + C^{\alpha 1}_{\mathcal{N}_{r1}}\alpha + C^{\alpha 0}_{\mathcal{N}_{r1}}$$

$$\boldsymbol{f}_{\boldsymbol{C}_{\mathcal{N}_{\delta_a}}}(\delta_a) = C_{\mathcal{N}_{\delta_{a3}}}\delta_a^3 + C_{\mathcal{N}_{\delta_{a2}}}\delta_a^2 + C_{\mathcal{N}_{\delta_{a1}}}\delta_a + C_{\mathcal{N}_{\delta_{a0}}}$$

$$\boldsymbol{f}_{\boldsymbol{C}_{\mathcal{N}_{\delta_r}}}(\delta_r) = C_{\mathcal{N}_{\delta_{r3}}}\delta_r^3 + C_{\mathcal{N}_{\delta_{r2}}}\delta_r^2 + C_{\mathcal{N}_{\delta_{r1}}}\delta_r + C_{\mathcal{N}_{\delta_{r0}}}$$

2.2.2 Engine Configuration for Trail KC-135R

The KC-135R has four engines that are identically modeled as for the EQ-II using Fig. 2.6. These engines independently generate propulsive forces with three components that are functions of thrust magnitude and direction of the thrust vector.

These components are parameterized by the angles of the thrust vector with the body xy- and xz- planes of the aircraft. Thus, as seen in Fig. 2.15, which depicts a general thrust vector with two inclination angles, the components of the thrust are

$$T_X = (T_1 + T_4)\cos\delta_{T_{z_o}}\cos\delta_{T_{y_o}} + (T_2 + T_3)\cos\delta_{T_{z_i}}\cos\delta_{T_{y_i}} \quad (2.75)$$

$$T_Y = (T_1 - T_4)\sin\delta_{T_{z_o}} + (T_2 - T_3)\sin\delta_{T_{z_i}} \quad (2.76)$$

$$T_Z = -(T_1 + T_4)\cos\delta_{T_{z_o}}\sin\delta_{T_{y_o}} - (T_2 + T_3)\cos\delta_{T_{z_i}}\sin\delta_{T_{y_i}} \quad (2.77)$$

where δ_{T_y} and δ_{T_z} are the inclination angles of the engine in the xz- plane and xy-plane respectively, measured from the positive x axis. The subscript 'o' and 'i' denote the outboard and inboard engines respectively.

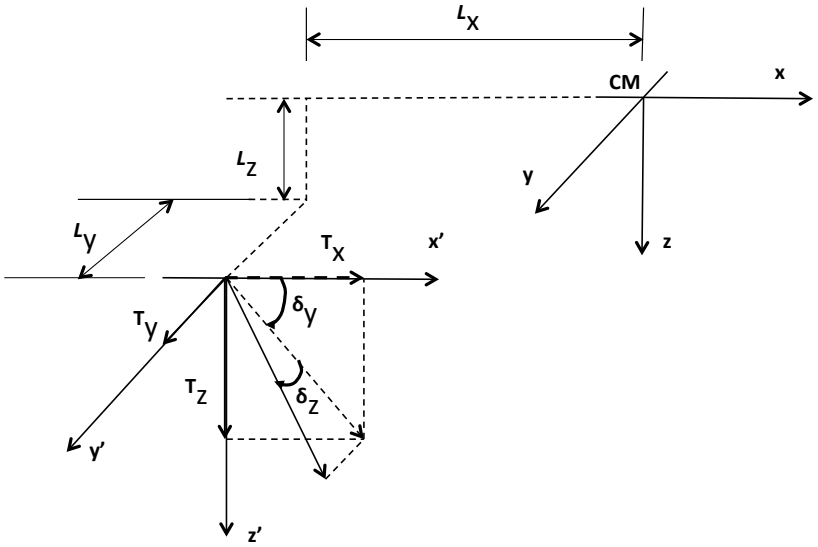

Figure 2.15. Components of the Thrust Vector.

Unlike the EQ-II, the engines of the KC-135R generate thrust in the different directions of Fig. 2.15. For the inboard engines, the inclination angle in the x-y plane, δ_{T_z}, is non-zero implying that thrust is generated in both the x and y directions of the

body frame. For the outboard engines, both inclination angles, δ_{T_y} in the x-z plane, and δ_{T_z} in the x-y plane, are non-zero and the engines generate thrust in the x-y plane, the x-z plane, and the y-z plane of the body frame. An additional implication of the KC-135R engines having inclination angles in these planes with thrust generation or even differential thrusting, the outboard engines can generate pitching, rolling, and yawing moments.

2.2.3 Fuel Tank Configuration for Trail KC-135R

In the KC-135R trail aircraft, there are six tanks modeled in the wings (two wing reserve tanks, two outboard wing tanks, two inboard wing tanks) and three tanks modeled in the fuselage (a forward body tank, a center wing tank, and an aft wing tank) as shown in shown in Fig. 2.16. All fuselage tanks are modeled in the shape of a prismoid while the wing tanks are modeled in the shape of a parallelepiped. This enables the centroid formulation algorithm developed in Reference [58] to be used for the trail KC-135R.

In developing the models for the wing tanks for implementation in the simulation, the parallelepipeds were modeled to have the same volumes as the actual KC-135R even though the width, depth, and height dimensions may differ. These geometric variations in the approximations for the model and the truth are shown in Figs. 2.17 and 2.18 which depict top and front view cross sections, respectively, of the KC-135R showing the true wing tank locations and the model approximations.

2.2.4 Actuator Dynamics for Trail KC-135R

Only actuator saturation and rate limit effects are considered for the trail KC-135R aircraft. The deflection ranges for the ailerons are (-20 deg, 20 deg), elevators

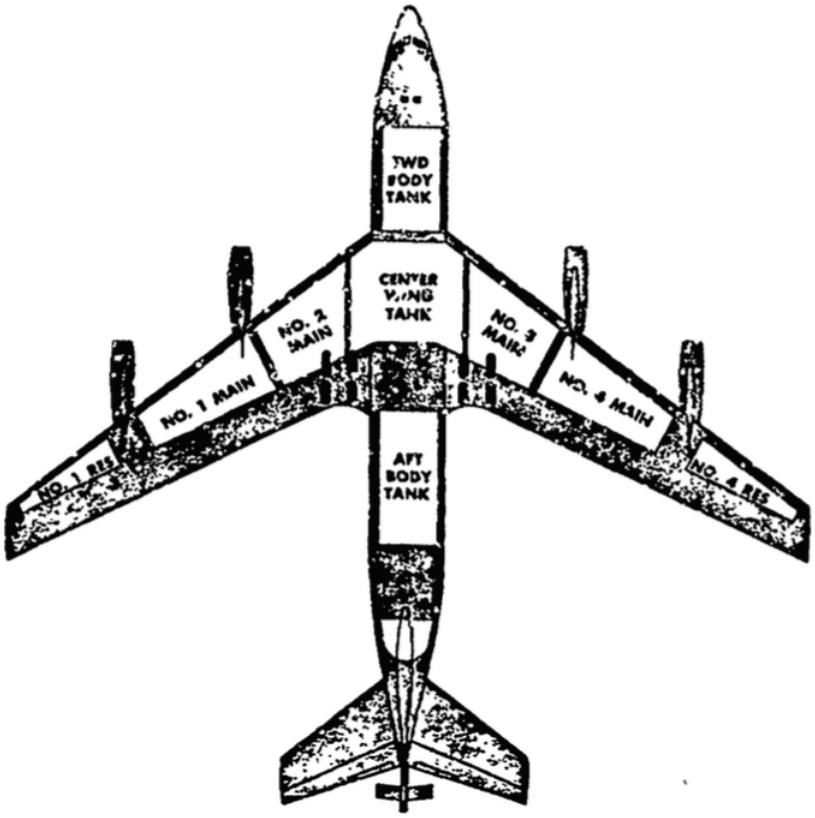

Figure 2.16. Fuel Tank Locations for Trail KC-135R [62].

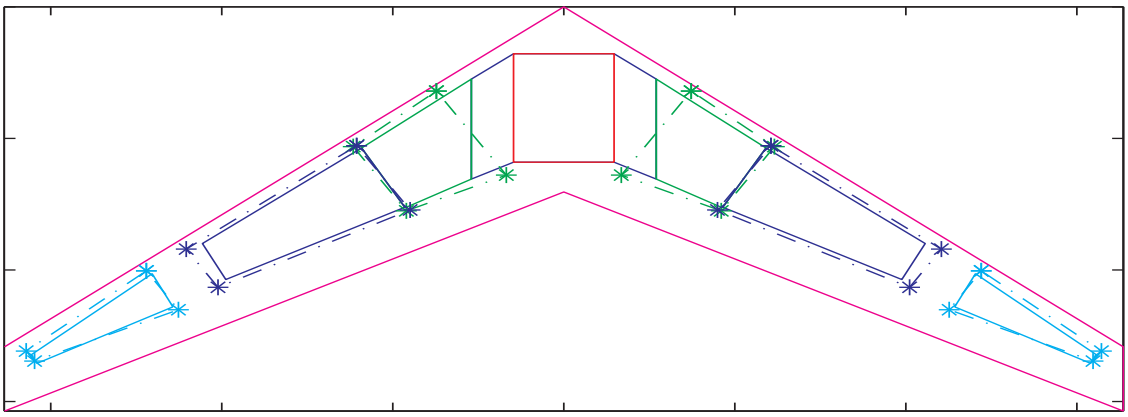

Figure 2.17. Actual and Model Locations for Fuel Tanks: Top View Cross Section.

are (15 deg, -23.5 deg), and rudder (25 deg, 25 deg). All three control surfaces have rate limits of ± 60 deg/s.

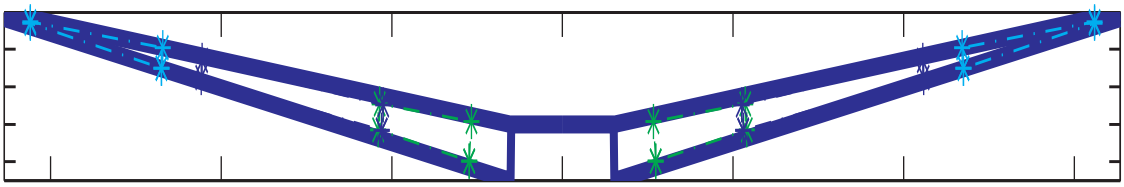

Figure 2.18. Actual and Model Locations for Fuel Tanks: Front View Cross Section.

2.3 Lead KC-135R Aircraft

The lead KC-135R in this dissertation is used primarily as a vortex/upwash generator which induces non-uniform wind distribution on the trail aircraft. As a result, its model is not as intricate or as detailed as that for the trail aircraft described in Section 2.2. The model of the lead KC-135R is adapted from Reference [63] and summarized in this dissertation for easy referencing. For additional details on Sections 2.3.1 and 2.3.2, Reference [63] should be consulted.

2.3.1 Aerodynamic Model for Lead KC-135R

2.3.1.1 Force Coefficients

The aerodynamic forces are given by the following standard expressions

$$D_T = \frac{1}{2}\rho V_T^2 \mathcal{S}_T C_{D_T} \tag{2.78}$$

$$S_T = \frac{1}{2}\rho V_T^2 \mathcal{S}_T C_{S_T} \tag{2.79}$$

$$L_T = \frac{1}{2}\rho V_T^2 \mathcal{S}_T C_{L_T} \tag{2.80}$$

where $\mathcal{S}_T$ is the reference area of the lead KC-135R and ρ is the ambient air density. The T subscripts are used in this section to indicate that the lead, and not the trail KC-135R, is being modeled. The aerodynamic force coefficients are

$$
\begin{aligned}
C_{D_T} &= C_{D0} + C_{D\alpha^2}\ \alpha_T^2 && (2.81)\\
C_{S_T} &= C_{S0} + C_{S\beta}\beta_T + C_{S\delta_r}\delta_{r_T} && (2.82)\\
C_{L_{wing,body}} &= C_{L0} + C_{L\alpha}\alpha_T + C_{L\alpha 2}\ (\alpha_T - \alpha_{ref})^2 + C_{Lq}\frac{c_T}{2V_T}q_T && (2.83)\\
C_{L_{tail}} &= C_{L\alpha_{tail}}\ \alpha_{T_{tail}} + \frac{S_T}{S_{T_{tail}}}\ C_{L\delta_e}\delta_e && (2.84)\\
C_{L_T} &= C_{L_{wing,body}} + C_{L_{tail}} && (2.85)
\end{aligned}
$$

where $(\delta_{a_T},\ \delta_{e_T},\ \delta_{r_T})$ are the deflections of the control surfaces (aileron, elevator, rudder, respectively), c_T is the chord length, and $\mathcal{S}_{T_{tail}}$ is the reference area of the horizontal tail of the lead KC-135R. The lift coefficients for the wing and the horizontal tail are defined separately. This is utilized in modeling the non-uniform wind induced by the lead on the trail aircraft as explained in Section 2.6.

2.3.1.2 Moment Coefficients

The moments of external forces around the origin of the lead KC-135R body frame in the x, y, and z directions, respectively are given by

$$
\begin{aligned}
\mathcal{L}_T &= \frac{1}{2}\rho V_T^2 \mathcal{S}_T b_T C_{\mathcal{L}_T} && (2.86)\\
\mathcal{M}_T &= \frac{1}{2}\rho V_T^2 \mathcal{S}_T c_T C_{\mathcal{M}_T} + \Delta_{z_T} T_T && (2.87)\\
\mathcal{N}_T &= \frac{1}{2}\rho V_T^2 \mathcal{S}_T b_T C_{\mathcal{N}_T} && (2.88)
\end{aligned}
$$

where b_T is the wingspan of the lead KC-135R aircraft and Δ_{z_T} is the moment arm of the thrust in the body frame of the lead KC-135R. The aerodynamic moment coefficients are

$$\begin{aligned} C_{\mathcal{L}_T} &= C_{\mathcal{L}0} + C_{\mathcal{L}\delta_a}\delta_{a_T} + C_{\mathcal{L}\delta_r}\delta_{r_T} + C_{\mathcal{L}\beta}\beta_T + C_{\mathcal{L}p}\frac{b_T}{2V_T}p_T \\ &\quad + C_{\mathcal{L}r}\frac{b_T}{2V_T}r_T \end{aligned} \tag{2.89}$$

$$C_{\mathcal{M}_T} = C_{\mathcal{M}\alpha}\alpha_T + C_{\mathcal{M}\delta_e}\delta_{e_T} + C_{\mathcal{M}q}\frac{c_T}{2V_T}q_T \tag{2.90}$$

$$\begin{aligned} C_{\mathcal{N}_T} &= C_{\mathcal{N}0} + C_{\mathcal{N}\delta_a}\delta_{a_T} + C_{\mathcal{N}\delta_r}\delta_{r_T} + C_{\mathcal{N}\beta}\beta_T + C_{\mathcal{N}p}\frac{b_T}{2V_T}p_T \\ &\quad + C_{\mathcal{N}r}\frac{b_T}{2V_T}r_T \end{aligned} \tag{2.91}$$

2.3.2 Engine Configuration for Lead KC-135R

The thrust generated by the engine (T_T) is

$$T_T = \xi_T \, T_{max_T} \tag{2.92}$$

where ξ_T denotes the instantaneous throttle setting and T_{max_T} is the maximum available thrust of the tanker and assumed to be constant in this dissertation. The engine dynamics is modeled as that of a first order system with time constant τ_T. Therefore,

$$\dot{\xi}_T = \frac{\xi_T - \xi_{t_T}}{\tau_T} \ , \tag{2.93}$$

where ξ_{t_T} is the commanded throttle setting ($0 \leq \xi_t \leq 1$).

2.3.3 Fuel Tank Configuration for Lead KC-135R

For the lead aircraft, no fuel tank subsystem is created to model the fuel flow or fuel transfer. Thus, the inertia, mass, and weight configuration remain constant for a majority of the simulations presented in this dissertation. Chapter 1 discusses a contribution of this dissertation which is a study of a reduction of the weight of the

lead aircraft, due to fuel consumption, on the benefits of a formation of long-duration. The approach taken to incorporate the effect of fuel consumption on the mass and inertia of the lead KC-135R is to first determine the fuel burned based on the thrust at each time step. This fuel burned causes a reduction in the mass of the lead aircraft at each time step and the time-varying mass can be determined as a function of the fuel burn. A similar approach is taken to vary the inertia matrix of the lead aircraft. The ratio of the mass at each time step to the initial mass of the aircraft is used to scale the inertia matrix as well in an effort to incorporate the effect of fuel consumption on the inertia matrix. The details of modifying the mass and inertia matrix of the lead to create dependencies on the time-varying fuel consumption are given in Chapter 8.

2.3.4 Actuator Dynamics for Lead KC-135R

Only actuator saturation limits are considered for the lead KC-135R. The deflection ranges for all three control surfaces is (-20 deg, 20 deg).

2.4 Equations of Motion

The equations of motion for the lead and trail aircraft are presented in this section. The trail aircraft, KC-135R and EQ-II, have their equations of motion derived relative to the body frame of the lead aircraft, which is a non-inertial frame. These equations of motion for the trail aircraft are adapted from Reference [64], which develops the equations of motion for a receiver aircraft during aerial refueling. For the lead KC-135R, the equations are developed relative to the inertial frame and are adapted from Reference [63].

2.4.1 Equations of Motion of the Trail Aircraft

In order to accurately model the dynamics of the following aircraft, it was important to account for all the factors that significantly influence its dynamics. A set of non-linear 6-DOF equations of motion were developed for a receiver aircraft undergoing aerial refueling which models (i) the relative motion of the receiver with respect to the leading tanker (ii) the time-varying mass and inertia properties during the fuel transfer into the receiver, and (iii) the exposure to non-uniform wind induced by the leading tanker's wake vortex [47].

For the derivation of the equations of motion, a system of receiver aircraft and the fuel that will join the aircraft is defined. The expressions for the time rates of change of linear and angular momenta of this system of constant mass are derived by formulating the momenta before and after the fuel joins the receiver and moves into the fuel tanks. This allows the application of Newtons Law, which is valid for a system of constant mass. Since the fuel before joining the receiver aircraft is considered in the formulation of the linear and angular momentum variation, the speed and direction of fuel flow into the receiver, as well as the location of the receptacle in the receiver, are included in the equations of motion.

The fuel transfer into the receiver changes its total mass, location of the center of mass (CM), and inertia matrix. To handle the effects of these time-varying inertia properties, the body frame of the receiver is placed at a geometrically fixed position, rather than at the center of mass of the aircraft. The origin of this body frame is chosen to be at the CM of the empty receiver aircraft, i.e., without fuel in the fuel tanks. This enables the mass and inertia matrix of the receiver aircraft without fuel to be identified in the derivation of the equations, and the aerodynamic variables such as airspeed, angle of attack, sideslip angle, and stability derivatives to be used directly without any modification or re-interpretation.

The dynamic effects due to fuel transfer are modeled by considering the mass change to be confined only to a finite number of lumped masses. These lumped masses represent fuel in each fuel tank. As fuel is transferred into the fuel tanks of the receiver, the mass and CM of the corresponding lumped mass change depending on the configuration parameters such as the shape, size, location of the individual fuel tank, and the rate of fuel flowing into it [64]. The final forms of the translational and rotational dynamics and kinematics equations for the follower are presented in the following paragraphs.

The equations are derived in terms of the position and orientation of the receiver relative to the tanker aircraft because an efficient and safe aerial refueling operation requires the control of the motion of the receiver relative to the tanker. Since the position of the receiver needs to be modeled with respect to the tanker, the translational kinematics was derived in terms of the position vector of the receiver relative to the tanker using rotation matrices to and from the inertial frame, tanker's body frame, and receiver's body frame. The translational kinematics equation is given by

$$\dot{\xi} = \mathbf{R}^{\mathbf{T}}_{\mathbf{B_R B_T}} \mathbf{R}_{\mathbf{B_R W_R}} U + \mathbf{R}^{\mathbf{T}}_{\mathbf{B_R B_T}} W - \mathbf{R}_{\mathbf{B_T I}}\, \dot{r}_{B_T} + \mathbf{S}(\omega_{\mathbf{B_T}})\xi \tag{2.94}$$

where ξ is the representation of the receiver position relative to the tanker in the tanker's body frame, U is the representation of the velocity of the receiver relative to the surrounding air in the receiver's wind frame, W is the velocity of the wind relative to the inertial frame expressed in the receiver's body frame, $\mathbf{R}_{\mathbf{B_R B_T}}$ is the rotation matrix from the tanker's to the receiver's body frame, and $\omega_{\mathbf{B_T}}$ is the angular velocity of the tanker relative to the inertial frame. Also, $\mathbf{S}(.)$ is the skew-symmetric matrix operation on the representation of the vector in parenthesis.

The translational dynamics equations include the dynamic effect of fuel transfer and wind exposure. The final form in terms of $\mathcal{X}_R = [V \quad \beta \quad \alpha]^T$, airspeed, sideslip angle, and angle of attack, is given as

$$
\begin{aligned}
\dot{\mathcal{X}}_R &= \mathcal{E}_{\mathbf{R}}^{-\mathbf{1}} \left[\mathbf{S}(\omega_{\mathbf{B_R B_T}}) + \mathbf{S}(\mathbf{R}_{\mathbf{B_R B_T}}\omega_{\mathbf{B_T}})\right] \left(\mathbf{R}_{\mathbf{B_R W_R}}\, U + W\right) - \mathcal{E}_{\mathbf{R}}^{-\mathbf{1}}\dot{W} \\
&+ \frac{1}{(M+m)}\mathcal{E}_{\mathbf{R}}^{-\mathbf{1}}\Bigg[\mathbf{R}_{\mathbf{B_R B_T}}\mathbf{R}_{\mathbf{B_T I}}\left(F + \dot{m}\, \dot{r}_{B_T}\right) \\
&\quad -\dot{m}\Bigg(\mathbf{R}_{\mathbf{B_R W_R}}\, U + W - \mathbf{R}_{\mathbf{B_R B_T}}\, V_{\dot{m}} + \mathbf{R}^{\mathbf{T}}_{\mathbf{B_R B_T}}\mathbf{S}(\omega_{\mathbf{B_T}})\rho_C\Bigg)\Bigg] \\
&- \frac{1}{(M+m)}\mathcal{E}_{\mathbf{R}}^{-\mathbf{1}}\sum_{j=1}^{k}\Bigg(\dot{m}_j\Big\{\dot{\rho}_{m_j} - \left[\mathbf{S}(\omega_{\mathbf{B_R B_T}}) + \mathbf{S}(\mathbf{R}_{\mathbf{B_R B_T}}\omega_{\mathbf{B_T}})\right]\rho_{m_j}\Big\} \\
&\quad + m_j\Big\{\ddot{\rho}_{m_j} + \mathbf{S}(\omega_{\mathbf{B_R B_T}})\left[\mathbf{S}(\omega_{\mathbf{B_R B_T}})\rho_{m_j} - 2\dot{\rho}_{m_j}\right] \\
&\quad + 2\mathbf{S}(\mathbf{R}_{\mathbf{B_R B_T}}\omega_{\mathbf{B_T}})\left[\mathbf{S}(\omega_{\mathbf{B_R B_T}})\rho_{m_j} - \dot{\rho}_{m_j}\right] \\
&\quad + \left[\mathbf{S^2}(\mathbf{R}_{\mathbf{B_R B_T}}\omega_{\mathbf{B_T}}) - \mathbf{S}(\mathbf{R}_{\mathbf{B_R B_T}}\dot{\omega}_{\mathbf{B_T}})\right]\rho_{m_j} + \mathbf{S}(\rho_{\mathbf{m_j}})\dot{\omega}_{B_R B_T}\Big\}\Bigg)
\end{aligned}
\tag{2.95}
$$

where m_j is the amount of fuel in the 'j^{th}' fuel tank, $\dot{m}_j$ is the fuel flow rate into the 'j^{th}' fuel tank, and ρ_{m_j} is the location of the CM of the fuel in the 'j^{th}' fuel tank.

The rotational dynamics equation is

$$
\begin{aligned}
\dot{\omega}_{B_R B_T} \;=\; & \underline{\underline{\mathbf{I}}}_{\mathbf{t}}^{-\mathbf{1}} M_{B_R} + \underline{\underline{\mathbf{I}}}_{\mathbf{t}}^{-\mathbf{1}} \mathbf{S}(\omega_{\mathbf{B_R B_T}} + \mathbf{R}_{\mathbf{B_R B_T}} \omega_{\mathbf{B_T}}) \underline{\underline{\mathbf{I}}}_{\mathbf{M}} \left(\omega_{B_R B_T} + \mathbf{R}_{\mathbf{B_R B_T}} \omega_{B_T}\right) \\
& + \underline{\underline{\mathbf{I}}}_{\mathbf{t}}^{-\mathbf{1}} \sum_{j=1}^{k} \mathbf{S}(\rho_{\mathbf{m_j}}) \Big[m_j \;\left(\omega_{B_R B_T}^T + \omega_{B_T}^T \mathbf{R}_{\mathbf{B_R B_T}}^{\mathbf{T}}\right) \rho_{m_j} \left(\omega_{B_R B_T} + \mathbf{R}_{\mathbf{B_R B_T}} \omega_{B_T}\right) \Big] \\
& + \underline{\underline{\mathbf{I}}}_{\mathbf{t}}^{-\mathbf{1}} \sum_{j=1}^{k} \mathbf{S}(\rho_{\mathbf{m_j}}) \Big(m_j \; \ddot{\rho}_{m_j} + \dot{m}_j \; \dot{\rho}_{m_j} \Big) \\
& + \underline{\underline{\mathbf{I}}}_{\mathbf{t}}^{-\mathbf{1}} \left[\sum_{j=1}^{k} \mathbf{S}(\rho_{\mathbf{m_j}}) \; m_j \right] \; \Big\{ - \left[\mathbf{S}(\omega_{\mathbf{B_R B_T}}) + \mathbf{S}(\mathbf{R}_{\mathbf{B_R B_T}} \; \omega_{\mathbf{B_T}}) \right] \left(\mathbf{R}_{\mathbf{B_R W_R}} \; U + W \right) \Big\} \\
& + \underline{\underline{\mathbf{I}}}_{\mathbf{t}}^{-\mathbf{1}} \left[\sum_{j=1}^{k} \mathbf{S}(\rho_{\mathbf{m_j}}) \; m_j \right] \; \Big(\mathcal{E}_{\mathbf{R}} \; \dot{\mathcal{X}}_R + \dot{W} \Big) \\
& + \underline{\underline{\mathbf{I}}}_{\mathbf{t}}^{-\mathbf{1}} \left[\sum_{j=1}^{k} \mathbf{S}(\rho_{\mathbf{m_j}}) \; \dot{m}_j \right] \; \left(\mathbf{R}_{\mathbf{B_R w_R}} \; U + W \right) \\
& - 2 \, \underline{\underline{\mathbf{I}}}_{\mathbf{t}}^{-\mathbf{1}} \sum_{j=1}^{k} m_j \; \left[\Big(\rho_{m_j}^T \; \dot{\rho}_{m_j} \Big) \, \mathbf{I_{3\times 3}} - \dot{\rho}_{m_j} \rho_{m_j}^T \right] \left(\omega_{B_R B_T} + \mathbf{R}_{\mathbf{B_R B_T}} \omega_{B_T} \right) \\
& - \underline{\underline{\mathbf{I}}}_{\mathbf{t}}^{-\mathbf{1}} \sum_{j=1}^{k} \dot{m}_j \; \left[\Big(\rho_{m_j}^T \; \rho_{m_j} \Big) \, \mathbf{I_{3\times 3}} - \rho_{m_j} \rho_{m_j}^T \right] \left(\omega_{B_R B_T} + \mathbf{R}_{\mathbf{B_R B_T}} \omega_{B_T} \right) \\
& - \mathbf{S}(\omega_{\mathbf{B_R B_T}}) \; \mathbf{R}_{\mathbf{B_R B_T}} \omega_{B_T} - \mathbf{R}_{\mathbf{B_R B_T}} \dot{\omega}_{B_T} \\
& - \underline{\underline{\mathbf{I}}}_{\mathbf{t}}^{\;-1} \dot{m} \mathbf{S}(\rho_R) \left(\mathbf{R}_{\mathbf{B_R B_T}} \mathbf{R}_{\mathbf{B_T I}} \dot{r}_{B_T} + \mathbf{R}_{\mathbf{B_R B_T}} V_{\dot{m}} - \mathbf{R}_{\mathbf{B_R B_T}} \mathbf{S}(\omega_{\mathbf{B_T}}) \rho_C \right) \qquad (2.96)
\end{aligned}
$$

where $\underline{\underline{\mathbf{I}}}_{\mathbf{t}}$ represents the total inertia matrix of the system, M_{B_R} is the body frame representation of the applied moment vector which includes the moment due to the fuel weight in each fuel tank, ρ_C is the tanker frame representation of the position of the refueling port/receptacle of the receiver aircraft measured from the origin of the tanker's body frame, ρ_R is the receiver frame representation of the position of the refueling port/receptacle of the receiver aircraft measured from the origin of the receiver body frame, and $\underline{\underline{\mathbf{I}}}_{\mathbf{M}}$ is the inertia matrix of the receiver excluding the fuel in the fuel tanks and in transit. The contributions of the fuel weight in each fuel tank,

the aerodynamic forces, and the differential thrusting to the applied moment, M_{B_R}, on the follower aircraft, are expressed as

$$M_{B_R} = M_A + \sum_{j=1}^{k} \left[m_j \, \mathbf{S}(\rho_{m_j}) \right] \, \mathbf{R_{B_R B_T}} \mathbf{R_{B_T I}} \, G + M_P \tag{2.97}$$

where M_A is the representation of the aerodynamic moment vector in the body frame of the receiver (follower) aircraft. The second term on the right is the moment generated by the weight of the fuel in each of the k fuel tanks; m_j is the fuel mass in the j^{th} fuel tank, ρ_{m_j} is the position of the CM of the m_j in the body frame and G is the representation of the gravitational acceleration in the inertial frame. These terms formulate the mechanism to generate moment by transferring fuel between fuel tanks. The last term on the right hand side of Eq. (2.97) represents the moment generated by the engine thrusts. Both trail KC-135R and EQ-II aircraft have the capacity of generating moments by using differential thrusting. The EQ-II has the capacity to generate yawing moments as shown in Section 2.1.2 and the trail KC-135R has the capacity to generate rolling, pitching, and yawing moments as described in Section 2.2.2.

The derived equations for a receiver aircraft in aerial refueling, presented above, are versatile enough to be used for the analysis of any flight condition involving mass transfer. These equations have the rates of fuel transfer into each fuel tank explicitly which allows for the study of fuel transfer effects in aerial refueling [64] and thus, formation flight. For a formation of extended duration, the fuel flow rate out of the individual fuel tanks is non-zero and is accounted for using the equations of motion described above. In the case of internal fuel transfer as an alternative moment generation mechanism, the dynamic effect of the fuel transfer within the fuel tank is incorporated into the equations of motion. Also, the equations are expressed with respect to a point geometrically fixed in the body frame of the receiver/trail aircraft.

Thus, the effect of changes in the center of mass location during the fuel transfer process has been accounted for by the equations.

2.4.2 Equations of Motion of the Lead Aircraft

For brevity, the "lead aircraft" or "lead KC-135R" will be referred to simply as the "aircraft" in this section. In matrix form, the translational kinematics equation is

$$\dot{r}_{B_T} = \mathbf{R}^{\mathbf{T}}_{\mathbf{B_T I}} \mathbf{R}_{\mathbf{B_T w_T}} V_{w_T} + W \tag{2.98}$$

where r_{B_T} is the position of the aircraft relative to the inertial frame expressed in the inertial frame, $\mathbf{R_{B_T I}}$ is the rotation matrix from the inertial frame to the body frame of the aircraft, $\mathbf{R_{B_T w_T}}$ is the rotation matrix from the aircraft wind frame to body frame, V_{w_T} is the velocity of the aircraft relative to the surrounding air expressed in the aircraft wind frame, and W is the wind the aircraft is subjected to expressed in the inertial frame.

The translational dynamics equation of the aircraft in matrix form is

$$\begin{bmatrix} \dot{V}_T \\ \dot{\beta}_T \\ \dot{\alpha}_T \end{bmatrix} = \mathcal{E}^{-\mathbf{1}}_{\mathbf{T}} \mathbf{S}(\omega_{\mathbf{B_T}}) \mathbf{R}_{\mathbf{B_T w_T}} V_{w_T} + \frac{1}{m_T} \mathcal{E}^{-\mathbf{1}}_{\mathbf{T}} \left(\mathbf{R}_{\mathbf{B_R I}} M_T + \mathbf{R}_{\mathbf{B_T w_T}} A_T + P_T \right) - \mathcal{E}^{-\mathbf{1}}_{\mathbf{T}} R_{B_R I} \dot{W} \tag{2.99}$$

where

$$\mathcal{E}^{-\mathbf{1}}_{\mathbf{T}} = \begin{bmatrix} \cos\alpha_T \cos\beta_T & \sin\beta_T & \cos\beta_T \sin\alpha_T \\ -\frac{1}{V_T} \cos\alpha_T \sin\beta_T & \frac{1}{V_T} \cos\beta_T & -\frac{1}{V_T} \sin\alpha_T \sin\beta_T \\ -\frac{1}{V_T} \sec\beta_T \sin\alpha_T & 0 & \frac{1}{V_T} \cos\alpha_T \sec\beta_T \end{bmatrix} \tag{2.100}$$

The external forces acting on the aircraft are the gravitational force M_T (expressed in the inertial frame), the aerodynamic force A_T (expressed in the wind frame of the aircraft) and propulsive force P_T (expressed in the body frame of the aircraft).

The rotational kinematics equation in matrix form is the well known standard equation:

$$\mathbf{R_{B_TI}}\dot{\mathbf{R}}_{\mathbf{B_TI}} = -\mathbf{S}(\omega_{\mathbf{B_T}}) \tag{2.101}$$

where $\omega_{\mathbf{B_T}}$ is the representation of the angular velocity vector of the aircraft relative to the inertial frame expressed in its own body frame.

The matrix form of the rotational dynamics of the aircraft is modeled with the standard rotational dynamics equation.

$$\dot{\omega}_{B_T} = \underline{\underline{\mathbf{I}}}_{\mathbf{T}}^{-\mathbf{1}} M_{B_T} + \underline{\underline{\mathbf{I}}}_{\mathbf{T}}^{-\mathbf{1}} \mathbf{S}(\omega_{\mathbf{B_T}}) \underline{\underline{\mathbf{I}}}_{\mathbf{T}} \omega_{B_T} \tag{2.102}$$

where $\underline{\underline{\mathbf{I}}}_{\mathbf{T}}$ is the inertia matrix of the tanker aircraft, M_{B_T} is the moment of the external forces around the origin of aircraft body frame and expressed in the aircraft body frame.

2.5 Control Design

2.5.1 Trajectory-Tracking Control Design for Trail

This section explains the control design procedure for the trailing aircraft to follow the commanded trajectory relative to the lead KC-135R. A MIMO (multi-input multi-output) state-feedback integral controller, developed for aerial refueling objectives, is designed based on LQR (linear quadratic regulator) optimal control and gain scheduling methods in References [63, 65, 66, 67, 68]. This controller is adapted for the trail KC-135R and EQ-II aircraft and reproduced in this section for easy referencing. The control variables calculated by the controller are control surface

deflections and thrust magnitudes from the engines on each side. The outputs to track for the aircraft are the components of the position relative to the tanker and are determined by the desired trajectory. The LQR control design technique allows the relative allocation of the control variables through the choice of the weighting matrices in the cost index. Thus, it is easy to specify which and how much of a control variable to use.

This controller can be used in formation flight without any modification for the follower aircraft control. This is because the follower should be flown relative to the leading aircraft as in the case of the aerial refueling. The follower aircraft is required to stay at the sweet spot, which is defined relative to the lead aircraft since the non-uniform wind field is generated by the vortices of the lead aircraft. Further, control allocation capability through the weighting matrices is also used for investigating different trimming schemes of the follower aircraft at the sweet spot.

For conciseness, the trail aircraft control design presented is for the trail KC-135R. The EQ-II control design is similar to that for the trail KC-135R except for the number of control inputs. While the KC-135R is modeled to have three conventional control surfaces, aileron, elevator, and rudder, the EQ-II has six control surfaces: left and right clamshell, left and right outboard elevon, and left and right inboard elevon as described in Section 2.1.

2.5.1.1 Nonlinear Aircraft Equations in Compact Form

The equations of motion for both aircraft are full 6-DOF nonlinear and account for the non-uniform wind effect, mass/inertia variation effect, and the effect of relative motion with respect to a non-inertial frame of reference [6, 7, 47]. The control design,

developed in Reference [63], however, is based on LQR method with integral control implemented in a given scheduling scheme. The state vector of the trailing aircraft is

$$\underline{x} = [V\ \beta\ \alpha\ p\ q\ r\ \psi\ \theta\ \phi\ x\ y\ z]^T \tag{2.103}$$

where orientation (ψ, θ, ϕ). angular velocity (p, q, r), and position (x, y, z) are with respect to the lead aircraft. The control input vector is

$$\underline{u}_o = [\delta_a\ \delta_e\ \delta_r\ T_{c_1}\ T_{c_2}\ T_{c_3}\ T_{c_4}]^T \tag{2.104}$$

where $(\delta_a, \delta_e, \delta_r)$ are the aileron, elevator, and rudder deflections, respectively, and T_{c_i} is the commanded thrust from the i^{th} engine. The disturbance vector due to the motion of the lead aircraft is

$$\underline{w} = [V_{xT}\ V_{yT}\ V_{zT}\ \psi_T\ \theta_T\ \phi_T\ p_T\ q_T\ r_T\ \dot{p}_T\ \dot{q}_T\ \dot{r}_T]^T \tag{2.105}$$

The force and moment vector is

$$\underline{v} = [D\ S\ L\ \mathcal{L}\ \mathcal{M}\ \mathcal{N}\ T_x\ T_y\ T_z]^T \tag{2.106}$$

The thrust vector is defined to consist of the thrust level from each engine as

$$\underline{e} = [T_1\ T_2\ T_3\ T_4]^T \tag{2.107}$$

The equations of translational and rotational dynamics and kinematics are written in compact form in terms of the defined state, control, and disturbance vectors as

$$\dot{\underline{x}} \ = \ \underline{\mathbf{f}}(\underline{x}, \underline{v}, \underline{w}) \tag{2.108}$$

The constitutive equations for aerodynamic forces, aerodynamic moments, and thrust can be written in compact form as

$$\underline{v} \ = \ \underline{\mathbf{g}}(\underline{x}, \dot{\underline{x}}, \underline{u}_o, \underline{e}, \underline{w}) \tag{2.109}$$

2.5.1.2 Linearization of Aircraft Equations

To linearize the equations of motion of the trailing aircraft, the trimmed values of its states and control variables should be determined. This is done by solving the nonlinear translational and rotational dynamics equations along with the $\dot{z}$ equation from the translational kinematics. The $\dot{z}$ equation is included to have the trimmed flight conditions at constant altitude. The steady-state nominal conditions are defined based on the speed, V, yaw rate, $\dot{\psi}$ and altitude of the lead aircraft. At the nominal condition, the side slip, β and the yaw, ψ angles of the trailing aircraft are required to be zero. Note that the yaw angle ψ of the trailing aircraft is relative to the lead aircraft

The linearization of the aircraft equations of motion could be carried out by first substituting $\underline{v}$ from Eq. (2.109) into Eq. (2.108). However, a simpler method of linearization, developed in Reference [63], is to linearize Eqs. (2.108) and (2.109) separately, and then carry out the substitution with the respective linearized equations. The linearizations of Eqs. (2.108) and (2.109) yield, respectively,

$$\Delta\underline{\dot{x}} = \mathbf{A}\ \Delta\underline{x} + \mathbf{B}\ \Delta\underline{v} + \mathbf{H}\ \Delta\underline{w} \tag{2.110}$$

$$\Delta\underline{v} = \mathbf{E_1}\ \Delta\underline{x} + \mathbf{E_2}\ \Delta\underline{\dot{x}} + \mathbf{F}\ \Delta\underline{u}_o + \mathbf{C_T}\ \Delta\underline{e} + \mathbf{G}\ \Delta\underline{w} \tag{2.111}$$

where the matrix dimensions are: $\mathbf{A} \in \Re^{12x12}$, $\mathbf{B} \in \Re^{12x9}$, $\mathbf{H} \in \Re^{12x12}$, $\mathbf{E_1} \in \Re^{9x12}$, $\mathbf{E_2} \in \Re^{9x12}$, $\mathbf{F} \in \Re^{9x7}$, and $\mathbf{G} \in \Re^{9x12}$. Also, $\mathbf{C_T} \in \Re^{9x4}$ is

$$\mathbf{C_T} = \begin{bmatrix} \mathbf{0}_{3x1} & \mathbf{0}_{3x1} & \mathbf{0}_{3x1} & \mathbf{0}_{3x1} \\ \rho_{x_o} & \rho_{x_i} & -\rho_{x_i} & -\rho_{x_o} \\ \rho_{y_o} & \rho_{y_i} & \rho_{y_i} & \rho_{y_o} \\ \rho_{z_o} & \rho_{z_i} & -\rho_{z_i} & -\rho_{z_o} \\ \cos\delta_{T_{z_o}} \cos\delta_{T_{y_o}} & \cos\delta_{T_{z_i}} \cos\delta_{T_{y_i}} & \cos\delta_{T_{z_i}} \cos\delta_{T_{y_i}} & \cos\delta_{T_{z_o}} \cos\delta_{T_{y_o}} \\ \sin\delta_{T_{z_o}} & \sin\delta_{T_{z_i}} & -\sin\delta_{T_{z_i}} & -\sin\delta_{T_{z_o}} \\ -\cos\delta_{T_{z_o}} \sin\delta_{T_{y_o}} & -\cos\delta_{T_{z_i}} \sin\delta_{T_{y_i}} & -\cos\delta_{T_{z_i}} \sin\delta_{T_{y_i}} & -\cos\delta_{T_{z_o}} \sin\delta_{T_{y_o}} \end{bmatrix} \tag{2.112}$$

where, ρ_x, ρ_y, ρ_z are the rolling, pitching, and yawing moment arms of the thrust with subscript 'o' and 'i' denote the outboard and inboard engines, respectively. The expressions for the outboard and inboard moment arms of the thrust are given as

$$\rho_{x_o} = -l_{z_o} \sin\delta_{T_{z_o}} + l_{y_o} \cos\delta_{T_{z_o}} \sin\delta_{T_{y_o}} \tag{2.113}$$

$$\rho_{y_o} = l_{z_o} \cos\delta_{T_{z_o}} \cos\delta_{T_{y_o}} + l_{x_o} \cos\delta_{T_{z_o}} \sin\delta_{T_{y_o}} \tag{2.114}$$

$$\rho_{z_o} = l_{y_o} \cos\delta_{T_{z_o}} \cos\delta_{T_{y_o}} + l_{x_o} \sin\delta_{T_{z_o}} \tag{2.115}$$

and

$$\rho_{x_i} = -l_{z_i} \sin\delta_{T_{z_i}} + l_{y_i} \cos\delta_{T_{z_i}} \sin\delta_{T_{y_i}} \tag{2.116}$$

$$\rho_{y_i} = l_{z_i} \cos\delta_{T_{z_i}} \cos\delta_{T_{y_i}} + l_{x_i} \cos\delta_{T_{z_i}} \sin\delta_{T_{y_i}} \tag{2.117}$$

$$\rho_{z_i} = l_{y_i} \cos\delta_{T_{z_i}} \cos\delta_{T_{y_i}} + l_{x_i} \sin\delta_{T_{z_i}} \tag{2.118}$$

The matrix $\mathbf{C_T}$ indicates the fact with non-zero moment arms and inclination angles, the thrust can generate both rolling, pitching, and yawing moments. After the linearization is complete, the substitution of Eq. (2.111) into Eq. (2.110) results in

$$\Delta\dot{\underline{x}} = (\mathbf{I} - \mathbf{BE_2})^{-1}\big\{(\mathbf{A} + \mathbf{BE_1})\,\Delta\underline{x} + (\mathbf{BF})\,\Delta\underline{u}_o + (\mathbf{BC_T})\,\Delta\underline{e} + (\mathbf{BG} + \mathbf{H})\,\Delta\underline{w}\big\} \tag{2.119}$$

2.5.1.3 Engine Model

Equation (2.119) has $\underline{e}$, thrusts generated by each engine while control vector $\underline{u}_o$ has commanded thrust for each engine. This implies that a linear engine model should be included in the state-space representation to define the linear relation between commanded thrust and generated thrust for each of the four engines. To develop this linear model, the rate limit and saturation nonlinearities in the nonlinear engine model are ignored. Further, the transport delay is modeled by a Pade approximation with a 2^{nd}-order polynomial denominator and a 1^{st}-order polynomial numerator. With these approximations, the transfer function from the commanded thrust to generated thrust becomes

$$\frac{\Delta T_i(s)}{\Delta T_{ci}(s)} = \frac{w_1(s + w_2)(-2\tau s + 6)}{(\tau^2 s^2 + 4\tau s + 6)[(s + w_1)(s + w_2) + K_{eng} w_1 s]} \tag{2.120}$$

where $i = \{1, 2, 3, 4\}$. A state space representation with four states of this transfer function is given as

$$\dot{\underline{z}}_{e_i} = \mathbf{A_e}\underline{z}_{e_i} + \mathbf{B_e}\,\Delta T_{c_i} \tag{2.121}$$

$$\Delta T_i = \mathbf{C_e}\underline{z}_{e_i} \tag{2.122}$$

where

$$\underline{z}_{e_i} = [z_{i_1}\ z_{i_2}\ z_{i_3}\ z_{i_4}]^T \tag{2.123}$$

and $i = \{1, 2, 3, 4\}$ as all four engines are identical. In Eqs. (2.121)-(2.123), the state, input, and output matrices are

$$\mathbf{A_e} = \begin{bmatrix} 0 & 1 & 0 & 0 \\ 0 & 0 & 1 & 0 \\ 0 & 0 & 0 & 1 \\ -\frac{A_0}{A_4} & -\frac{A_1}{A_4} & -\frac{A_2}{A_4} & -\frac{A_3}{A_4} \end{bmatrix} \tag{2.124}$$

(2.125)

$$\mathbf{B_e} = \begin{bmatrix} 0 \\ 0 \\ 0 \\ \frac{1}{A_4} \end{bmatrix} \tag{2.126}$$

(2.127)

$$\mathbf{C_e} = \begin{bmatrix} C_0 & C_1 & C_2 & 0 \end{bmatrix} \tag{2.128}$$

where

$$C_2 = -2\tau w_1 \tag{2.129}$$

$$C_1 = w_1(6 - 2\tau w_2) \tag{2.130}$$

$$C_0 = 6w_1w_2 \tag{2.131}$$

$$A_4 = \tau^2 \tag{2.132}$$

$$A_3 = \tau(4 + \tau[(1 + K_{eng})w_1 + w_2]) \tag{2.133}$$

$$A_2 = \tau^2 w_1 w_2 + 4\tau[(1 + K_{eng})w_1 + w_2] + 6 \tag{2.134}$$

$$A_1 = 4\tau w_1 w_2 + 6[(1 + K_{eng})w_1 + w_2] \tag{2.135}$$

$$A_0 = 6w_1w_2 \tag{2.136}$$

A meta state-space model is constructed to represent the four identical engines together as

$$\dot{\underline{z}}_e = \mathbf{A_{eT}}\ \underline{z}_e + \mathbf{B_{eT}}\ \Delta\underline{T}_c \tag{2.137}$$

$$\Delta\underline{e} = \mathbf{C_{e_T}}\ \underline{z}_e \tag{2.138}$$

where

$$\underline{z}_e = [\underline{z}_{e_1}^T\ \underline{z}_{e_2}^T\ \underline{z}_{e_3}^T\ \underline{z}_{e_4}^T]^T \tag{2.139}$$

$$\Delta\underline{T}_c = [\Delta T_{c1}\ \Delta T_{c2}\ \Delta T_{c3}\ \Delta T_{c4}]^T \tag{2.140}$$

The state, control and output matrices are as follows.

$$\mathbf{A_{eT}} = \begin{bmatrix} \mathbf{A_e} & 0_{4\times4} & 0_{4\times4} & 0_{4\times4} \\ 0_{4\times4} & \mathbf{A_e} & 0_{4\times4} & 0_{4\times4} \\ 0_{4\times} & 0_{4\times4} & \mathbf{A_e} & 0_{4\times4} \\ 0_{4\times4} & 0_{4\times4} & 0_{4\times4} & \mathbf{A_e} \end{bmatrix} \in \Re^{16x16} \tag{2.141}$$

$$\mathbf{B_{eT}} = \begin{bmatrix} & \mathbf{B_e} & 0_{4\times3} \\ 0_{4\times1} & \mathbf{B_e} & 0_{4\times2} \\ 0_{4\times2} & \mathbf{B_e} & 0_{4\times2} \\ 0_{4\times3} & \mathbf{B_e} & \end{bmatrix} \in \Re^{16x4} \tag{2.142}$$

$$\mathbf{C_{e_T}} = \begin{bmatrix} \mathbf{C_e} & 0_{1\times4} & 0_{1\times4} & 0_{1\times4} \\ 0_{1\times4} & \mathbf{C_e} & 0_{1\times4} & 0_{1\times4} \\ 0_{1\times4} & 0_{1\times4} & \mathbf{C_e} & 0_{1\times4} \\ 0_{1\times4} & 0_{1\times4} & 0_{1\times4} & \mathbf{C_e} \end{bmatrix} \in \Re^{4x16} \tag{2.143}$$

Note from (2.104) that $\underline{T}_c$ is a subset of $\underline{u}_o$. Thus, (2.137) can be rewritten as

$$\dot{\underline{z}}_e = \mathbf{A_{eT}}\ \underline{z}_e + \mathbf{B_{eA}}\ \Delta\underline{u}_o \tag{2.144}$$

where

$$\mathbf{B_{eA}} = [\mathbf{0}_{16\times 3}\ \mathbf{B_{eT}}] \in \Re^{16x7} \tag{2.145}$$

2.5.1.4 Actuator Dynamics

Unlike engine dynamics, actuator dynamics for the control effectors are not included in the state-space representation while the simulation has the actuator dynamics included as defined in Refs. [56, 57].

2.5.1.5 Aircraft and Engine Model Combined

In this section, aircraft and engine models are combined to obtain the state-space representation of the aircraft together with four engines. First, a new meta state vector is defined as

$$\underline{x}_a = \begin{bmatrix} \Delta\underline{x} \\ \underline{z}_e \end{bmatrix} \in \Re^{28x1} \tag{2.146}$$

Substituting Eq. (2.138) in Eq. (2.119) and combining the resultant equation with Eq. (2.144) result in the meta state-space representation for the system of aircraft and four engines as

$$\dot{\underline{x}}_a = \mathbf{A_a}\ \underline{x}_a + \mathbf{B_a}\ \Delta\underline{u}_o + \mathbf{F_a}\ \Delta\underline{w} \tag{2.147}$$

where $\underline{x}_a \in \Re^{28x1}$, $\underline{u}_o \in \Re^{7x1}$ and $\underline{w} \in \Re^{12x1}$.

The state, control and disturbance matrices are as follows.

$$\mathbf{A_a} = \begin{bmatrix} (\mathbf{I}-\mathbf{BE_2})^{-1}(\mathbf{A}+\mathbf{BE_1}) & (\mathbf{I}-\mathbf{BE_2})^{-1}\mathbf{BC_T}\mathbf{C_{e_T}} \\ \mathbf{0}_{16\times 12} & \mathbf{A_{eT}} \end{bmatrix} \in \Re^{28x28} \quad (2.148)$$

$$\mathbf{B_a} = \begin{bmatrix} (\mathbf{I}-\mathbf{BE_2})^{-1}\mathbf{BF} \\ \mathbf{B_{eA}} \end{bmatrix} \in \Re^{28x7} \quad (2.149)$$

$$\mathbf{F_a} = \begin{bmatrix} (\mathbf{I}-\mathbf{BE_2})^{-1}\mathbf{BG}+\mathbf{H} \\ \mathbf{0}_{16\times 12} \end{bmatrix} \in \Re^{28x12} \quad (2.150)$$

2.5.1.6 Augmentation with Integral States for Position Error

The output of interest is the trajectory of the trailing aircraft relative to the leader; thus, the output vector is chosen to be

$$\underline{y} = [\Delta x \ \Delta y \ \Delta z]^T \quad (2.151)$$

which is written in terms of the state vector as

$$\underline{y} = \mathbf{C_a}\ \underline{x}_a \quad (2.152)$$

where $\mathbf{C_a} \in \Re^{3\times 28}$ and is chosen such that $\underline{y}$ is as defined in Eq. (2.151). To ensure zero tracking error at the steady state condition, three additional states are defined as the integral of the output error

$$\dot{\underline{e}}_r = \underline{y} - \underline{y}_c \quad (2.153)$$

where $\underline{y}_c$ is the commanded position for the receiver. With the integral states included, a new augmented state vector is defined as

$$\underline{x}_A = \begin{bmatrix} \underline{x}_a \\ \underline{e}_r \end{bmatrix} \in \Re^{31\times 1} \quad (2.154)$$

The augmented state-space equation for $\underline{x}_A$, then, becomes

$$\dot{\underline{x}}_A = \mathbf{A_A}\ \underline{x}_A + \mathbf{B_A}\ \Delta\underline{u}_o + \mathbf{F_A}\ \Delta\underline{w} - \mathbf{H_A}\ \underline{y}_c \tag{2.155}$$

where

$$\mathbf{A_A} = \begin{bmatrix} \mathbf{A_a} & \mathbf{0}_{28\times 3} \\ \mathbf{C_a} & \mathbf{0}_{3\times 3} \end{bmatrix} \in \Re^{31\times 31} \tag{2.156}$$

$$\mathbf{B_A} = \begin{bmatrix} \mathbf{B_a} \\ \mathbf{0}_{3\times 7} \end{bmatrix} \in \Re^{31\times 7} \tag{2.157}$$

$$\mathbf{F_A} = \begin{bmatrix} \mathbf{F_a} \\ \mathbf{0}_{3\times 12} \end{bmatrix} \in \Re^{31\times 12} \tag{2.158}$$

$$\mathbf{H_A} = \begin{bmatrix} \mathbf{0}_{28\times 3} \\ \mathbf{I}_{3\times 3} \end{bmatrix} \in \Re^{31\times 3} \tag{2.159}$$

2.5.1.7 New Control Vector

Instead of four independent thrust commands, total thrust command T_t and differential thrust T_d are defined as

$$T_t = T_{c_1} + T_{c_2} + T_{c_3} + T_{c_4} \tag{2.160}$$

$$T_d = (T_{c_3} + T_{c_4}) - (T_{c_1} + T_{c_2}) \tag{2.161}$$

A new control vector is defined using the new control variables as

$$\underline{u} = [\delta_a\ \delta_e\ \delta_r\ T_t\ T_d]^T \tag{2.162}$$

The mapping from the new control variable to the original one can be defined as

$$\Delta\underline{u}_o = \mathbf{M_u}\ \Delta\underline{u} \tag{2.163}$$

where

$$\mathbf{M_u} = \begin{bmatrix} \mathbf{I}_{3\times3} & \mathbf{0}_{3\times2} \\ \mathbf{0}_{4\times3} & \mathbf{M}_{td} \end{bmatrix} \in \Re^{7\times5} \tag{2.164}$$

and

$$\mathbf{M}_{td} = \frac{1}{4}\begin{bmatrix} 1 & -1 \\ 1 & -1 \\ 1 & 1 \\ 1 & 1 \end{bmatrix} \tag{2.165}$$

The augmented state-space equation from Eq. (2.155) is re-written with the new control vector as

$$\underline{\dot{x}}_A = \mathbf{A_A}\ \underline{x}_A + \mathbf{B_{AM}}\ \Delta\underline{u} + \mathbf{F_A}\ \Delta\underline{w} - \mathbf{H_A}\ \underline{y}_c \tag{2.166}$$

where

$$\mathbf{B_{AM}} = \mathbf{B_A}\ \mathbf{M_u} \tag{2.167}$$

where $\mathbf{B_{AM}} \in \Re^{31\times5}$ and $\mathbf{B_A} \in \Re^{31\times7}$.

2.5.1.8 LQR Design with Gain Scheduling

For gain scheduling, six different nominal conditions are defined and matrices of the linearized state-space equations in Eqs. (2.166) and (**??**) are computed for each nominal condition. This differs from Reference [63] which utilized four nominal conditions for the linearization and gain scheduling: two straight steady-level flight and two steady turn conditions. In this dissertation, the six nominal conditions, as summarized in Table 2.4, represent straight-level flight with two different airspeed and level turns (left and right) with the same two airspeeds. Based on Eq. (2.166), a state-space model is written as

$$\underline{\dot{x}}_A = \mathbf{A_{A_i}}\ \underline{x}_A + \mathbf{B_{AM_i}}\ \Delta\underline{u} + \mathbf{F_{A_i}}\ \Delta\underline{w} - \mathbf{H_{A_i}}\ \underline{y}_c \tag{2.168}$$

where $\mathbf{i} \in \{1, \cdots, 6\}$, corresponding to each nominal condition.

Using LQR design technique, the state feedback gain matrix $\mathbf{K_i}$ is obtained, for the state-space model in (2.168), to minimize the cost function:

$$J(\Delta \underline{u}) = \int_0^\infty \left\{ \underline{x}_A^T \, \mathbf{Q_i} \, \underline{x}_A + \Delta \underline{u}^T \, \mathbf{R_i} \, \Delta \underline{u} \right\} \mathrm{d}t \tag{2.169}$$

where $\mathbf{Q_i} \in \Re^{31 \times 31}$ are symmetric positive semidefinite and $\mathbf{R_i} \in \Re^{6 \times 6}$ are symmetric positive definite. Note that matrices $\mathbf{Q_i}$ and $\mathbf{R_i}$ can be selected separately for each nominal condition.

Thus, the state feedback control laws with the integral control are

$$\Delta \underline{u}_i = -\mathbf{K_i} \, \underline{x}_A \tag{2.170}$$

Note that the control laws assume the availability of full state measurement or estimation for feedback, including the four states of each engine. For the simulation implementation of this controller, an observer is designed and implemented to estimate the engine states based on the commanded and delivered thrust for each engine. Further, in the implementation of linear controllers, a Lagrange interpolation "scheduling" scheme is employed to determine effective values of the gains at a given flight condition. With this scheme, the non-linear gain scheduling controller based on the six linear designs is

Table 2.4. Nominal Conditions by Turn rate and Airspeed

Nominal Condition	Tanker Yaw Rate	Tanker Airspeed
1	$\dot{\psi}_{T1}$	V_{T1}
2	$\dot{\psi}_{T1}$	V_{T2}
3	$\dot{\psi}_{T2}$	V_{T1}
4	$\dot{\psi}_{T2}$	V_{T2}
5	$\dot{\psi}_{T3}$	V_{T1}
6	$\dot{\psi}_{T3}$	V_{T2}

$$
\begin{aligned}
\Delta\underline{u} \;=\; & \frac{\left(\dot{\psi}_c-\dot{\psi}_{T2}\right)\left(\dot{\psi}_c-\dot{\psi}_{T3}\right)(V_c-V_{T2})}{\left(\dot{\psi}_{T1}-\dot{\psi}_{T2}\right)\left(\dot{\psi}_{T1}-\dot{\psi}_{T3}\right)(V_{T1}-V_{T2})}\,\underline{u}_1+\frac{\left(\dot{\psi}_c-\dot{\psi}_{T2}\right)\left(\dot{\psi}_c-\dot{\psi}_{T3}\right)(V_c-V_{T1})}{\left(\dot{\psi}_{T1}-\dot{\psi}_{T2}\right)\left(\dot{\psi}_{T1}-\dot{\psi}_{T3}\right)(V_{T2}-V_{T1})}\,\underline{u}_2 \\
& \frac{\left(\dot{\psi}_c-\dot{\psi}_{T1}\right)\left(\dot{\psi}_c-\dot{\psi}_{T3}\right)(V_c-V_{T2})}{\left(\dot{\psi}_{T2}-\dot{\psi}_{T1}\right)\left(\dot{\psi}_{T2}-\dot{\psi}_{T3}\right)(V_{T1}-V_{T2})}\,\underline{u}_3+\frac{\left(\dot{\psi}_c-\dot{\psi}_{T1}\right)\left(\dot{\psi}_c-\dot{\psi}_{T3}\right)(V_c-V_{T1})}{\left(\dot{\psi}_{T2}-\dot{\psi}_{T1}\right)\left(\dot{\psi}_{T2}-\dot{\psi}_{T3}\right)(V_{T2}-V_{T1})}\,\underline{u}_4 \\
& \frac{\left(\dot{\psi}_c-\dot{\psi}_{T1}\right)\left(\dot{\psi}_c-\dot{\psi}_{T2}\right)(V_c-V_{T2})}{\left(\dot{\psi}_{T3}-\dot{\psi}_{T1}\right)\left(\dot{\psi}_{T3}-\dot{\psi}_{T1}\right)(V_{T1}-V_{T2})}\,\underline{u}_5+\frac{\left(\dot{\psi}_c-\dot{\psi}_{T1}\right)\left(\dot{\psi}_c-\dot{\psi}_{T2}\right)(V_c-V_{T1})}{\left(\dot{\psi}_{T3}-\dot{\psi}_{T1}\right)\left(\dot{\psi}_{T3}-\dot{\psi}_{T2}\right)(V_{T2}-V_{T1})}\,\underline{u}_6
\end{aligned}
\tag{2.171}
$$

2.5.2 VHRCAH Control Design for Lead

The controller for the lead aircraft is a "velocity/heading rate command-altitude hold" (VHRCAH) developed in Reference [63] which implements a control design to hold the speed and altitude and track the yaw rate for the tanker aircraft in aerial refueling. This control design is utilized and reproduced in this dissertation. Similar to the control design for the trail aircraft, the lead KC-135R uses a MIMO state-feedback LQR and integral control technique. The control variables available are the three conventional control surfaces and the throttle setting while the outputs to be controlled are the airspeed, altitude and yaw rate. A gain scheduling scheme is implemented based on the commanded speed and yaw rate and the procedure is described in this section.

The tanker's equations of motion given in Section 2.4.2 are linearized at six different steady-state trimmed nominal conditions described in Section 2.5.1.8. Six different sets of linearized equation of motion, in state-space form, for the lead aircraft are

$$
\Delta\underline{\dot{x}}_T = \mathbf{A}_{T,i}\;\Delta\underline{x}_T + \mathbf{B}_{T,i}\;\Delta\underline{u}_T \tag{2.172}
$$

where $\mathbf{A}_{T,i} \in \Re^{9\times 9}$, $\mathbf{B}_{T,i} \in \Re^{9\times 4}$, $i \in \{1-6\}$, for the six nominal conditions.

The state vector for the lead aircraft is

$$\Delta \underline{x}_T = [\Delta V_T \ \Delta\beta_T \ \Delta\alpha_T \ \Delta p_T \ \Delta q_T \ \Delta r_T \ \Delta\theta_T \ \Delta\phi_T \ \Delta z_T \ ]^T \tag{2.173}$$

The control input vector is

$$\Delta \underline{u}_T = [\Delta\delta_{a_T} \ \Delta\delta_{e_T} \ \Delta\delta_{r_T} \ \Delta\xi_{t_T} \ ]^T \tag{2.174}$$

where $(\delta_{a_T}, \delta_{e_T}, \delta_{r_T})$ are the control surface deflections of the lead aircraft and ξ_{t_T} is its throttle setting. In all equations above, Δ indicates that the corresponding variable is the deviation from its nominal value. Since the requirements of the controller are to track commanded speed, altitude and yaw rate, the following output vector of the lead aircraft is chosen

$$\underline{y}_T = \left[\Delta V_T \ \Delta z_T \ \Delta\dot{\psi}_T\right]^T \tag{2.175}$$

To ensure zero tracking error at the steady state condition, the state space equations are augmented by three integrators for speed error, altitude error and yaw rate error:

$$\dot{\underline{e}}_T = \underline{y}_T - \underline{y}_{T,c} \tag{2.176}$$

where $\underline{y}_{T,c} = [\Delta V_{T,c} \ \Delta z_{T,c} \ \Delta\dot{\psi}_{T,c}]^T$ is the commanded output vector of the lead aircraft. By including the augmentation states in the state space equations, the augmented state equation becomes

$$\begin{bmatrix} \Delta\dot{\underline{x}}_T \\ \dot{\underline{e}}_T \end{bmatrix} = \begin{bmatrix} \mathbf{A}_{T,i} & \mathbf{0_{9\times 3}} \\ \mathbf{C_T} & \mathbf{0_{3\times 3}} \end{bmatrix} \begin{bmatrix} \Delta\underline{x}_T \\ \underline{e}_T \end{bmatrix} + \begin{bmatrix} \mathbf{B}_{T,i} \\ \mathbf{0_{3\times 4}} \end{bmatrix} \Delta\underline{u}_T - \begin{bmatrix} \mathbf{0_{9\times 3}} \\ \mathbf{I_{3\times 3}} \end{bmatrix} \underline{y}_{T,c} \tag{2.177}$$

Using LQR design technique, the state feedback gain matrix $[\mathbf{K_{T,x}} \ \mathbf{K_{T,e}}]$ is obtained to minimize the cost function:

$$J(\underline{u}_T) = \int_0^\infty \left\{ [\ \Delta\underline{x}_T^T \ \ \underline{e}_T^T \ ]\mathbf{Q}_{T,i} \begin{bmatrix} \Delta\underline{x}_T \\ \underline{e}_T \end{bmatrix} + \Delta\underline{u}_T^T \mathbf{R}_{T,i} \, \Delta\underline{u} \right\} \mathrm{d}t \tag{2.178}$$

where $\mathbf{Q}_{T,i} \in \Re^{12\times12}$ are symmetric positive semidefinite, $\mathbf{R}_{T,i} \in \Re^{4\times4}$ are symmetric positive definite and $\mathbf{N}_{T,i} \in \Re^{12\times4}$ are symmetric positive definite. Note that matrices $\mathbf{Q}_{T,i}$, $\mathbf{R}_{T,i}$ and $\mathbf{N}_{T,i}$ can be selected separately for each nominal condition. Thus, the state feedback control laws with the integral control are

$$\Delta\underline{u}_{T,i} = -\mathbf{K}_{\mathbf{x_{T,i}}}\,\Delta\underline{x}_T - \mathbf{K}_{\mathbf{e_{T,i}}}\,\underline{e}_T \tag{2.179}$$

where $i \in \{1-6\}$, corresponding to the six nominal conditions. A gain scheduling control law is employed to interpolate between the linear controllers at the six nominal conditions using Eq. 2.171 as was done for the trail aircraft.

2.6 Non-uniform Wind Effect Modeling

This section presents an overview of the implementation and validation of the NUWEMT (Non-Uniform Wind Effect Modeling Technique) used to model the effect of the non-uniform wind induced by the wake vortex of the lead on the follower aircraft. The NUWEMT has been successfully implemented in simulations for aerial refueling [49, 47, 69, 70] and formation flight [7, 71]. The biggest advantage of the NUWEMT is that it can be implemented directly in real time simulations and thus eliminates the need for generating and managing lookup tables in simulation. For additional details, the previous publications [5, 6, 7, 65, 72] should be referred to for further details of the NUWEMT modeling of the non-uniform wind from the leader and the averaging technique used to estimate the vortex-effect on the receiver [69].

2.6.1 Description

During aerial refueling and formation flight, the leader and follower aircraft experience a prevailing wind and turbulence from the general atmospheric conditions. In addition to these two sources of wind, the follower is also subject to the wind field

in the wake of the lead aircraft. This wind field is modeled using the lifting line theory. There are three vortex filaments contributing to the the wind: one wing-bound vortex, and 2 trailing wing-tip vortices. The magnitude of the wind at a point is dependent on the strength of each vortex filament and is computed using Biot-Savart law and the Modified Helmholtz vortex model [65]. The vortices induce a non-uniform wind distribution over the follower aircraft with varying magnitude and direction depending on its location relative to the leader. The dynamic effect of this non-uniform wind is modeled using NUWEMT, which approximates a non-uniform wind along each direction with an approximate uniform wind component and a uniform wind gradient [5, 6, 7]. This approximation leads to three components of effective translational wind velocity, W_x, W_y, and W_z and three components of effective rotational wind velocity, p_{eff}, q_{eff}, and r_{eff} [65]. The translational kinematics and dynamics equations, Eqs. (2.94) and (2.95) respectively, have explicit terms with the translational wind components and their time derivatives. Furthermore, the translational dynamics equation in Eq. (2.95) is written in terms of $\mathcal{X}_R = [V \quad \beta \quad \alpha]^T$, where V, β, and α are the parameters of the velocity vector of the aircraft relative to the air, and thus account for the presence of wind. This mechanism models how the translational wind components affect the velocity vector of the aircraft. The effect of the translational wind on the aerodynamics is also modeled through the aerodynamic force and moment expressions which have explicit terms of angle of attack and sideslip.

The effect of the rotational wind components is incorporated through the aerodynamic force and moment expressions, as in the case of the second mechanism of the translational wind components. The rotational velocity of an aircraft relative

to "rotating" air is the difference between the velocity of the aircraft relative to the inertial frame and the velocity of the air relative to the inertial frame as

$$\{p, q, r\}_{rel} = \{p, q, r\} - \{p, q, r\}_{eff} \tag{2.180}$$

where $\{p, q, r\}_{rel}$ is the angular velocity of the aircraft relative to the air, $\{p, q, r\}$ is the velocity of the aircraft relative to the inertial frame, and $\{p, q, r\}_{eff}$ is the rotational wind relative to the inertial frame, which is calculated by the NUWEMT. Since the aerodynamics of an aircraft is about its motion relative to air, the aerodynamic expressions have $\{p, q, r\}_{rel}$, not $\{p, q, r\}$. Thus, the effect of the rotational wind on the aircraft dynamics is modeled through the terms with $\{p, q, r\}_{rel}$ in the aerodynamic force and moment coefficients.

2.6.2 Validation

NUWEMT has previously been validated against CFD [73], wind tunnel [5, 6] and flight data [65, 74]. The formation simulations in this dissertation use the NUWEMT which is again validated for a pair of KC-135R aircraft in formation. This section shows a comparison of the variations in aerodynamic force and moment coefficients calculated by NUWEMT against those calculated by CFD as the position of the trailing aircraft changes relative to the lead aircraft. Fig. 2.19 shows the two KC-135R models in one of the CFD runs. The comparison helps validate the technique used before extensive simulations and analyses are carried out. CFD results are generated by NASA's Cart3D package, which consists of both the Cartesian grid generation tool Cubes as well as the finite-volume, upwind-differencing, Euler flow solver flowCart [75].

In the CFD runs, the trailing KC-135R model is placed at various positions relative to the lead KC-135R model and the aerodynamic forces and moments acting

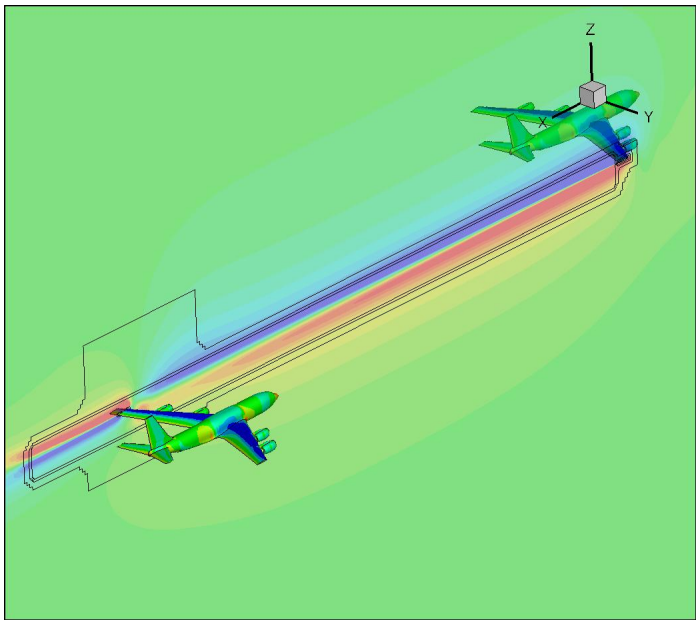

Figure 2.19. KC-135R Configuration for CFD Runs, x=3.82b.

on the trailing aircraft are recorded. All CFD runs are set up such that the freestream Mach number is 0.66 and altitude is 25 000 ft. In all CFD runs, the trailing KC-135R model is placed longitudinally 3.82 wingspans behind the lead model. Based on the lateral and vertical separation, there are two sets of CFD runs: (1) Lateral sweep and (2) Vertical sweep. In the lateral sweep, the lateral separation (relative position) is varied from 0 (right behind the lead aircraft) to a wingspan (the right wingtip of the lead aircraft is aligned with the left wingtip of the trailing aircraft) by increments of 5 feet while the vertical separation is kept at zero. The pitch angles are set to 1.2 degrees and 1.8 degrees for the lead and trailing aircraft models, respectively. In the vertical sweep, the vertical separation is varied from 12 feet below to 12 feet above the lead aircraft by increments of 2 feet as the lateral separation is kept at 0.96 wingspan on the right. In these runs, the pitch angles of both models are set to be 0.5 degrees. To validate the NUWEMT using the CFD results, the MATLAB/Simulink integrated simulation is run, similar to CFD and wind tunnel tests by disregarding trim, to

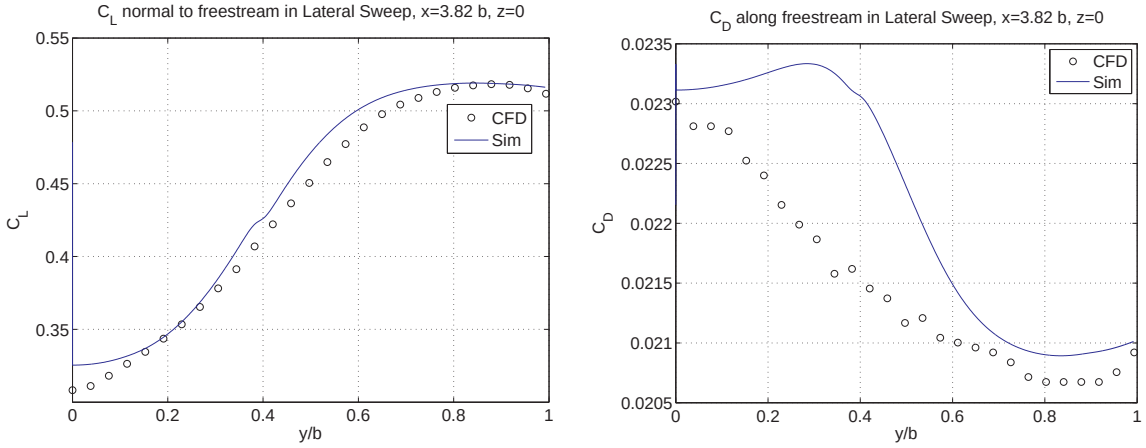

Figure 2.20. Aerodynamic Force Coefficients in Lateral Sweep, x=3.82b, z=0.

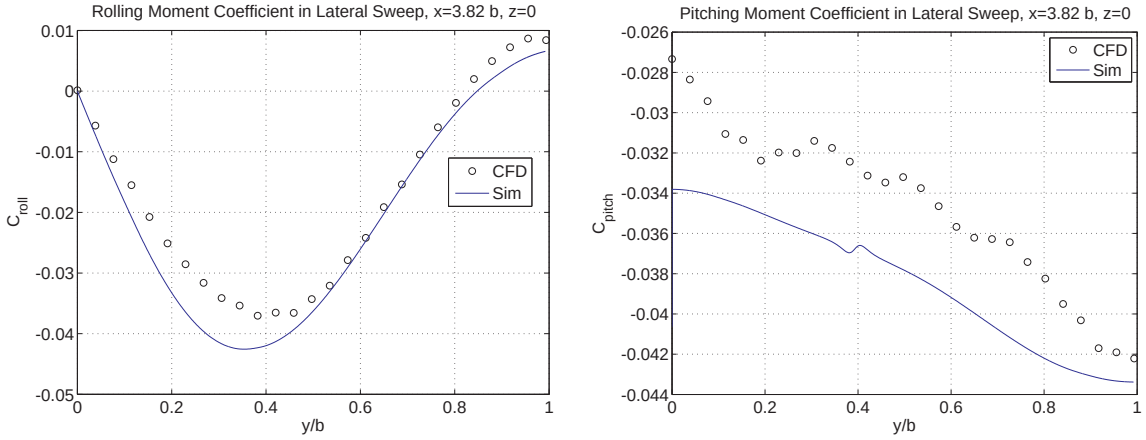

Figure 2.21. Aerodynamic Moment Coefficients in Lateral Sweep, x=3.82b, z=0.

generate the aerodynamic force and moment coefficients based on NUWEMT along the same relative position ranges in the lateral and vertical sweeps. In the following, the comparisons of the aerodynamic coefficients are presented in Figs. 2.20 and 2.21 for lateral sweep and in Figs. 2.22 and 2.23 for vertical sweep.

The lift and drag coefficients generated by the simulation and seen in Fig. 2.20 provide a close match with the CFD results especially around 0.7 to 1 wingspan which is the region of interest for the sweet spot. The rolling and pitching moment

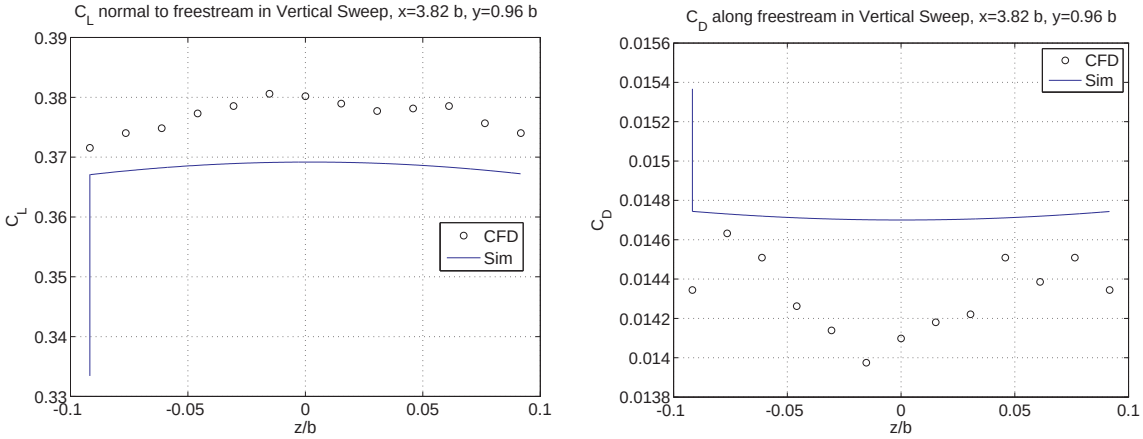

Figure 2.22. Aerodynamic Force Coefficients in Vertical Sweep, x=3.82b, y=0.96b.

coefficient curves in Fig. 2.21 also compare very well with the CFD data. Overall, the trends of the aerodynamic force and moment coefficients during the lateral sweep are well predicted by the simulation.

For the vertical sweep, the simulation trends and the CFD results are not as close as in the lateral sweep. Although the simulations seemingly under-predict/over-predict the trends, the disparity in magnitudes is very small. For instance, the simulation lift coefficient curve of the trail aircraft seen in Fig. 2.22, in the sweet spot region of interest, z=0 wingspans relative to the lead, is about 0.01 less than the CFD results, equivalent to a percentage difference of only 2.6. This difference in magnitudes is similar for the other coefficients. This will suffice for the purposes of this study as subsequent simulations will be done using the aircraft configuration of the lateral sweep.

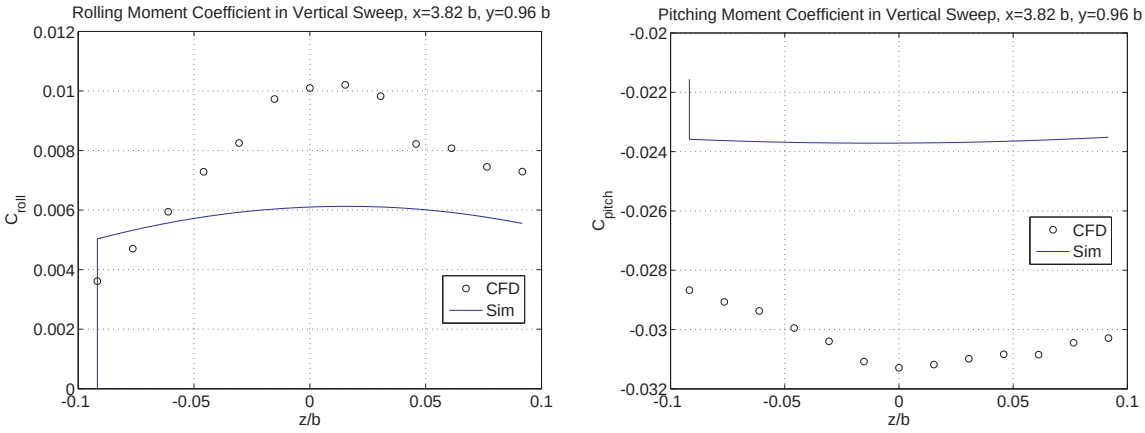

Figure 2.23. Aerodynamic Moment Coefficients in Vertical Sweep, x=3.82b, y=0.96b.

CHAPTER 3

SWEET SPOT EVALUATION

This chapter discusses the procedure used to determine the optimum location for formation flight and associated benefits using the mathematical model and integrated simulation environment, referred to in Section 2. Section 3.1 discusses the relative position configuration of both KC-135R and EQ-II trail aircraft models with respect to the leading KC-135R tanker. Section 3.2 then gives the details of the analysis employed to determine the sweet spot for the trailing aircraft relative to the lead.

3.1 Configuration

The formation benefit for the trail aircraft varies depending on its position within the wake of the lead. Prior research [4, 76, 77] suggests that there is a specific position relative to the lead aircraft where the formation flight benefit for the trail aircraft is maximum. This specific relative position for the trail aircraft is a safe distance behind the lead aircraft, around the same altitude and wing-tip to wing-tip in the lateral direction. For a pair of similar size aircraft, this means the centerline of the follower aircraft should be about a wing span laterally on the right or the left side of the centerline of the lead aircraft.

To accurately determine the relative position for optimum formation flight, the benefit to the trail aircraft should be calculated at a given relative position and this procedure should be repeated by changing the relative position to cover a sufficient expanse of area behind the lead. This would help to determine not just the relative position with the largest benefit, but would show how the benefit is degraded as the

trail aircraft moves away from the optimal position. To this effect, a grid is defined so that the effect of the induced wind from the lead on the trail aircraft can be mapped out at different relative locations. Since the trailing vortices are modeled to be aligned with the translational velocity vector of the lead aircraft, not by the orientation of the aircraft, the grid is defined in the vertical plane parallel to the Y-Z plane of the lead aircraft's wind frame. This grid is positioned at a distance of 3.8 KC-135R wingspans behind the C.G. (center of gravity) of the lead KC-135R to match the longitudinal separation between the lead and trail KC-135R for the CFD validation runs described in Chapter 2.6.2. The effect of longitudinal separation between the two aircraft is not investigated as it has been shown by Blake and Multhopp [4], using Munk's theorem [78] that, the vortex of the lead aircraft continues unchanged downstream except for very large separation distances. Formation effects are more sensitive to lateral and vertical displacements than longitudinal variations, thus, to obtain the relative position with optimum benefit, the trail aircraft position is set to vary only its lateral and vertical direction in this grid behind the leader. The grid with 1521 placement points for the trailing aircraft expands from 0.2 wingspans above to 0.2 wingspans below the leader in the z direction and from 0.25 to 1.2 wingspans laterally in the y direction. These placement points and grid expanse were chosen as a compromise between simulation run time and grid resolution in order to provide a clear depiction of the lead KC-135R non-uniform wind effects on the trail. The grid behind the KC-135R is shown in Fig. 3.1.

3.2 Analysis

This dissertation uses two methods to determine the sweet spot for different pairs of aircraft: a static and dynamic analysis. The static analysis involves running a simulation analogous to wind tunnel tests in the sense that two aircraft are placed

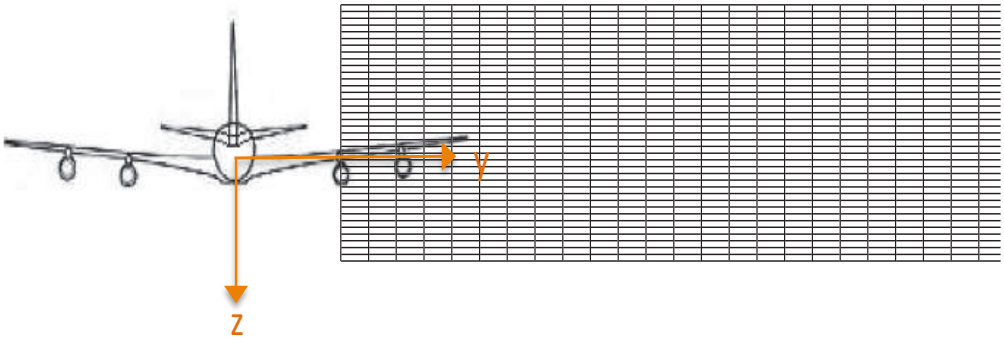

Figure 3.1. Depiction of Grid used in Static and Dynamic Simulations.

statically in formation and the aerodynamic forces and moments acting on the follower aircraft are calculated/measured. The position of the trail aircraft is varied along each vertical line in the grid shown in Fig. 3.1 for each lateral position while recording the lift, drag, and side force coefficients, as well as the roll, pitch, and yaw moment coefficients. These are the relevant variables for the static study. In addition, the aerodynamic force and moment coefficients for the trail aircraft in solo flight with the same flight conditions are stored for comparison. These coefficients in the solo case are obtained by running the simulations with the effective translational and rotational wind components induced by the lead aircraft turned off. The lift-to-drag ratio in solo flight is subtracted from the lift-to-drag ratio in formation flight at all points in the grid to isolate the benefits of formation flight. The sweet spot is defined for the static study as the relative position of the trail at which the increase in lift to drag ratio from solo flight is the largest for the trail aircraft.

The dynamic analysis uses a simulation analogous to actual flight tests of formation flight. In the dynamic case, the trail aircraft is commanded to fly at each point of the grid in Fig. 3.1. At each specified position of the trail aircraft relative to the lead, the trail aircraft is trimmed with certain control surface deflections and

thrust values. The controller moves the control variables (control surfaces and thrust) to the required trim values after the transient. It is expected that there would be locations in the grid where the controller would be unable to trim the aircraft because of the large magnitudes of the induced moments on the follower that would require control surface deflections and/or thrust levels larger than saturation limits. A simulation stop parameter is introduced to track these locations. This parameter also tracks locations where the Euler angles and velocity of the trail aircraft exceed specified thresholds. The simulation is set to return one if any of these conditions were reached and zero if the controller successfully trimmed the aircraft at the commanded position. The thrust levels and control surface deflections are recorded at the end of the simulation after the aircraft settles at the steady-state for each specified position in the grid. Similar to the static case, the thrust and control effector deflections for the trail aircraft in solo flight with the same flight conditions are utilized for comparison with the formation flight. For the dynamic study, the sweet spot is the relative position corresponding to the lowest thrust level for the trail aircraft.

For both static and dynamic analyses, contour plots are generated to visualize the variation of the formation benefits within the grid as well as other recorded parameters. At the minimum, all cases present contour plots of the percentage increase in lift-to-drag ratio for the static formations and contour plots of the percentage increase in thrust levels for the dynamic formations as compared to solo flight. In the contour plots presented in this dissertation, the lateral and vertical spacing denotes the distance from the C.G. of the leader KC-135R, in lengths of KC-135R wingspans, to the C.G. of the trail aircraft. Also, the positive z direction is downwards in alignment with the wind frame of the lead aircraft.

CHAPTER 4

KC-135R - EQ-II FORMATION

This chapter presents the static and dynamic analyses for a heterogenous aircraft pair: a KC-135R as the lead with an Equivalent Model II (EQ-II) as the trail. As described in Chapter 3.2, this involves analyzing the magnitudes of the aerodynamic force and moment coefficients in the static case and the thrust and control effector deflections in the dynamic case.

The static and dynamic studies using the EQ-II as the trail aircraft were carried out for three aircraft pairs in formation as given in Table 4.1. First the large EQ-II trailing a lighter KC-135R was investigated. Then the weight of the leading KC-135R was increased by 26 percent while the large trail EQ-II was left the same. This was done because the vortex strength of the lead aircraft is dependent on the lift, which is in turn dependent on the weight of the leading KC-135R and it was sought to make a comparison of the two different lead KC-135R weights. The small variant of the EQ-II was then used to examine the effect of the follower size on the sweet spot. All static and dynamic formation cases for the EQ-II are presented in the order listed in Table 4.1.

Table 4.1. Aircraft Formation Pairs

Lead KC-135R Weight	Trail EQ-II Size
Nominal	Large
Heavy	Large
Nominal	Small

4.1 Static Study

Although all the state and aerodynamic variables are recorded in the static simulation, the primary purpose is to find the sweet spot and thus only the most relevant variables are presented in the analysis. These are the lift to drag ratio, side force coefficient, and along with the pitching, rolling, and yawing moment coefficients of the trail aircraft. For the both variants of the EQ-II aircraft, the nominal lift-to-drag ratio in solo flight is 12.66 as determined from running the static simulation with no translational and rotational wind components induced from the lead.

4.1.1 Large EQ-II Variant behind KC-135R of Nominal Weight

This section presents the results of the large variant of the EQ-II aircraft flying behind the KC-135R of nominal weight. The contour plot for the percentage increase in lift-to-drag ratio from solo flight is presented in Fig. 4.1. Fig. 4.1 shows that as the EQ-II moves laterally, starting from 0.5 wingspans away from the lead aircraft, the increment in lift-to-drag ratio increases from 0 till a maximum of 12.59 percent from the baseline case. The exact location of the static sweet spot with largest lift-to-drag ratio is 1.0282 wingspans laterally and 0.05 wingspans below the leading KC-135R. This region is promising as there is a large expanse in which the follower can deviate and still experience increased lift-to-drag. The lift-to-drag increment in the surrounding regions are positive, thus no negative lift will occur with changes in location around 1.0282 KC-135R wingspans.

In addition, the elliptical shape of the contours in Fig. 4.1 signify that the slope in the vertical direction is higher than the lateral. This means that a vertical deviation from the sweet spot will cause a higher drop in lift-to-drag ratio. Based on these static analysis results, the sweet spot for the large EQ-II aircraft placed 3.8

wingspans behind the leader KC-135R is 1.0282 KC-135R wingspans laterally and 0.05 wingspans below the leading KC-135R.

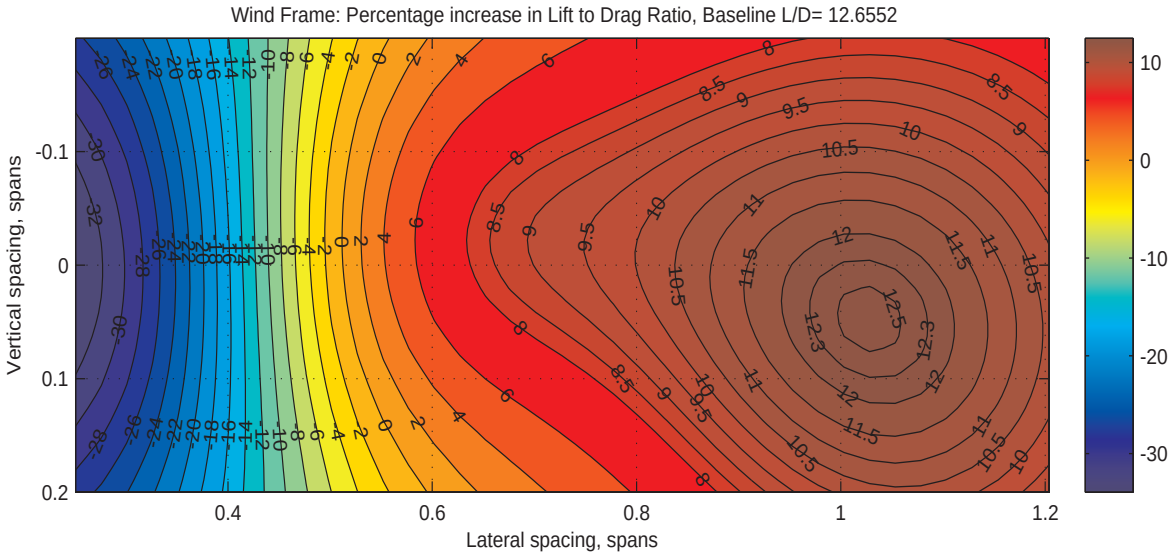

Figure 4.1. Percentage increase in Lift to Drag Ratio from Nominal Flight: Large EQ-II.

Figures 4.2 and 4.3 show the contour plots for the rolling and yawing moment coefficients, respectively, of the large EQ-II. At the static sweet spot, non-zero moments are visible in the roll and yaw. This is similar to the results of Hanson and Cobleigh who observed moment peaks at the same area of maximum drag reduction for the trail aircraft in a two-ship F/A-18 formation [9]. This implies that there will be non-zero control surface deflections required to trim the EQ-II at the static sweet spot. The pitching moment coefficient and side force coefficients are also depicted in Figs. 4.4 and 4.5. Blake et al [79] compared wind tunnel and analytical predictions of a delta-wing UAV behind a KC-135R in formation. Their study noted that a lack of vertical tail on the UAV possibly resulted in significantly small side force and yaw moments. In this chapter, the EQ-II yaw and side force are an order of magnitude

smaller than the pitch and roll and this possibly stems from the fact that there is no vertical tail on the EQ-II aircraft.

In addition, Fig. 4.1 also shows when the large EQ-II is around 0.25 wingspans laterally and at the same altitude as the leader, the lift-to-drag ratio difference is a large negative value of -32 percent. This decrease in lift-to-drag ratio from the baseline condition persists till about 0.5 lateral wingspans. This region is in the downwash area behind the lead aircraft in which the induced aerodynamic moments are the largest as evidenced in Figs. 4.2, 4.4, and 4.3. The side force coefficient is also large in this region as seen in 4.5. If the trailing aircraft is placed at this location in formation flight, trimming these moments will require the largest control surface deflections than at anywhere else in the grid as the trailing EQ-II experiences the largest moments in this area between 0.2 and 0.5 wingspans. There is also no lift-to-drag ratio benefit in this region as the lift-to-drag ratio is lower than the baseline case.

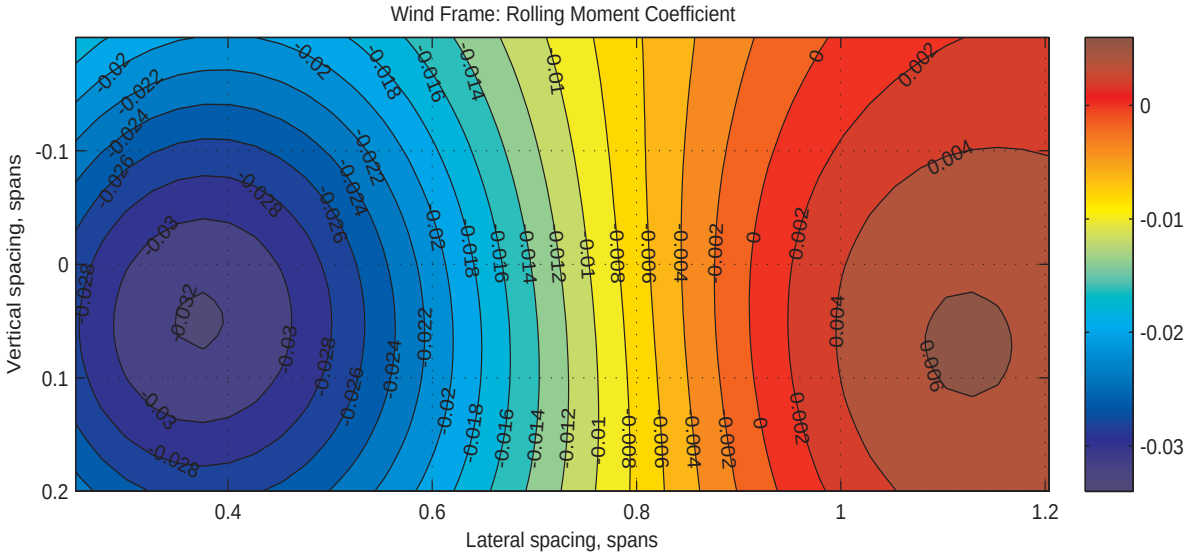

Figure 4.2. Aerodynamic Rolling Moment of Large EQ-II .

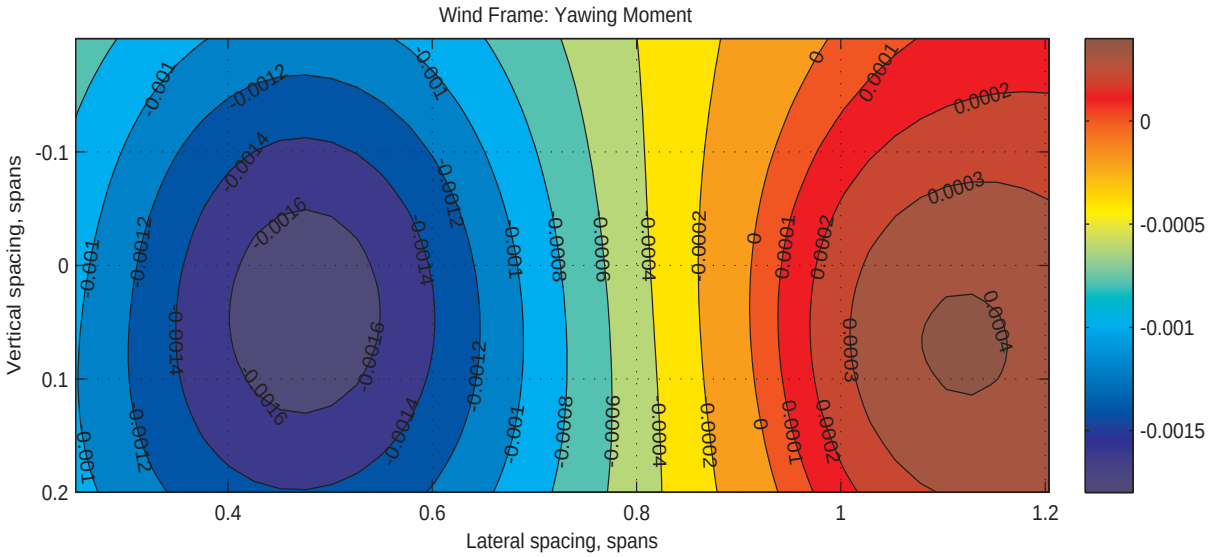

Figure 4.3. Aerodynamic Yawing Moment of Large EQ-II .

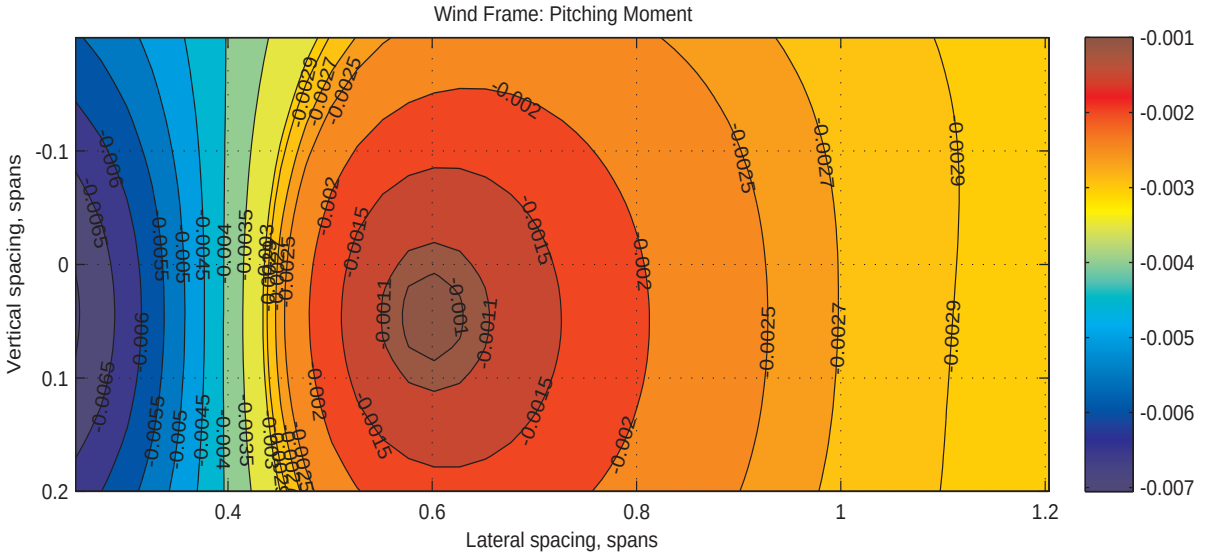

Figure 4.4. Aerodynamic Pitching Moment of Large EQ-II .

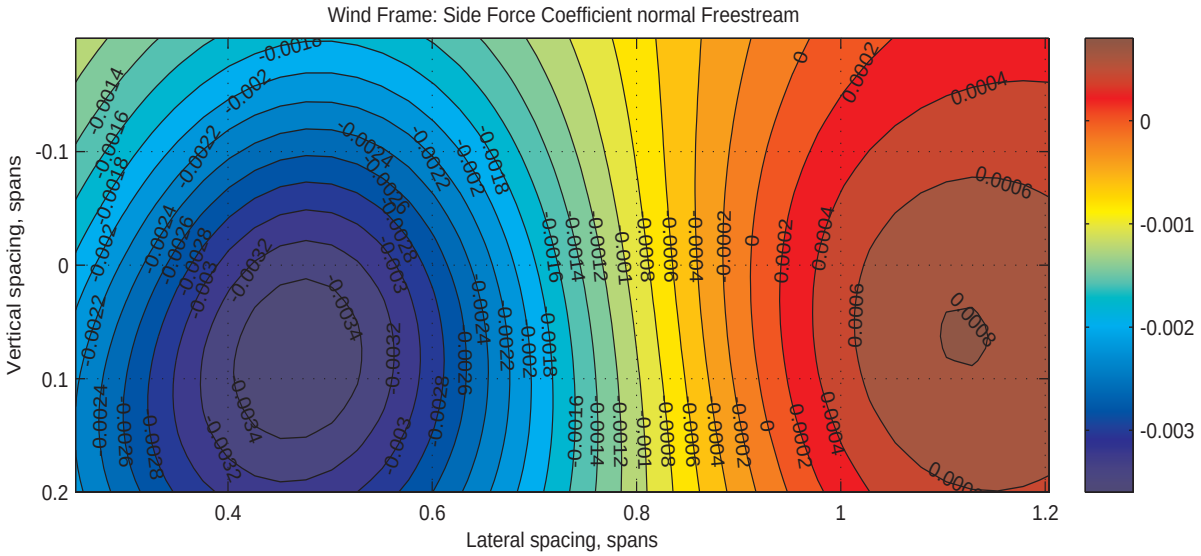

Figure 4.5. Side Force Coefficient of Large EQ-II .

4.1.2 Large EQ-II Variant behind Heavy KC-135R

The results of the large variant of the EQ-II behind a 26 percent heavier KC-135R are shown in Figs. 4.6 and 4.7. Fig. 4.6 shows that the largest increase in lift-to-drag ratio from the baseline is 14.79 percent at 1.028 wingspans laterally and 0.04 wingspans below the lead KC-135R. This location coincides with the static sweet spot for the large EQ-II trailing a lighter KC-135R, which means that the static sweet spot remains the same when the lead aircraft weight is changed. The moment and side force coefficients also have similar patterns with those in Figs. 4.2 through 4.5 at all locations except that their magnitudes are slightly greater. For this reason, only one moment coefficient contour, Fig. 4.7, is presented for comparison with Fig. 4.2. Figure 4.7 looks similar to Fig. 4.2 except that there is a subtle shift in the contour lines laterally further away from the lead KC-135R. For instance, the zero rolling moment coefficient line is shifted slightly further from the lead. This zero line signifies the location of zero induced aerodynamic rolling moment coefficient on the trail aircraft and its importance will be made apparent subsequently where the relationship between trimming and the location of the dynamic sweet spot is established.

4.1.3 Small EQ-II Variant behind KC-135R of Nominal Weight

The variation in lift-to-drag ratio increment for the small EQ-II trailing the nominal KC-135R is shown in Fig. 4.8. The largest increase in lift-to-drag ratio of 17.29 percent is obtained when the small EQ-II is placed 0.777 KC-135R wingspans laterally and 0.02 KC-135R wingspans below the lead KC-135R. Based on the static analysis, the lateral separation between the KC-135R and the small EQ-II at the sweet spot, is smaller than that between the KC-135R and the large EQ-II at its sweet spot.

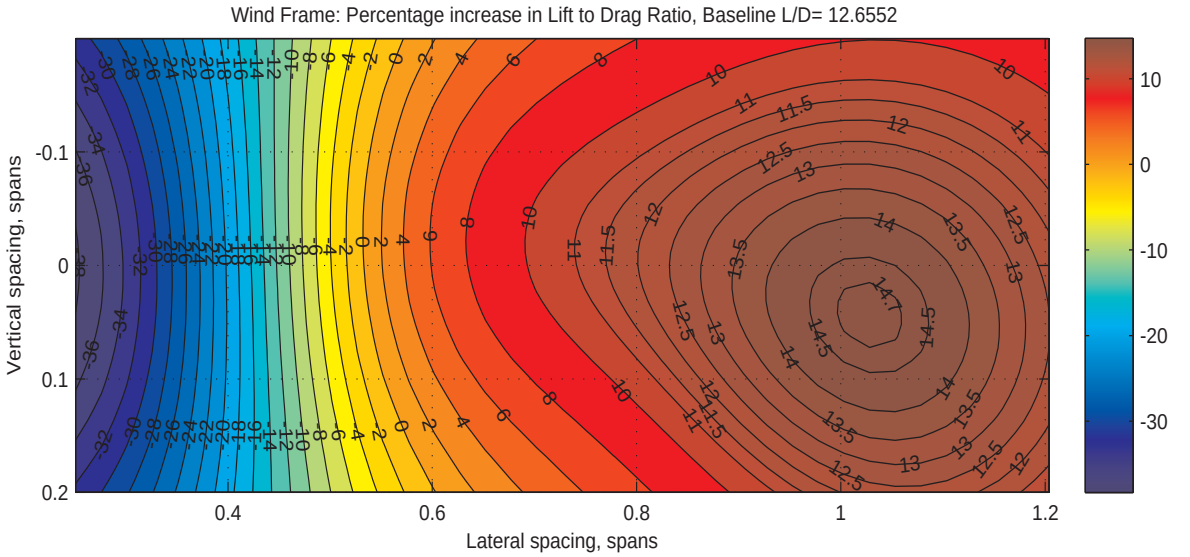

Figure 4.6. Percentage increase in Lift to Drag Ratio from Nominal Flight: Large EQ-II with Heavier KC-135R.

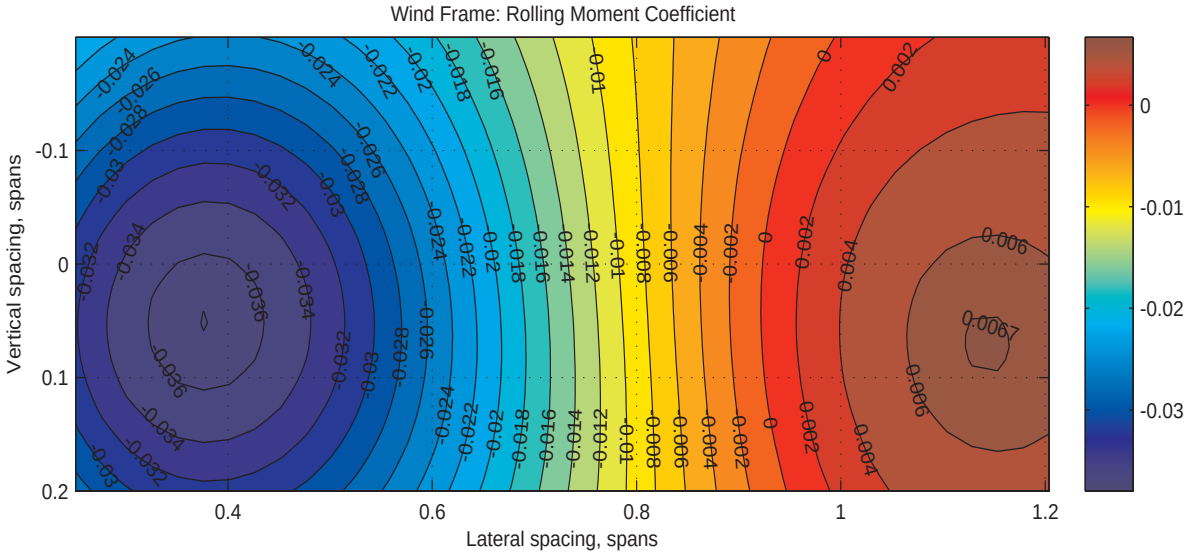

Figure 4.7. Aerodynamic Rolling Moment of Large EQ-II using Heavier KC-135R.

The rolling moment coefficient results are presented in Fig. 4.9, which looks similar to Fig. 4.2 except that the contour levels move laterally closer to the lead

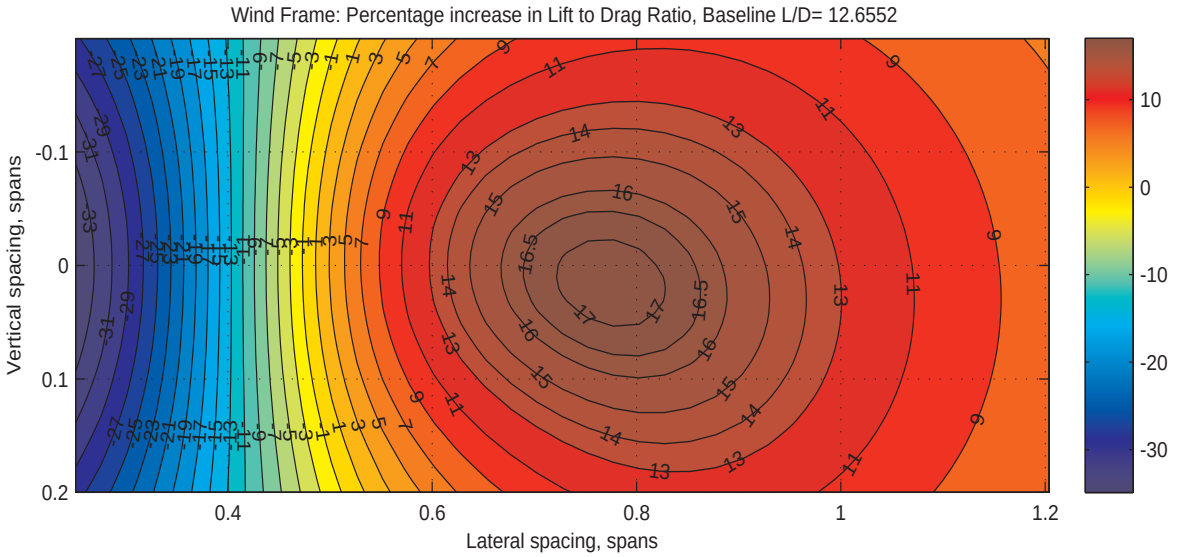

Figure 4.8. Percentage increase in Lift to Drag Ratio from Nominal Flight: Small EQ-II.

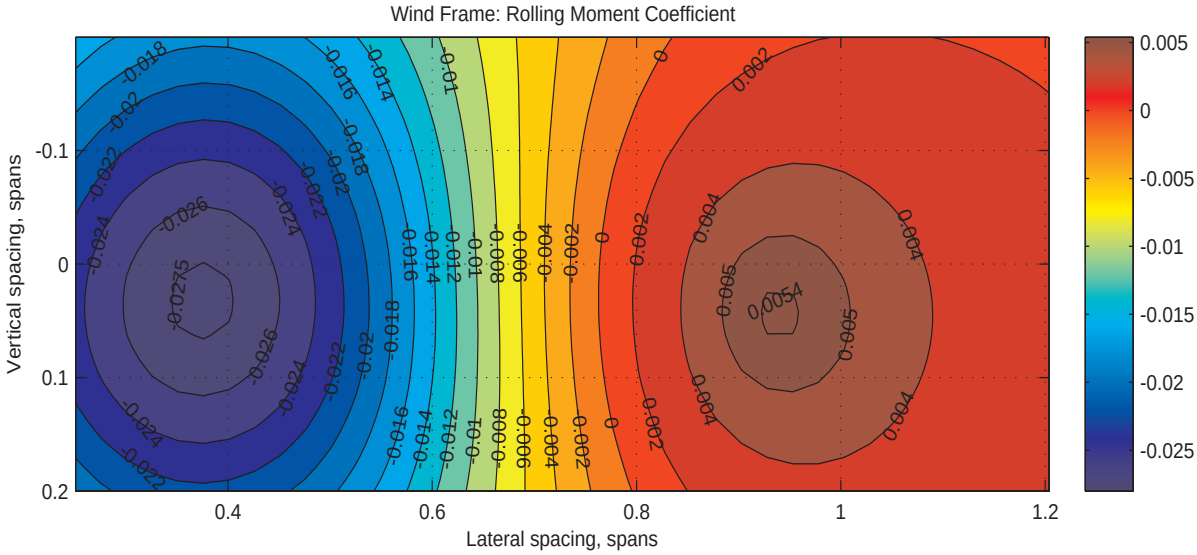

Figure 4.9. Aerodynamic Rolling Moment of Small EQ-II.

aircraft. For instance, the zero rolling moment coefficient line is shifted laterally closer to the lead KC-135R.

The small variant of the EQ-II aircraft behind the leader KC-135R has similar contour patterns of the aerodynamic force and moment coefficients as the large variant but with different locations in the grid. The magnitudes of the aerodynamic force and moment coefficients of the small EQ-II variant also differ from the large EQ-II at the same locations in the grid. Thus, only Figs. 4.8 and 4.9 are presented.

4.2 Dynamic Study

The thrust levels and the control surface deflections at the steady-state: the ailerons, elevators, and rudder deflections are presented in this section. As in the static case, the two aircraft cases, listed in Table 4.1, are investigated. The results of the dynamic simulations are then compared with the static results in Section 4.1 to determine if the sweet spot location remains the same.

4.2.1 Large EQ-II Variant behind KC-135R of Nominal Weight

The results of the large variant of the EQ-II aircraft behind the KC-135R of nominal weight are presented in this section. Fig. 4.10 is a contour plot of the simulation stop parameter. It shows that less than 0.4 wingspans laterally, the simulation stop parameter is one because the controller could not trim the EQ-II mostly due to the saturation of the thrust. As a result of this, all contour plots generated from the results of the dynamic simulation exclude this area.

A contour plot of the percentage thrust increment is presented in Fig. 4.11. The thrust plot depicted is representative of all engines of the large EQ-II as this plot is identical to those for the other engines. The largest thrust reduction of over 6 percent, equivalently the least thrust required to fly in formation, is obtained in a vertical strip located 0.903 lateral wingspans relative to the lead KC-135R. This is the dynamic sweet spot for the large variant of the EQ-II to fly 3.8 wingspans behind

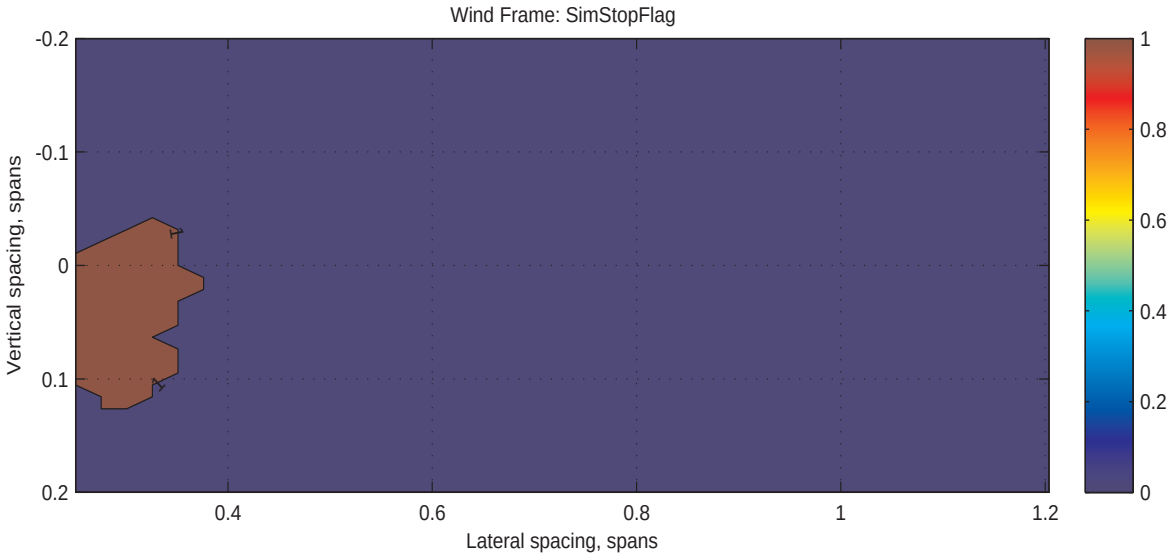

Figure 4.10. Simulation Stop Parameter of Large EQ-II.

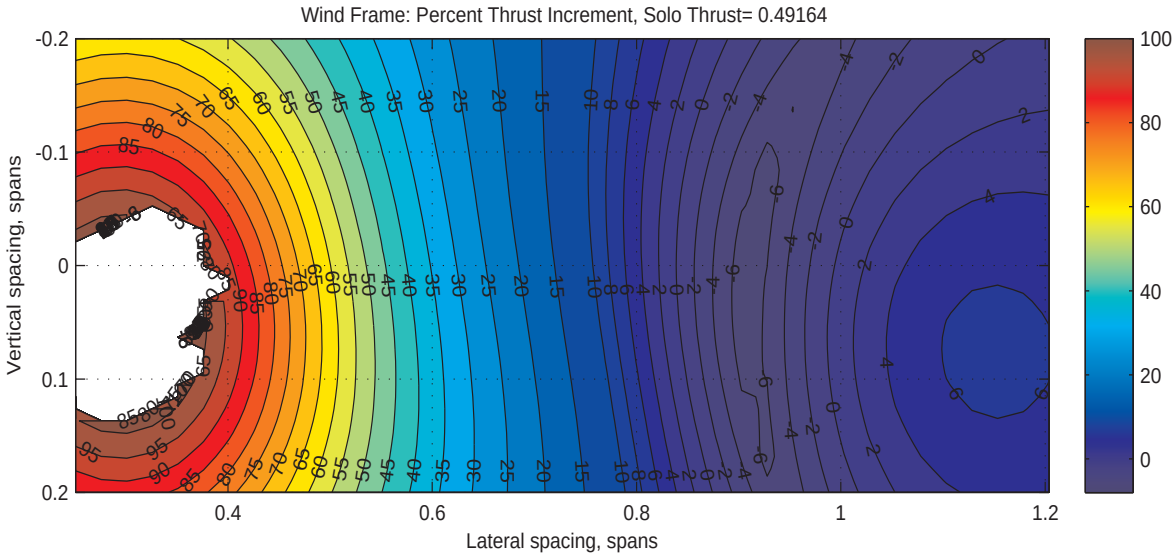

Figure 4.11. Percentage increase in Thrust from Nominal Flight: Large EQ-II.

the lead KC-135R. Furthermore, the elliptical shape of the thrust contours around the dynamic sweet spot shows that there is a lower slope along the vertical direction compared to the lateral direction. This means deviation from the sweet spot in the lateral direction results in higher reduction in formation benefit, in terms of thrust.

Further, the shape of the thrust contours in the saturation region, and the large increase in thrust in the downwash region, indicates that the thrust required exceeds the saturation limits of the EQ-II engines, causing the simulation stop parameter to become one in that region. Specifically, the thrust reaches about 100 % of the baseline case in the downwash region. With a baseline thrust required of almost half the maximum available thrust from the engines, a 100 % increase will lead to thrust requirement in excess of what is available for the aircraft.

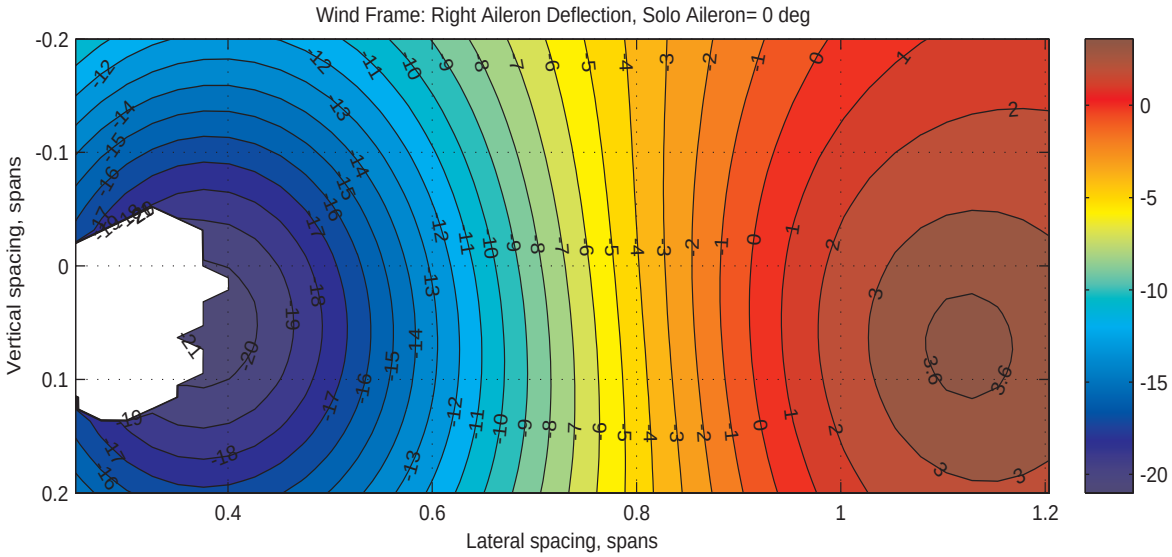

Figure 4.12. Aileron Deflection of Large EQ-II.

The contours of the left and right aileron deflections are identical in trends but have different directions. For this reason, only the right aileron deflection is presented in Fig. 4.12. The magnitude of the deflection of the aileron is seen to decrease as the dynamic sweet spot is approached from either the right or the left of 0.903 lateral wingspans. At the dynamic sweet spot, the aileron deflection is about 0.25 degrees. This is a slight increase in the deflection compared to that required for solo flight,

which is zero degree. As stated in Section 1, a trailing aircraft experiences induced aerodynamic moments due to the non-uniform wind field generated from the leader [4]. As such, non-zero control effector deflections are required to trim the trailing aircraft when it flies behind the leader.

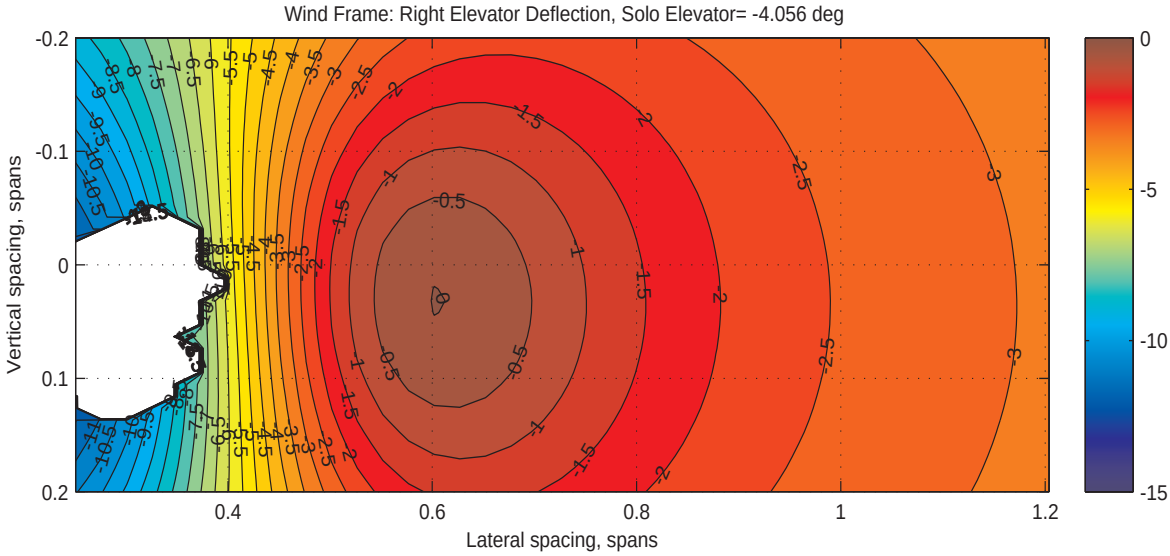

Figure 4.13. Elevator Deflection of Large EQ-II.

The right elevator deflection of the large EQ-II behind the KC-135R is depicted in Fig. 4.13. At the dynamic sweet spot, there is a required elevator deflection of -2.1 degrees. This is less than the value in solo flight which requires some elevator deflection to keep the aircraft trimmed. The rudder deflection is presented in Fig. 4.14. At the dynamic sweet spot, the rudder deflection is a very small value of -0.11 degree. In comparison to the dynamic sweet spot, other areas require larger control surface deflections to trim. Further, the trend of the contours of the control surface deflections in the saturation region, confirm that the thrust is indeed what saturates first, as opposed to the ailerons, elevators, and rudders.

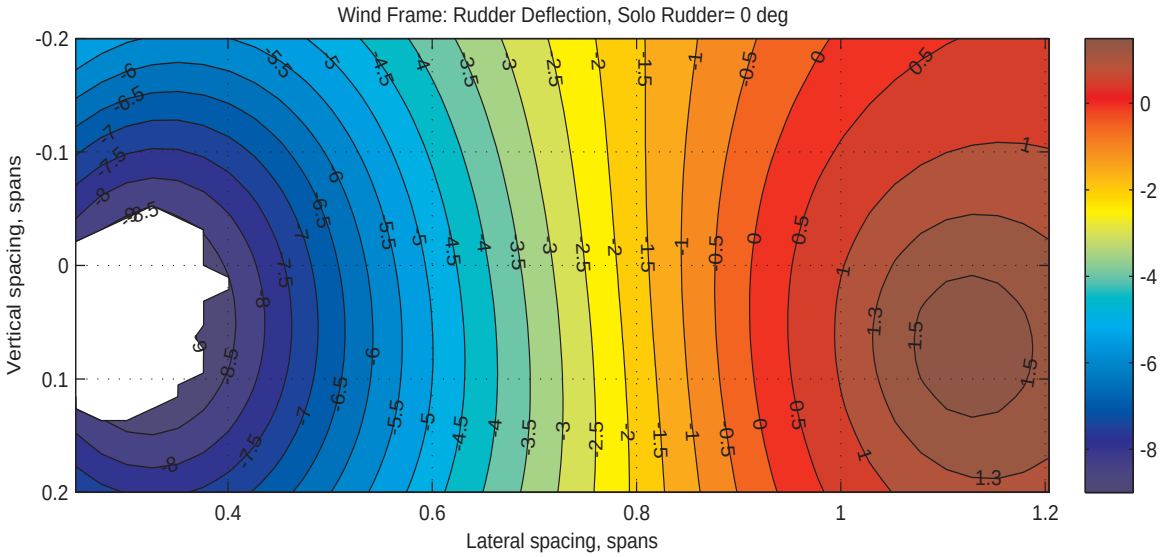

Figure 4.14. Rudder Deflection of Large EQ-II.

4.2.2 Large EQ-II Variant behind Heavy KC-135R

The dynamic results of the large EQ-II behind a 26 percent heavier KC-135R are shown in Figs. 4.15 and 4.16. Fig. 4.15 shows that the dynamic sweet spot with 8.92 percent thrust reduction is in a vertical band located 0.928 lateral wingspans relative to the heavy lead KC-135R. Also, Fig. 4.15 shows contours with magnitudes slightly larger than Fig. 4.11 and almost the same location for the dynamic sweet spot. Since the magnitudes are larger, the expanse of the region in which the trail aircraft can not be trimmed due to thrust saturation is larger than those seen in Section 4.2.1.

The aileron, elevator, and rudder deflections also have similar patterns with those in Figs. 4.12 through 4.14 at all locations except that their magnitudes are slightly greater. For this reason, only the right aileron deflection contour, Fig. 4.16, is presented. Fig. 4.16 has similar patterns with Fig. 4.12. The trends are almost

identical except for the slightly larger magnitudes of the aileron deflection at each point.

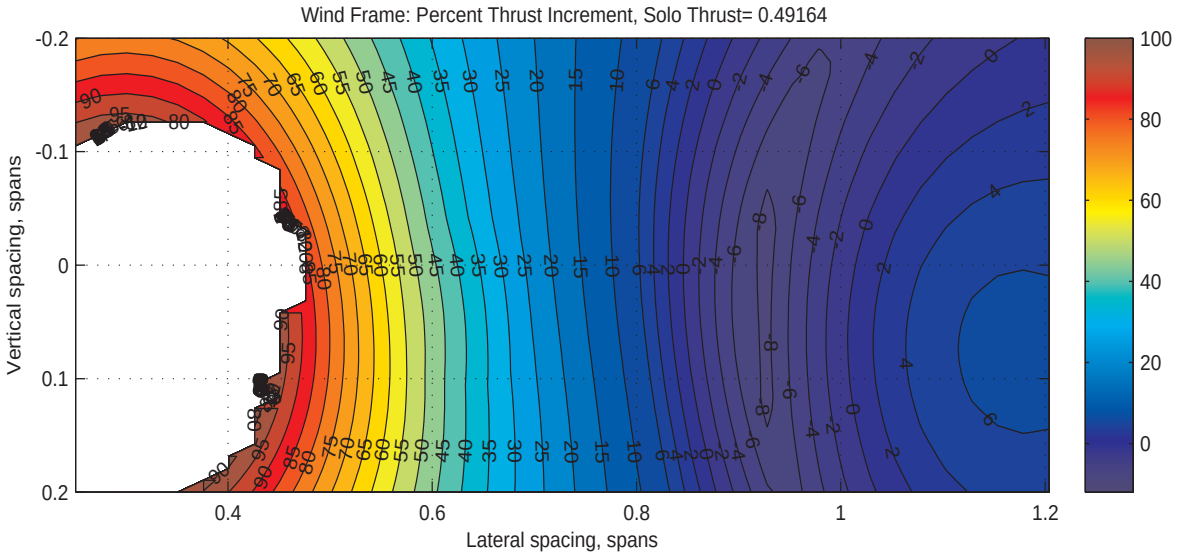

Figure 4.15. Percentage increase in Thrust from Nominal Flight: Large EQ-II with Heavier KC-135R.

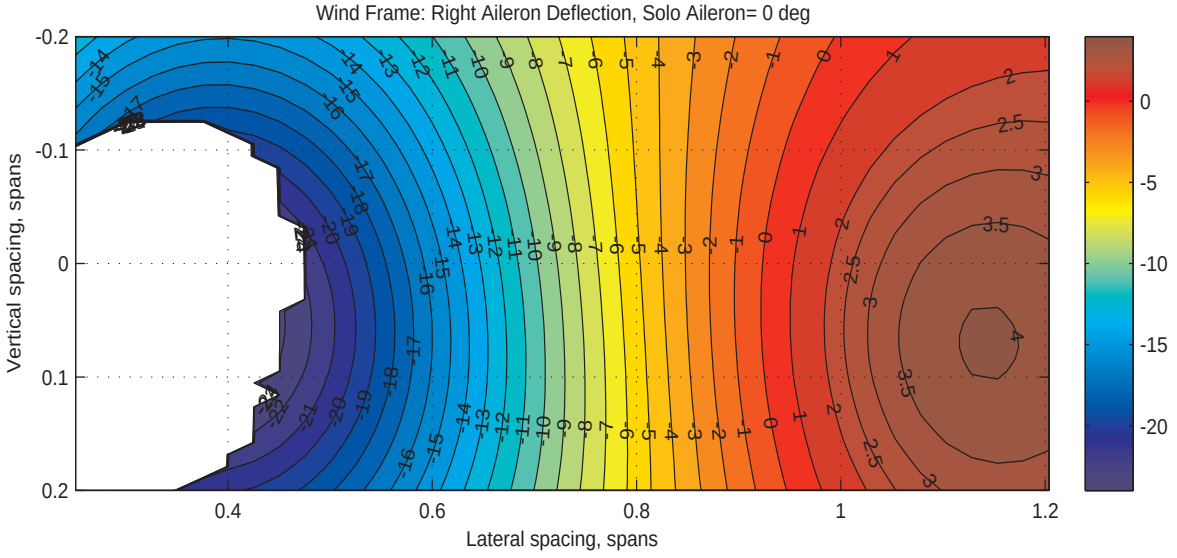

Figure 4.16. Aileron Deflection of Large EQ-II using Heavier KC-135R.

4.2.3 Small EQ-II Variant behind KC-135R of Nominal Weight

The variation in thrust is shown in Fig. 4.17. The largest reduction in thrust of 10.34 percent is obtained when the small EQ-II is placed 0.752 KC-135R wingspans laterally and 0.02 wingspans below the lead KC-135R. The dynamic sweet spot of the small EQ-II is laterally closer to the lead aircraft than that of the large variant. The small variant of the EQ-II aircraft behind the leader KC-135R has similar contour patterns of the thrust and control surface deflections as the large variant but with different locations in the grid. The magnitudes of the thrust and control surface deflections of the small EQ-II variant also differ from the large EQ-II at the same locations in the grid. For instance, in the case of the small variant, the thrust levels do not exceed their saturation limits at any point in the grid. The thrust required, in the downwash region, increases to a maximum which is less than 100 percent. The baseline value is 33 % of the maximum available thrust, thus, the thrust never exceeds 66 % of the available thrust at any point in the grid. This explains the absence of a blanked out region in the downwash region in the contour plots. Since the control effector deflection contours for the small variant are similar to the large variant, only the right aileron deflections are presented in this Section as seen in Fig. 4.18. The location of least aileron deflection has also shifted laterally closer to the dynamic sweet spot.

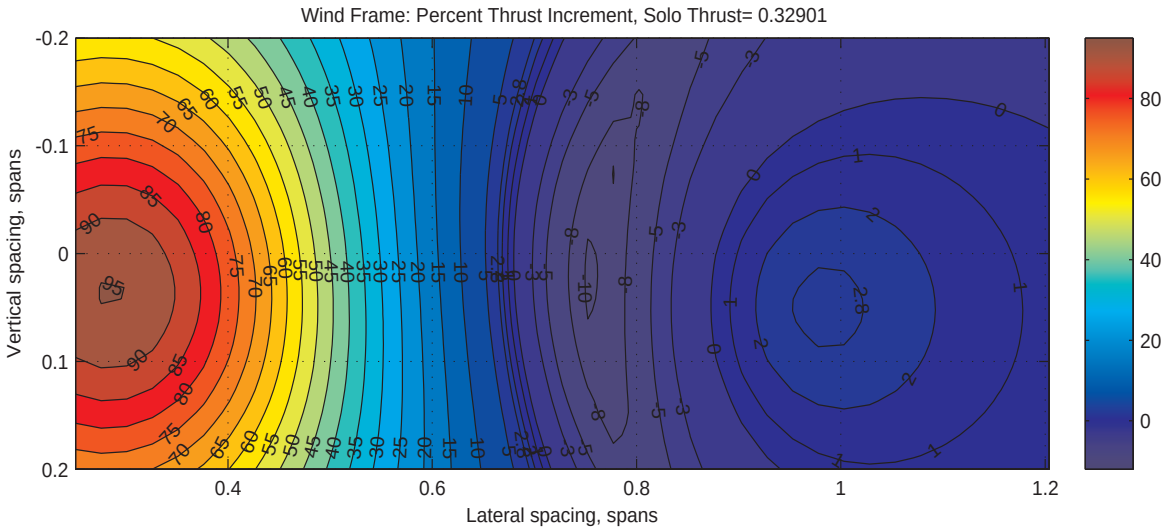

Figure 4.17. Percentage increase in Thrust from Nominal Flight: Small EQ-II.

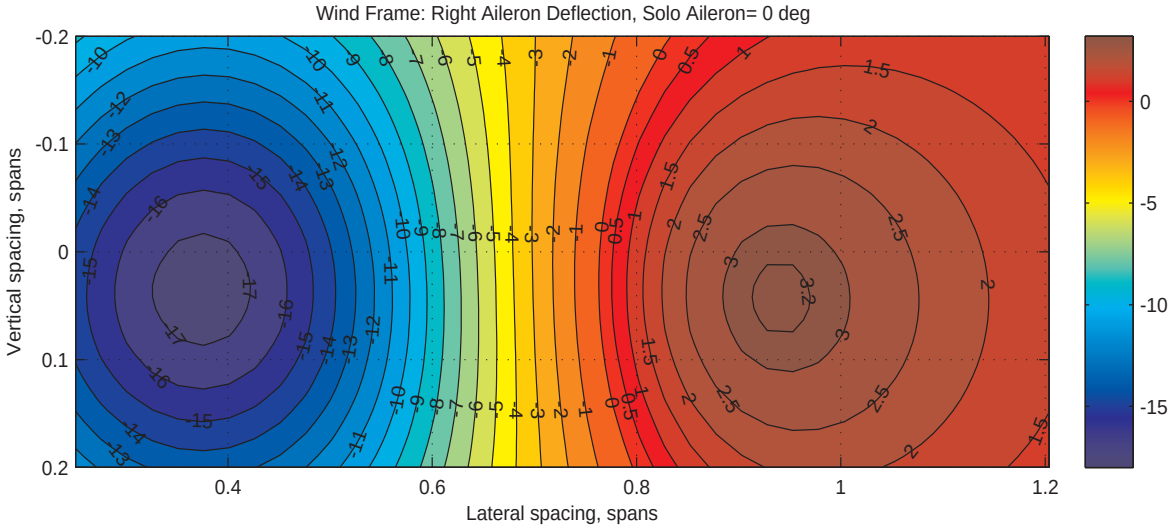

Figure 4.18. Aileron Deflection of Small EQ-II.

4.3 Comparison of Results of EQ-II Static and Dynamic Study

Table 4.2 summarizes the results of the static and dynamic simulations for the KC-135R aircraft pair with regards to the location of the sweet spot and aerodynamic force and moment coefficients. It presents the aerodynamic rolling, pitching, and yawing moment coefficients as $C_{\mathcal{L}}$, $C_{\mathcal{M}}$, $C_{\mathcal{N}}$ respectively at the static sweet spot, and the aileron, elevator, and rudder deflections as δ_a, δ_e, and δ_r respectively at the dynamic sweet spot. The incremental lift-to-drag ratio at the static sweet spot is tabulated under Δ L/D (%) while the reduction in thrust at the dynamic sweet spot is given by Δ Thrust (%). The sweet spot locations are given in terms of the separation of the C.G. of the lead KC-135R and trail EQ-II aircraft. They are also presented in terms of wing tip overlap as a percentage of the geometric mean of the wingspans of the two aircraft in formation. The expression for this overlap is given as

$$\delta_{WT_{GM}} = \frac{\sqrt{b_L b_T}}{b_L b_T}\left(\frac{b_L + b_T}{2} - l_{ss}\right) \tag{4.1}$$

where $\delta_{WT_{GM}}$ is the wing tip overlap as a fraction of the geometric mean of the two aircraft wingspans, b_L and b_T are the wingspans of the lead aircraft and trail aircraft respectively, and l_{ss} is the C.G. to C.G separation distance of the two aircraft as depicted in Fig. 4.19. The wing tip overlap was obtained from:

$$\delta_{WT} = \frac{b_L}{2} - \left(l_{ss} - \frac{b_T}{2}\right) = \frac{b_L + b_T}{2} - l_{ss} \tag{4.2}$$

with $\delta_{WT_{GM}}$ obtained by dividing δ_{WT} given in Eq. (4.2) by the geometric mean of the two aircraft wingspans, $\sqrt{b_L b_T}$. This division was done to normalize the overlap and introduce a metric for comparison that could be applied to different aircraft of varying sizes and configurations.

Table 4.2 shows that although the static sweet spot remains constant with a change in the weight of the lead aircraft, the dynamic sweet spot does not. In the

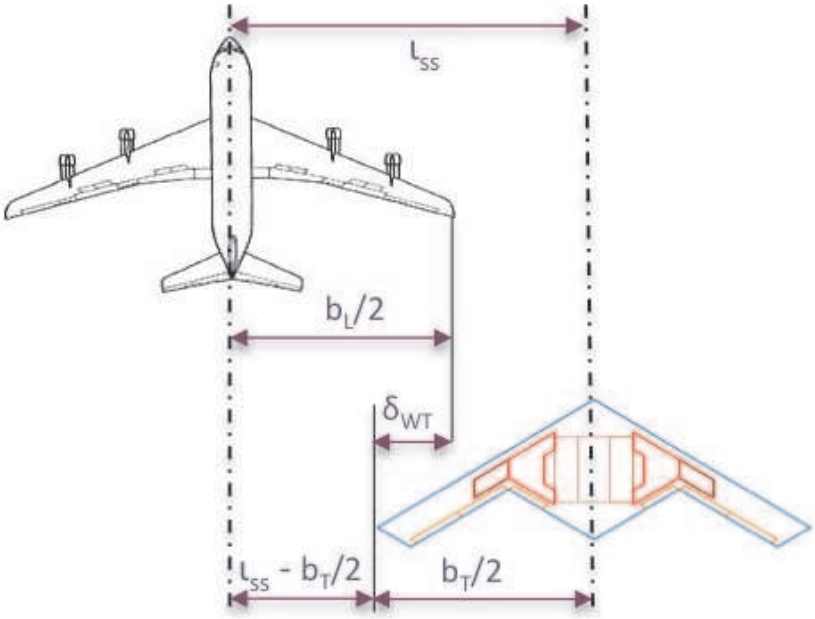

Figure 4.19. Depiction of Wingtip Overlap Parameters.

dynamic case, the wingtip overlap decreases from 23.35% to 20.95% when the lead aircraft weight is increased by 26%. Another difference in the overlap for the static and dynamic sweet spots is that for the large trail aircraft, a significantly larger wingtip overlap (about 14% increase) is required to maintain the dynamic sweet sweet spot than the static. Although for the smaller trail aircraft, a larger overlap is also required going from static to dynamic, this overlap is only about 2% larger. Essentially, all cases require a closer lateral trail aircraft position to the lead for the dynamic case as opposed to the static.

Figure 4.20 presents the static sweet spot, dynamic sweet spot band, and the zero roll moment curves for the small and large variants of the EQ-II trailing the nominal KC-135R. For the large EQ-II, the dynamic sweet spot is located significantly laterally closer to the lead than the static sweet spot is. The dynamic simulations account for the trimming of the aircraft with deflections of the control surfaces. Figs.

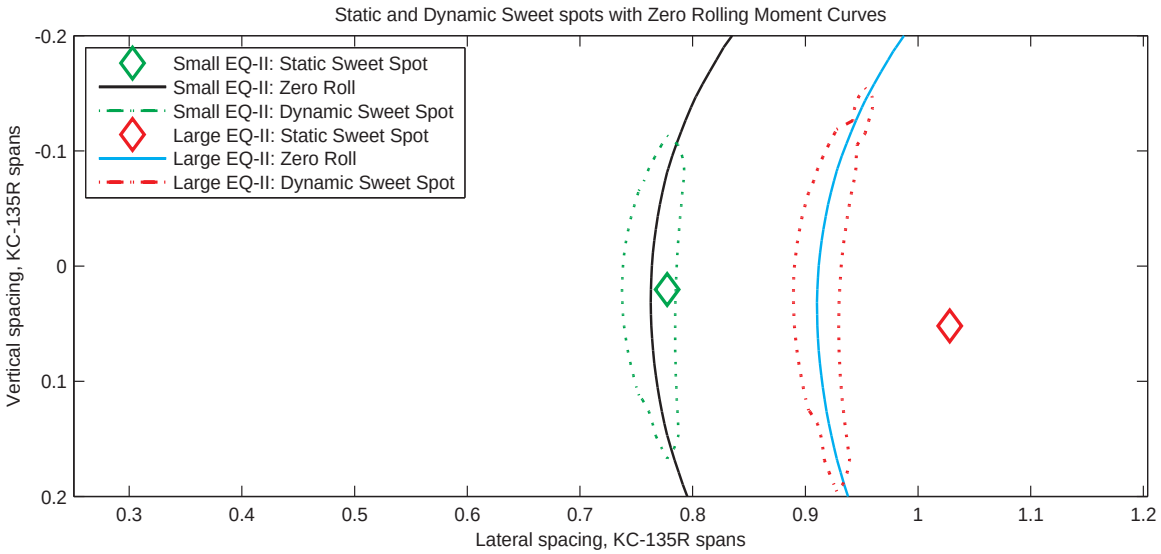

Figure 4.20. Static and Dynamic Sweet Spots for Large and Small EQ-II showing Zero Roll Moment Curves.

4.12, 4.13, and 4.14 show that aileron, elevator, and rudder deflections are needed for trimming the aircraft at the static sweet spot. Figs. 4.12 and 4.14 show that small aileron and rudder deflections are needed to trim the aircraft in the dynamic sweet spot band which is located over the zero aileron (rudder) isolines as seen in Fig. 4.20. This explains the mechanisms that move the dynamic sweet spot away from the static sweet spot. In the case of the small EQ-II, the zero aileron (rudder) isolines are close to the static sweet spot. Thus, little difference is seen between the locations of the static and dynamic sweet spots. There are two possible reasons for this disparity: (1) the trail EQ-II is not a conventional aircraft like the lead KC-135R, and (2) the trail EQ-II is of a significantly different size than the lead aircraft. Chapters 6 and 7 respectively address the first and second possible reasons for the observed disparity.

Another difference between the static and dynamic sweet spot regions is the slopes of the lift-to-drag ratio and required thrust. The lift-to-drag ratio contours have circular shapes in the sweet spot region, implying that deviation from the sweet

spot in the vertical or lateral direction will lead to similar drops in formation benefit, in terms of lift-to-drag ratio. On the other hand, the thrust reduction has lower slope along the vertical direction compared to the lateral direction. This means deviation from the sweet spot in the lateral direction results in higher reduction in formation benefit, in terms of thrust. An implication of this observation on the control design for station keeping is that the deviation from the desired position along the lateral direction should have more stringent requirements. One similarity in the results of the static and dynamic analysis is seen when the simulation stop parameter contour of the large EQ-II aircraft in Fig. 4.10, is compared with the lift-to-drag and moment coefficient contours in Figs. 4.1 through 4.3. In the downwash region, the drag and aerodynamic moments are the largest as expected. This region also coincides with the locations where the thrust saturates as depicted in Fig. 4.10.

Finally, Table 4.2 shows that the static study overestimates the formation benefit in all aircraft pairs studies. For instance, the large EQ-II variant trailing the nominal KC-135R is seen to have a lift-to-drag percentage increase of 12.6 % from the baseline case. When the dynamic study is done, the formation benefit is seen to be a 7 % drop in thrust from the baseline. The quantification of lift-to-drag benefit seen in the static case, does not translate directly to that of the thrust seen in the dynamic case. These results are similar to those obtained in prior NASA formation flight runs of F/A-18 aircraft, which found fuel flow reductions which were about 3 % less than the drag reductions [80].

Table 4.2. Summary of Static and Dynamic Results for EQ-II

Static Simulation						
	Sweet Spot (Wingspans)					
Aircraft	C.G. to C.G.	Overlap (%)	Δ L/D (%)	$C_{\mathcal{L}}$	$C_{\mathcal{M}}$	$C_{\mathcal{N}}$
Large EQ-II	x=3.8 y=1.028 z=0.05	9.69	12.6	0.005	-0.0028	3.3E-4
Large EQ-II with Heavy KC-135R	x=3.8 y=1.028 z= 0.04	9.69	14.79	0.005	-0.0026	3.4E-4
Small EQ-II	x=3.8 y=0.777 z= 0.02	16.1	15.0	0	-0.002	0
Dynamic Simulation						
	Sweet Spot (Wingspans)					
Aircraft	C.G. to C.G.	Overlap (%)	Δ Thrust (%)	$\delta_a(^\circ)$	$\delta_e(^\circ)$	$\delta_r(^\circ)$
Large EQ-II	x=3.8 y=0.903 z=0.03	23.45	7.02	-0.253	-2.115	-0.11
Large EQ-II with Heavy KC-135R	x=3.8 y=0.928 z=-0.03	20.95	8.92	0.023	-1.87	1.95E-3
Small EQ-II	x=3.8 y=0.752 z=0.02	18.8	10.34	0.42	-1.36	-0.176

CHAPTER 5

ALTERNATE LATERAL TRIMMING METHODS FOR LARGE EQ-II AT STATIC SWEET SPOT

In a realistic long duration formation flight, the aircraft weights will vary due to fuel burn and the strength of the vortices generated by the lead aircraft will vary accordingly. It was shown in Chapter 4 that for the large EQ-II, the location of the dynamic sweet spot changes when the weight of the lead KC-135R is increased by 26% but the static sweet spot does not. This implies that in an actual extended-duration formation in which fuel burn may yield a significant weight reduction of up to 26% for the lead aircraft, the dynamic sweet spot will move. In that case, for the trail aircraft to fly at the dynamic sweet spot, it will require online control algorithms [16, 15] to drive it to the continuously-varying minimum thrust location. The constant static sweet spot on the other hand, will be relatively easier to track.

At the static sweet spot, the induced aerodynamic moments require that the control effectors of the trailing aircraft be trimmed with such deflections that they induce additional drag which reduces the benefits of fuel efficiency. Thus, if alternate methods of trimming can be found to reduce the need for the control surfaces, then equivalent or possibly higher fuel savings could be obtained at the static sweet spot. Two alternate trimming method employed in this dissertation are moving-mass actuation and differential thrusting to generate moments to trim. Internal fuel transfer is used to generate a rolling moment to reduce the need for the aileron and differential thrusting is employed to generate a yawing moment and reduce the rudder deflection required to trim. This chapter presents the details of the two alternate trimming

techniques used to augment the thrust/fuel savings for the large EQ-II at the static sweet spot.

5.1 Configuration

The simulation is done at an altitude of 7,600 meters and a speed of 205 m/s. The EQ-II is placed 3.8 KC-135R wingspans behind the lead KC-135R at the static sweet spot, 1.03 wingspans laterally and 0.05 wingspans below the lead. At the beginning of the simulation, the inner fuel tanks of the EQ-II are 24 % full while the outer fuel tanks are half full to their capacities. As stated in Section 4.3, varying the lead KC-135R weight from light to heavy had no impact on the location of the static sweet spot. Thus, for brevity, all subsequent simulation discussions apply to the EQ-II aircraft trailing a KC-135R of nominal weight. The results of the alternate trimming techniques of the EQ-II behind a heavy KC-135R will be summarized in a table.

5.2 Effect of Rotational Wind in Trim

This section presents the impact of the induced aerodynamic moments on the thrust levels and control effectors of the trail EQ-II as it flies at the static sweet spot without employing any alternative trimming methods. When the simulation starts, it simulates the case in which the aircraft flies solo or flies too far away from the leader to experience any induced wind and aerodynamic interference. This is the baseline case and the effects of the non-uniform wind exposure and fuel transfer will be compared against this case. After 150 seconds, the wind model is started and the translational and rotational wind components gradually reach their normal values at about 200 seconds. The activation of the wind model is to simulate non-

uniform wind experienced by the EQ-II. Fig. 5.1 depicts the duration and time of the induced translational and rotational wind components. Around 450 seconds while both the translational and rotational wind components are on, the de-activation of the rotational wind begins. It becomes completely off around 700 seconds leaving only the translational wind. The rotational wind components are turned off while the translational wind components are left on to isolate the effect of the rotational wind in the trim condition of the EQ-II flying at the sweet spot. While the wind condition experienced by the EQ-II is artificially altered, the controller keeps the aircraft at the commanded position, the sweet spot, by adjusting the control variables. Once the transient in the wind condition ends and the wind components go to steady-state, the aircraft goes to a new trim state, with different control surface deflections and thrust settings.

Figure 5.2 shows the responses of the control variables of the EQ-II to the variation in the induced wind components. In the absence of wind, the aileron deflection is zero, signifying a cruise condition at trim in solo flight. After 200 seconds, with the translational and rotational wind completely on, representing the induced wind from the KC-135R, there is an aileron deflection of about -3 degrees. Once the rotational wind is turned off after 700 seconds, the aileron deflection goes to zero. The same phenomenon is observed for the deflection of the rudder in Fig. 5.2. It is initially zero degrees but once the wind is turned on, it increases to 1.4 degrees. With the elimination of the rotational wind, it goes back down to zero. The elimination of the rotational wind leads to the increase in elevator deflection back to its original value when there is no induced translational or rotational wind as in solo flight. In essence, trimming the aircraft no longer requires control surface deflections when the rotational wind is turned off. This observation is the manifestation of the induced mo-

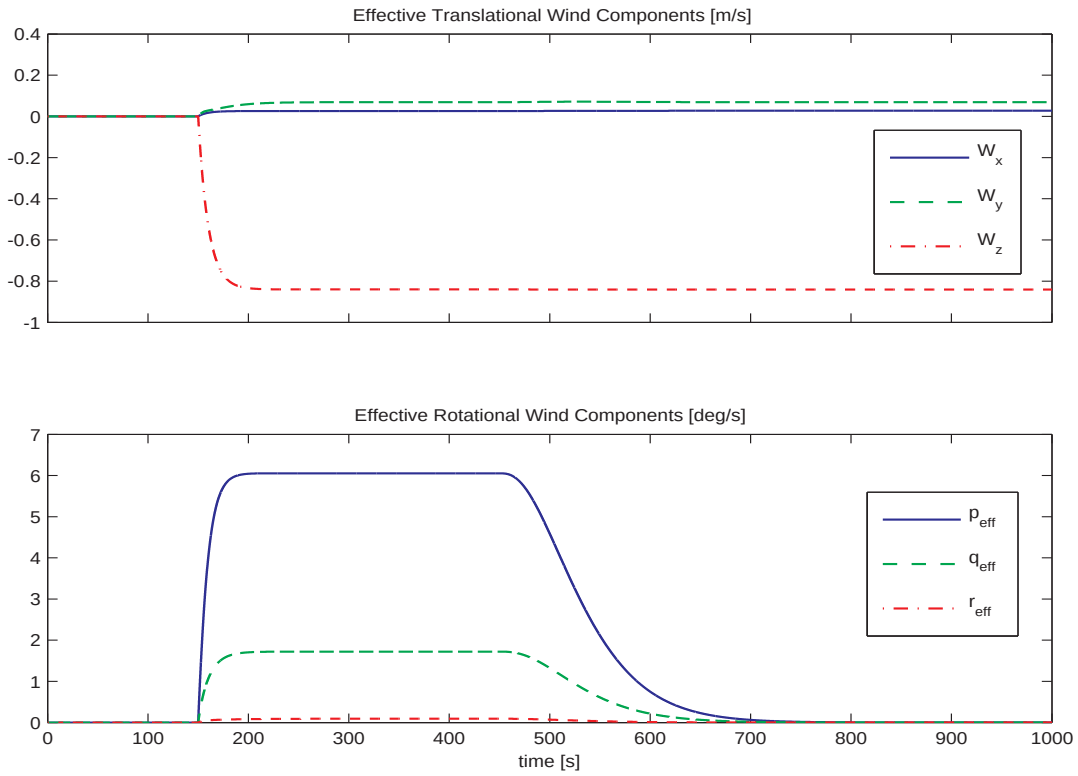

Figure 5.1. Induced Translational and Rotational Wind.

ments by the non-uniform wind field and the response of the controller by adjusting the control surfaces to keep the aircraft trimmed.

Figure 5.2 also shows the variation of the EQ-II thrust required to keep the aircraft trimmed at the sweet spot behind the lighter KC-135R. Table 5.1 summarizes the steady-state values of thrust at the three phases of the simulation: (i) no wind, (ii) translational and rotational wind, and (iii) only translational wind. T_l and T_r in Fig. 5.2 show the required thrust levels on the left and right side of engines, respectively. Since no differential thrust is used in this case, thrust levels on both sides are exactly the same. The thrust required is seen to experience a 3 percent increase from its initial value once the wind is turned on. This is contrary to the common expectation that formation flight yields reduction in required thrust and

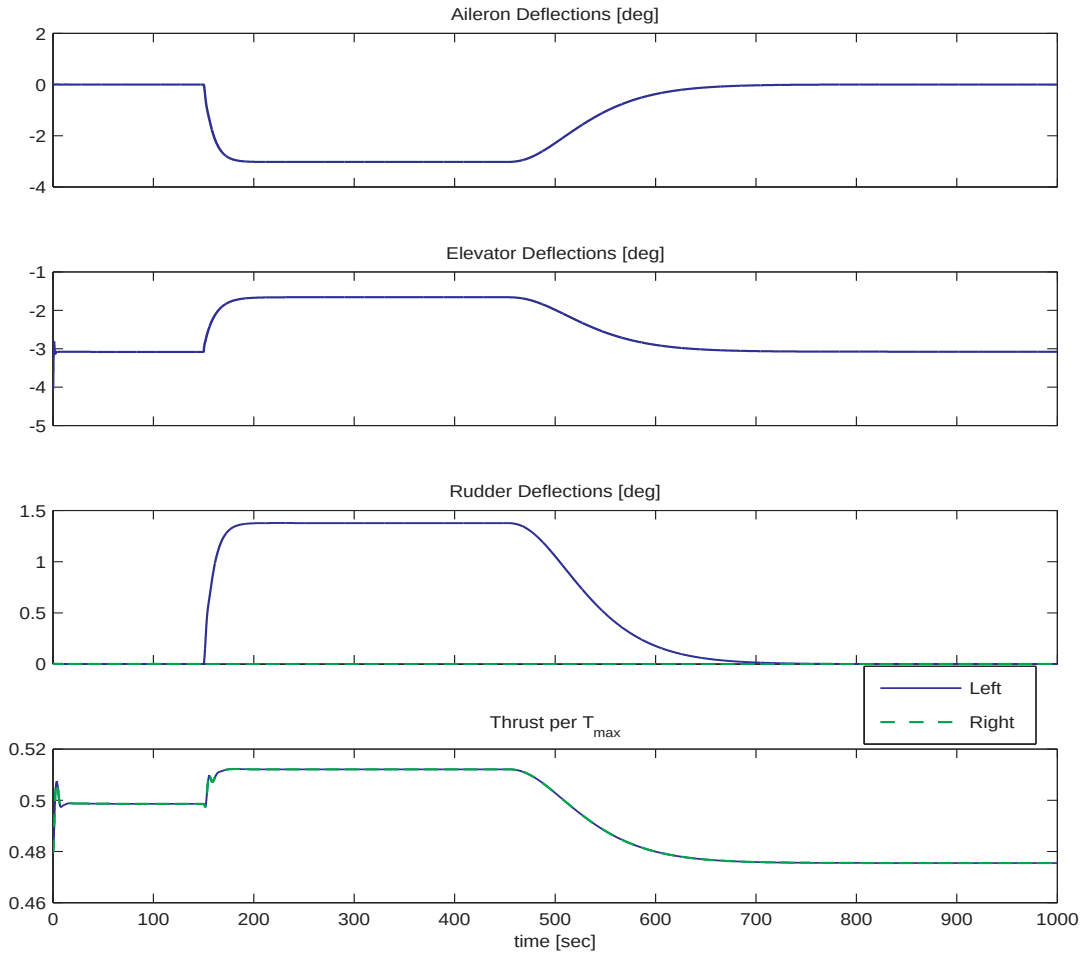

Figure 5.2. Response of Control Variables to Induced Wind.

thus fuel saving when the follower aircraft is placed at the sweet spot relative to the lead aircraft. The next phase of the simulation helps explain this unexpected observation. When the rotational wind is turned off while the translational wind stays on, the thrust experiences a reduction of about 5 percent of its original value. As seen in the first three plots of Fig. 5.2, in the third phase of the simulation when the rotational wind is off, the deflections of the aileron and rudder go to zero, the trim values when there is no induced wind. The deflection of the control surfaces generates drag, which is included in the aerodynamic model of the EQ-II as presented in Eq.

Table 5.1. Thrust Comparison (T/T_{max})

No Wind	Translational and Rotational Wind	Percent Reduction	Only Translational Wind	Percent Reduction	Cost of Control Effector Deflections
0.4986	0.5121	-2.71%	0.4755	4.63%	7.34%

(2.10). Thus, the reduction in the required thrust can be partially attributed to the elimination of the aileron and rudder deflections. As summarized in Table 5.1, the required thrust increases by 2.7% in phase 2 and decreases by 4.6% in phase 3. Since the main difference in the trim condition of the aircraft between these two phases is the deflection of the aileron and rudder, the cost of the control surface deflection in terms of thrust is considered to be 7.3%. When the thrust level in phase 3 is compared to that in phase 1 (no wind), the potential benefit of formation flight appears to be more than 4%, if the aircraft can be trimmed without the deflection of the control surfaces. This is a motivation for investigating alternative trimming mechanisms.

5.3 Fuel Transfer and Differential Thrust Analysis

One of the alternative moment generation mechanisms investigated in this dissertation is internal fuel transfer between fuel tanks to produce a lateral shift in the center of gravity. This will generate a rolling moment for the configuration of the fuel tanks in the EQ-II and is expected to decrease the aileron deflections required to trim. The other is differential thrusting to produce a yawing moment and reduce the need for the rudder. These non-conventional methods are presented in this section. In the two cases presented, the same fuel transfer scheme is followed. The first case uses only the rudder while the second case employs differential thrusting and reduced use of the rudder. This is accomplished by re-designing the LQR controller by adjusting

the weighting matrices of the cost function. Initially, the outer fuel tanks are half full, the inner fuel tanks are a quarter full, and the wind is off, as in the previous simulation. At 150 seconds, the wind components, both translational and rotational, start to increase and they reach their normal levels after 200 seconds. When the aircraft is trimmed at the sweet spot while under the influence of the induced wind, at 400 seconds, the fuel transfer starts between the fuel tanks. The fuel is moved from the right side of the aircraft to the left by transferring fuel (i) from tank 4 to 1, and (ii) from tank 3 to 2. Fig. 5.3 shows how the amount of fuel in each fuel tank changes as well as how the CM of the fuel mass in each fuel tank moves in the three directions as the fuel is transferred. The fuel is moved to the left to shift the CM of the aircraft to the left, which generates negative rolling moment, because the aerodynamic moment induced by the wind at the sweet spot is positive. When the induced aerodynamic moment will be compensated by the CM shift, a smaller aileron deflection should be needed. Since the inner fuel tanks, 2 and 3, hold more fuel than the larger outer fuel tanks 1 and 4 the fuel transfer from 4 to 1 completes before that from 3 to 2 as seen in the first subplot of Fig. 5.3. For fuel tanks 2 and 3, the center of gravity variations of the fuel in the x and y directions is as a result of the complicated geometry of the tanks. In the z direction, there is a change in the center of gravity for all fuel tanks (1 through 4) during the transfer.

Figure 5.4 shows the variations of thrust and control effector deflections with fuel transfer. When the wind is turned on, the aileron deflection increases. As the fuel transfer process begins, the aileron deflection starts to decrease back to zero as a result of the shift in the center of gravity which generates a rolling moment. The aileron deflection continues to decrease to zero till the fuel transfer process is completed and tank 1 is full, tank 2 is half full, and tanks 3 are 4 empty. The fuel transfer has no impact on the steady-state deflections of the rudder and elevator

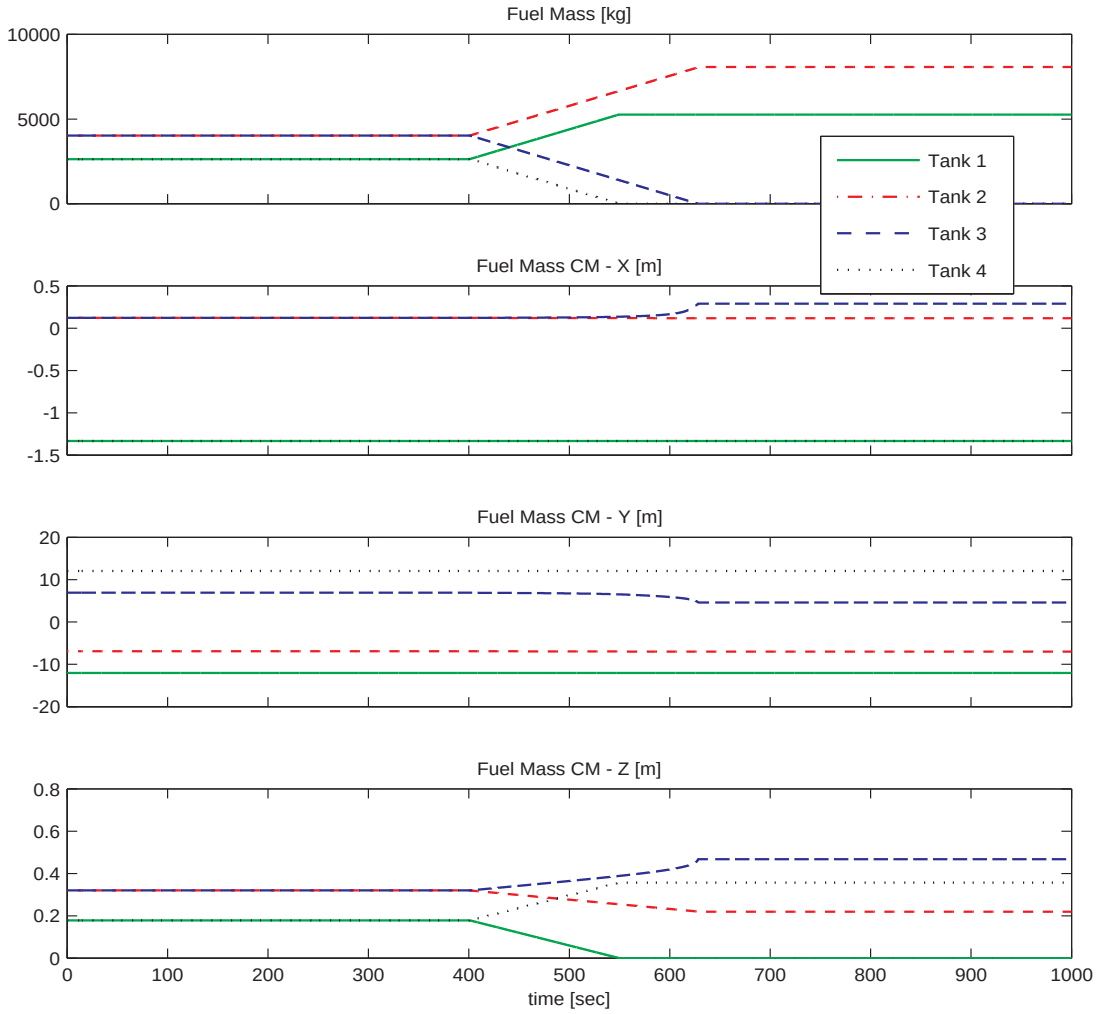

Figure 5.3. Mass and Center of Mass of Fuel Tanks.

as they both deviate during the fuel transfer but eventually return to their original values in formation flight once the fuel transfer is completed. The deflection levels of aileron and rudder during the fuel transfer depend on the fuel transfer rate. The higher the transfer rate, the larger the deflections. In the simulation, the fuel transfer rate is intentionally kept much higher than the actual pump capability to shorten the simulation time. Since this study focuses on the steady-state trim values, the transient behavior during the fuel transfer process should be ignored.

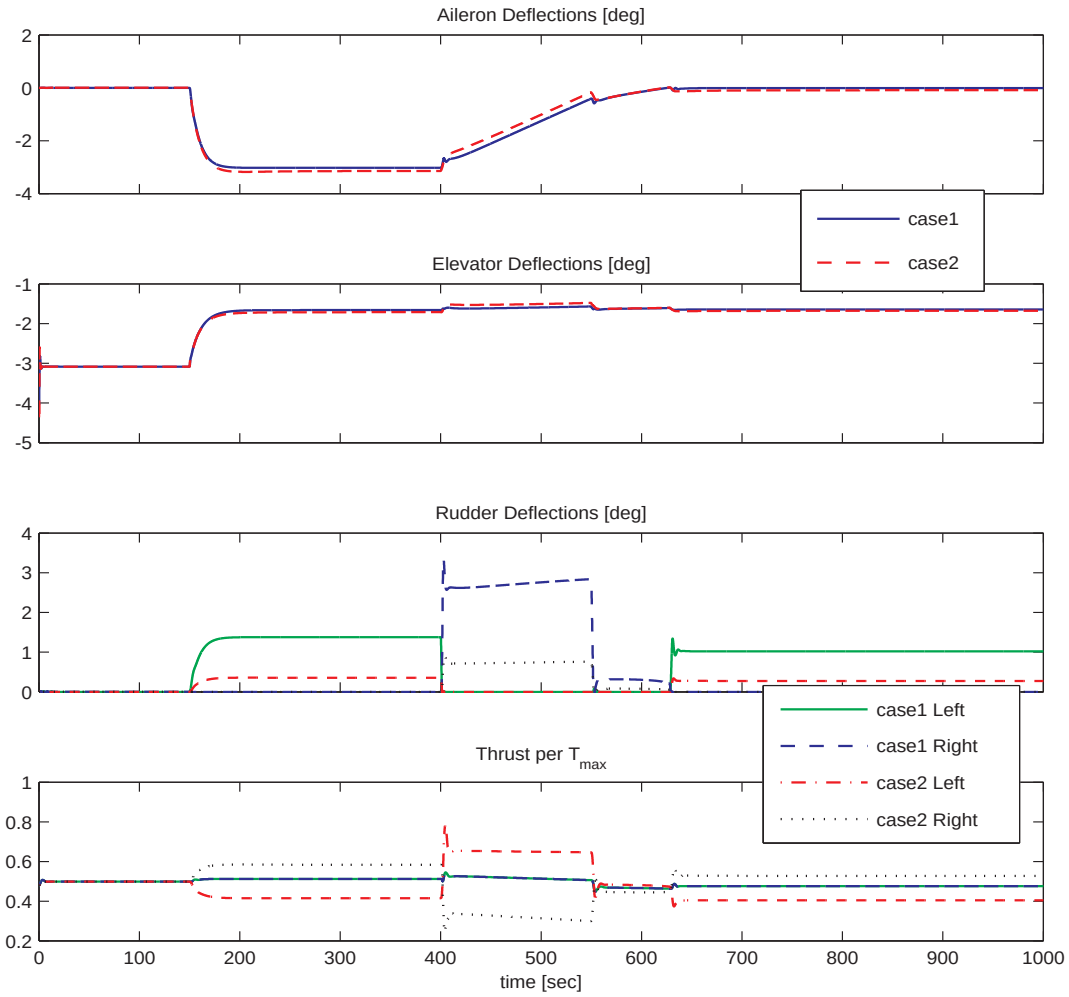

Figure 5.4. Control Variables with Fuel Transfer.

There are barely any differences between case 1 and case 2 in terms of aileron and elevator deflections. The effect of the difference in controllers of case 1 and 2 manifests itself in the rudder and thrust responses. The controller of case 2 is tuned to utilize differential thrusting and to reduce the use of the rudder. As a result, the controller commands different right and left thrust levels to generate yawing moment. This leads to smaller rudder deflections in case 2.

Table 5.2 summarizes the steady-state results of the two cases in terms of the thrust levels. This comparison helps clearly quantify the benefits of the alternative

trimming mechanisms in terms of the thrust reduction. The first comparison is done between the columns to quantify the benefit of fuel transfer. In case 1, the thrust level increases 2.71% when the EQ-II is flown in formation. This observation is already made in the previous section and attributed to the deflection of the control surfaces to keep the aircraft trimmed under the effect of the induced aerodynamic moments. When the fuel transfer is done, the formation flight brings about 4.61% thrust reduction. The difference between the thrust levels before and after the fuel transfer is 7.32% and quantifies the benefit of fuel transfer. In case 2, a similar observation is made; the benefit of fuel transfer is about 7% reduction in the required thrust. The second comparison is done between the rows of Table 5.2, between the two cases, to quantify the benefit of differential thrusting. When the aircraft flies in formation without fuel transfer, case 1 has 2.71% thrust increase and case 2 has about 0.12% thrust increase. This indicates about 3% thrust reduction when differential thrusting is used. A similar thrust reduction benefit of differential thrusting is observed based on the thrust levels after the fuel transfer in both cases. In summary, thrust reduction of about 6.56%, is obtained when (i) the aircraft is placed at the sweet spot in formation flight, (ii) fuel transfer between the fuel tanks is performed to reduce, or eliminate if possible, the aileron deflection, and (iii) differential thrusting is used to reduce, or eliminate if possible, the rudder deflection.

Table 5.3 presents the steady-state results for the EQ-II behind a heavier KC-135R, similar to Table 5.2. The conclusions are similar regarding the benefits of fuel transfer and differential thrusting but in this case, when a heavier KC-135R is used, the benefit of using both alternate trimming methods is higher. Thus, the largest thrust reduction of about 8% is seen when both internal fuel transfer and differential thrusting are used to reduce the aileron and rudder deflections, respectively, of the EQ-II aircraft at the sweet spot behind a heavier KC-135R.

Table 5.2. Thrust Comparison (T/T_{max}) Employing Rudder and Differential Thrusting

Case	No Wind	With Wind	Percent Reduction	After Fuel Transfer	Percent Reduction	Benefit of Fuel Transfer
1 - Rudder	0.4986	0.5121	-2.71%	0.4756	4.61%	7.32%
2 - Differential Thrust	2×0.4986	0.5832 + 0.4152	-0.12%	0.5273 + 0.4045	**6.56**%	6.68%
Benefit of Differential Thrust			2.99%		2.07%	

Table 5.3. Thrust Comparison (T/T_{max}) Employing Rudder and Differential Thrusting for Large EQ-II Trailing Heavier KC-135R

Case	No Wind	With Wind	Percent Reduction	After Fuel Transfer	Percent Reduction	Benefit of Fuel Transfer
1 - Rudder	0.4986	0.5045	-1.18%	0.4685	6.04%	7.22%
2 - Differential Thrust	2×0.4986	0.5748 + 0.4085	1.39%	0.5209 + 0.3964	**8.01**%	6.62%
Benefit of Differential Thrust			2.58%		1.98%	

CHAPTER 6

KC-135R - KC-135R FORMATION

The results of the EQ-II variants trailing the KC-135R motivated the results of this chapter and the next. For the small variant of the EQ-II aircraft trailing the KC-135R, the static and dynamic sweet spot were observed to be at the same location. The large variant of the EQ-II, on the other hand, had a lateral separation of about 0.1 KC-135R wingspans (approximately 4 meters) between the static and dynamic sweet spot.

The formation flight study of the KC-135R - large EQ-II pair showed that the static and dynamic sweet spots differ and unconventional control surfaces on the EQ-II were too costly for formation flight at the static sweet spot. There are two possible reasons for this disparity in static and dynamic sweet spot locations: (1) the trail EQ-II is not a conventional aircraft like the lead KC-135R, and (2) the trail EQ-II is of a significantly different size than the lead aircraft. The approach taken in this chapter is to hypothesize that the disparity between the static and dynamic sweet spot locations is due to the former and to test this hypothesis by replacing the unconventional EQ-II aircraft with a trail KC-135R so as to have two similar conventional aircraft in the formation. This chapter presents the static and dynamic results of the two KC-135R tanker aircraft in formation.

The static and dynamic studies were carried out for two KC-135R aircraft pairs in formation as given in Table 6.1. First the KC-135R trailing a nominal KC-135R was investigated. Then, the weight of the leading KC-135R was increased by 26

Table 6.1. KC-135R - KC-135R Aircraft Formation Studies

Lead KC-135R Weight	Trail KC-135R Weight
Nominal	Nominal
Heavy	Nominal

percent while the trail KC-135R was left the same as in the case of the KC-135R - Large EQ-II study in Chapter 4.

6.1 Static Study

6.1.1 KC-135R Trailing KC-135R of Nominal Weight

This section presents the results of the KC-135R flying behind the KC-135R of nominal weight. The lift-to-drag ratio in solo flight, a value of 21.59, was subtracted from the lift-to-drag ratio in formation flight at all points in the grid. The contour plot for the percentage difference in lift-to-drag ratio is presented in Fig. 6.1 while the contour plots for the moment and side force coefficients of the KC-135R trailing the KC-135R of nominal weight are presented in Figs. 6.2 through 6.5.

Figure 6.1 shows that as the trail KC-135R moves from 0.5 wingspans laterally further away from the lead KC-135R, the increment in lift-to-drag ratio increases from 0 till a maximum of 17.7 percent from the baseline case. The exact location of the static sweet spot is 0.877 wingspans laterally and 0.01 wingspans above the leader.

All contour plots show adversely large magnitudes of the force and moment coefficients for lateral separations less than 0.5 wingspans. This is due to the downwash area behind the lead KC-135R in which no formation benefits for the trail KC-135R are obtained.

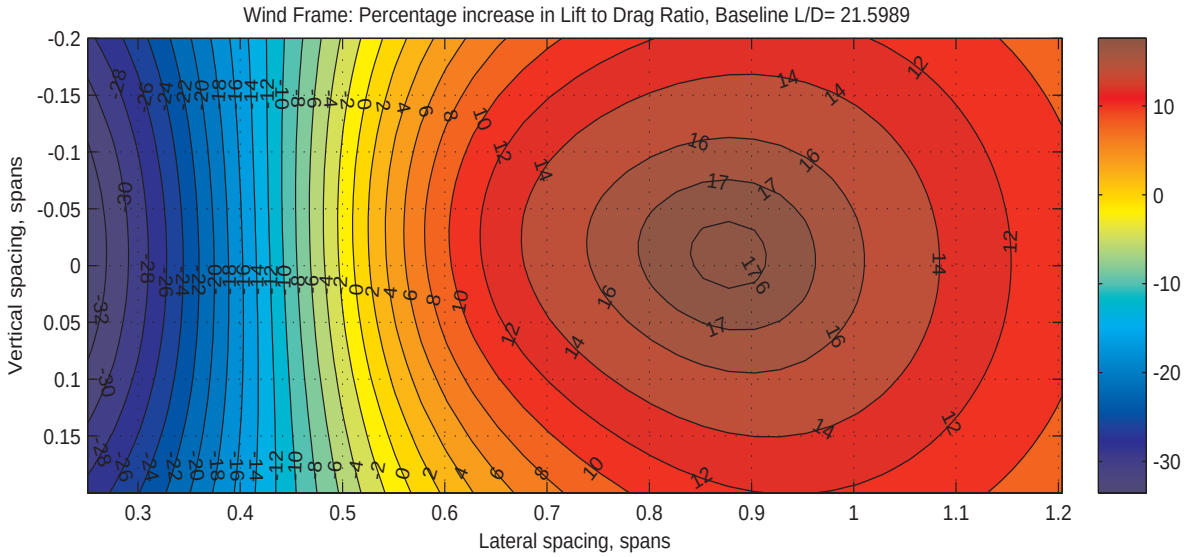

Figure 6.1. Percentage increase in Lift to Drag Ratio from Nominal Flight: KC-135R.

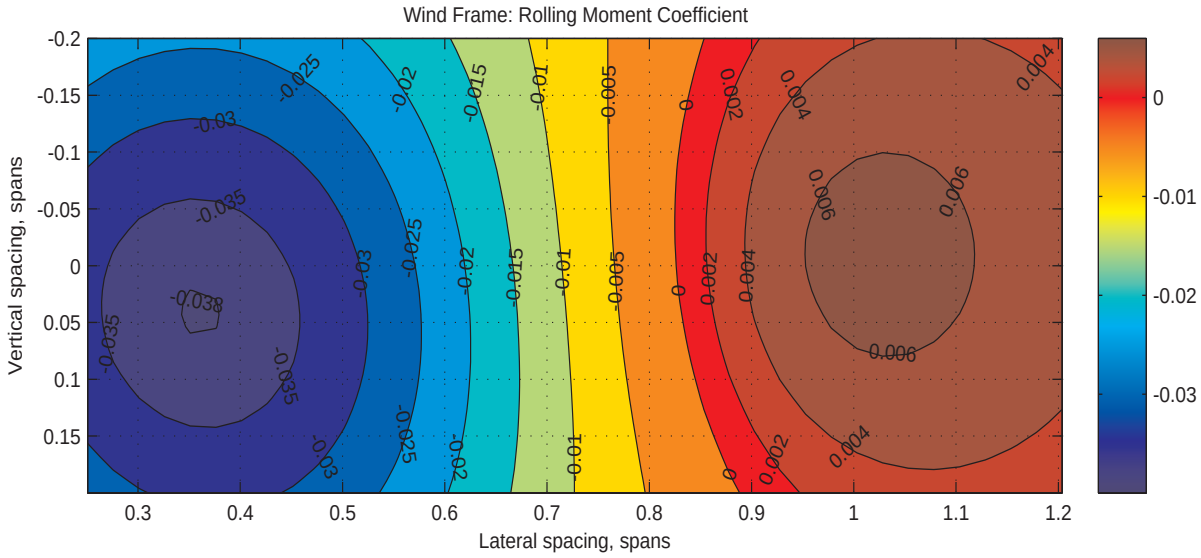

Figure 6.2. Aerodynamic Rolling Moment of KC-135R .

6.1.2 KC-135R Trailing Heavy KC-135R

The results of the KC-135R trail aircraft behind a 26 percent heavier KC-135R are shown in Figs. 6.6 and 6.7. Fig. 6.6 shows the same location for the highest lift-to-drag ratio increase with magnitudes slightly larger than Fig. 6.1. The largest

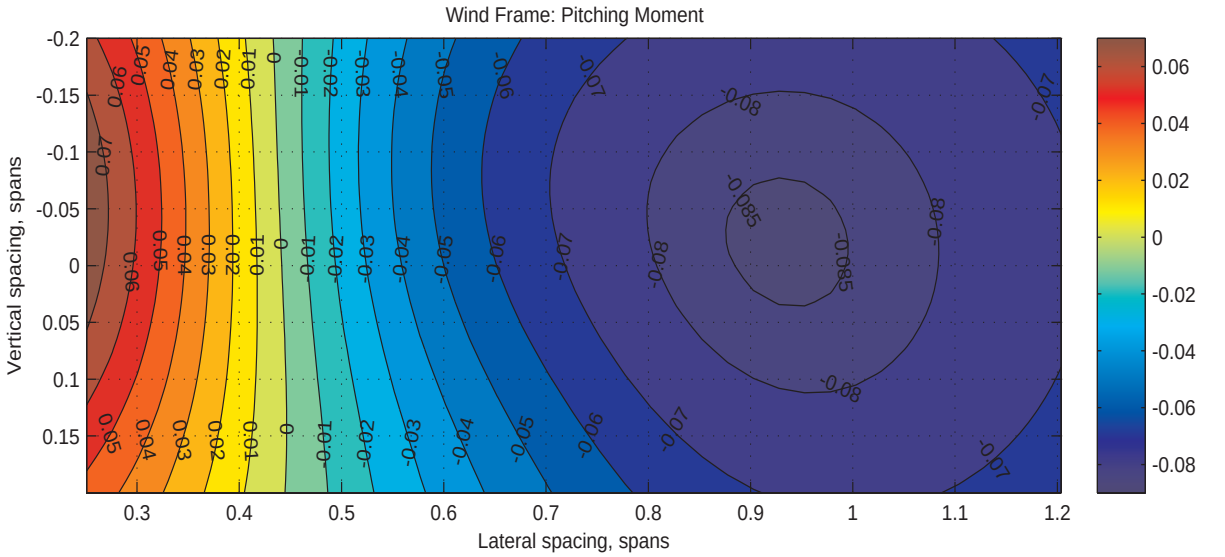

Figure 6.3. Aerodynamic Pitching Moment of KC-135R .

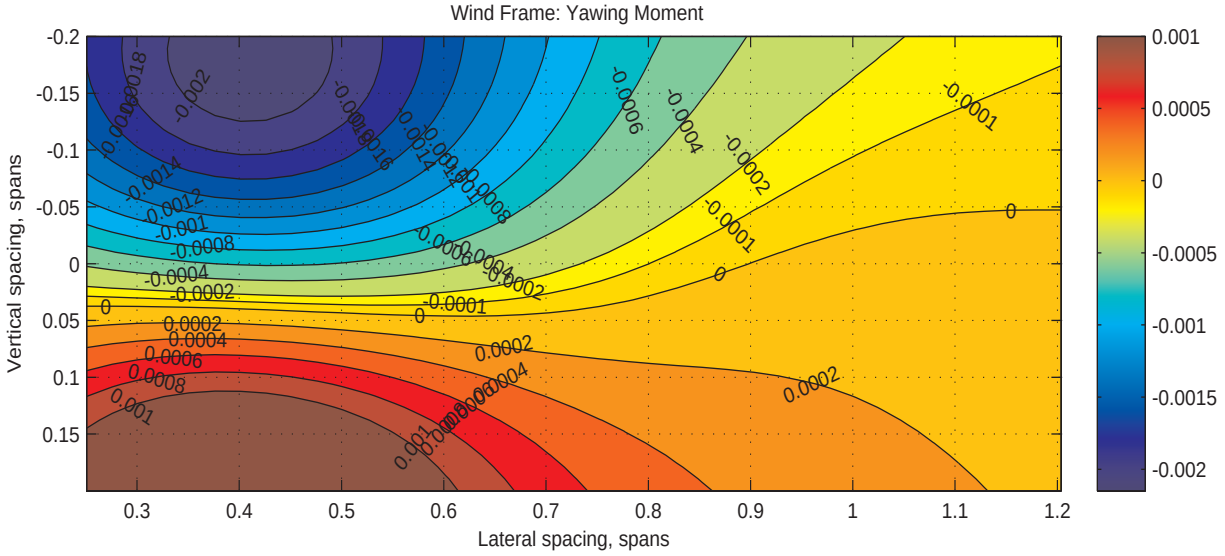

Figure 6.4. Aerodynamic Yawing Moment of KC-135R .

increase in lift-to-drag ratio from the baseline is 21.1 percent at 0.8777 wingspans laterally and 0.01 wingspans above the leader. This is the location of the sweet spot based on the static analysis for the KC-135R aircraft behind a heavier lead KC-135R. The side force and moment coefficients also have similar patterns at all locations

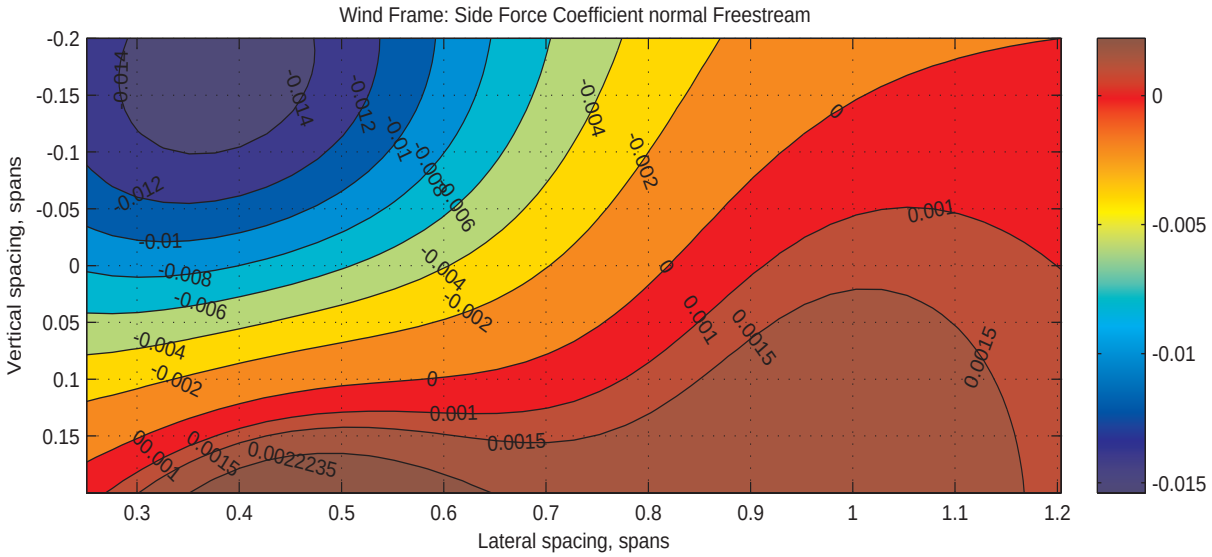

Figure 6.5. Side Force on KC-135R.

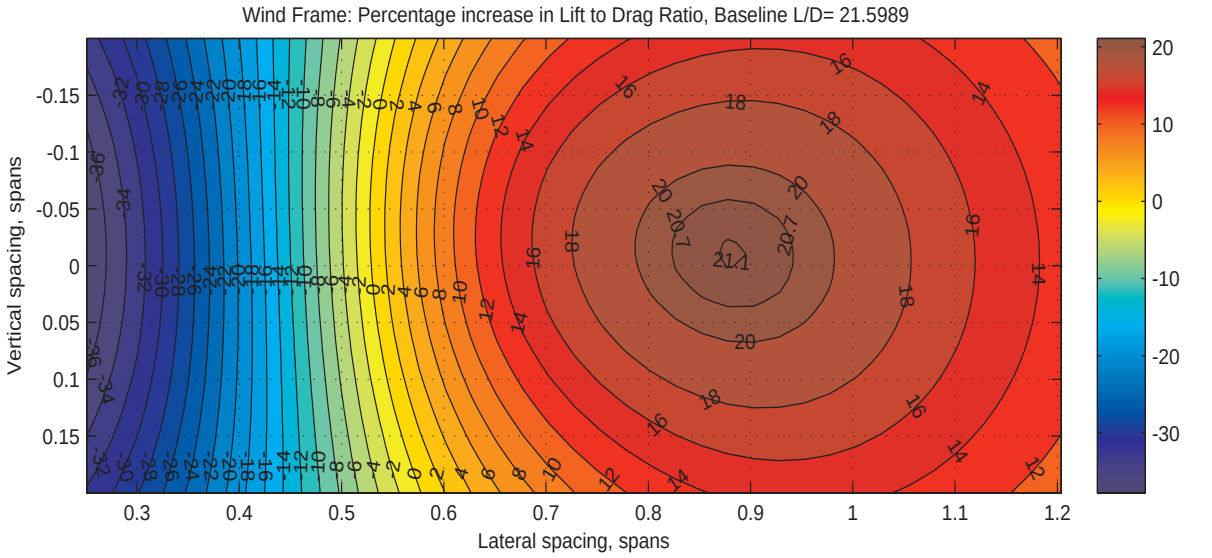

Figure 6.6. Percentage increase in Lift to Drag Ratio from Nominal Flight using a Heavier Lead KC-135R.

except that their magnitudes are slightly greater. For this reason, only one moment coefficient contour, Fig. 6.7, is presented for comparison with Fig. 6.2. Figure 6.7

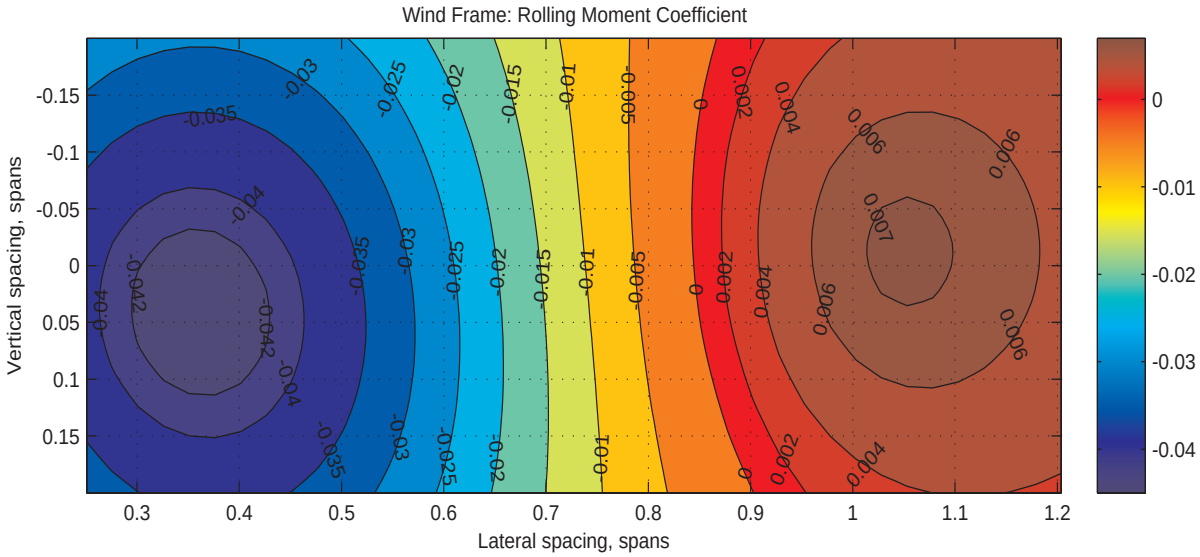

Figure 6.7. Aerodynamic Rolling Moment of KC-135R using a Heavier Lead KC-135R.

looks similar to Fig. 6.2 except in the almost imperceptible different magnitudes of the contour levels as in the case of the large EQ-II in Chapter 4.

6.2 Dynamic Study

The primary control surfaces of the KC-135R are the aileron, elevator, rudder, and the spoilers. In this study, the spoilers are not used to provide additional roll control authority since they are primarily drag devices which would reduce the formation flight benefit. It was thus expected, even more than for the EQ-II aircraft as seen in Chapter 4.2, that there would be a large expanse in the grid in which the controller would be unable to trim the aircraft because of the large magnitudes of the induced moments on the follower that would require control surface deflections and/or thrust levels larger than saturation limits. Sections 6.2.1 and 6.2.2 present the dynamic simulation results for the trail KC-135R behind the lead KC-135R of nominal and heavy weights respectively.

6.2.1 KC-135R Trailing KC-135R of Nominal Weight

Figure 6.8 is a contour plot of the simulation stop parameter. It shows that up until around 0.7 lateral wingspans, the simulation stop parameter is one because the controller could not trim the trailing KC-135R mostly due to the saturation of the control variables. As a result of this, all contour plots generated from the results of the dynamic simulation exclude this area.

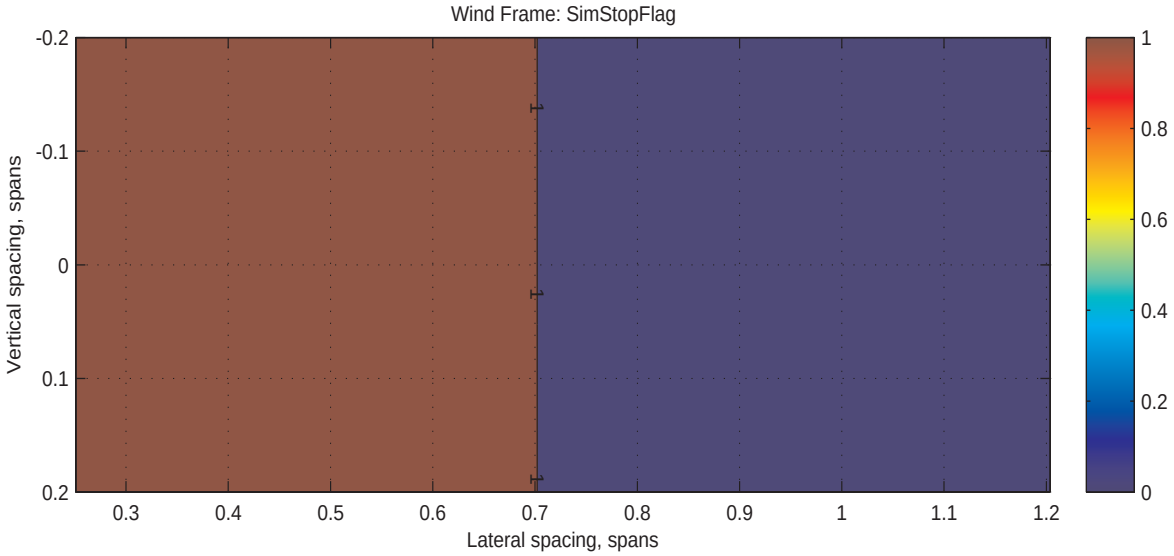

Figure 6.8. Simulation Stop Parameter of KC-135R.

A contour plot of the percentage thrust increment is presented in Fig. 6.9. The largest thrust reduction of 10.7 percent, equivalently the least thrust required to fly in formation, is obtained at 0.8276 wingspans laterally and 0.01 wingspans below the lead KC-135R. This is the sweet spot based on the dynamic study for the KC-135R trail to fly 3.8 wingspans behind the lead KC-135R.

The aileron, elevator, and rudder deflections are presented in Figs. 6.10 through 6.12, respectively. The deflections of the aileron is seen to decrease as the dynamic

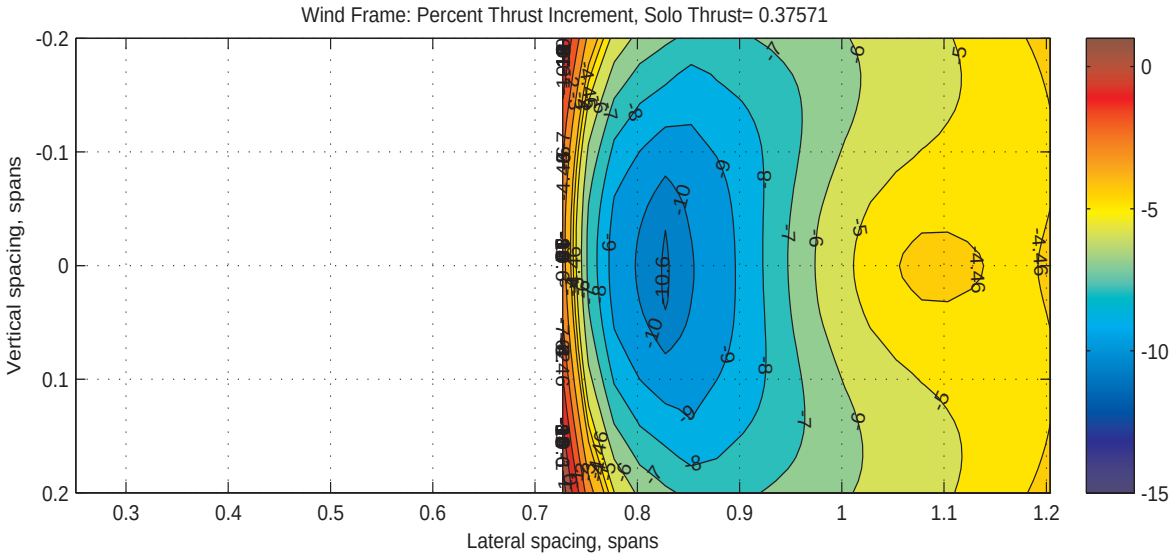

Figure 6.9. Percentage increase in Thrust from Nominal Flight of KC-135R.

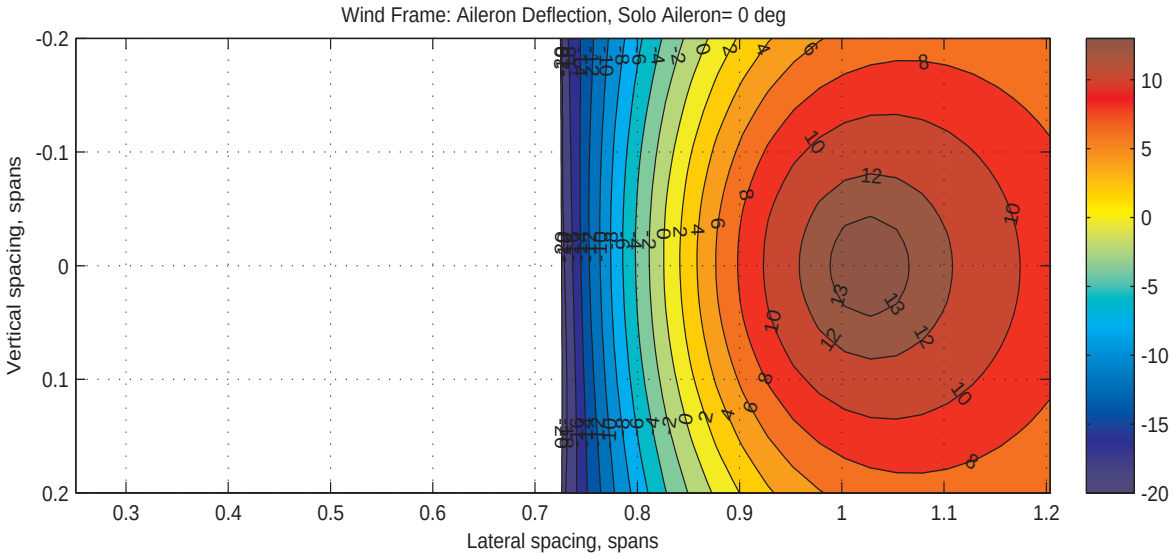

Figure 6.10. Aileron Deflections of KC-135R.

sweet spot is approached from either the right or the left of 0.8276 lateral wingspans. At the dynamic sweet spot, the aileron deflection is 0.2 degrees, a slight increase from 0 degree which is required for solo flight. This is a slight increase in the deflection compared to that required for solo flight which is 0 degree. The elevator and rudder

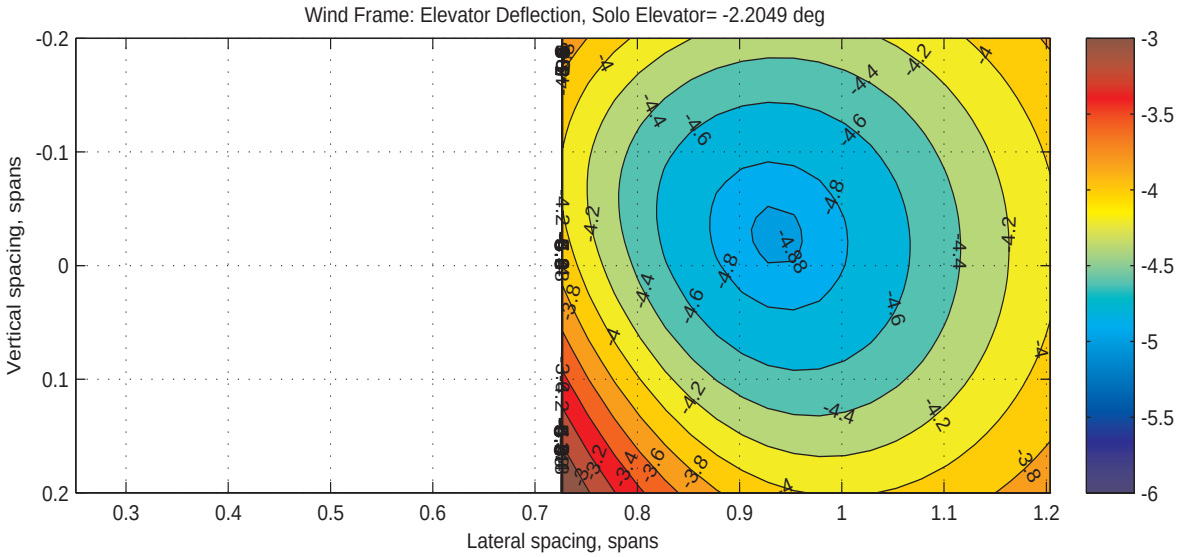

Figure 6.11. Elevator Deflections of KC-135R.

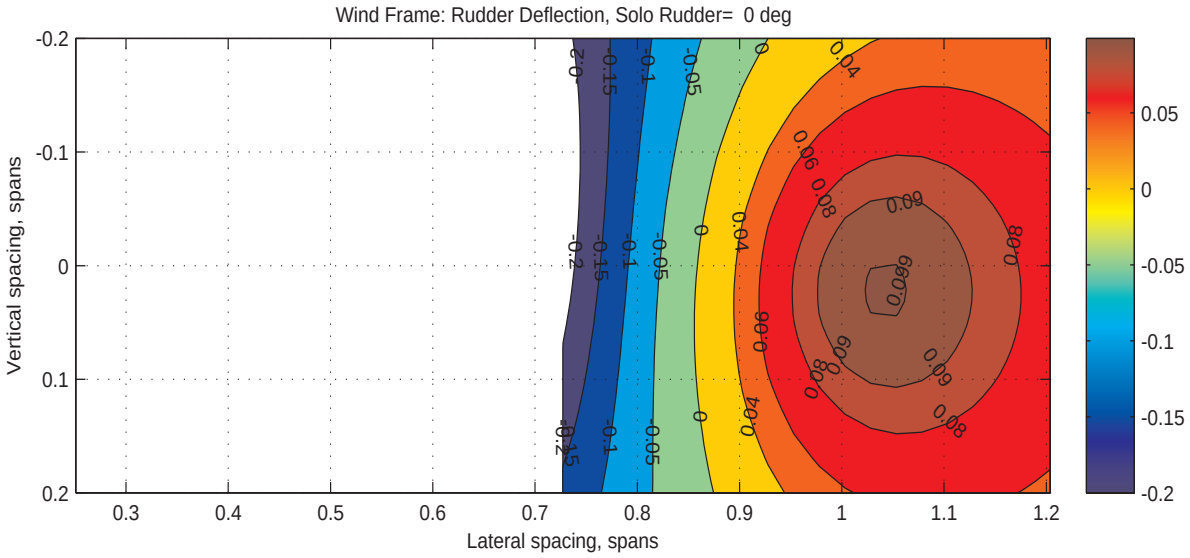

Figure 6.12. Rudder Deflections of KC-135R.

also experience an increase in deflection from solo flight to formation flight as seen in the contour plot of Figs. 6.11 and 6.12 respectively. This is in agreement with the expectations of induced aerodynamic moments from the lead aircraft requiring

non-zero control effector deflections as a trail aircraft flies in the non-uniform wind field induced by the lead.

Figs. 6.10 through 6.12 also show that the control effectors saturate and fail to stabilize the trail aircraft when it is in the downwash region behind the leader from 0.25 wingspans to about 0.7 wingspans laterally. Analyzing the trends of the control surface deflections as the trail aircraft moves away from the sweet spot towards the lead aircraft in the lateral direction shows clearly that the aileron saturates first as compared to the elevator and rudder. This is consistent with the observation in the static case that the induced rolling moment is the highest. The spoilers could have provided additional roll authority and reduced the expanse in Fig. 6.8 in which the aircraft cannot be stabilized due to large induced rolling moments. As stated earlier, the spoilers were not employed due to their detrimental effect on the lift-to-drag ratio.

6.2.2 KC-135R Trailing Heavy KC-135R

The dynamic results of the KC-135R trail aircraft behind a 26 percent heavier KC-135R lead are shown in Figs. 6.13 and 6.14. As in the static case, the impact of the heavier KC-135R lead aircraft is seen primarily in the magnitudes of the thrust and control surface deflections. The trends and location of the sweet spot based on the dynamic study are almost identical with an increase in leader weight, for this reason, only Figs. 6.13 and 6.14 are presented. Figure 6.13 shows that the benefit of flying in formation is increased when a heavier lead aircraft is used. The aileron deflections in Fig. 6.14 are also larger than those in Fig. 6.10 because there is an increase in the magnitude of the induced aerodynamic moments when the leader aircraft weight is increased as discussed in Section 6.1.

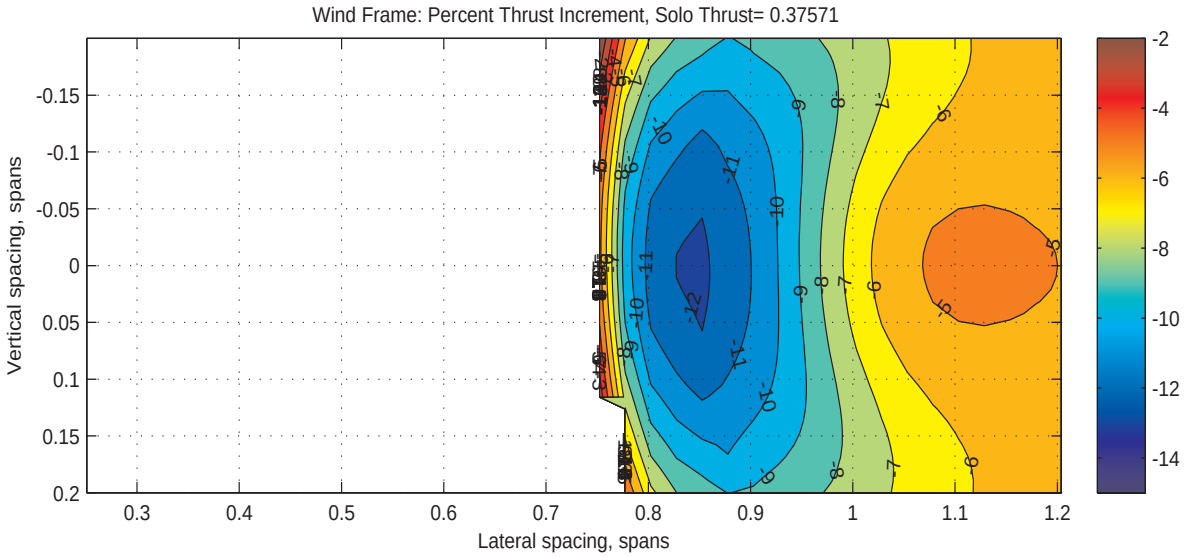

Figure 6.13. Percentage increase in Thrust from Nominal Flight of KC-135R using a Heavier Lead KC-135R.

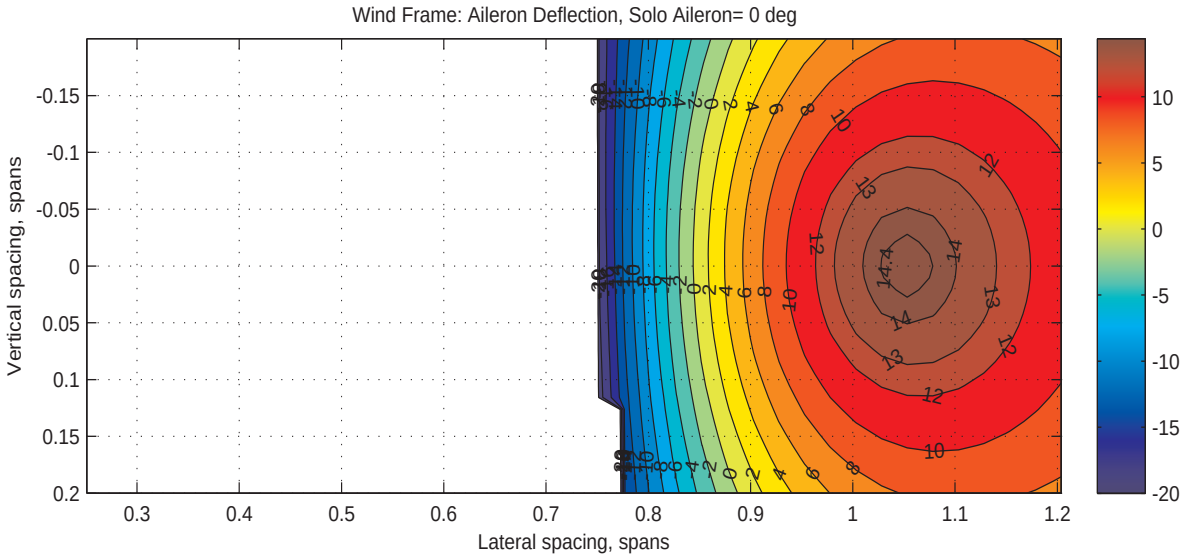

Figure 6.14. Aileron Deflections of KC-135R using a Heavier Lead KC-135R.

Table 6.2. Summary of Static and Dynamic Results for Trail KC-135R

Static Simulation						
	Sweet Spot (Wingspans)					
Leader Weight	C.G. to C.G.	Overlap (%)	Δ L/D (%)	$C_{\mathcal{L}}$	$C_{\mathcal{M}}$	$C_{\mathcal{N}}$
Nominal	x=3.8 y=0.8777 z=-0.01	12.2	17.76	0.0033	-0.0850	0
Heavier	x=3.8 y=0.8777 z=-0.01	12.2	21.13	0.0024	-0.0912	0
Dynamic Simulation						
	Sweet Spot (Wingspans)					
Leader Weight	C.G. to C.G.	Overlap (%)	Δ Thrust (%)	$\delta_a(^\circ)$	$\delta_e(^\circ)$	$\delta_r(^\circ)$
Nominal	x=3.8 y=0.8276 z=0.01	17.2	10.69	0.202	-4.564	-0.040
Heavier	x=3.8 y=0.8526 z=0.01	14.7	12.16	1.2	-5.03	-0.032

6.3 Comparison of Static and Dynamic Results for KC-135R Pair

Table 6.2 summarizes the results of the static and dynamic simulations with regards to the location of the sweet spot and the aerodynamic force and moment coefficients of the trail KC-135R.

Table 6.2 shows that although the static sweet spot remains constant with a change in the weight of the lead aircraft, the dynamic sweet spot changes slightly. In the dynamic case, the wingtip overlap decreases from 17.2% to 14.7% when the lead aircraft weight is increased by 26%. This is in agreement with the results of the large EQ-II aircraft which showed that the location of the static sweet spot was

independent of a 26% weight increase of the lead KC-135R while the location of the dynamic sweet spot was not.

In addition, Table 6.2 shows that the static and dynamic sweet spot are in the same region for both nominal and heavier weights of the lead KC-135R. The location of the static sweet spot is close to that where the induced aerodynamic moments on the trail KC-135R were the least. As a result, the control surface deflections required to trim the trail KC-135R aircraft were very small in that region, leading to the least trim drag and thus required thrust at the sweet spot [10]. For this reason, the dynamic sweet spot was in the same region. In fact, for the heavier weight of the lead aircraft, the static sweet spot almost coincides with the dynamic. For a pair of conventional identical aircraft like the KC-135R pair, the static and dynamic sweet spots are very close but do not coincide. It is thus worthwhile to investigate the second reason of the relative sizes of the aircraft in the formation for the significant difference in static and dynamic locations for the large EQ-II aircraft.

CHAPTER 7

SCALED KC-135R TRAILING KC-135R

Chapter 4 showed that for the large Q-II aircraft trailing the KC-135R, the static and dynamic sweet spots do not coincide. The converse was observed when a KC-135R was used as the trail aircraft. In that case, the locations of the static and dynamic sweet spots coincide. This chapter seeks to determine if the size of the trail aircraft is the dominant reason for the difference in static and dynamic sweet spot locations for the large EQ-II. This is achieved by replacing the unconventional EQ-II aircraft with a conventional aircraft like the lead KC-135R while keeping the same relative sizes between the lead and trail aircraft in terms of the wingspans. This chapter presents the static and dynamic results of the formation of a KC-135R tanker leading (1) a KC-135R scaled down to match the small EQ-II aircraft in wingspan, and (2) a KC-135R scaled up to match the large EQ-II in wingspan.

7.1 Trail Aircraft Re-Sizing

To include conventional trail aircraft with the wingspans of the small and large EQ-II aircraft in the formation flight simulation, the existing KC-135R model is utilized by scaling its 3-D geometry to have the new wingspan match those of the EQ-II aircraft, which also requires scaling the mass and inertia properties, and thrust capabilities of the engines. This dynamic scaling in addition to the dimensional scaling is particularly important in order to capture and understand the dynamic response of the trail aircraft in the dynamic sweet spot determination. To achieve this, the approach taken is to first obtain two scaling factors which are ratios of the wingspans

Table 7.1. Aircraft Wingspan

Aircraft	Wingspan (ft)
Unscaled KC-135R	130.83
Large EQ-II	166.8
Small EQ-II	111.2

of the KC-135R and the small and large variants of the EQ-II. Table 7.1 gives the wingspans of the KC-135R, EQ-II large and small, which are used for computing the scaling factors for the large and small KC-135R models.

To create the large model of the trailing KC-135R to match the large EQ-II variant, a single scaling factor of 1.2749 is used on the unscaled KC-135R tanker model. For the small KC-135R, the unscaled KC-135R is scaled by a factor of 0.85 to create a smaller KC-135R with a wingspan that matches the small variant of the EQ-II. These scaling factors are then used to scale the the spatial dimensions linearly, weight and thrust to the second power, and inertias to the fourth power as outlined in the following sections. With this approach, the aerodynamic model of the KC-135R aircraft is used without any modification for various "scaled KC-135R" aircraft. In addition, this scaling approach assumes rigid body dynamics and does not incorporate any aeroelastic effects in the re-sizing.

7.1.1 Dimensional Scaling

The geometry scaling of the KC-135R requires re-sizing the geometric parameters such as the chord length, wing span, and surface area for instance. For the

lengths, a linear scaling is done in the three co-ordinate directions, x, y, and z. The length scaling is

$$x_{new} = c_{scale}\ x \tag{7.1}$$

$$y_{new} = c_{scale}\ y \tag{7.2}$$

$$z_{new} = c_{scale}\ z \tag{7.3}$$

where c_{scale} is the previously determined scaling factor and the x, y, and z correspond to the unscaled length parameter for the KC-135R. As an example, the wingspan of the large KC-135R is

$$b_{large} = 1.2749\ b \tag{7.4}$$

where b is the true wingspan of the KC-135R. Since the lengths are all scaled linearly, all other parameters which powers of length are scaled to the corresponding power. The areas are scaled to the second power and the volumes are scaled to the third power. As an illustration, the derivation of scaling the reference surface area, S is provided:

$$S_{new} = x_{new}\ y_{new} \tag{7.5}$$

$$= c_{scale}x\ c_{scale}y \tag{7.6}$$

$$= c_{scale}^2\ xy \tag{7.7}$$

$$= c_{scale}^2\ S \tag{7.8}$$

7.1.2 Dynamic Scaling

This section contains the details of the mass/weight, engine thrust, and inertia scaling using the same scaling factor as in Section 7.1.1. For the mass and weight scaling, assuming lift, L, equals weight, W, in cruise,

$$W_{new} = L_{new} \tag{7.9}$$

$$= \frac{1}{2}\rho V^2 S_{new} C_L \tag{7.10}$$

$$= \frac{1}{2}\rho V^2 \; c_{scale}^2 S \; C_L \tag{7.11}$$

$$= \frac{1}{2}\rho V^2 S C_L \; c_{scale}^2 \tag{7.12}$$

$$= W \; c_{scale}^2 \tag{7.13}$$

$$= c_{scale}^2 W \tag{7.14}$$

Thus, the mass, m, is scaled as

$$m_{new} = c_{scale}^2 m \tag{7.15}$$

This derivation assumes the density, ρ, velocity, V, and lift coefficient C_L remain the same and are independent of aircraft size. The thrust, T, is scaled in a similar manner. Assuming thrust equals drag in cruise and using the drag dependence on dynamic pressure, reference area, and drag coefficient, the engine thrust for the scaled aircraft is obtained as

$$T_{new} = c_{scale}^2 T \tag{7.16}$$

In scaling the mass moments of inertia about the x, y, and z axes, as well as the products of inertia about the xy, xz, and yz planes, the definition of the inertia is used. For instance, the mass moment of inertia about the x axis, a measure of the distribution of the aircraft mass about the x axis, is given in Eq. 7.17 as

$$I_{xx} = \int (y^2 + z^2) dm \tag{7.17}$$

Thus,

$$I_{xx} \propto m(y^2 + z^2) \tag{7.18}$$

$$I_{xx_{new}} \propto m_{new}(y_{new}^2 + z_{new}^2) \tag{7.19}$$

$$I_{xx_{new}} \propto c_{scale}^2 m \ \left[(c_{scale}y)^2 + (c_{scale}z)^2\right] \tag{7.20}$$

$$I_{xx_{new}} \propto c_{scale}^2 m \ \left(c_{scale}^2 y^2 + c_{scale}^2 z^2\right) \tag{7.21}$$

$$I_{xx_{new}} \propto c_{scale}^2 m \ c_{scale}^2 \left(y^2 + z^2\right) \tag{7.22}$$

$$I_{xx_{new}} \propto c_{scale}^4 \ m \left(y^2 + z^2\right) \tag{7.23}$$

$$I_{xx_{new}} \propto c_{scale}^4 I_{xx} \tag{7.24}$$

Similarly, the other mass moments of inertia can be scaled as

$$I_{yy_{new}} \propto c_{scale}^4 I_{zz} \tag{7.25}$$

$$I_{zz_{new}} \propto c_{scale}^4 I_{zz} \tag{7.26}$$

And the products of inertia can all be derived as

$$I_{xy_{new}} \propto c_{scale}^4 I_{xy} \tag{7.27}$$

$$I_{xz_{new}} \propto c_{scale}^4 I_{xz} \tag{7.28}$$

$$I_{yz_{new}} \propto c_{scale}^4 I_{yz} \tag{7.29}$$

As an illustration, Fig. 7.1 depicts the unscaled KC-135R with the smaller and larger KC-135R models. The static and dynamic studies are then carried out for two aircraft pairs in formation as presented in Sections 7.2 and 7.3: (1) the large KC-135R trailing the lead KC-135R and (2) the small KC-135R trailing the lead KC-135R. In both cases, the lead KC-135R is the nominal KC-135R without any scaling done.

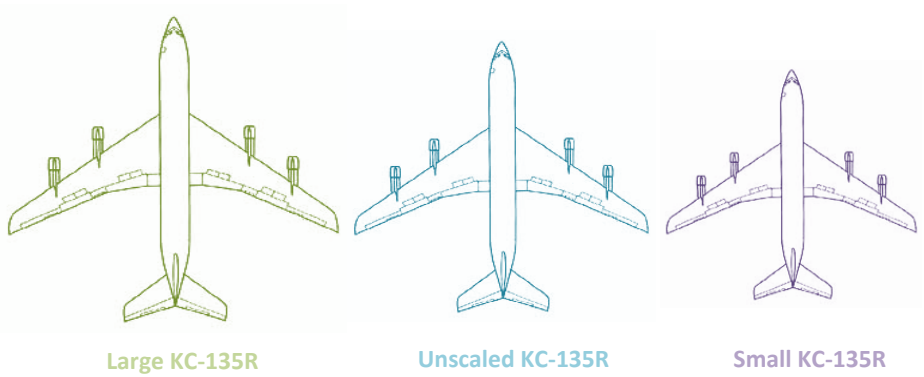

Figure 7.1. Unscaled KC-135R versus Larger and Smaller Scaled KC-135R Models.

7.2 Static Simulation Results

First presented are the static simulation results of the large KC-135R behind the lead, after which the small KC-135R results are shown.

7.2.1 Large KC-135R Trail

This section presents the results of the large KC-135R aircraft flying behind the lead KC-135R. The contour plot for the percentage difference in lift-to-drag ratio as compared to solo flight is presented in Fig. 7.2. It shows that as the trailing KC-135R moves laterally, starting from 0.6 wingspans away from the lead aircraft, the increment in lift-to-drag ratio increases from 0 till a maximum of 16.4 percent from the baseline case. The exact location of the static sweet spot with largest lift-to-drag ratio is 1.0282 wingspans laterally and 0.01 wingspans above the leading KC-135R. This region is promising as there is a large expanse in which the follower can deviate and still experience increased lift-to-drag. The lift-to-drag increment in the surrounding regions are positive, thus no negative lift will occur with changes in location around 1.0282 KC-135R wingspans.

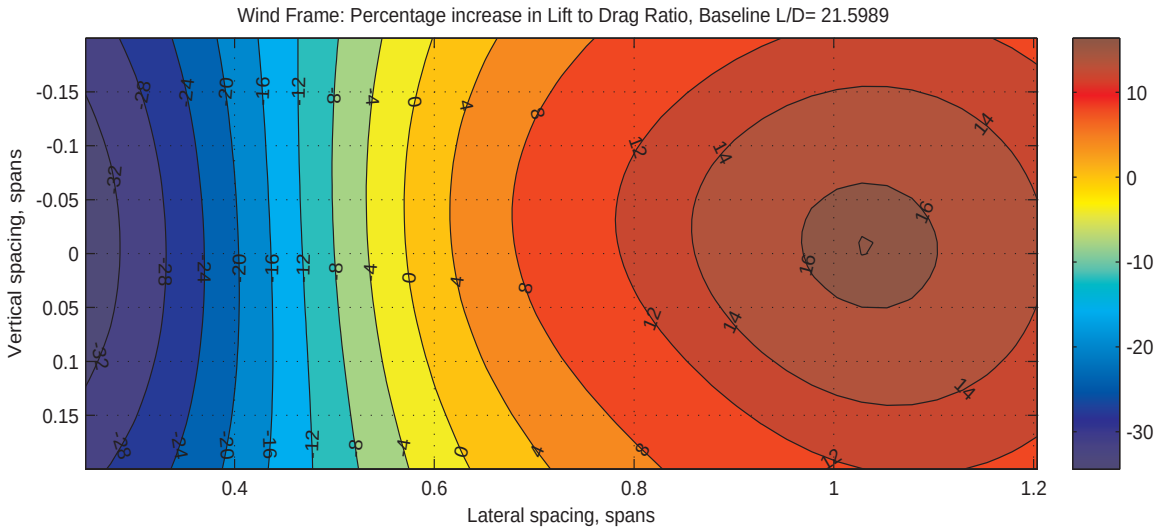

Figure 7.2. Percentage increase in Lift to Drag Ratio from Nominal Flight: Large KC-135R.

Figures 7.3 and 7.4 show the contour plots for the rolling and yawing moment coefficients, respectively, of the large KC-135R. At the static sweet spot, non-zero moments are visible in the roll and yaw. This implies that there will be non-zero control surface deflections required to trim the trail KC-135R at the static sweet spot. The pitching moment coefficient is also depicted in Figs. 7.5. All contour plots show adversely larger magnitudes of the force and moment coefficients for lateral separations less than 0.6 wingspans as compared to the sweet spot region. This is due to the downwash area behind the lead KC-135R in which no formation benefits for the KC-135R are obtained.

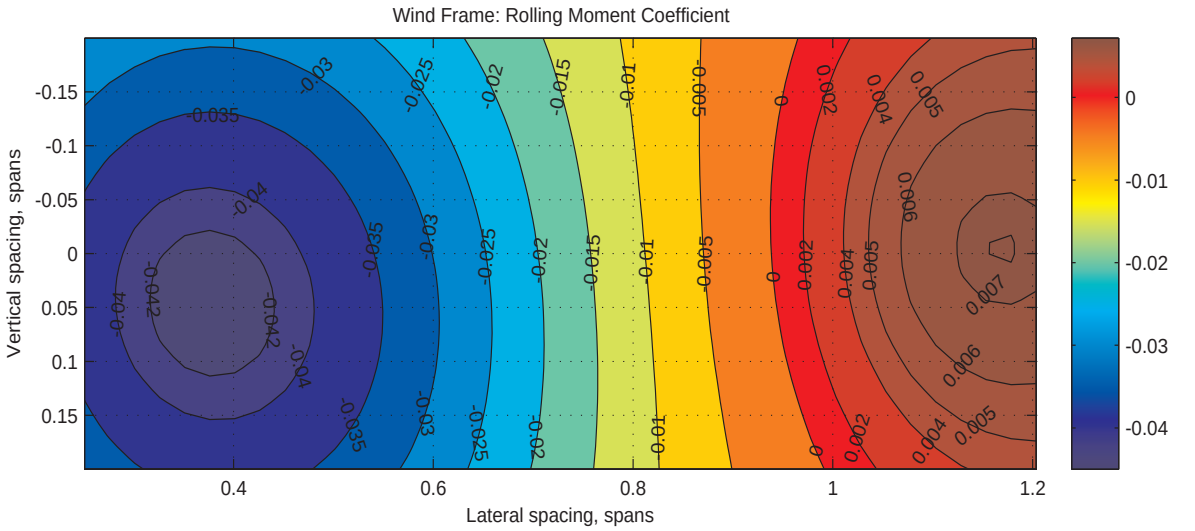

Figure 7.3. Aerodynamic Rolling Moment of Large KC-135R .

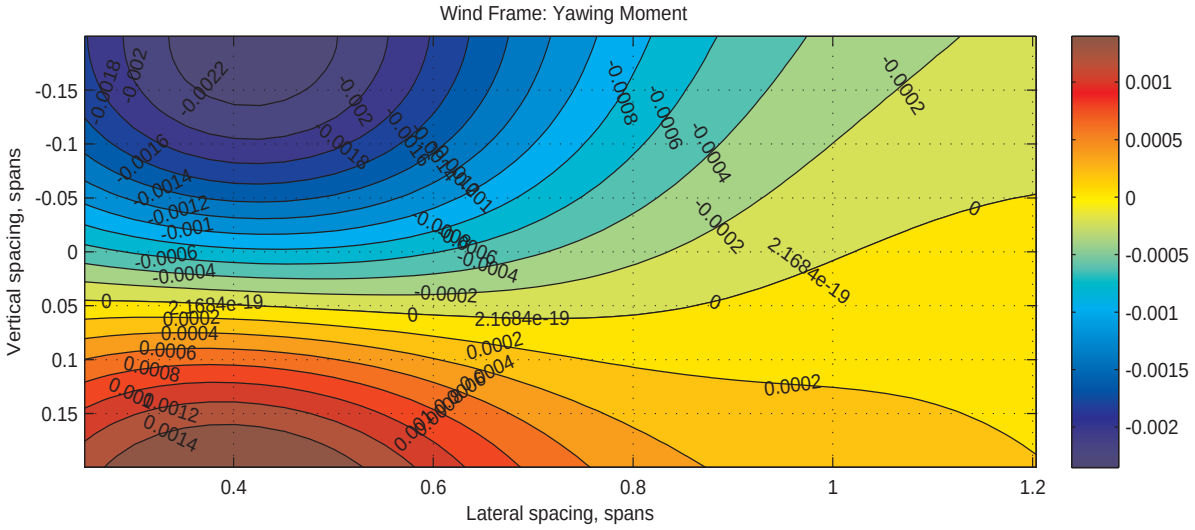

Figure 7.4. Aerodynamic Yawing Moment of Large KC-135R .

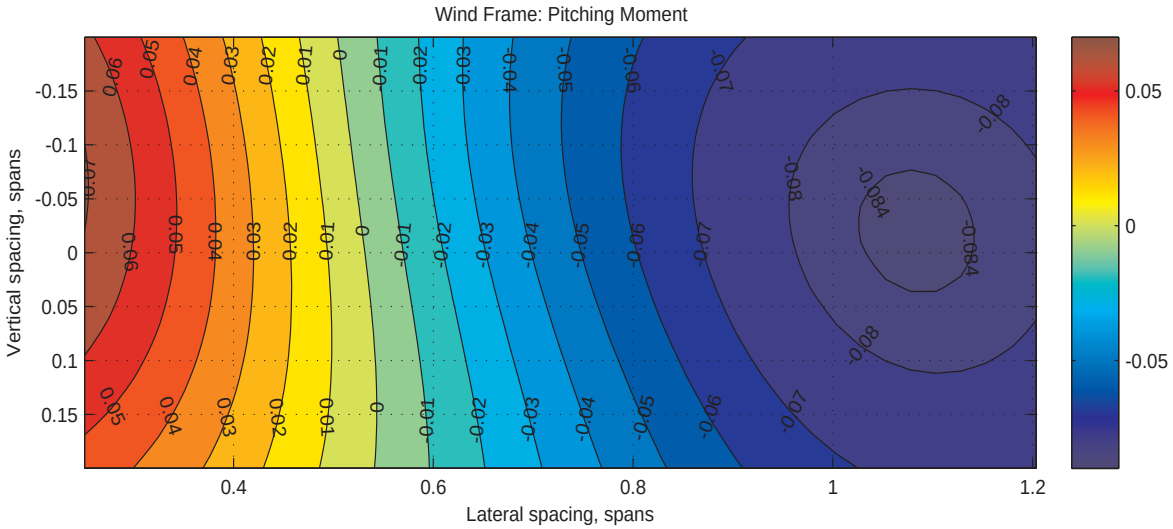

Figure 7.5. Aerodynamic Pitching Moment of Large KC-135R .

7.2.2 Small KC-135R Trail

The variation in lift-to-drag ratio increment for the small KC-135R trailing the nominal KC-135R is shown in Fig. 7.6. The largest increase in lift-to-drag ratio of 24.7 percent is obtained when the small KC-135R is placed 0.802 KC-135R wingspans laterally and 0.01 KC-135R wingspans above the lead KC-135R. Based on the static analysis, the lateral separation between the lead and the small KC-135R at the sweet spot, is smaller than that between the lead and the large KC-135R at its sweet spot.

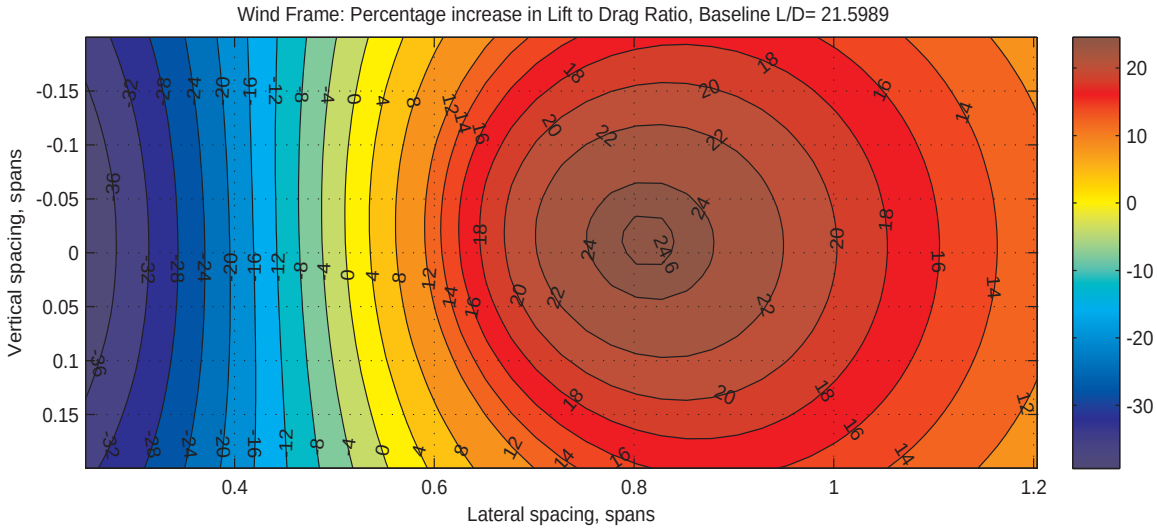

Figure 7.6. Percentage increase in Lift to Drag Ratio from Nominal Flight: Small KC-135R.

The rolling moment coefficient results are presented in Fig. 7.7, which looks similar to Fig. 7.3 except that the contour levels move laterally closer to the lead aircraft. For instance, the zero rolling moment coefficient line is shifted laterally closer to the lead KC-135R. This zero line signifies the location of zero induced aerodynamic rolling moment on the KC-135R and has been shown to be an indicator of the dynamic sweet spot location which is dependent on trimming.

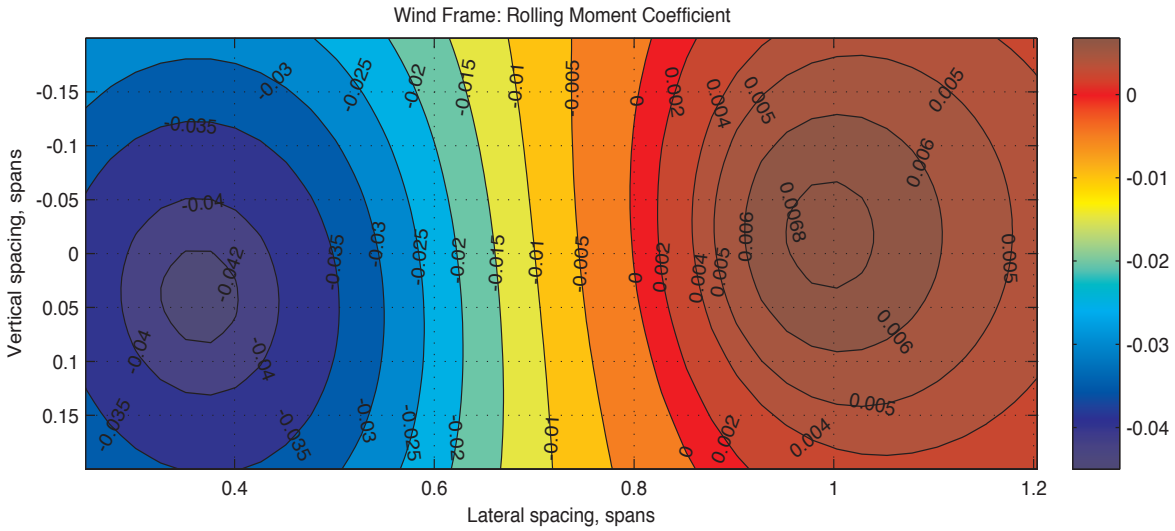

Figure 7.7. Aerodynamic Rolling Moment of Small KC-135R.

The small variant of the KC-135R aircraft behind the lead KC-135R has similar contour patterns of the aerodynamic force and moment coefficients as the large variant but with different locations in the grid. The magnitudes of the aerodynamic force and moment coefficients of the small KC-135R variant also differ from the large KC-135R at the same locations in the grid. Thus, only Figs. 7.6 and 7.7 are presented.

7.3 Dynamic Simulation Results

The dynamic results of the large KC-135R behind the lead are first presented, followed by the results of the small KC-135R trail.

7.3.1 Large KC-135R Trail

The dynamic simulation results of the large KC-135R trailing the lead KC-135R are presented in this section. Fig. 7.8 is a contour plot of the simulation stop parameter. It shows that less than 0.8 wingspans laterally, the simulation stop parameter is one because the controller could not trim the trail aircraft mostly due to

the saturation of the control variables. As a result of this, all contour plots generated from the results of the dynamic simulation exclude this area.

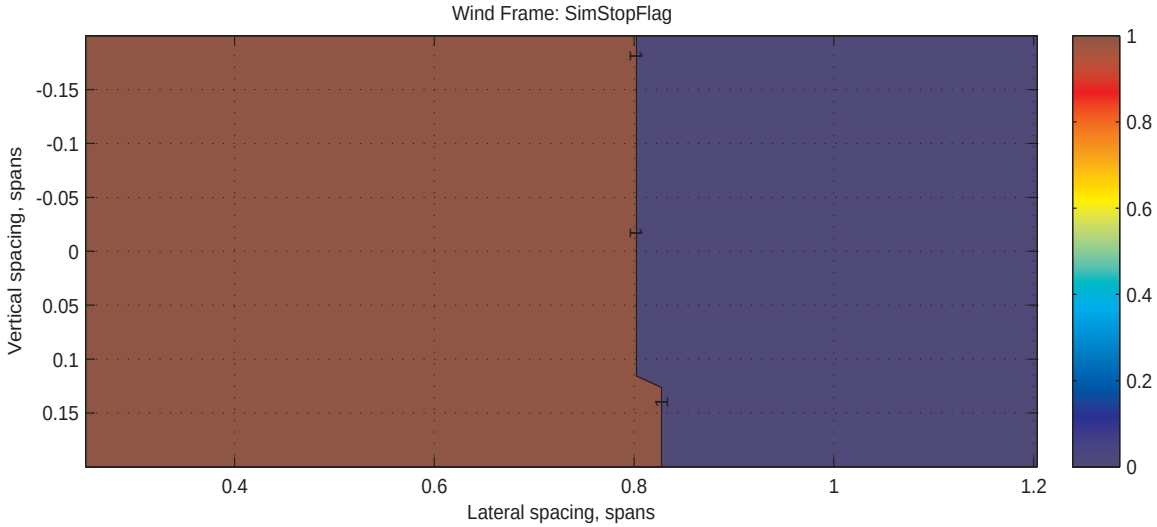

Figure 7.8. Simulation Stop Parameter of Large KC-135R.

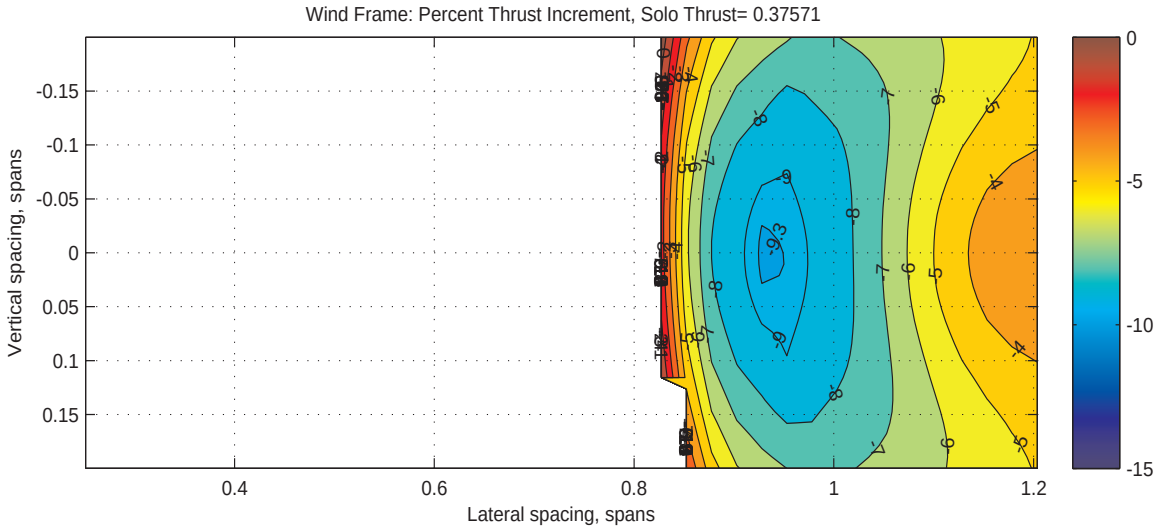

Figure 7.9. Percentage increase in Thrust from Nominal Flight: Large KC-135R.

A contour plot of the percentage thrust increment is presented in Fig. 4.11. The largest thrust reduction of over 9 percent, equivalently the least thrust required to fly in formation, is obtained in a vertical strip located 0.928 lateral wingspans relative to the lead KC-135R. This is the dynamic sweet spot for the large KC-135R to fly 3.8 wingspans behind the lead KC-135R. Furthermore, the elliptical shape of the thrust contours around the dynamic sweet spot shows that there is a lower slope along the vertical direction compared to the lateral direction. This means deviation from the sweet spot in the lateral direction results in higher reduction in formation benefit, in terms of thrust.

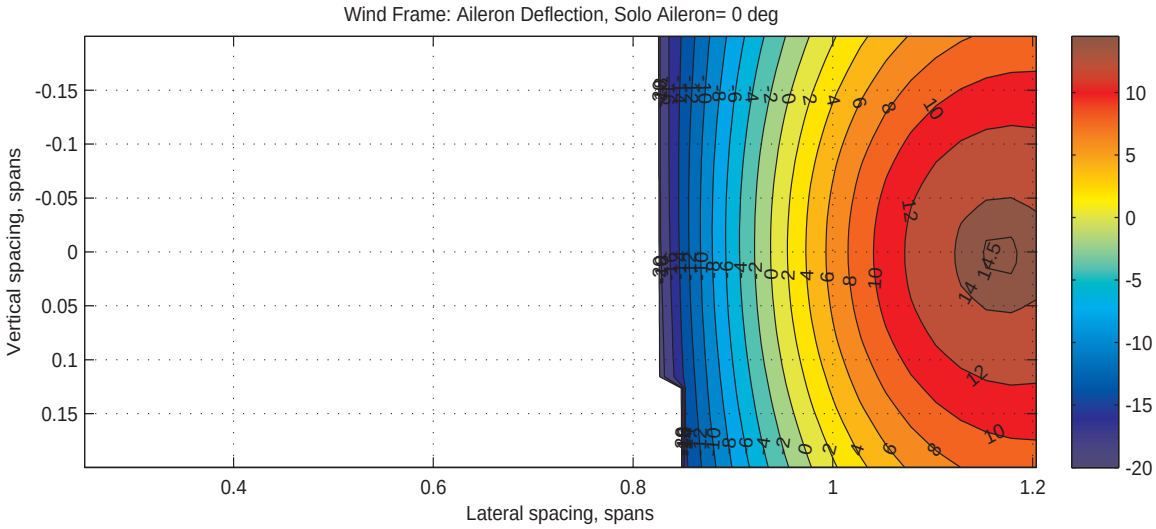

Figure 7.10. Aileron Deflection of Large KC-135R.

The aileron deflection is presented in Fig. 7.10. The magnitudes of the deflections of the aileron is seen to decrease as the dynamic sweet spot is approached from either the right or the left of 0.903 lateral wingspans. At the dynamic sweet spot, the aileron deflection is about -1.19 degrees. This is an increase in the deflection compared to that required for solo flight, which is zero degree. This is to be expected as

non-zero control effector deflections are required to trim the trail aircraft when it flies in formation. The elevator and rudder also experience an increase in deflection from solo flight to formation flight as seen in Figs. 7.11 and 7.12. Analyzing the trends of the control surface deflections as the trail aircraft moves away from the sweet spot towards the lead aircraft in the lateral direction shows that the aileron saturates first as compared to the elevator and rudder. This is consistent with the observation in the static case that the induced rolling moment is the highest. The spoilers could have provided additional roll authority to reduce the expanse in Fig. 7.8 in which the aircraft cannot be stabilized but the spoilers are not employed due to their adverse effect on the lift-to-drag ratio.

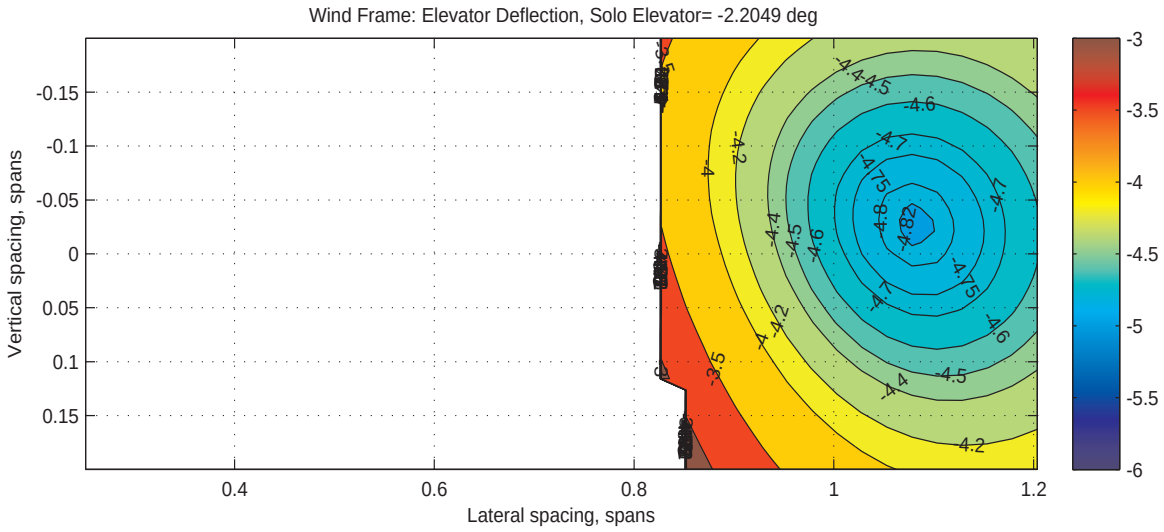

Figure 7.11. Elevator Deflection of Large KC-135R.

7.3.2 Small KC-135R Trail

The variation in thrust is shown in Fig. 7.13. The largest reduction in thrust of 13.95 percent is obtained when the small KC-135R is placed 0.802 KC-135R wingspans

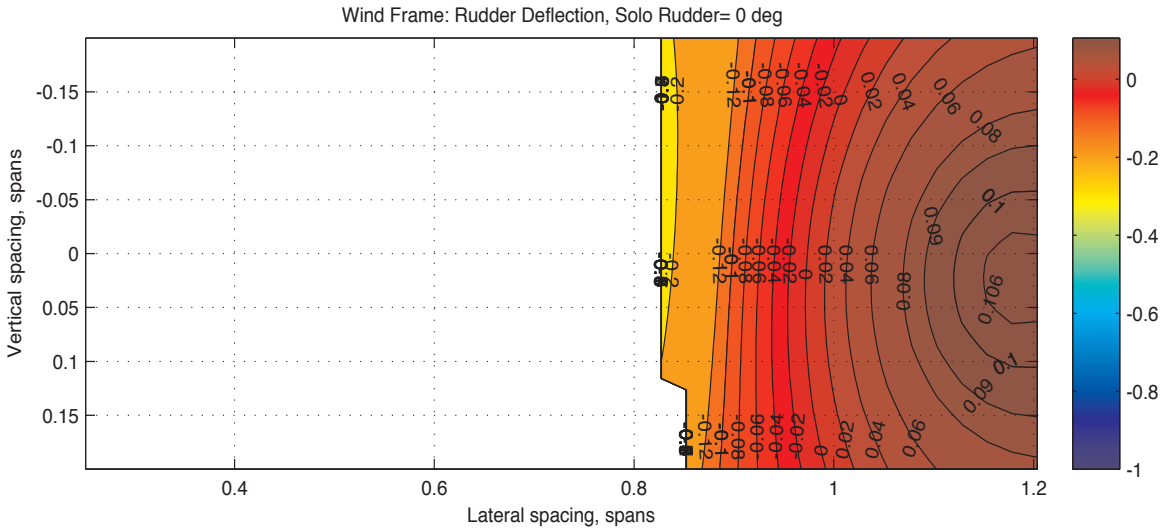

Figure 7.12. Rudder Deflection of Large KC-135R.

laterally and 0.01 wingspans below the lead KC-135R. The dynamic sweet spot of the small KC-135R is laterally closer to the lead aircraft than that of the large variant. The small KC-135R aircraft behind the leader KC-135R has similar contour patterns of the thrust and control surface deflections as the large variant but with different locations in the grid. The magnitudes of the thrust and control surface deflections of the small KC-135R variant also differ from the large KC-135R at the same locations in the grid. Since the control effector deflection contours for the small KC-135 are similar to the large, only the aileron deflections is presented in this Section as seen in Fig. 7.14. The location of least aileron deflection has also shifted laterally closer to the dynamic sweet spot.

7.4 Discussion and Comparison of Results with Prior EQ-II Variants

Table 7.2 summarizes the results of the static and dynamic simulations with regards to the location of the sweet spot and the aerodynamic force and moment coefficients. It presents the aerodynamic rolling, pitching, and yawing moment coeffi-

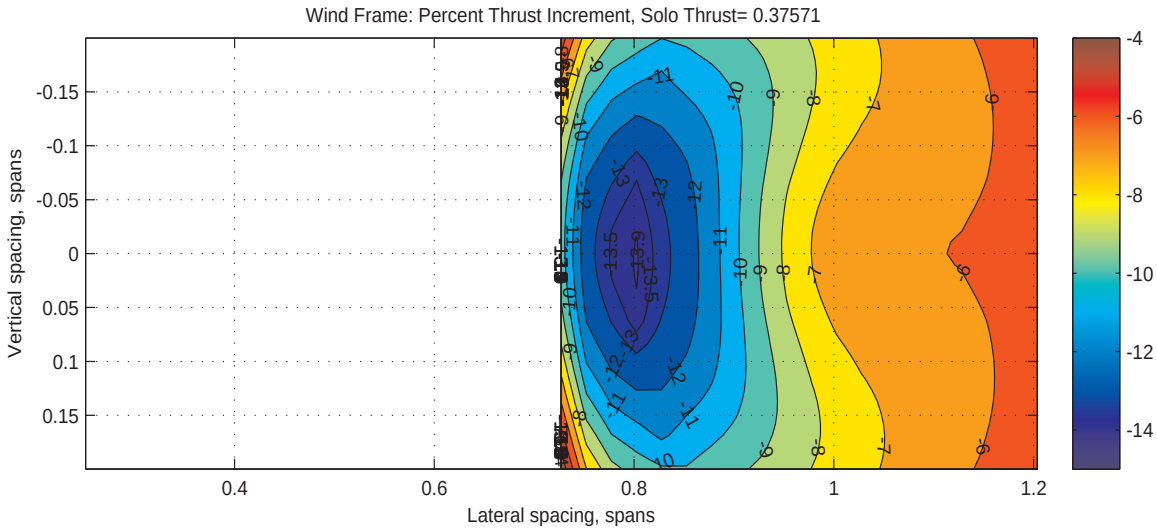

Figure 7.13. Percentage increase in Thrust from Nominal Flight: Small KC-135R.

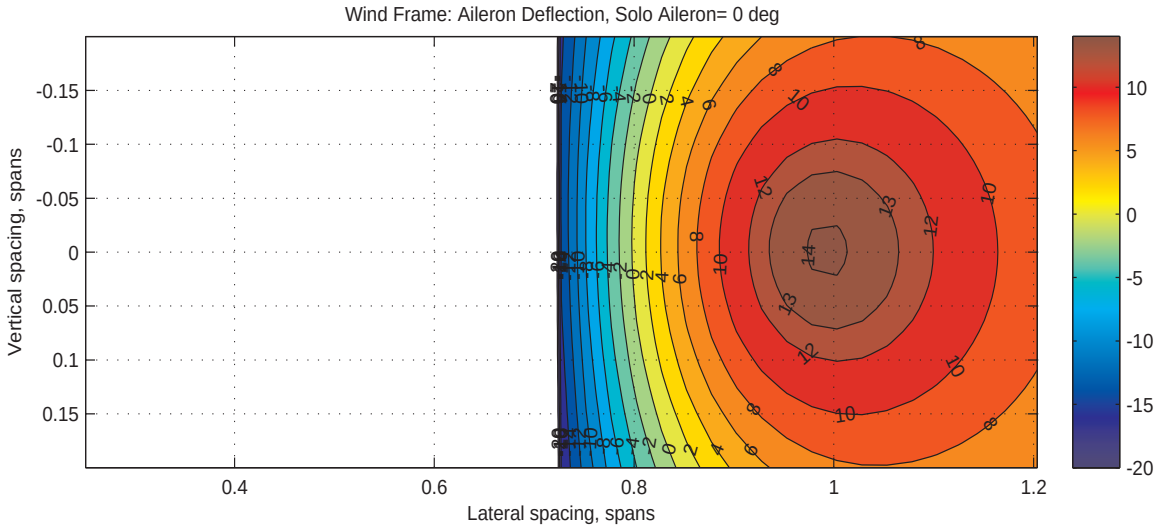

Figure 7.14. Aileron Deflection of Small KC-135R.

cients as $C_{\mathcal{L}}$, $C_{\mathcal{M}}$, $C_{\mathcal{N}}$ respectively at the static sweet spot, and the aileron, elevator, and rudder deflections as δ_a, δ_e, and δ_r respectively at the dynamic sweet spot. The incremental lift-to-drag ratio at the static sweet spot is tabulated under Δ L/D (%) while the reduction in thrust at the dynamic sweet spot is given by Δ Thrust (%). The sweet spot locations are given in terms of the separation of the C.G. of the trail

Table 7.2. Summary of Static and Dynamic Results for Scaled KC-135R

Static Simulation						
	Sweet Spot (Wingspans)					
Aircraft	C.G. to C.G.	Overlap (%)	Δ L/D (%)	$C_{\mathcal{L}}$	$C_{\mathcal{M}}$	$C_{\mathcal{N}}$
Large KC-135R	x=3.8 y=1.028 z=-0.01	9.69	16.41	0.005	-0.084	-1.3E-5
Small KC-135R	x=3.8 y=0.802 z= -0.01	13.34	24.73	4.1E-4	-0.097	-1.1E-4
Dynamic Simulation						
	Sweet Spot (Wingspans)					
Aircraft	C.G. to C.G.	Overlap (%)	Δ Thrust (%)	$\delta_a(^\circ)$	$\delta_e(^\circ)$	$\delta_r(^\circ)$
Large KC-135R	x=3.8 y=0.928 z=0	20.95	9.37	-1.185	-4.301	-0.057
Small KC-135R	x=3.8 y=0.802 z=0	13.34	13.94	0.738	-5.516	-0.039

and lead KC-135R aircraft. The locations of the sweet spots are also presented in terms of wing tip overlap as a percentage of the geometric mean of the wingspans of the two aircraft in formation.

Figure 7.15 presents the static sweet spot, dynamic sweet spot band, and the zero roll moment curves for the small and large trailing KC-135R. For the large KC-135R trail, the dynamic sweet spot is located significantly laterally closer to the lead than the static sweet spot is. The dynamic simulations account for the trimming of the aircraft with deflections of the control surfaces. Figs. 7.10 - 7.12 show that aileron, elevator, and rudder deflections are needed for trimming the aircraft at the static sweet spot. Figs. 7.10 and 7.12 show that little aileron and rudder deflections

are needed to trim the aircraft in the dynamic sweet spot band which is located over the zero aileron (rudder) isolines as seen in Fig. 7.15. This explains the mechanisms that move the dynamic sweet spot away from the static sweet spot. In the case of the small KC-135R trail, the zero aileron (rudder) isolines are close to the static sweet spot. Thus, little difference is seen between the locations of the static and dynamic sweet spots. These results are similar to the large and small variant of the EQ-II

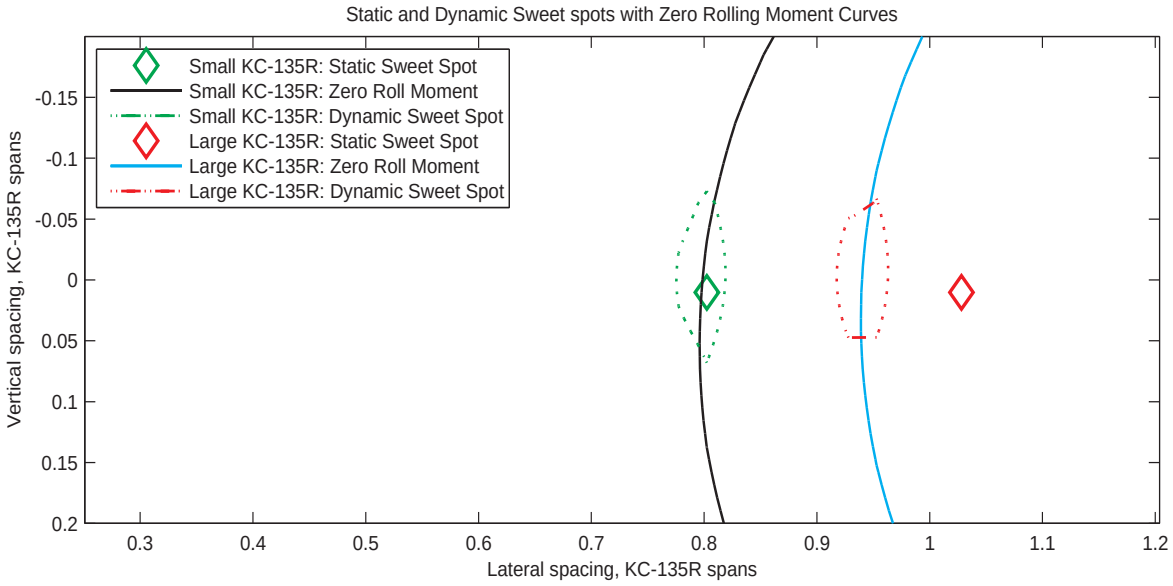

Figure 7.15. Static and Dynamic Sweet Spots for Scaled KC-135R showing Zero Roll Moment Curves.

aircraft trailing the KC-135R. In those cases the static and dynamic sweet spots were seen to almost coincide for the small variant of the EQ-II as previously discussed. For the large variant, the static and dynamic sweet spot had a lateral relative separation of about 0.1 KC-135R wingspans.

The results presented in this chapter have shown that this variation in static and dynamic sweet spot is an artifact of the relative sizes of the aircraft in the formation

and not the type/configuration of the aircraft. Whether an unconventional delta-wing aircraft or a conventional airplane with a fuselage and tail is utilized in the formation, if the trail aircraft size is at least as large as the lead, there is a significant difference in the location of the static and dynamic sweet spots.

CHAPTER 8

FORMATION FLIGHT OF EXTENDED DURATION

During long flights, the mass of airplanes flying in formation will decrease as they burn fuel. As a result of the reduced weight of the lead aircraft, the strength of the wake vortices the lead generates, and thus the magnitude of the non-uniform wind field the trail aircraft experiences, will decrease since vortex strength is proportional to the lift generated. This means the trail aircraft will experience smaller upwash at the sweet spot, which reduces the overall benefit of formation flight. Thus, it is important to determine the actual benefit of formation flight by evaluating the vortex effect in a long endurance flight. A pair of KC-135R aircraft is considered flying this mission in formation. The KC-135R aircraft is similar to the C-17 aircraft which the Air Force Research Laboratory utilized in recent formation flight tests as part of the Surfing Aircraft Vortices for Energy ($\$AVE$) program [43, 81, 82].

The $AVE program first demonstrated the formation flight savings by conducting flight tests in which the trail aircraft flew at a variety of lateral and vertical positions relative to the sweet spot. The dwell time at each position, where fuel flow and other data was gathered, was either five or thirty minutes in duration. Typical C-17 missions are about seven hours long. Twenty percent of missions are longer than nine hours. The $AVE tests were conducted in a condition of no or low atmospheric turbulence. Preliminary analyses of the tests showed a reduction of fuel consumption of up to ten percent on the trail C-17 while flying about 4000 feet behind the lead C-17. Subsequent flight testing was done with an actual operational mission from Edwards Air Force Base, California to Joint Base Pearl Harbor-Hickam, Hawaii and

back [43]. The significant fuel savings obtained in the flight test demonstrate the benefit of flying long endurance missions in formation.

Based on recent United States Air Force long endurance missions identified as potential formation flights, a representative long flight mission is defined. This representative flight lasts 6.5 hours and is chosen to represent a transatlantic flight from Europe to the United States.

8.1 Simulation Modification

To extend the current simulation environment for the lead and trail KC-135R to represent an actual long-duration formation simulation, some modifications are made to reflect the variations in the weight and inertia of the two aircraft with time. For both the lead and trail aircraft, the total fuel burn rate is computed from the thrust generated/required by the engines. In the trail aircraft, this total fuel burn rate, $\dot{m}_T$, is passed as an input to the fuel subsystem where it is assigned as the fuel flow rate out of the fuel tanks. Depending on the fuel tank usage schedule, one or more fuel tanks may be used at a time. In the case of one fuel tank being used, the total fuel burn rate is assigned as the fuel flow rate out of that tank while the other tanks have fuel flow rates set to zero. As an example, if fuel tank 9 alone is used, the fuel flow rates are

$$\dot{m}_j = \begin{cases} \dot{m}_T, & for\ j = 9 \\ 0, & for\ j = 1:8 \end{cases} \tag{8.1}$$

When multiple tanks are used at a time, the total fuel burn rate is split evenly by the number of tanks used. For instance, if tanks 2, 3, 5, and 6 are used at the same time, the fuel flow rates out of the tanks are

$$\dot{m}_j = \begin{cases} \frac{1}{4}\,\dot{m}_T, & for\ j = 2,3,5,6 \\ 0, & for\ j = 1,4,7,8,9 \end{cases} \tag{8.2}$$

Since the equations of motion of the trail aircraft model the dynamic effects during fuel transfer as shown in Chapter 2.4.1, the mass and inertia properties correspondingly change to reflect the effect of the fuel consumption.

The lead KC-135R does not have the details of the fuel tanks built in. Thus, the fuel burn rate computed from the thrust cannot be passed to a fuel subsystem. Instead, the fuel burn rate is integrated over time to obtain the amount of fuel burned by the lead KC-135R. At each time step, the mass, m_c, is then derived by subtracting the amount of fuel burned, m_f, from the mass of the lead aircraft at the beginning of the simulation, m_i.

$$m_c(t) = m_i - m_f(t) \tag{8.3}$$

Thus, the lead aircraft has a mass, m_c which varies with time. The ratio of the current mass to the initial mass, m_{ratio} is used to vary the inertia matrix as well in an effort to capture the dynamic effect of the fuel burn on the inertia of the aircraft.

$$\mathbf{I}_c(t) = m_{ratio}(t)\ \mathbf{I}_i \tag{8.4}$$

where $\mathbf{I}_c$ is the time-varying inertia matrix for the lead aircraft and $\mathbf{I}_i$ is the inertia matrix of the lead aircraft at the beginning of the simulation.

8.2 Full Mission Set-Up

For the trail KC-135R, the fuel usages from the fuel tanks implemented in the simulation are representative of recommended fuel usage schedule for the KC-135R.

The commanded fuel usage for the KC-135R, from take-off to landing, is scheduled to be used in a manner that prevents a significant shift in the C.G. during flight. The fuel tanks used in any flight depend on the schedule and length of the mission the aircraft is flying. For extremely long-duration missions, all fuel tanks may be used. Fig. 8.1 shows the locations of the fuel tanks as well as the numbering scheme used in this dissertation.

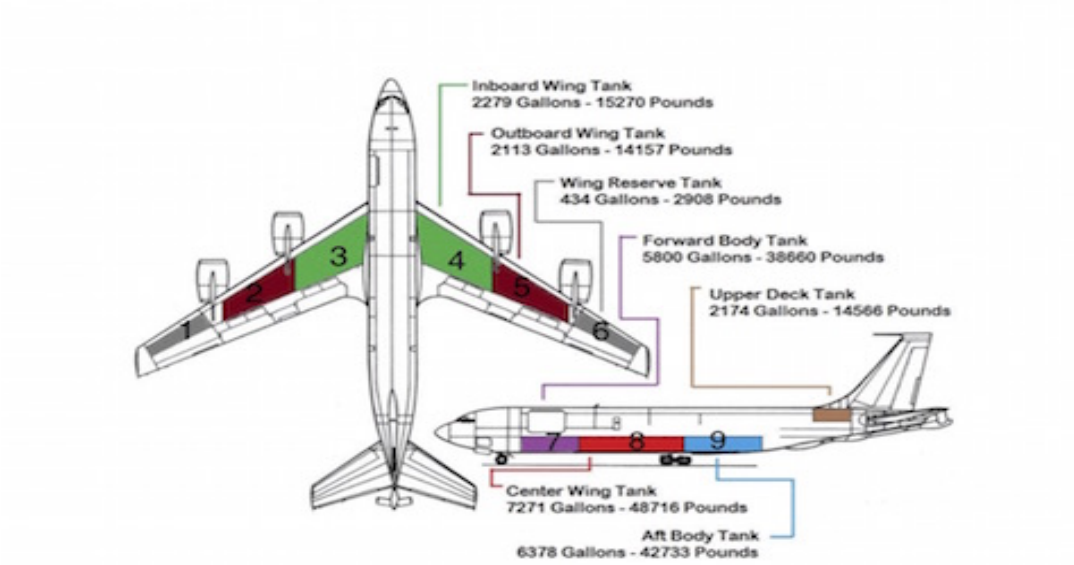

Figure 8.1. Fuel Tank Numbering for Trail KC-135R[83].

Based on the schedule and length of the chosen 6.5-hour mission, the fuel tanks used are the center wing and the aft body tanks only. These correspond to tanks 8 and 9 in Fig. 8.1. The formation simulations of extended duration start out with all fuel tanks full except for the center wing tank which is used during climb. To illustrate the fuel flow usage based on the schedule, Fig. 8.2 is presented. Fig. 8.2 shows the amounts of fuel and the rate of fuel flow out of each individual tank of the trail KC-135R as it flies for 6.5 hours in formation with the lead. In this illustrative

case, the fuel usage is commanded between the center wing and aft body tanks, 8 and 9, with the switch triggered by the amount of fuel remaining in the tank. For instance, per the commanded fuel tank schedule usage after climb, the aft tank is used till a certain amount is left. Then the fuel flow rate out of the aft tank is set to zero while the center tank begins to output the fuel flow required by the engines. After a certain amount of fuel in the center tank is depleted, the aft tank is then used. This switch continues per the fuel tank schedule usage. All fuel tanks remain full for this mission except for the center wing and aft body tanks which are used alternatively throughout the simulation.

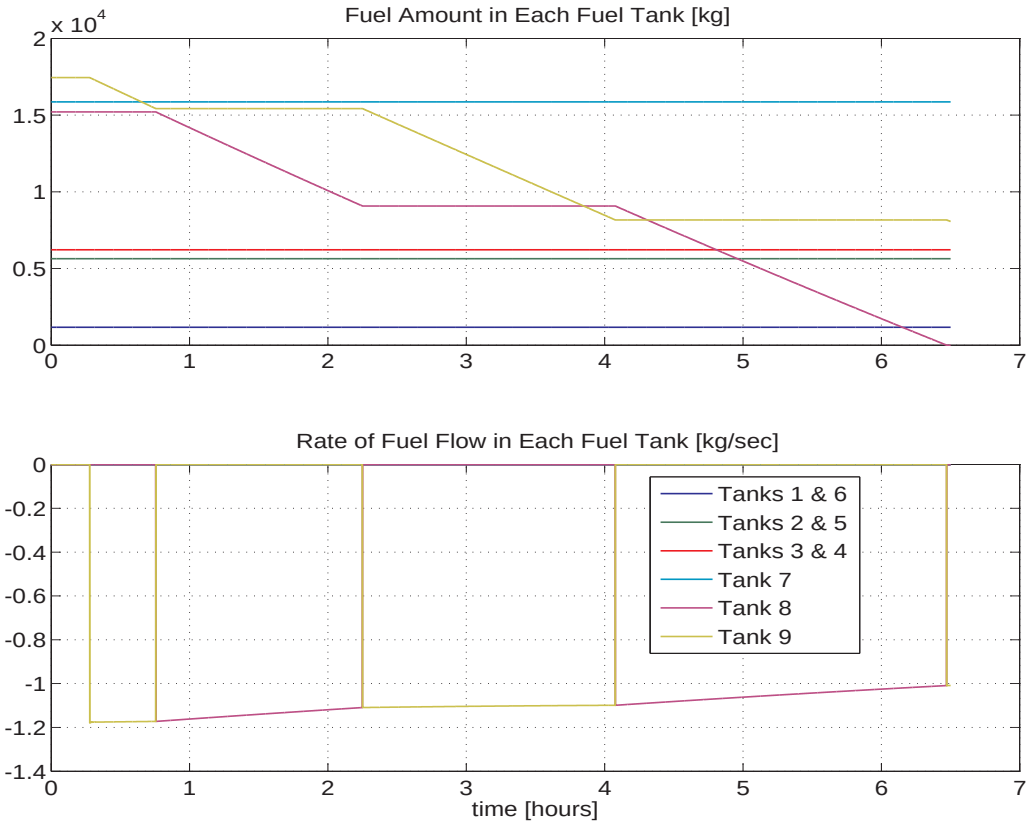

Figure 8.2. Fuel Flow and Amount in Each Tank for Trail KC-135R.

The weight of the lead aircraft is set to match that of the trail at the beginning of the simulation. For both lead and trail, the masses are held constant for the first few minutes till steady state is reached as the controller works to adjust the control variables of the aircraft to the flight configuration. This is an artifact of the simulation and will not occur in an actual flight. After the transient is over, the masses of the lead and trail aircraft are set to decrease with fuel consumption. As the weight of the lead aircraft decreases, the lift reduces correspondingly. Fig. 8.3 depicts time histories of the wing-body and tail lift coefficients of the lead KC-135R as it burns fuel and loses mass. For the first few minutes, there is no change in the lift as the mass is held constant, after which there is a steady continuous decrease in lift with fuel burn.

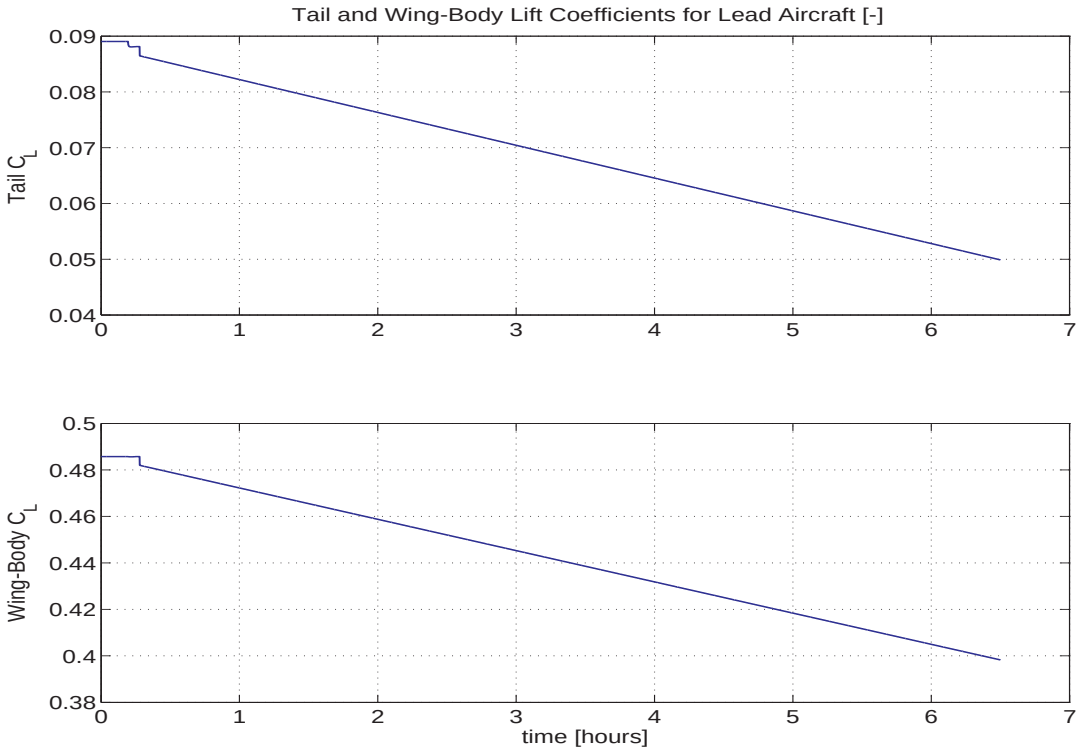

Figure 8.3. Lift Coefficients for Lead KC-135R.

As a result of the reduction in the weight of the lead aircraft, there is a variation in the non-uniform wind which the trail aircraft is subjected to. The translational and rotational wind components induced on the trail KC-135R as it flies in an extended-duration formation with the lead KC-135R, are presented in Fig. 8.4.

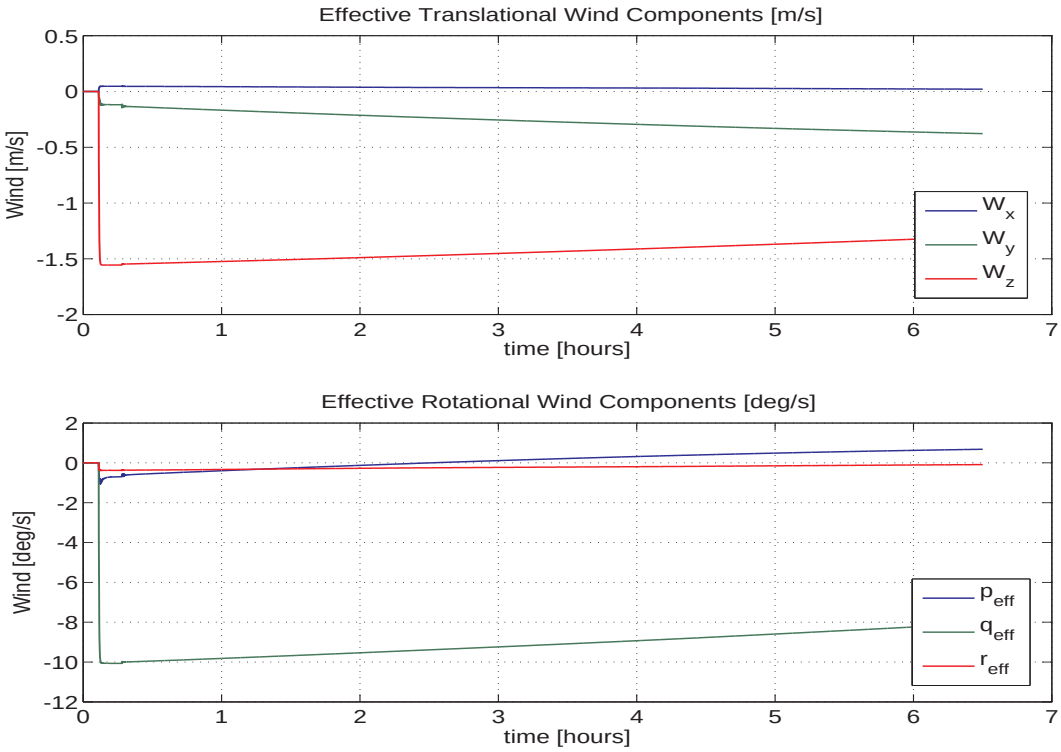

Figure 8.4. Induced Wind Components on Trail KC-135R.

For the formations of long duration, the trail aircraft is placed at the dynamic sweet spot which is close to the static sweet spot for the pair of KC-135R in formation. The dynamic sweet spot for the trail KC-135R was seen in Chapter 6 to move with a 26% decrease in the weight of the lead aircraft. With a shift in the dynamic sweet spot during this formation of extended duration, the position of the trail with respect to the lead aircraft should change based on the location of the dynamic sweet spot. Beginning with the starting weight of the lead aircraft, the weight of the

lead every two hours as it burns fuel is obtained for a theoretical eight-hour flight with fuel burned at a constant rate. This yields five different weight configurations: the starting weight and the weights at four two-hour increments. The trail and lead aircraft weights are set to equal these five weights and the dynamic sweet spot analysis is carried out. It was seen that for the first four weights representing a six-hour flight, the dynamic sweet spot remains the same. When the fifth weight configuration was run, the dynamic sweet spot moved. This implies that for the first six hours in which the percentage reduction in the aircraft weight from the starting weight is 16.7 %, the dynamic sweet spot remains constant. After eight hours, when the weight has decreased by 22.2%, the dynamic sweet spot changes. The representative mission chosen lasts 6.5 hours. Thus, the relative position for the trail aircraft can be maintained at the dynamic sweet spot which does not move for the simulation duration.

The extended-duration simulations are first run with no atmospheric turbulence on the lead or trail aircraft as the trail KC-135R flies at the dynamic sweet spot (i) solo and (ii) in formation with the lead. These results are given in Section 8.3. Turbulence is then introduced for both the lead and trail aircraft and the solo and formation comparisons are done and presented in Section 8.4. This is done to study the effect on the fuel savings when the trail aircraft deviates from the sweet spot due atmospheric effects such as turbulence. Section 8.5 analyzes the effect of turbulence on the benefits of formation by comparing the turbulent formation case with the turbulence-free formation case.

8.3 Comparisons without Atmospheric Turbulence

The 6.5 hour formation simulation is first run with the non-uniform wind from the lead aircraft switched off to simulate a solo flight. Then, the simulation is run

with the non-uniform wind from the lead aircraft on to simulate a formation. The fuel burn rate for the trail KC-135R is recorded for the two cases and plotted in Fig. 8.5. Fig. 8.5 shows that at all times, the fuel flow rate in formation is less than that in solo flight. The difference in the fuel flow rate between the two cases, is larger immediately after the transient than at the end of the simulation. Essentially, the fuel flow rate in formation gets closer to that in solo flight as time goes by and the magnitude of the initial benefit observed is not sustained throughout the flight. These results are in agreement with the statement at the beginning of this chapter that the upwash effect will decrease in magnitude as lead aircraft weight decreases due to fuel burn.

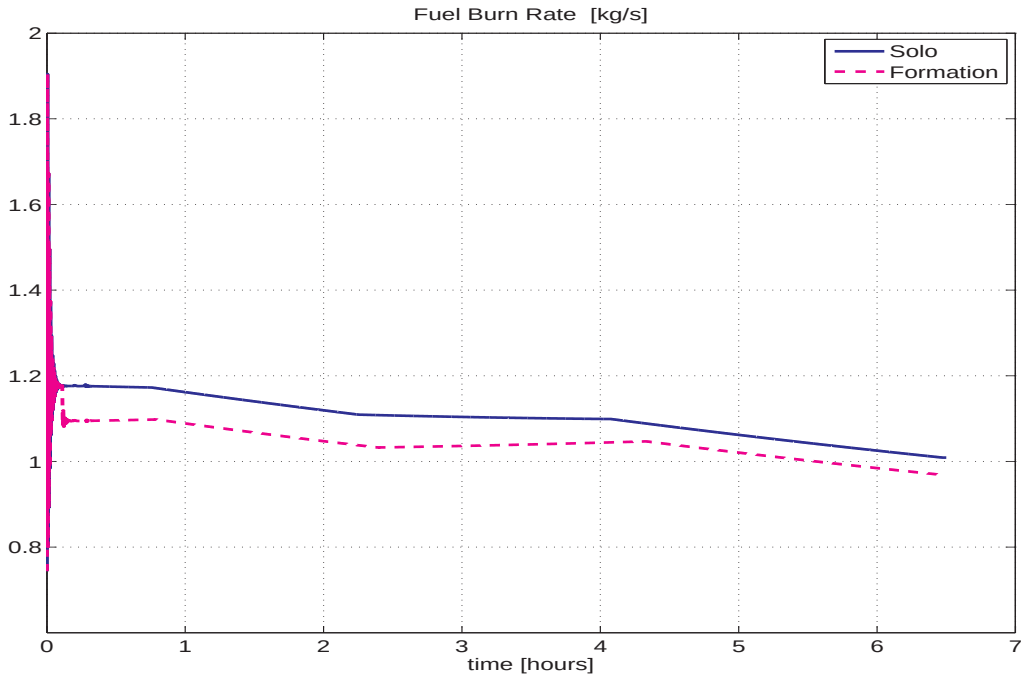

Figure 8.5. Fuel Burn Rate for Trail KC-135R.

Fig. 8.5 also shows instantaneous changes in the fuel flow rate at different times. This can be explained by looking at the fuel flow rates as scheduled by fuel tanks.

Using the commanded fuel tank schedule for the trail KC-135R requires switching between fuel tanks. This switch from one fuel tank to another, is instantaneous as seen in Fig. 8.2 which shows the amounts and fuel flow rate out of each tank. At any instant, either tank 8 or 9 provides the total fuel flow needed by each engine while the other fuel tanks have zero fuel flow rate and thus maintain their initial fuel amounts as seen in Fig. 8.2.

The actual amount of fuel burned is obtained by subtracting the mass of the trail aircraft, at each point in time, from the initial mass. For the solo and formation cases, the fuel amount is depicted in Fig. 8.6. The difference in fuel amounts between the two cases is also plotted as function of time in Fig. 8.6. Fig. 8.6 shows that there is a reduction in the slope of fuel saved with time, implying that less fuel is saved as time goes on. This is a direct consequence of the weight reduction of the lead aircraft due to fuel burn in comparison to that of the trail. Overall, fuel savings are obtained for the entirety of the simulation run.

8.4 Comparisons in the Presence of Atmospheric Turbulence

This section investigates the effect of atmospheric turbulence on the long-duration solo and formation simulations. Light turbulence with intensity of 0.39 m/s and length scale of 533.4 m in the x, y, and z directions was introduced on the lead and trail aircraft for the formation simulation, and for the trail alone for the solo simulation run. The atmospheric disturbance lasts from 14 minutes into the simulation till the end of the 6.5 hour simulation run. For the formation case, the trail aircraft is first subjected to only the non-uniform wind induced by the lead aircraft, after which it is subjected to a combination of the stochastic turbulence and the deterministic non-uniform wind induced from the lead aircraft. The translational and rotational wind components of this wind combination are depicted in Fig. 8.7.

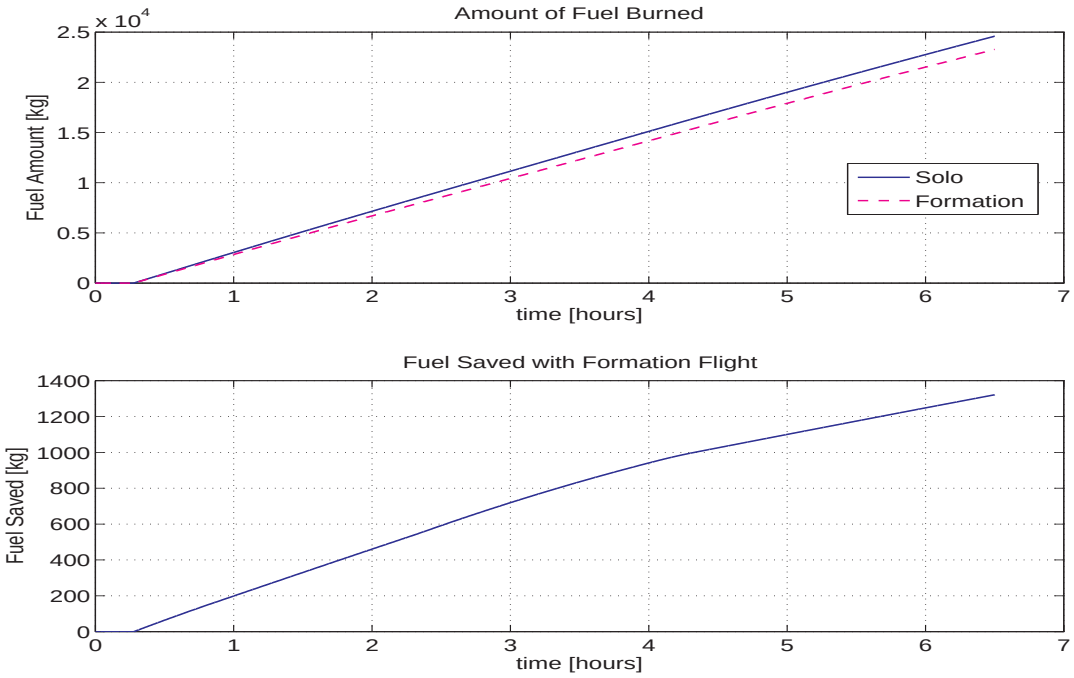

Figure 8.6. Fuel Saved for Trail KC-135R.

In the simulated flights, the trail aircraft position oscillates around the desired position due to the effect of atmospheric turbulence. This oscillation is captured in Fig. 8.8 which shows the commanded and actual positions for the trail aircraft in the x, y, and z directions. Fig. 8.8 shows that of the three co-ordinate directions, the longitudinal position has the largest deviations from the commanded position of 3.8 wingspans behind the lead. In the y direction, the largest deviation from the commanded position is about 1 m, corresponding to approximately 0.025 KC-135R wingspans. In the z direction, the maximum deviation of 0.55 m (0.014 KC-135R wingspans) is even smaller than in the y direction. Since variations in the longitudinal direction are assumed to have no effect on the formation benefits for up to 10 wingspans behind the lead, as discussed in Chapter 1, excursions from the commanded position in the x direction are acceptable for the purpose of this study. In the lateral and vertical directions, the magnitudes of the excursions from the

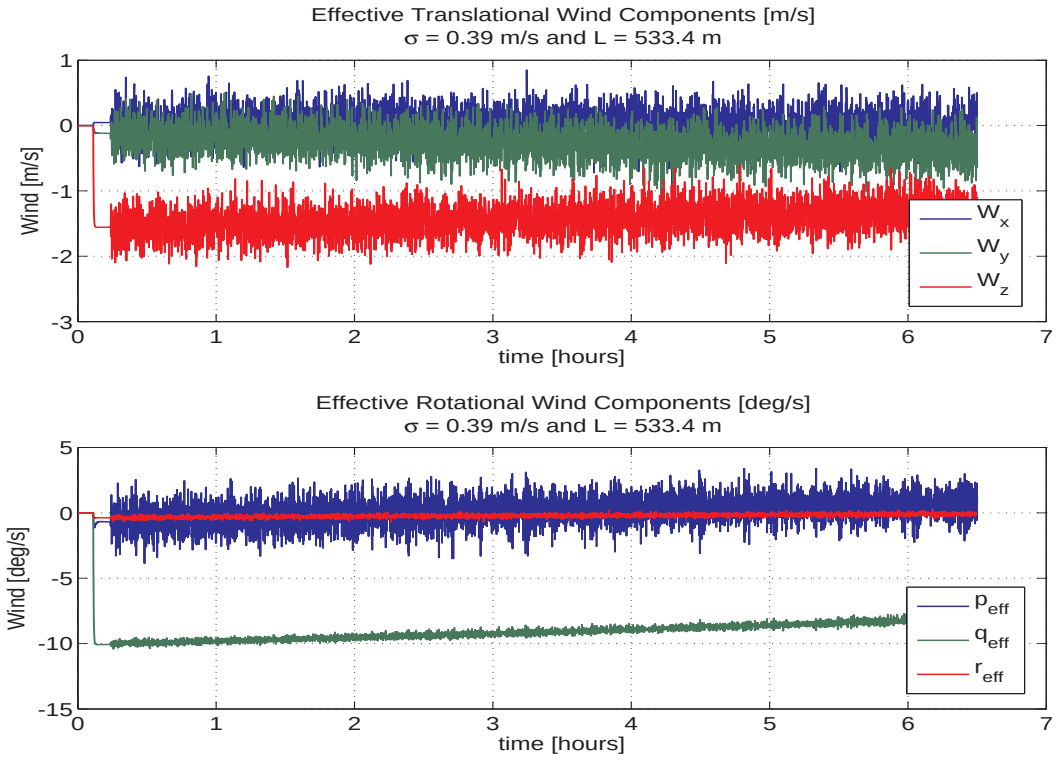

Figure 8.7. Induced Wind Components with Turbulence on Trail KC-135R.

commanded positions are small enough to keep the trail aircraft at the sweet spot to obtain the fuel-saving benefits.

The fuel flow rate for the trail aircraft in turbulent solo flight and in turbulent formation flight are presented in Fig. 8.9. Although the effects of the turbulence on the fuel flow rates is visible in Fig. 8.9, the fuel consumption is larger for the solo case than for the formation case. Thus, even with such adverse atmospheric conditions that cause excursions of the trail aircraft from the sweet spot, there is still a benefit of flying the trail KC-135R in formation in the region of the sweet spot behind the lead KC-135R. As in Section 8.3, this benefit is quantified and plotted in Fig. 8.10.

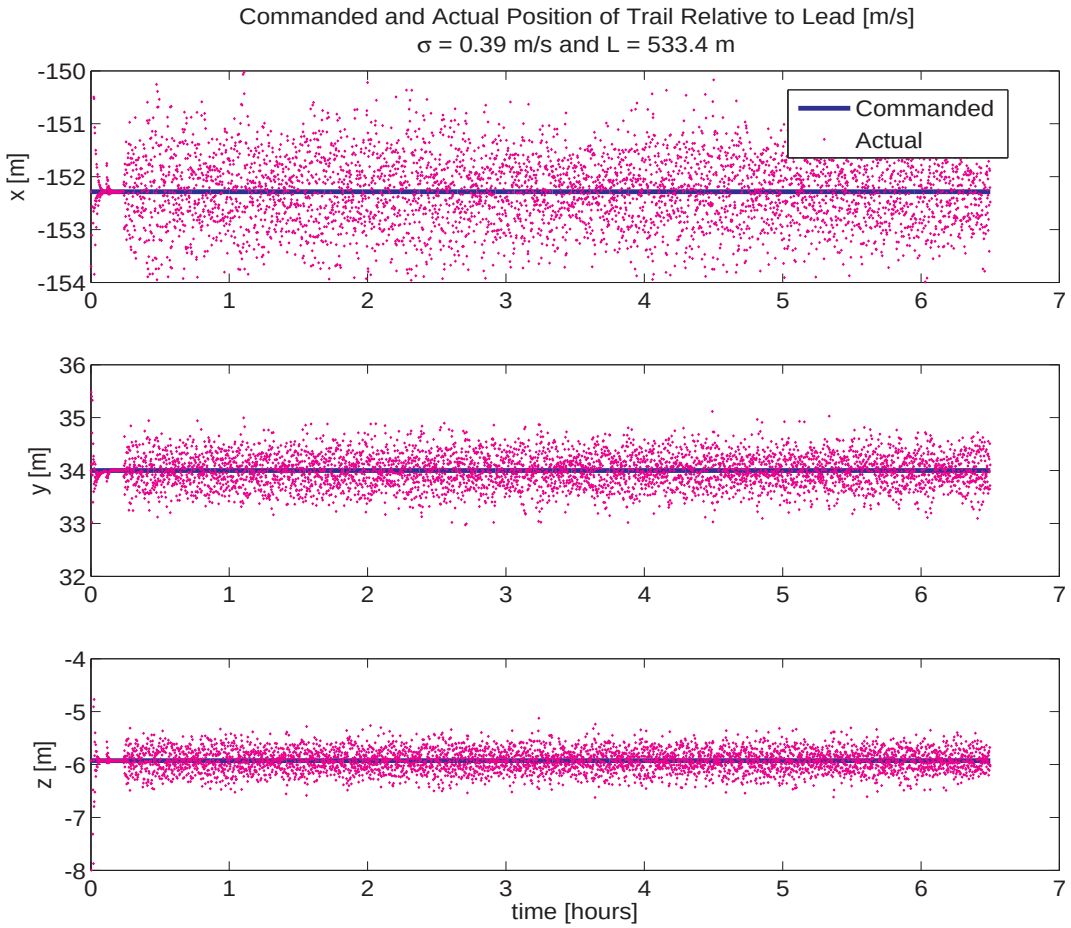

Figure 8.8. Commanded and Actual Positions of Trail KC-135R in Turbulent Formation.

8.5 Impact of Turbulence on the Formation Benefits

Sections 8.3 and 8.4 showed the benefits of formation flight on the trail aircraft as it flies without and with atmospheric turbulence respectively. This section compares flying in formation with and without turbulence to investigate the impact of the light turbulence on the formation benefits. Fig. 8.11 presents the amount of fuel saved over time as the trail aircraft flies in formation with turbulence-free and turbulent conditions.

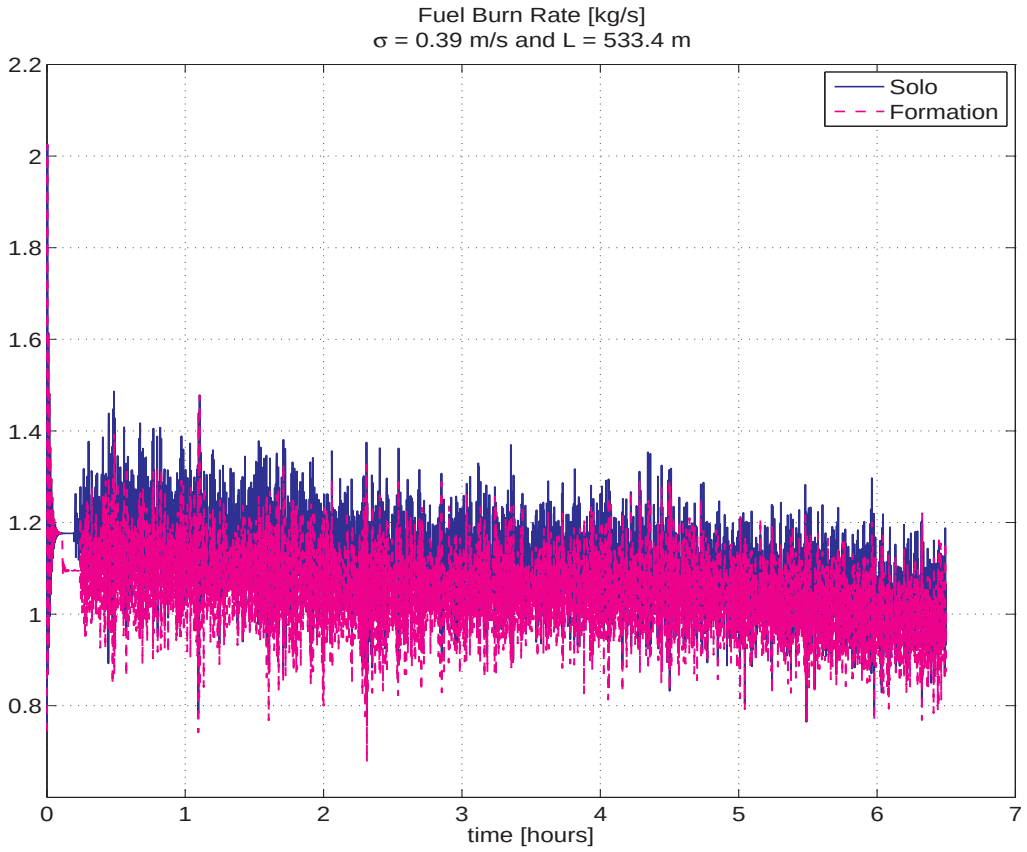

Figure 8.9. Turbulent Fuel Burn Rate for Trail KC-135R.

The amount of fuel burned in turbulent formation is slightly larger than that burned in turbulence-free conditions. At the end of the simulations, the turbulent case uses 150 kg more fuel than the turbulence-free case. Compared to the total amount of fuel burned, this is a relatively small number. The trajectory-tracking controller is able to maintain the commanded position well enough that the benefits of flying in formation are comparable in turbulent and turbulence-free atmospheric conditions. The fact that only 150 kg more fuel is used in turbulent formation also goes to show that significant benefit of formation is still obtained as long as the trail aircraft is able to maintain the sweet spot behind the lead.

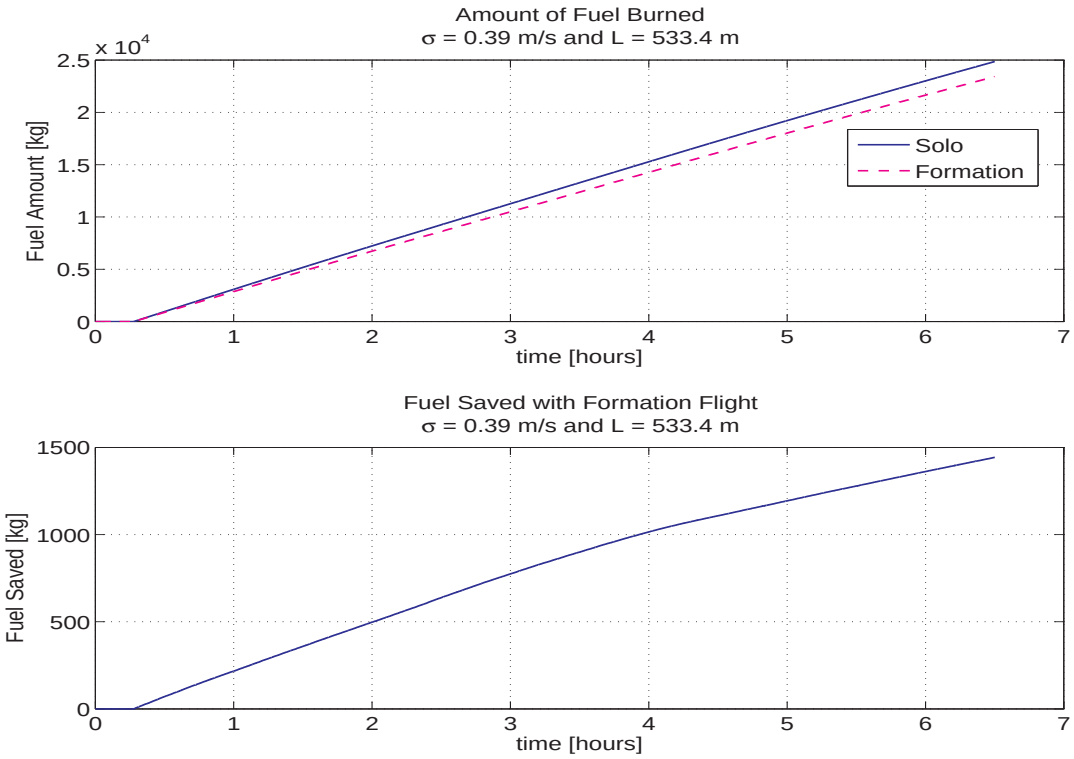

Figure 8.10. Fuel Saved for Trail KC-135R in Turbulent Flight.

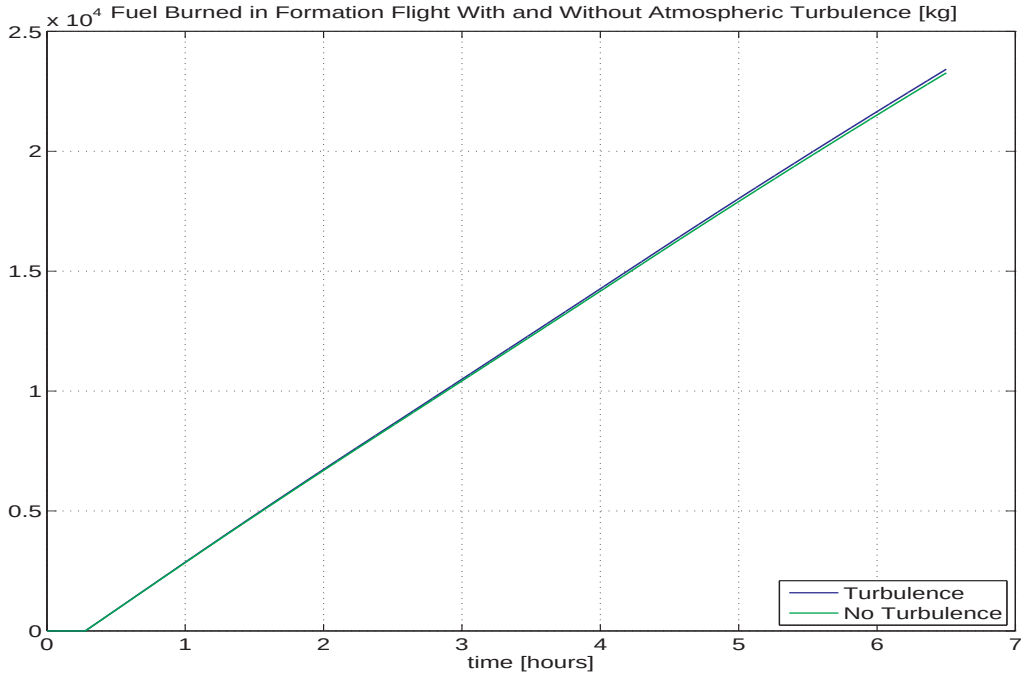

Figure 8.11. Fuel Burned by Trail KC-135R in Turbulent and Turbulence-Free Flight.

CHAPTER 9

RIDE QUALITY ANALYSIS

The details of the ride quality (comfort levels) for passengers/aircrew seated within the trail aircraft are presented in this chapter. Different assessments of the ride quality are done for simulations of two different trailing aircraft behind a lead KC-135R (1) the KC-135R trail and (2) the large EQ-II trail. For the trail KC-135R, the non-uniform wind field induced from the lead KC-135R is turned on or off to simulate a formation flight with or without the aerodynamic/fuel-saving benefits of flying in formation respectively. In addition, for the trail KC-135R, accelerations at the origin of the body frame are studied using atmospheric turbulence of different intensities. The origin of the body frame, placed at the center of mass of the empty trail aircraft, is denoted CM_E in this chapter. Accelerations offset from the CM_E of the KC-135R are also analyzed as the KC-135R flies with the non-uniform wind field induced from the lead KC-135R turned on. For the large EQ-II aircraft, the ride quality study is done using the accelerations at the cockpit as the EQ-II flies with the wake on at the (i) dynamic sweet spot and (ii) static sweet spot. This analysis differs from that of the trail KC-135R because (i) the intent is to make an additional qualitative comparison, in terms of ride quality, between the static and dynamic sweet spots which differ for the large EQ-II, and (ii) the EQ-II aircraft configuration restricts passenger/aircrew locations of interest to the cockpit alone. The details of these analyses are presented in subsequent sections.

In this chapter, flying the trail aircraft in formation with the non-uniform wind field induced by the lead turned on will be referred to as "wake on" and with the

non-uniform wind turned off is referred to as "wake off" for brevity. Furthermore, flying the trail aircraft with the wake off does not constitute a solo (non-formation) flight. Although there may be no aerodynamic effect from the lead on the trail, the controller of the trail aircraft is a trajectory-tracking controller designed to maintain a position/trajectory relative to the lead. Thus, by the nature of the control design/set-up, all ride quality analyses are done with cases which simulate formation flight for the trail aircraft with the lead's wake on or off.

9.1 Methods

9.1.1 Evaluating Comfort Levels using ISO Standards

The International Organization for Standardization outlines a guide, ISO 2631, for evaluating vibrations transmitted to the human body from supporting surfaces such as the feet, buttocks, and back of an individual as he stands, sits, or reclines in a vibrating vehicle or building. The vibrations may be periodic, random, or non-periodic but are limited to a frequency range of 0.1 to 80 Hz for the assessment of comfort levels [38]. The direction of vibrations correspond to an orthogonal axis system as depicted in Fig. 9.1 for a person sitting, standing, or laying down.

Translational and rotational accelerations are the primary metric used to describe the magnitude/intensity of the vibrations and are the quantities used in evaluating the comfort levels using the ISO standards. These accelerations should be expressed in meters per second squared and radians per second squared for the translational and rotational components, respectively. Before employing the outlined guide limits, a spectral density analysis of the accelerations should be done within the ISO 2631 frequency range of 0.1 to 80 Hz. The frequency range can be divided into unequal segments known as octaves. Each octave can be further divided into three separate

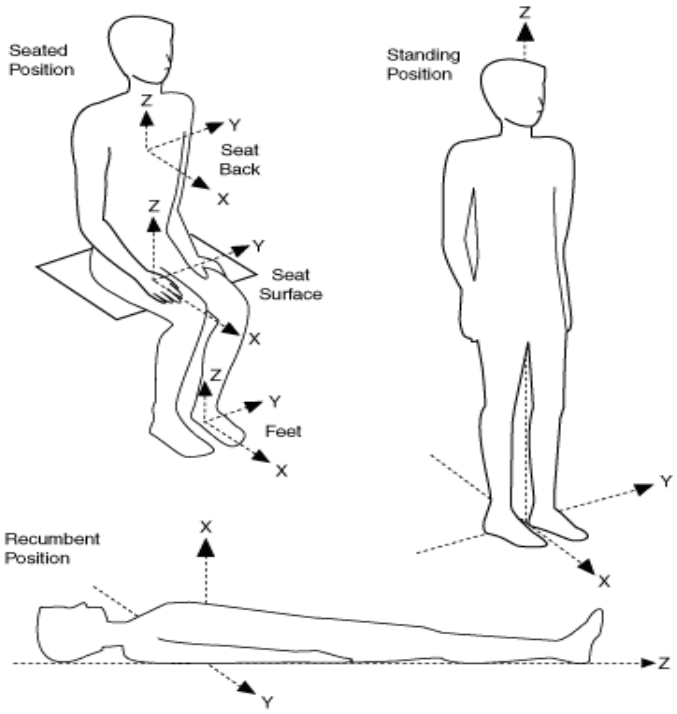

Figure 9.1. Axis System for ISO 2631 [38].

segments or one-third octave bands with a lower band limit, a center frequency, and an upper band limit. The ISO 2631 standards outline the center frequencies for each one-third octave band in the frequency range of 0.1 to 80 Hz and delineates weighting factors with which the accelerations should be weighted for each center frequency. First a power spectral density should be obtained for the accelerations and the root mean square (RMS) acceleration within each one-third octave band must be determined and weighted by center frequencies as outlined in ISO 2631:

$$a_w = \left[\sum_i (W_i a_i) \right]^{\frac{1}{2}} \tag{9.1}$$

where a_w is the frequency-weighted translational or rotational acceleration in one co-ordinate direction, a_i is the RMS acceleration for the ith one-third octave band containing the ith center frequency, and W_i is the frequency weighting factor for the

Table 9.1. ISO 2631-1 Vibration Total Values and Comfort Levels [38]

Vibration Total Value	Likely Reaction
Less than 0.315 m/s^2	Not uncomfortable
0.315 m/s^2 to 0.63 m/s^2	A little uncomfortable
0.5 m/s^2 to 1 m/s^2	Fairly uncomfortable
0.8 m/s^2 to 1.6 m/s^2	Uncomfortable
1.25 m/s^2 to 2.5 m/s^2	Very uncomfortable
Greater than 2 m/s^2	Extremely uncomfortable

ith one-third octave band. The frequency weighting factors, provided in one-third octave bands, are specified based on the co-ordinate direction of the acceleration component. These factors are identical in the x and y directions, the transverse plane, but are different from the weightings in the z direction, the longitudinal direction per the ISO co-ordinate system.

A vibration total value, a_v of weighted RMS accelerations should then be determined by combining each scalar frequency-weighted translational acceleration, a_w, as

$$a_v = \left(k_x^2 a_{wx}^2 + k_y^2 a_{wy}^2 + k_z^2 a_{wz}^2\right)^{\frac{1}{2}} \tag{9.2}$$

where a_{wx}, a_{wy}, and a_{wz} are the weighted RMS accelerations with respect to the x, y, and z directions as determined using Eq. 9.1 and k_x, k_y, and k_z are multiplying factors which all equal 1 for comfort assessments of seated persons. The vibration total values are then compared to values which give approximate indications of likely reactions to different overall vibration total values. These values and likely reactions are given in Table 9.1.

The procedure described above is a basic evaluation method that can be applied under certain criteria. If the ratio of the maximum instantaneous peak value of the frequency-weighted acceleration to its RMS value is less than or equal to 9, the basic

evaluation method can be applied. This ratio is called the crest factor. ISO 2631-1 outlines two additional methods of evaluating the comfort levels when the crest factors are greater than 9, the running RMS and the fourth power vibration dose value [38]. These two techniques attempt to account for the transient vibrations, occasional shocks, and peaks associated with high crest factors. In this dissertation, all crest factors are less than 9 and the basic evaluation method suffices for determining the passenger/aircrew comfort levels.

9.1.2 Analysis Procedure

The process of analyzing the accelerations for a passenger located in the trail aircraft to obtain a vibration total value is given in this section. First the simulations are run and the translational and rotational accelerations are recorded at a frequency of 160 Hz. Since the largest frequency component in the ISO 2631 spectrum of interest is 80 Hz, the sampling frequency of the accelerations, from Shannon's sampling theorem, should be at least greater than two times the maximum frequency to prevent frequency aliasing [84]. The accelerations recorded in the body frame of the trail aircraft are transformed to the ISO co-ordinate system using the rotation matrix:

$$R_{ISO-B} = \begin{bmatrix} 1 & 0 & 0 \\ 0 & -1 & 0 \\ 0 & 0 & -1 \end{bmatrix}$$

where R_{ISO-B} is the rotation matrix from the body frame of the trail aircraft to the ISO frame. The mean of each acceleration component in the ISO frame is obtained using a moving average window of size 100. This moving average mean is removed from the acceleration and the PSD estimate is obtained using the Welch method, a modification of the periodogram spectral estimator.

The periodogram is an asymptotically unbiased estimator in that as the number of samples of the signal increases without bound, the bias in the estimate of the PSD decreases to zero [84].

$$\lim_{N\to\infty} E\{\hat{\phi}_p(w)\} = \hat{\phi}(w) \tag{9.3}$$

where $\hat{\phi}(w)$ is the true PSD, $\hat{\phi}_p(w)$ is the estimate of the PSD using the periodogram, and w is the frequency, and N is the number of samples of the signal. On the other hand, the PSD estimate obtained using the periodogram always fluctuates around the true PSD with a non-zero variance even for sufficiently long data lengths. The Welch method attempts to reduce the variance of the periodogram PSD estimate at the expense of the bias and average resolution [84]. The approach of the Welch method is to split the available samples into sub-sequences of observations, compute the windowed periodogram of each sub-sequence, and then average the windowed periodograms as

$$\hat{\phi_w}(w) = \frac{1}{S}\sum_{j=1}^{S} \hat{\phi}_j(w) \tag{9.4}$$

where $\hat{\phi_w}(w)$ is the Welch estimate, $\hat{\phi}_j$ is the windowed periodogram of the jth sub-sequence, w is the frequency, and S is the number of sub-sequences of the signal. The windows used in the Welch method can be set to overlap, causing more periodograms to be averaged in a hope of reducing the variance of the estimated PSD. This dissertation uses an implementation of the Welch method in MATLAB developed by Lewis et. al [72] based on Reference [85]. In estimating the PSD of the accelerations, the overlap is set to 50% as recommended by Reference [84]. The window size and type is used to control the bias/resolution properties of the estimated PSD and is dependent on the length of the samples. This work uses a Hanning window type with a size of 0.04 times the signal length.

After the PSD is estimated over the frequency range specified in the ISO 2631, 0.1 to 80 Hz, the next task is to calculate the RMS accelerations for each one-third octave band with the specified center frequencies. The upper and lower frequencies, f_u and f_l respectively, for each center frequency are obtained from:

$$f_l = \frac{1}{2^{1/6}} f_i \tag{9.5}$$

$$f_u = 2^{1/6} f_i \tag{9.6}$$

where f_i is the ith center frequency. The area under the PSD in each frequency band is the mean square acceleration in that band which is estimated using a trapezoidal integration. The square root is taken to give the RMS acceleration which is then combined with the ISO frequency weighting for that center frequency (with corresponding frequency band). These frequency weighted accelerations are summed over each frequency band and squared as in Eq. 9.1 to give the total frequency-weighted acceleration. The vibration total value is then combined for the frequency-weighted translational accelerations in the three co-ordinate directions as in Eq. 9.2.

To evaluate the ride quality at points offset from the CM_E, the off-CM_E accelerations are obtained using Eq. 9.7 and the analysis is done as discussed in the preceding paragraphs. In Eq. 9.7, all vector representations are expressed in the body frame of the trail aircraft.

$$\mathbf{a}_L = \mathbf{a}_{CM_E} + \mathbf{S}(\dot{\omega}_{\mathbf{B_R}})\mathbf{r}_L + \mathbf{S}(\omega_{\mathbf{B_R}})\left(\mathbf{S}(\omega_{\mathbf{B_R}})r_L\right) \tag{9.7}$$

where $\mathbf{a}_{CM_E}$ is the acceleration at the CM_E, $\dot{\omega}_{\mathbf{B_R}}$ is the angular acceleration of the aircraft, $\omega_{\mathbf{B_R}}$ is angular velocity of the aircraft, and r_L is the location of the point relative to the CM_E.

Table 9.2. Ride Quality Cases for Trail KC-135R

Case	Wake On/Off	Turbulence
1	Off	No
2	On	No
3	Off	Yes ($\sigma = 0.39m/s$)
4	On	Yes ($\sigma = 0.39m/s$)
5	On	Yes ($\sigma = 0.2m/s$)

9.2 KC-135R Trail

For the KC-135R trail, a heavier lead KC-135R is utilized as the lead aircraft. In these formations, the ride quality is investigated for passengers/aircrew within the trail aircraft as it flies at the dynamic sweet spot which is close to the static. The trail KC-135R is considered to fly in formation with the wake off and with the wake on to obtain fuel savings for about 4 minutes. In addition, atmospheric turbulence is added to the simulation for both the lead and trail aircraft. The effect of having turbulence of different intensities is also studied as the trail KC-135R flies with the wake on. Table 9.2 summarizes all ride quality cases studied for a person located at the CM_E of the trail KC-135R as it flies in formation with the lead.

The KC-135R is positioned at the dynamic sweet spot and in this section will hereinafter be referred to simply as the sweet spot for the KC-135R trail. For Case 1, the wake of the lead aircraft is off along with the turbulence for the entirety of the simulation run. This is to simulate a turbulence-free flight for the trail KC-135R with the wake off. In the second case, the simulation initially starts out like Case 1 as the wake is off for the first 150 seconds. After 150 seconds, the wake is switched on and the trail aircraft is subjected to the non-uniform wind induced by the leader. Case 3 again begins like Case 1 but starting at 250 seconds, the trail KC-135R is exposed to a light turbulence of intensity 0.39m/s and length scale 533.7 m in the x, y, and z

directions. Case 4 is similar to Case 3 but the trail aircraft is subjected to turbulence with the wake on, simulating a turbulent flight in formation. Case 5 is the same as Case 4 but with a lighter turbulence intensity of 0.2 m/s. All ride quality analyses exclude the transient regions before the non-uniform wind or turbulence levels reach steady state in the simulations. Fig. 9.2 depicts the combination of the stochastic atmospheric turbulence and deterministic effective translational and rotational wind components in the x, y, and z directions for a thirty-minute run of the five cases. For the cases where the wake is off and there is no turbulence, the wind components are effectively zero as depicted in Fig. 9.2.

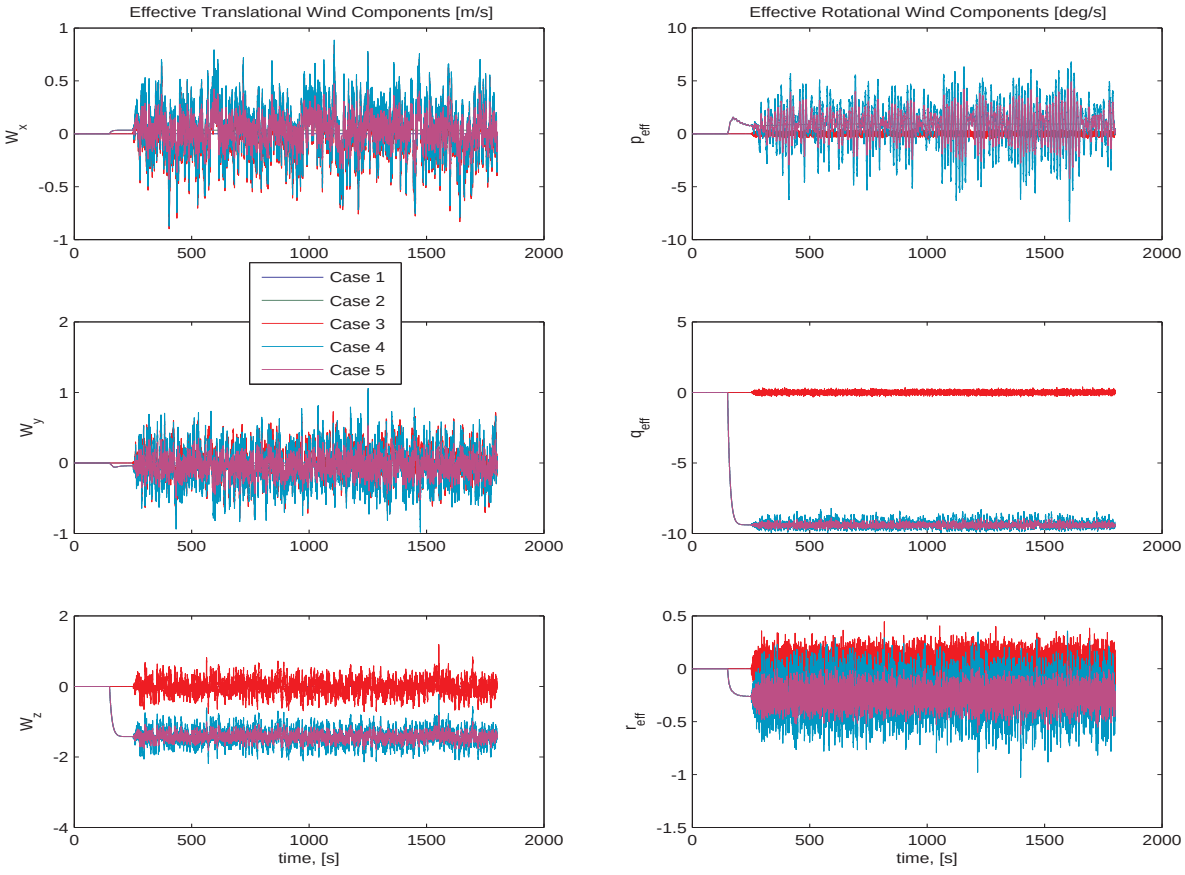

Figure 9.2. Effective Rotational and Translational Winds for Trail KC-135R.

For all five cases, the accelerations at the CM_E are recorded as depicted in Fig. 9.3. The power spectral densities are estimated over a frequency band of 0.1 to 80 Hz after which ISO 2631 RMS accelerations are calculated and used to determine the level of passenger comfort during the simulation as explained in Section 9.1. The values for the overall vibration total values given in the ISO standards are not limits but are used to provide approximate indications of likely reactions to various magnitudes of overall vibration total values in public transport. Thus, these values will be used more in comparison to one another rather than to the ISO standards.

In addition, the standard deviations of power spectral density estimates of the accelerations are used as a metric of ride quality to evaluate the comparisons between any two cases. For instance, if Cases 1 and 2 are being compared, a ratio factor $k_{1/2}$ is obtained by dividing the standard deviation of Case 1 by that of Case 2. If $k_{1/2}$ is less than 1, it implies that the standard deviation for Case 1 is less than that of Case 2. If $k_{1/2}$ is $<< 1$, then Case 1 is said to be significantly better than Case 2 in terms of ride quality.

9.2.1 Accelerations at the CM_E

9.2.1.1 Turbulence-Free Flight With Lead's Wake On versus Off

Fig. 9.4 presents the PSD estimates of the linear and angular accelerations of a person located at the CM_E of the KC-135R as it flies turbulence-free at the sweet spot with the wake off, Case 1, and turbulence-free at the sweet spot with the wake on, Case 2. The standard deviations for the six accelerations, σ_1 and σ_2, for Case 1 and 2 respectively, are also given on the plots along with the previously defined ratio factors. Fig. 9.4 shows that there is a visible increase in the PSD estimates of all the accelerations components with the wake on as compared with the wake off. The ratio

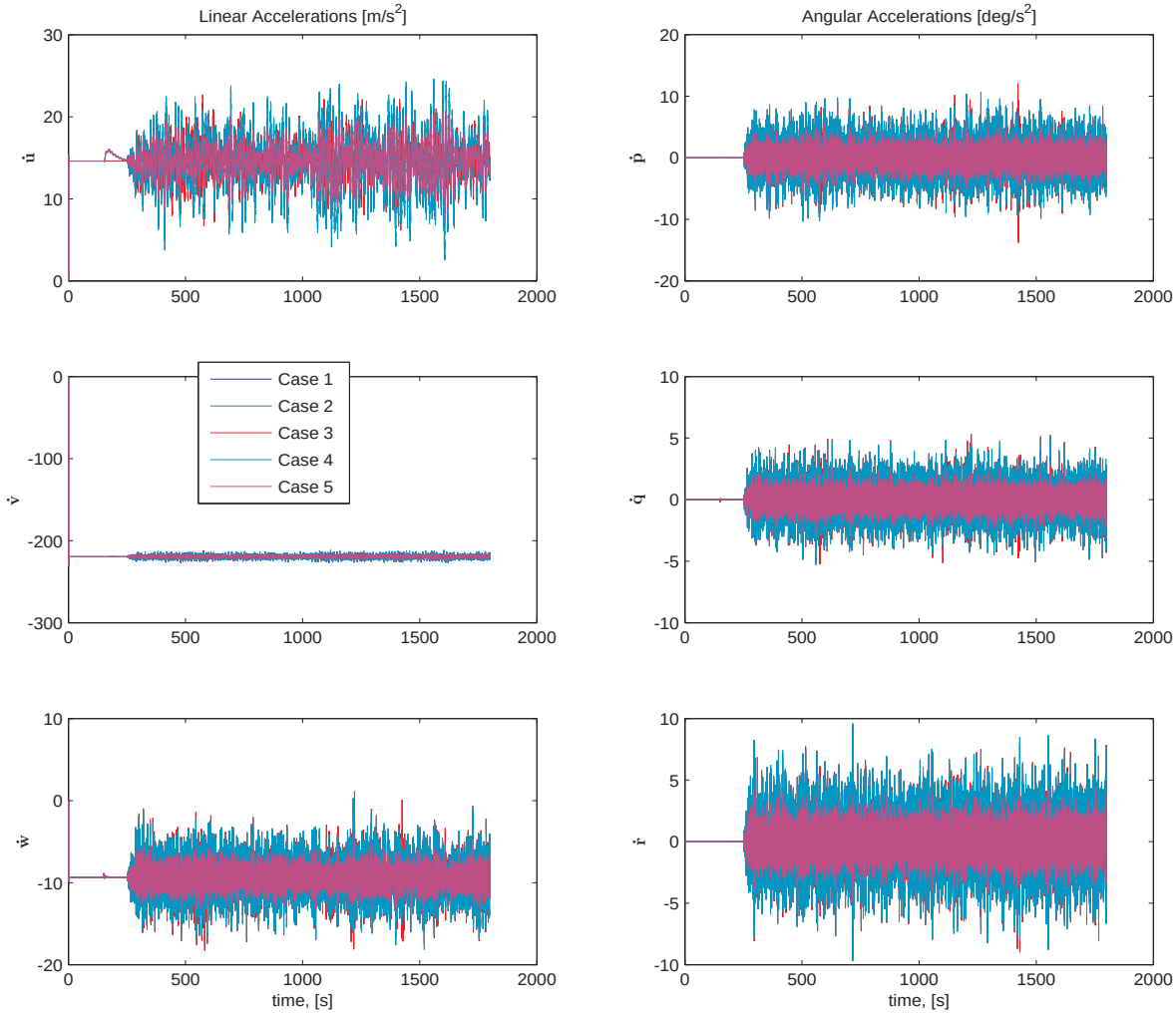

Figure 9.3. Linear and Angular Accelerations for Trail KC-135R.

factor is less than one for each component confirming the increase in the PSD of the accelerations from solo to formation flight.

The vibration value for Case 1 is approximately 0 m/s^2 while that for Case 2 is a small value of 0.22E-6 m/s^2. By the ISO standards, the comfort levels for these two cases is "not uncomfortable" as they fall well below the guide limit of 0.315 m/s^2. This implies that wake-induced non-uniform wind does not lead to a

significant degradation in ride quality. Thus, from a perspective of ride quality, there is no additional detrimental impact to a person onboard a trail aircraft in formation.

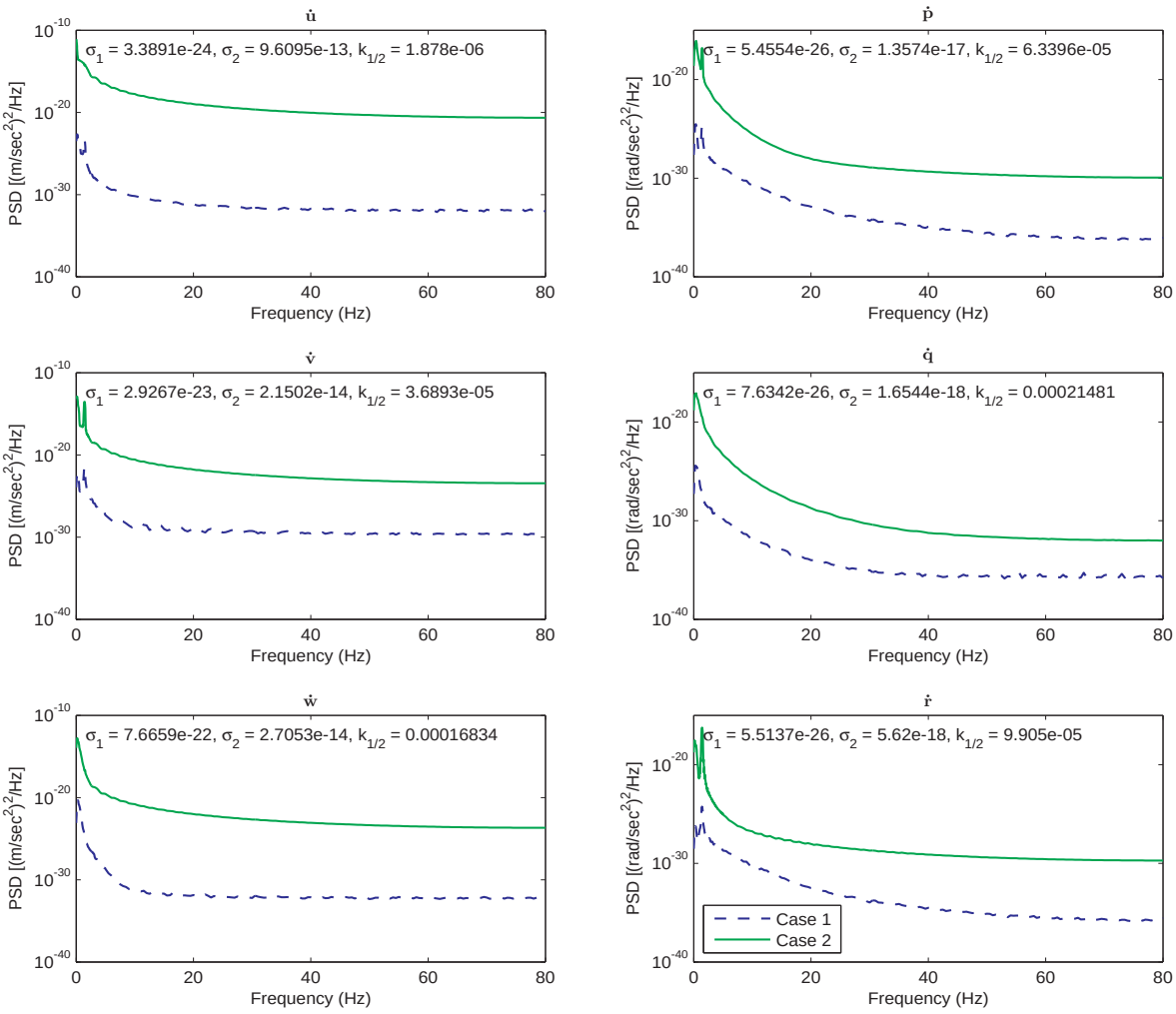

Figure 9.4. Acceleration PSD Estimates for Cases 1 and 2.

9.2.1.2 Turbulent Flight With Lead's Wake On versus Off

Fig. 9.5 presents the PSD estimates of the linear and angular accelerations for turbulent flight with the wake off, Case 3, and turbulent flight with the wake on,

Case 4 of a person located at the CM_E of the KC-135R flying at the sweet spot. For both cases, the turbulence intensity levels are 0.39 m/s with length scales of 533.4 m in the x, y, and z directions. Fig. 9.5 shows almost identical PSD estimates for the two cases implying that the turbulence is a more dominant factor in the acceleration PSD estimates than the non-uniform wind induced from the lead aircraft. Thus, for an aircraft subjected to similar turbulence levels, the ride quality/passenger comfort levels are similar whether the aircraft flies in formation with the wake of the lead aircraft turned on or off. This hypothesis is corroborated by the values of the variances of the PSD estimates for the two cases which are much closer in magnitude than Case 1 and 2.

The vibration values for Case 3 and 4 are 1.66 m/s^2 and 1.65 m/s^2 respectively. By ISO standards, these levels of vibration magnitude are "very uncomfortable" and this is to be expected as the turbulence, such as that which was introduced for these two cases, should not be "comfortable". It is important to note that the source of the discomfort is not the induced wind from the leader as observed in Section 9.2.1.1. In addition, the ride quality analyses for all turbulent cases assume that the stochastic nature of the turbulence does not prevent repeatability of the results. To justify this assumption, Case 4, which represents a turbulent flight with the lead's wake on, is simulated numerous times and the conclusion, in terms of comfort levels, remains the same for each simulation run.

9.2.1.3 Different Turbulent Intensities Within Lead's Wake On

Fig. 9.6 presents the PSD estimates of the linear and angular accelerations for two different intensities of turbulence as the trail KC-135R flies within the aerodynamic influence of the lead aircraft. This section compares Case 4 in the previous section to a new case with a smaller turbulence intensity. Case 4 has a turbulence

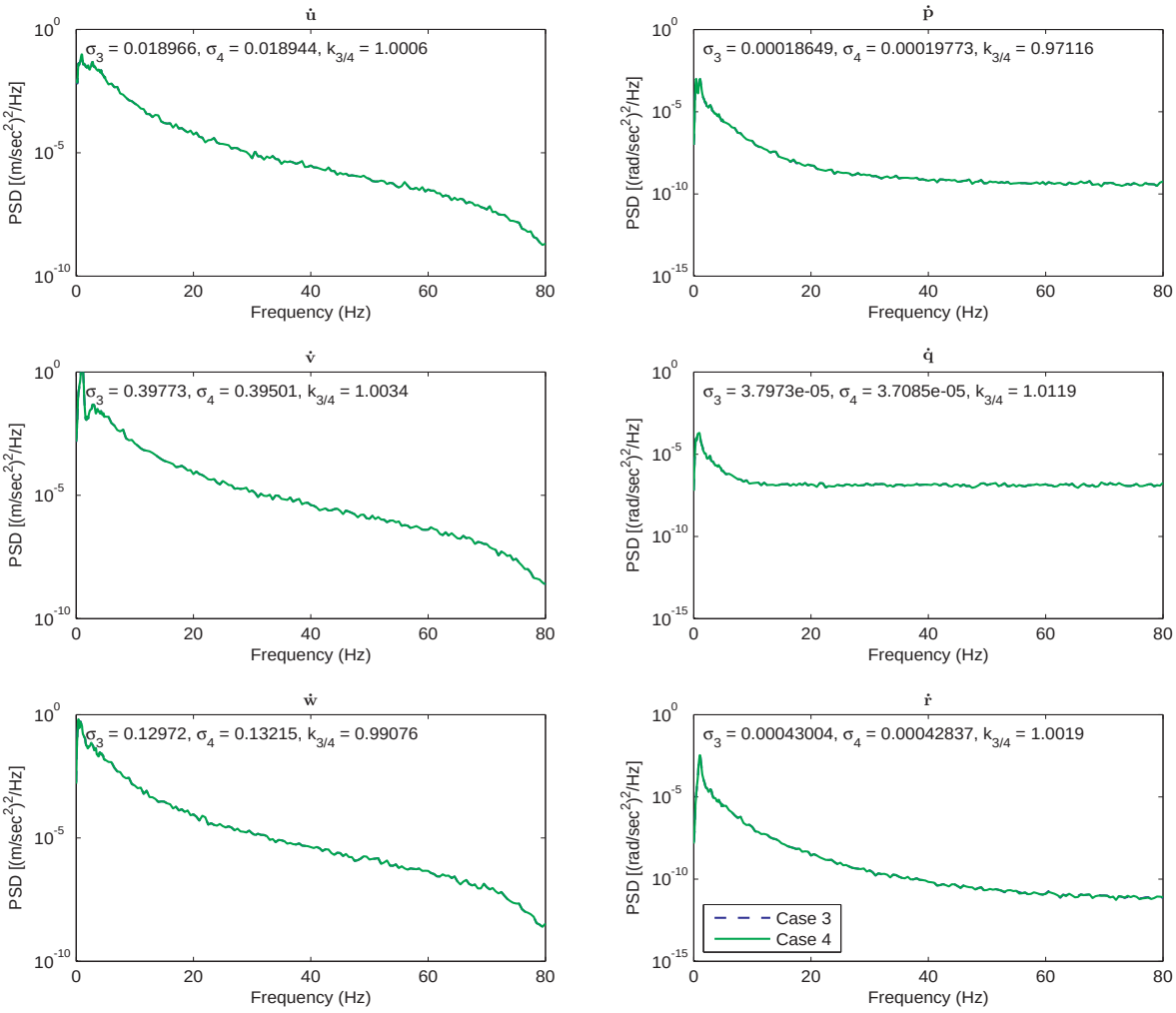

Figure 9.5. Acceleration PSD Estimates for Cases 3 and 4.

intensity level of 0.39 m/s while Case 5 has a turbulence intensity of 0.2 m/s in the x, y, and z directions. For both cases, the turbulence length scales are identically 533.4 m in the x, y, and z directions.

Fig. 9.6 shows that the lower intensity turbulence case, Case 5, has smaller PSD estimates and standard deviations for all linear and angular accelerations. The vibration value for Case 5 is 0.85 m/s^2 corresponding to a comfort reaction of "fairly uncomfortable" by ISO standards. Case 4 was previously determined to be "very

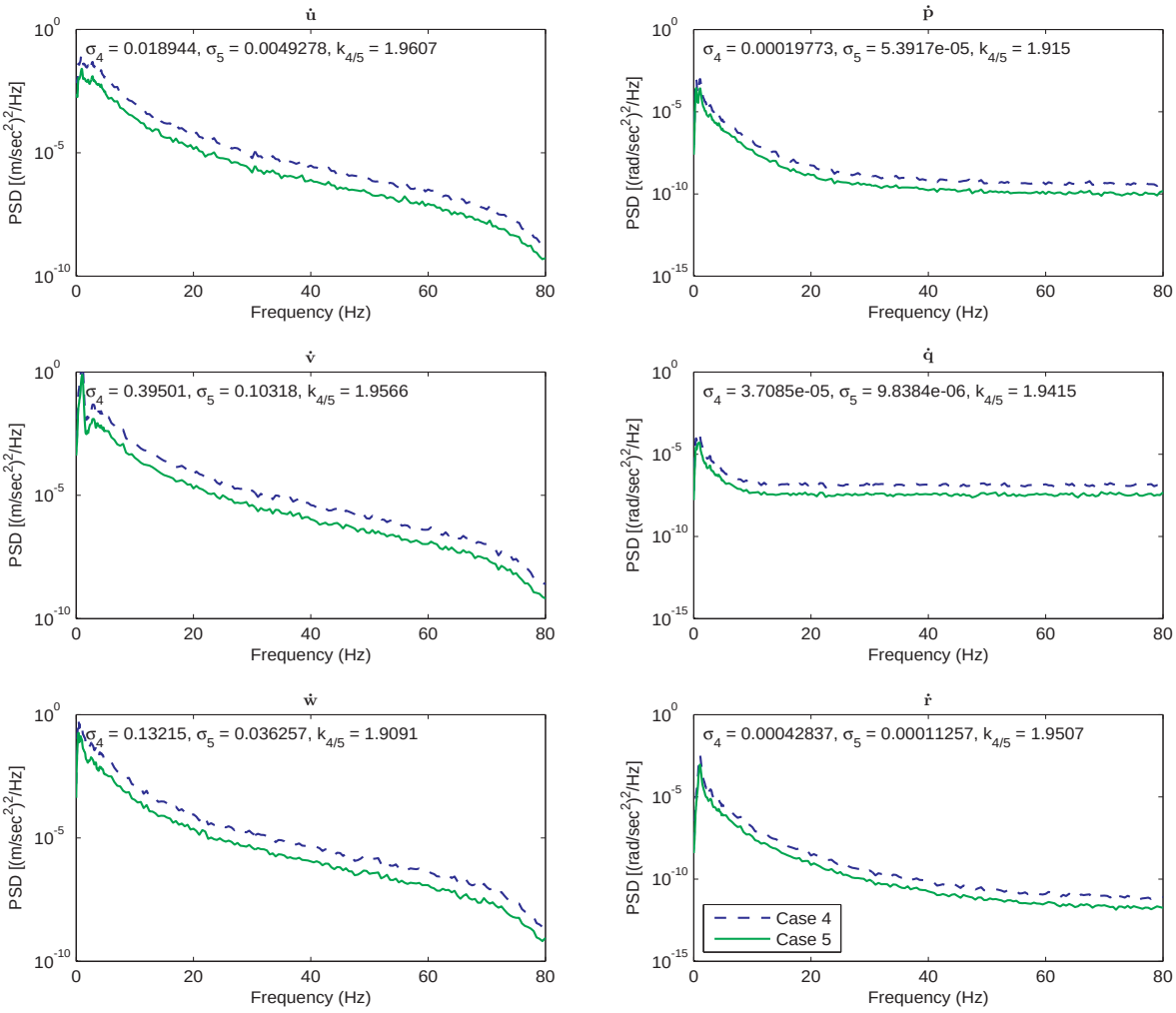

Figure 9.6. Acceleration PSD Estimates for Cases 4 and 5.

uncomfortable" as it yielded a vibration value of 1.65 m/s^2. These two cases serve as verification cases to ensure that the ride quality analyses done are in agreement with expectations. The ratio factors, $k_{4/5}$ for all acceleration PSD components are a little less than 2, implying that the standard deviations for Case 4 are almost twice as large as those for Case 5. This is an indication that Case 4 is significantly worse than Case 5. As is seen going from Case 4 to Case 5, a decrease in the turbulence intensity of the trail aircraft in formation should yield a "better" ride quality for a person located

Table 9.3. Passenger Locations (Relative to CM_E) within KC-135R Trail

Location	x (m)	y (m)	z (m)
Forward and Left of CM_E (Point F_L)	8	-1.83	0
Forward and Right of CM_E (Point F_R)	8	1.83	0
Aft and Left of CM_E (Point A_L)	8	-1.83	0
Cockpit (Point C)	16.59	0	0
CM_E	0	0	0

within the trail. Even though by the ISO standards, which are not limits but are a guide to evaluate human comfort levels, a case deemed to be uncomfortable can still be compared to another case as long as the metric for evaluation is the same. The results of Case 4 and 5, which are in line with expectations, show that the ISO standards provide a consistent metric which can be used to quantitatively compare the passenger comfort levels for different atmospheric conditions.

9.2.2 Accelerations Offset from the CM_E

Using Case 2 of a turbulent-free formation flight, the 6-DOF accelerations at four other locations within the trail KC-135R, offset from the CM_E, are derived and compared to those at the CM_E using ISO 2631-1 standards. These locations are tabulated in Table 9.3.

Fig. 9.7 presents the PSD estimates of the linear and angular accelerations for the five locations offset from the CM_E as tabulated in Table 9.3. Since the trail aircraft is a rigid body, the angular accelerations and thus their associated PSD estimates remain the same at all points within the aircraft as illustrated in Fig. 9.7. The linear accelerations will thus be the dominant factor in comparing and quantifying the ride quality at the different points. The vibration values obtained at each point are given in Table 9.4. Table 9.4 shows that the vibration values are all very small

and correspond to a ride quality of "not uncomfortable" by the ISO 2631-1 standards. This confirms the hypothesis in the previous sections that the ride quality of a trail aircraft is not degraded as a result of the non-uniform wind field induced by the lead on the trail. Table 9.4 confirms that all five locations investigated, which cover a large area of interest, have comfort levels which are acceptable by the ISO 2631-1 standards.

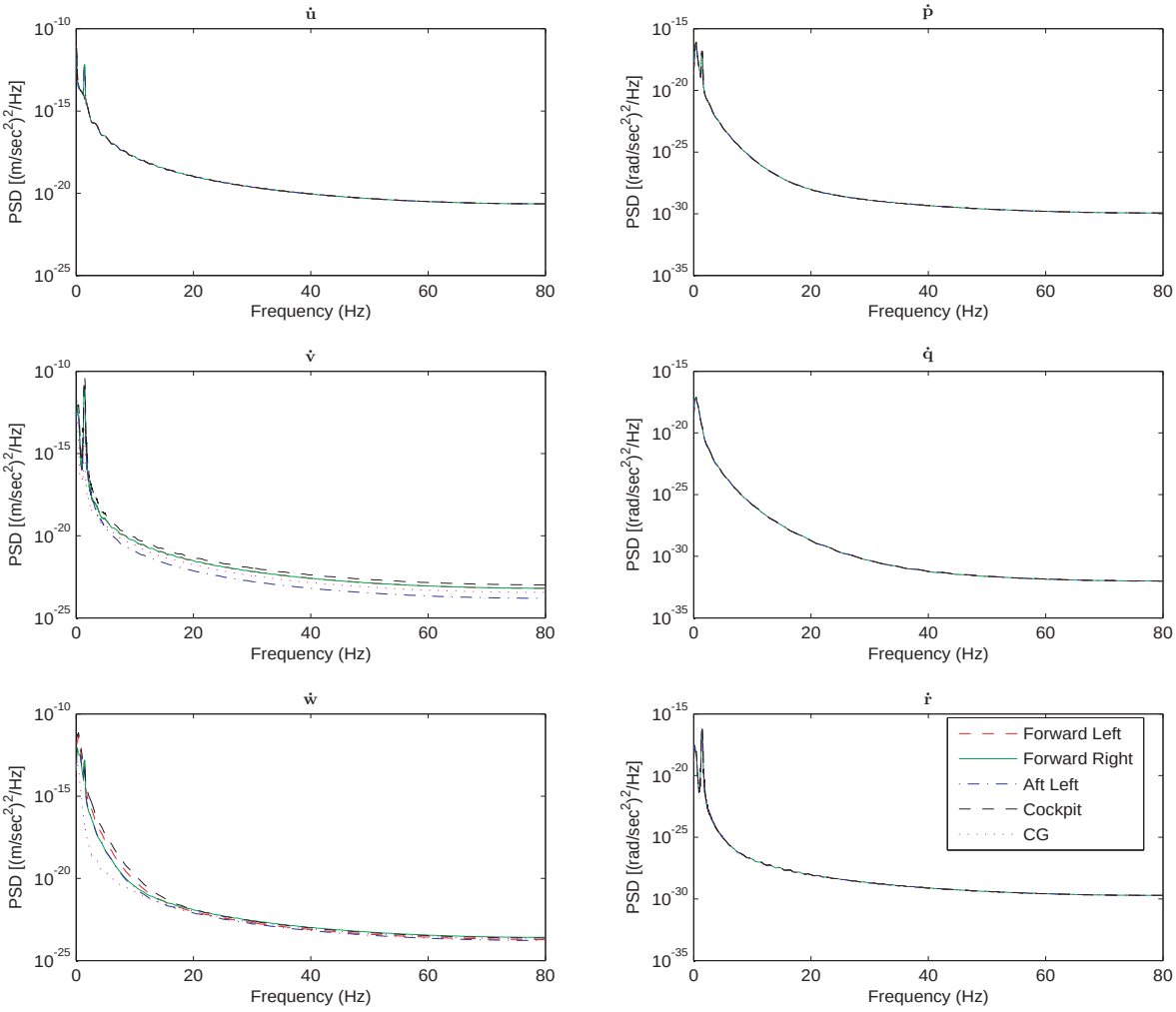

Figure 9.7. Acceleration PSD Estimates for Locations Offset from CM_E, Case 2.

Table 9.4. Vibration Values at Different Locations within the Trail KC-135R

	Vibration Magnitude (m/s^2)		
Location	Case 1	Case 2	Case 5
Forward and Left of CM_E (Point F_L)	0.222E-9	0.209E-5	11.94
Forward and Right of CM_E (Point F_R)	0.218E-9	0.203E-5	11.87
Aft and Left of CM_E (Point A_L)	0.229E-9	0.212E-5	12.20
Cockpit (Point C)	0.449E-9	0.417E-5	24.08
CM_E	0.017E-9	0.023E-5	0.85

Comparing the points forward of the CM_E, point F_R has a vibration magnitude smaller than that of point F_L. The aft location, point A_L has a vibration total value which is slightly greater than its corresponding forward location, point F_L. Another interesting observation is that the cockpit has the largest vibration magnitude in comparison to all the other points with the CM_E having the lowest vibration magnitude. This is contradictory to expectations and it is important to understand the reason for this disparity. Looking at the same locations for other cases in addition to Case 2 sheds some light on this interesting discovery. Table 9.4 also gives the vibration magnitudes for Case 1 in which the trail KC-135R flies in a turbulence-free environment outside the aerodynamic influence of the lead aircraft, and Case 5 in which the trail flies at the sweet spot with a turbulence intensity of 0.2 m/s. These additional cases, 1 and 5, also yield the same conclusions when the ride quality at each of the five locations are analyzed. This implies that the results are an artifact not of the formation flight, but of the acceleration magnitudes at these locations. The control design of the trajectory tracking controller of the trail KC-135R helps to explain this phenomenon. This control design, described in Section 2.5.1 uses an LQR gain scheduling scheme to minimize the position errors of the CM_E of the trail KC-135R with respect to the CM_E of the lead aircraft. This mimics a placement of

position sensors at the CM_E which is the norm in simulations but is atypical of in flight on-board sensor placement. As a result of minimizing these position deviations, the accelerations at the CM_E are kept at a minimum and deviations of locations outward of the CM_E are not penalized like the CM_E position deviations. Thus, the accelerations at the five points, which are obtained using the transport theorem as described in Section 9.1 are larger than those obtained at the CM_E As a result, the PSD estimates have higher magnitudes corresponding to larger values of the overall vibration total value used as a metric in this study and the ISO 2631-1 standards. Future work should involve a control design scheme that utilizes relative locations of the cockpit in the position/trajectory tracking of the trail aircraft in formation.

9.3 Large EQ-II Trail

Using the large EQ-II aircraft, the ride quality levels are assessed as the EQ-II flies at the static and dynamic sweet spots which differ in this case. The EQ-II is commanded to fly at the static sweet spot while employing alternate trimming mechanisms as described in Chapter 5 and the accelerations at the cockpit are obtained and used to provide a measure of passenger/aircrew comfort. The accelerations are recorded for a thirty-minutes simulation run as the alternative trimming process and duration is longer than the conventional trimming procedure. The ride quality is also investigated at the dynamic sweet spot of the large EQ-II aircraft after which a comparison of the ride quality is done for the static and the dynamic sweet spot. The cases for the large variant of the EQ-II are given in Table 9.5.

Fig. 9.8 presents the PSD estimates of the linear and angular accelerations for the turbulence-free flight with the wake on as the trail EQ-II flies at the dynamic sweet spot, Case 6, and the static sweet spot, Case 7. In both cases, the accelerations are evaluated at the cockpit of the large EQ-II aircraft. Fig. 9.8 shows that the PSD

Table 9.5. Ride Quality Cases for Large EQ-II Trail

Case	Sweet Spot	Turbulence	Location
6	Dynamic	No	Cockpit
7	Static	No	Cockpit

estimates for all linear and angular accelerations in the x, y, and z directions, are smaller for the dynamic case as compared to the static. The vibration magnitude for the dynamic case is 0.0045 m/s while that for the static is 0.0081 m/s which correspond to a comfort level of "not uncomfortable" for a person located at the CM_E Thus, even though Fig. 9.8 and the vibration total values indicate that the dynamic sweet spot is seemingly "better" than the static with alternative trimming mechanisms employed both cases do not result in any passenger discomfort. From a perspective of ride quality, flying the trail EQ-II aircraft at either sweet spot for the benefit of fuel savings does not pose any problems.

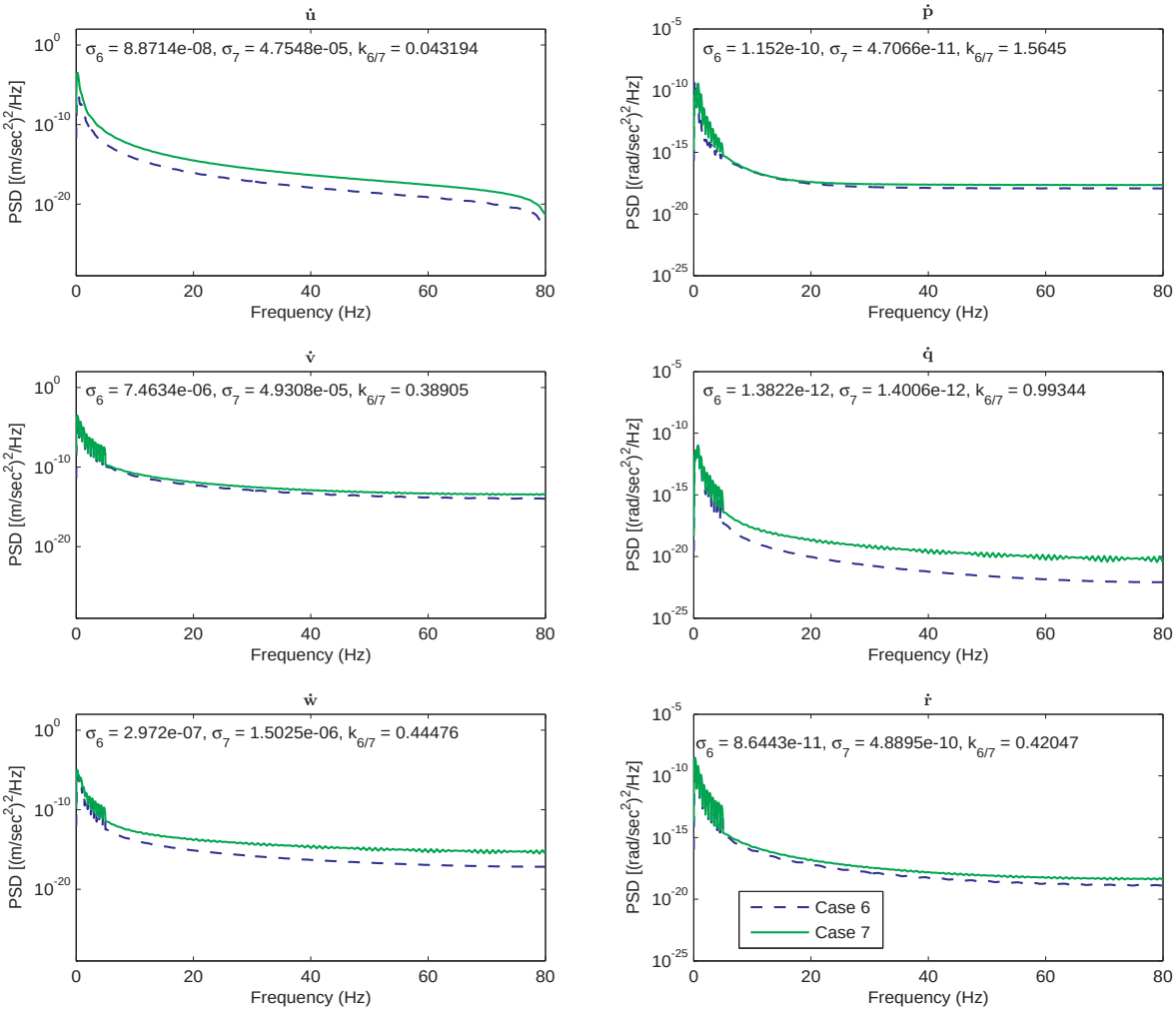

Figure 9.8. Acceleration PSD Estimates for Cases 6 and 7.

CHAPTER 10

CONCLUSIONS AND A GUIDE TO FUTURE WORK

Studying formations as a method of flight for fuel savings began in the late 20th century and has continued till date. The potential advantages of formation flight implementation have been shown to be significant across both the military and commercial aviation sectors, causing renewed interest by researchers across all sectors. This dissertation aims to provide a holistic approach to the formation flight endeavor. Specifically, the aim is to formulate the problem considering the benefits of flying different aircraft configurations in formation, accounting for the effect of trim on the formation benefits, exploring the feasibility of increasing the savings currently obtained by flying in formation, and determining the performance of formation from the perspective of ride quality. The contributions to the area of formation flight are outlined in the following paragraphs.

The various investigations on the formation benefits by researchers have utilized different methods to quantify the benefits of flying in formation. This yields different optimal locations for the trail aircraft to be placed relative to the lead aircraft and leads to different "sweet spots" based on the method of quantification. The disparities in the different techniques are recognized and the differences between the methods are noted in this research. This dissertation establishes two techniques of analyzing the optimal location for formation benefits under which the previous methods can be grouped. A static analysis, which does not account for trimming the aircraft and a dynamic analysis which does. The static analysis assigns the sweet spot as the relative placement for the trail aircraft, with respect to the lead, where the lift to drag ratio is

the highest. In the dynamic case, it is the relative location where the thrust required is the least. This dissertation shows that static sweet spot and dynamic sweet spot may or may not coincide, depending on the weight of the lead aircraft and the type of the trail aircraft in the formation.

Another contribution of this work is in the aircraft type utilized in the formations. Most prior assessments have involved homogenous formations in which the same aircraft have been utilized as the lead and trail. There are only a few mentions of heterogenous formations involving different aircraft types. The majority of the heterogenous formations involve trail aircraft that are similar in configuration to the leader, in terms of conventional fuselage-tail body configuration, but dissimilar in size. Research studies that utilize unconventional trail aircraft, such as flying-wing configurations, are not found as easily in the literature. This work extensively shows the possibilities of employing a trail aircraft, dissimilar in configuration to the lead, in formation.

The literature has also shown that there are non-zero induced aerodynamic moments on the trail aircraft at the sweet spot. These non-zero moments require deflecting the control surfaces at the sweet spot, causing trim drag and reducing the benefit of formation. This work utilizes two unconventional methods of trimming, (i) internal fuel transfer and (ii) differential thrusting, to reduce the drag-inducing control surface deflections and recover some of the formation benefit lost to trim drag. In this dissertation, the alternative trimming mechanism were employed at the static sweet spot where the aerodynamic moments were significant rather than the dynamic sweet spot which had negligible moments. Augmenting the benefits of formation as presented in this dissertation, can be done for a trail aircraft as it flies in formation with the lead at any sweet spot location with induced aerodynamic moments.

The amount of upwash from the lead aircraft's wake and thus, magnitude and direction of the non-uniform wind the trail aircraft is subjected to, decreases as the weight of the lead aircraft reduces. This translates to a reduction in the fuel savings for a trail aircraft over time as it flies at the sweet spot in the wake of the leader. In a formation with long enough duration, the weight of the lead aircraft will decrease due to fuel consumption. This is an important aspect of formation flight that should be accounted for in evaluating the benefits of formation over realistic flight. This dissertation contributes to this work by studying that decrease in savings over time as fuel is burned.

The final contribution of this dissertation is the study from a perspective of ride quality (comfort levels). With respective to formation flight, there are only a few mentions of evaluating the comfort levels for a person located within the trail aircraft. Most of them are qualitative in nature and assess the comfort levels in test flights as, "steady" or "unsteady." One quantitative study in this area assumes ideal control and does not account for compensatory control inputs by the pilot or autopilot. This dissertation makes the first quantitative assessment of comfort levels for person(s) in the trail aircraft considering the non-uniform wind the trail aircraft is subjected to and the control inputs required to maintain the trail aircraft at the sweet spot relative to the lead.

The notable results of these contributions and the areas of improvement are outlined in the following sections.

10.1 Evaluating Benefits: Static versus Dynamic Sweet Spot

10.1.1 Notable Results

- For the aircraft formations studied, the static sweet spot is relatively constant, as compared to the dynamic sweet spot, with a significant change in the weight of the lead aircraft.
- The magnitudes of the induced aerodynamic forces and moments of the trail aircraft, and thus control variables, decrease with a reduction in the weight of the lead aircraft.
- The percentage increase in benefits from solo flight, quantified by lift-to-drag ratio for the static sweet spot, is larger than that for the dynamic case, quantified by thrust.
- The induced aerodynamic moments at the static sweet spot are larger than at the dynamic sweet spot.
- Position deviations from the static sweet spot in either the lateral or vertical direction will lead to similar reductions in formation benefits. The dynamic sweet spot, on the other hand, has a larger drop in formation benefits for deviations in the lateral direction as compared to the vertical direction.

10.1.2 Future Work

The dynamic sweet spot is determined for an aircraft whose mass and inertia properties are constant. If these properties of the aircraft change, based on a different fuel distribution for instance, the trim configuration of the aircraft will be different at the same locations relative to the lead aircraft. This implies that the dynamic sweet spot may vary depending on the configuration, in terms of weight and mass distribution, of the trail aircraft. Thus, the dynamic sweet spot may be determined

by considering the effect of not just the control variables of aileron, elevator, rudder and thrust, but weight and inertia distribution.

10.2 Aircraft Sizes

10.2.1 Notable Results

- Relative to the lead aircraft, if a smaller conventional aircraft is utilized as the trail aircraft, the dynamic and static sweet spots coincide. If the conventional trail aircraft is at least as large as the leader, the dynamic and static sweet spots do not coincide. In fact, the dynamic sweet spot is laterally closer to the lead aircraft than the static sweet spot is.
- Relative to the lead aircraft, if a smaller flying-wing aircraft is utilized as the trail aircraft, the dynamic and static sweet spots are laterally very close to one another. If the flying-wing trail aircraft is at least as large as the leader, the dynamic and static sweet spots do not coincide. As in the case of the conventional trail, the dynamic sweet spot is laterally closer to the lead aircraft than the static sweet spot is.
- Thus, if the trail aircraft is at least as large as the lead aircraft, there is a noticeable difference in the location of the static and dynamic sweet spot, regardless of the trail aircraft type.

10.2.2 Future Work

Comparisons are not made between the actual locations of the static and dynamic sweet spots for the large variants of the trail flying-wing and the conventional aircraft. Similarly, no comparisons are done for the small trail variants. This is because different weights of the lead aircraft were utilized in the analysis for the conventional and the flying-wing vehicles. It was shown that the location of the sweet

spot shifts with significant weight change of the lead aircraft for any aircraft pairs. Thus, to isolate the effect of the aircraft type on the sweet spot locations using trail aircraft with similar sizes and dissimilar configurations, the weight of the lead aircraft should be kept the same.

10.3 Augmentation of Benefits using Alternate Trimming

10.3.1 Notable Results

- There are non-zero induced aerodynamic moments at the static sweet spot which differs from the dynamic sweet spot for the large variants of the trail aircraft. Trimming these moments induces additional trim drag which reduces the formation benefits.
- Alternate lateral trimming methods are employed to trim these moments and reduce the need for the control effectors for the large variant of the unconventional flying-wing trail aircraft. These alternate trimming methods are internal fuel transfer to generate roll moment and reduce the need for the aileron and differential thrusting to generate yaw moment and reduce the need for the rudder.
- These techniques provided thrust savings at the static sweet spot which are comparable to those at the dynamic sweet spot for the large variant of the flying-wing aircraft.

10.3.2 Future Work

Scheduling the fuel transfer to reduce the need for the aileron is not incorporated in the trajectory-tracking control scheme while the differential thrusting is. An improvement to the alternate lateral trimming mechanization would be to develop a control algorithm which uses both fuel transfer and differential thrusting as control

variables to augment the fuel savings and reduce the need for the control effector deflections. The controller could use fuel transfer as an additional variable in tracking the commanded position by reducing the aileron deflection. In addition, all control variables (differential thrust, fuel transfer, and control effector deflections) could be optimized online to find the trim configuration at the sweet spot which provides highest fuel savings.

10.4 Long-Duration Formations

10.4.1 Notable Results

- As the weight of the lead aircraft decreases, the benefit to the trail aircraft decreases. For a formation lasting 6.5 hours, this decrease is not significant enough to nullify the benefit of formation flight, showing that fuel savings are obtained for formations of long durations.
- Even with atmospheric turbulence of light intensity, there is significant benefit of flying in formation. This benefit is close in magnitude to that obtained with no atmospheric turbulence.

10.4.2 Future Work

- The effect of prevailing winds of different magnitudes and directions should be considered in assessing the benefit of a long-duration formation. Prevailing winds will shift the sweet spot and the trail aircraft may not obtain the full benefit of the formation as it flies at a location which is not optimal. A robust trajectory-tracking control design which can maintain the relative position of the trail aircraft in the presence of different prevailing winds should be considered. A reduction in fuel-savings due to the prevailing winds is expected and should be assessed in comparison to a solo flight.

- This work assumes the location of the sweet spot can be obtained in flight using an online control scheme such as an extremum-seeking controller. Determining the sweet spot will require the trail aircraft to expend some energy/fuel before it begins to track. For instance, an extremum-seeker could utilize aileron measurements at different discrete locations within the wake, determine the gradient of these aileron deflections, and use the gradient information to guide the trail aircraft to the sweet spot in a gradient descent approach. This may require that the trail aircraft obtain sufficient information about its environment by dithering its position till the sweet spot is found. Thus, in a long-duration formation, the fuel expended in determining the sweet spot should be taken into account when assessing the fuel saved in formation flight compared to a solo flight.
- In this dissertation, it was shown that increasing the weight of the lead aircraft leads to an increase in the fuel-saving benefits obtained by the trail aircraft. The effect of the weight of the trail aircraft on the formation benefits should also be assessed. If a a trail aircraft, which is less heavy and possibly different from the leader, is used in a formation of long duration, the benefits on the trail could be higher. This implies that the formation benefits could be significantly larger than that obtained in this dissertation for a tanker-tanker formation of identical starting weights. This is a motivation for heterogeneous formations in which the trail aircraft is less heavy than the lead aircraft.

10.5 Ride Quality Analysis

10.5.1 Notable Results

- From a perspective of ride quality, there is no additional detrimental impact to a person on board a trail aircraft in formation as it is subjected to the non-uniform wind field from the lead aircraft.
- Even with atmospheric turbulence, the ride quality levels in the trail aircraft are the same with the non-uniform wind from the lead aircraft switched on or off.
- A person in the large variant of the trail flying-wing aircraft has the same levels of comfort if the trail flies at the dynamic sweet spot or at the static sweet spot while employing alternative trimming mechanisms. Thus, from a perspective of ride quality, flying the trail aircraft at either sweet spot does not present any disadvantages.

10.5.2 Future Work

- Assessments of ride quality within the trail aircraft as it flies at different locations relative to the lead aircraft can be done. The static and dynamic analyses involved the creation of contour maps which showed spatial variations of aerodynamic force and moment coefficients and control variables for the trail aircraft at various locations relative to the lead. A ride quality assessment could be also be done which shows the spatial variation of the vibration total value at the same relative locations used for the static and dynamic analysis to determine if there is a sweet spot for the comfort levels of persons located within the trail aircraft.
- A control design which minimizes position deviations, and thus acceleration deviations, from the nose or cockpit rather than the C.G., should be imple-

mented. Penalizing deviations closer to the front of the aircraft would result in the forward accelerations kept smaller than the aft, reducing the vibration values at those locations. This would be a better representation of an aircraft sensor placement to better study the ride quality at different locations with the trail aircraft.

- Also, the ride quality cases with the wake of the lead aircraft switched off do not represent a solo flight as the control design is inherently a trajectory-tracking control design which maintains a commanded position of the trail aircraft relative to the lead. To truly compare the ride quality in formation with that in solo flight, a control design which is a non-trajectory tracking controller should be employed. The control design for the lead aircraft, which is a speed and altitude hold control, could be utilized on the trail aircraft to simulate a solo flight. The accelerations/vibrations of the lead aircraft can also be studied to provide a measure of the ride quality in solo flight.
- If an extremum-seeking control design with relative position dithering is utilized to find the sweet spot, this will degrade the comfort levels for persons in the trail aircraft. An assessment of ride quality should be done which accounts for the effect of the dither signal on the vibration levels.

APPENDIX A

EQ-II AERODYNAMIC MODEL DATA

This appendix contains additional plots aerodynamic force and moment coefficients of the EQ-II aircraft. In addition, the values for all coefficients and stability derivatives are given in this appendix.

A.1 Drag Coefficient

The relationship between C_D and angle of attack at different sideslip angles is shown in Figs. $A.1$. C_{D_q} versus angle of attack and C_D dependence on the rudder is depicted in Figs. A.2 and A.3 respectively. Table A.1 gives the values of the drag coefficients in Section 2.1.1.3.

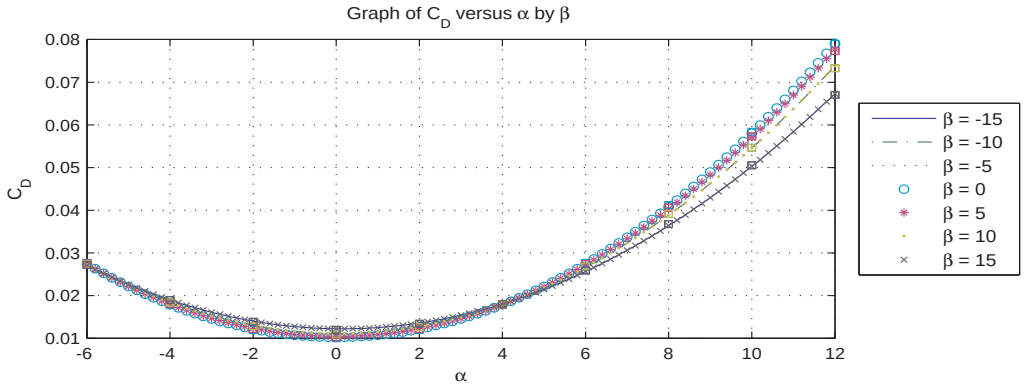

Figure A.1. C_D vs. α.

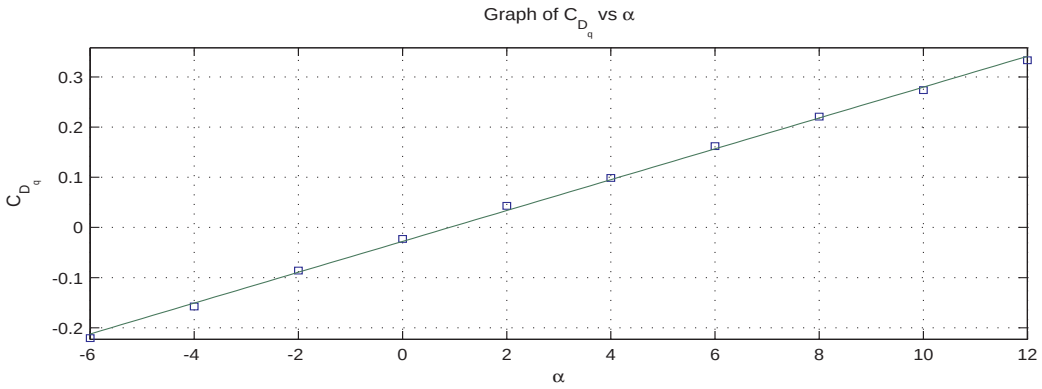

Figure A.2. C_D (Pitching Moment) vs. α.

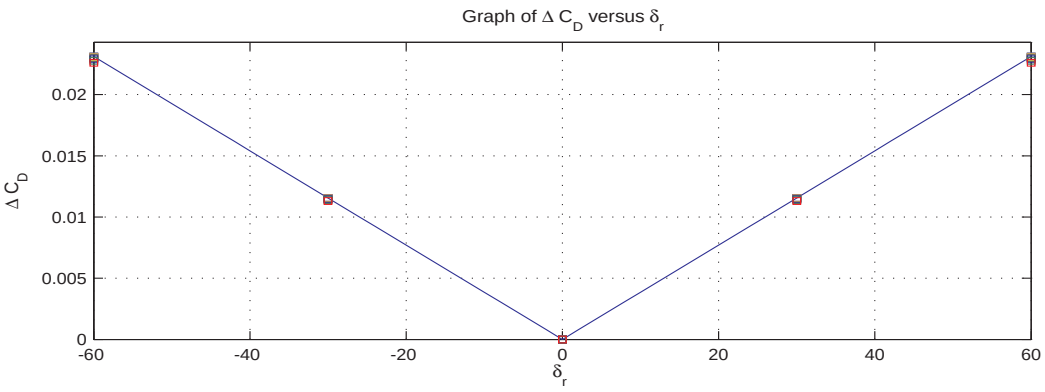

Figure A.3. C_D vs. δ_r.

Table A.1. Drag Coefficient Parameters

$C^{\beta 2}_{D_{\alpha 2}}$	-4.1140	$C^{\alpha 2}_{D_{\delta_{a2_p}}}$	0.0444	$C^{\alpha 2}_{D_{\delta_{e2_p}}}$	-1.5063
$C^{\beta 1}_{D_{\alpha 2}}$	-0.0000	$C^{\alpha 1}_{D_{\delta_{a2_p}}}$	-0.0513	$C^{\alpha 1}_{D_{\delta_{e2_p}}}$	-0.0580
$C^{\beta 0}_{D_{\alpha 2}}$	1.5684	$C^{\alpha 0}_{D_{\delta_{a2_p}}}$	0.0101	$C^{\alpha 0}_{D_{\delta_{e2_p}}}$	-0.0021
$C^{\beta 2}_{D_{\alpha 1}}$	0.0957	$C^{\alpha 2}_{D_{\delta_{a1_p}}}$	-0.0931	$C^{\alpha 2}_{D_{\delta_{e1_p}}}$	2.7517
$C^{\beta 1}_{D_{\alpha 1}}$	-0.0000	$C^{\alpha 1}_{D_{\delta_{a1_p}}}$	0.0937	$C^{\alpha 1}_{D_{\delta_{e1_p}}}$	0.1060
$C^{\beta 0}_{D_{\alpha 1}}$	-1.17e-6	$C^{\alpha 0}_{D_{\delta_{a1_p}}}$	0.0054	$C^{\alpha 0}_{D_{\delta_{e1_p}}}$	0.0038
$C^{\beta 2}_{D_{\alpha 0}}$	0.0291	$C^{\alpha 2}_{D_{\delta_{a3_n}}}$	-3.0483	$C^{\alpha 2}_{D_{\delta_{e3_n}}}$	-3.0489
$C^{\beta 1}_{D_{\alpha 0}}$	-0.0000	$C^{\alpha 1}_{D_{\delta_{a3_n}}}$	0.1165	$C^{\alpha 1}_{D_{\delta_{e3_n}}}$	0.1173
$C^{\beta 0}_{D_{\alpha 0}}$	0.0102	$C^{\alpha 0}_{D_{\delta_{a3_n}}}$	-0.0020	$C^{\alpha 0}_{D_{\delta_{e3_n}}}$	-0.0039
$C^{\alpha 1}_{D_q}$	1.7617	$C^{\alpha 2}_{D_{\delta_{a2_n}}}$	-5.0424	$C^{\alpha 2}_{D_{\delta_{e2_n}}}$	-5.0376
$C^{\alpha 0}_{D_q}$	-0.0278	$C^{\alpha 1}_{D_{\delta_{a2_n}}}$	0.1925	$C^{\alpha 1}_{D_{\delta_{e2_n}}}$	0.1937
$C^{\alpha 2}_{D_{\delta_{r1}}}$	-0.0110	$C^{\alpha 0}_{D_{\delta_{a2_n}}}$	0.0081	$C^{\alpha 0}_{D_{\delta_{e2_n}}}$	-0.0065
$C^{\alpha 1}_{D_{\delta_{r1}}}$	-0.0000	$C^{\alpha 2}_{D_{\delta_{a1_n}}}$	-3.6853	$C^{\alpha 2}_{D_{\delta_{e1_n}}}$	-3.6877
$C^{\alpha 0}_{D_{\delta_{r1}}}$	0.0221	$C^{\alpha 1}_{D_{\delta_{a1_n}}}$	0.1409	$C^{\alpha 1}_{D_{\delta_{e1_n}}}$	0.1418
–	–	$C^{\alpha 0}_{D_{\delta_{a1_n}}}$	-0.0060	$C^{\alpha 0}_{D_{\delta_{e1_n}}}$	-0.0048

A.2 Side Force Coefficient

Figs. *A*.4 - *A*.9 depict the side force dependencies on angle of attack and control effectors. Table A.2 gives the values of the side force coefficients in Section 2.1.1.3.

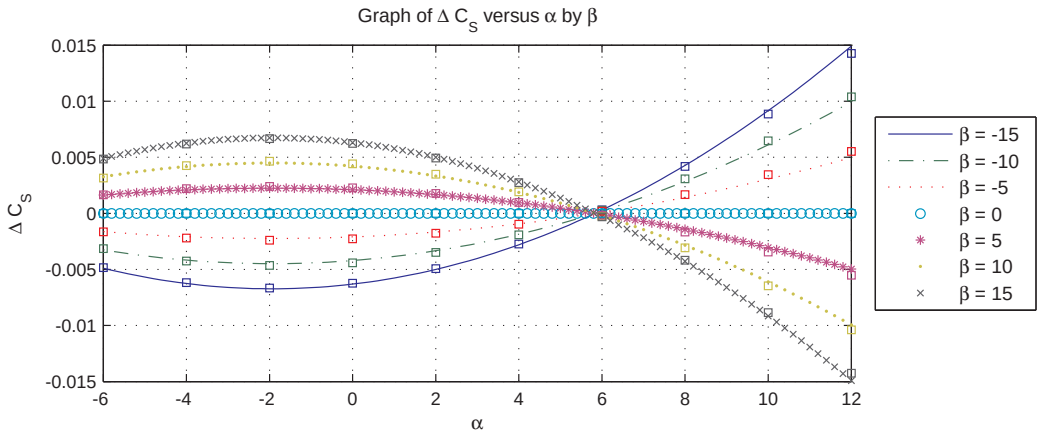

Figure A.4. C_S vs. α.

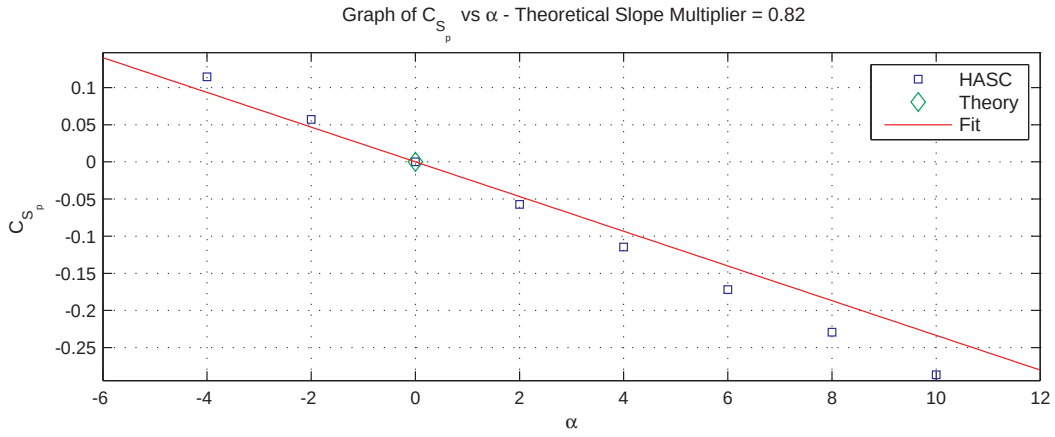

Figure A.5. C_S (Rolling Moment) vs. α.

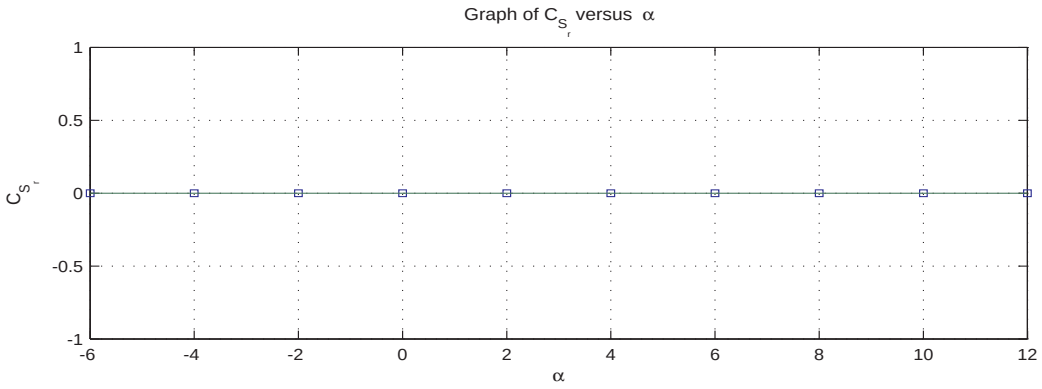

Figure A.6. C_S (Yawing Moment) vs. α.

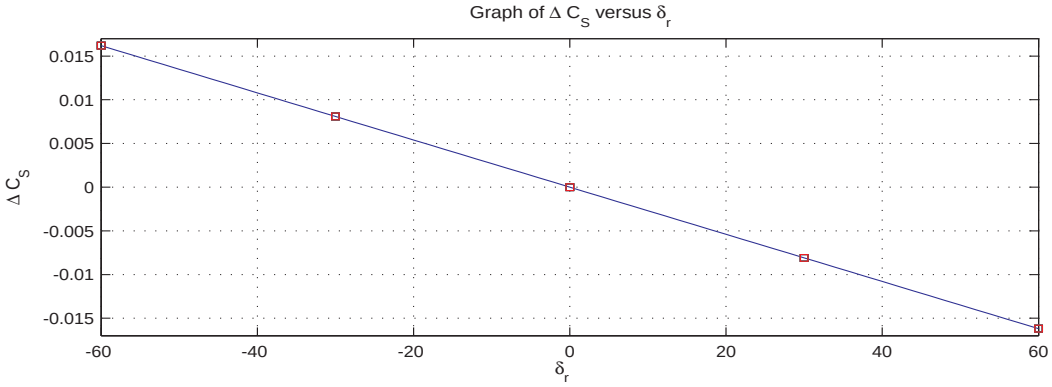

Figure A.7. C_S vs. δ_r.

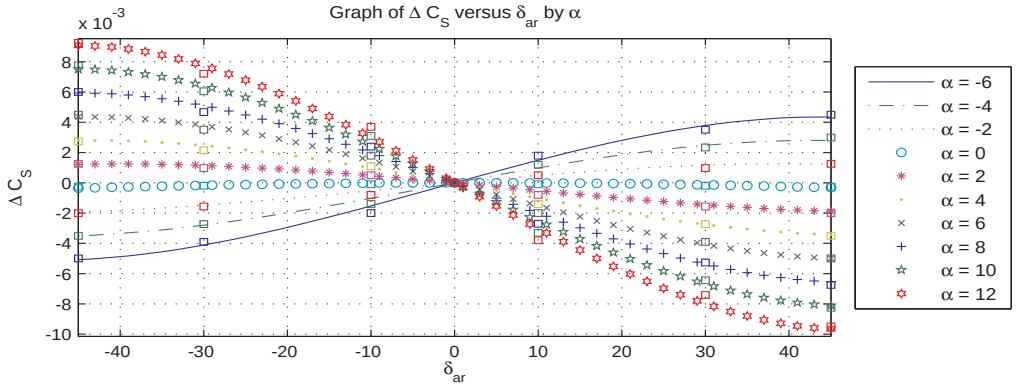

Figure A.8. C_S vs. δ_{ar}.

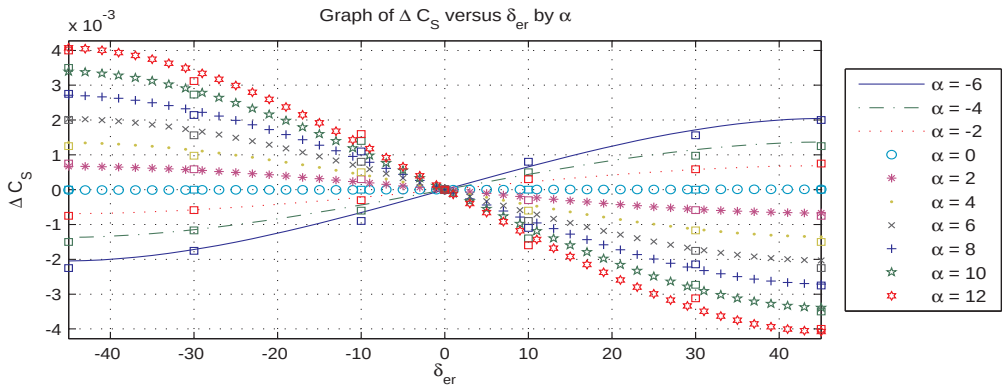

Figure A.9. C_S vs. δ_{er}.

Table A.2. Side Force Coefficient Parameters

$C^{\beta 1}_{S_{\alpha 2}}$	-1.3971	$C^{\alpha 0}_{S_{\delta_{a1}}}$	-2.93e-5
$C^{\beta 0}_{S_{\alpha 2}}$	0.0000	$C^{\alpha 1}_{S_{\delta_{e3}}}$	-0.0187
$C^{\beta 1}_{S_{\alpha 1}}$	-0.0946	$C^{\alpha 0}_{S_{\delta_{e3}}}$	8.61e-6
$C^{\beta 0}_{S_{\alpha 1}}$	-0.0000	$C^{\alpha 1}_{S_{\delta_{e2}}}$	-0.0000
$C^{\beta 1}_{S_{\alpha 0}}$	0.0241	$C^{\alpha 0}_{S_{\delta_{e2}}}$	-0.0000
$C^{\beta 0}_{S_{\alpha 0}}$	0.0000	$C^{\alpha 1}_{S_{\delta_{e1}}}$	0.0364
$C_{S_{\delta_{r1}}}$	-0.0155	$C^{\alpha 0}_{S_{\delta_{e1}}}$	-1.67e-5
$C^{\alpha 1}_{S_{\delta_{a3}}}$	-0.0430	$C^{\alpha 1}_{S_p}$	-1.3386
$C^{\alpha 0}_{S_{\delta_{a3}}}$	1.51e-5	$C^{\alpha 0}_{S_p}$	8.54e-5
$C^{\alpha 1}_{S_{\delta_{a2}}}$	-0.0004	$C^{\alpha 1}_{S_r}$	0.0000
$C^{\alpha 0}_{S_{\delta_{a2}}}$	0.0005	$C^{\alpha 0}_{S_r}$	0.0000
$C^{\alpha 1}_{S_{\delta_{a1}}}$	0.0836	–	–

A.3 Lift Coefficient

A graphical representation of some of the relationships depicted in Eq. (2.40) is shown in Figs. *A*.10 - *A*.13. Table A.3 gives the values of the lift coefficients in Section 2.1.1.3.

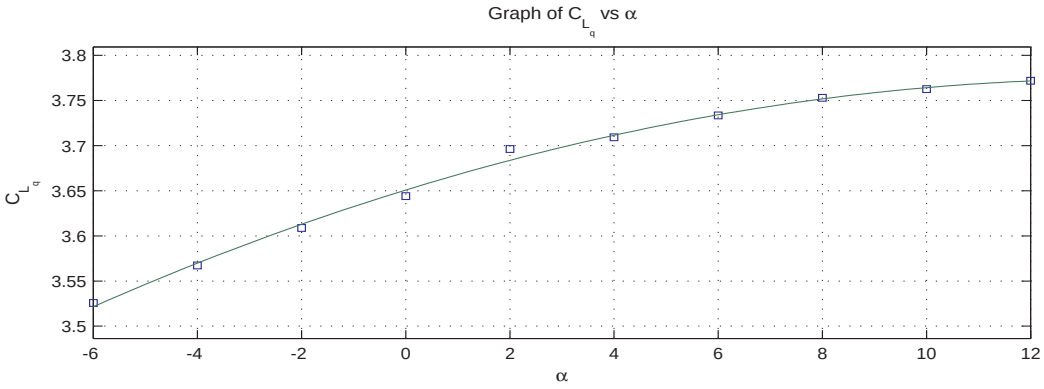

Figure A.10. C_L (Pitching Moment) vs. α.

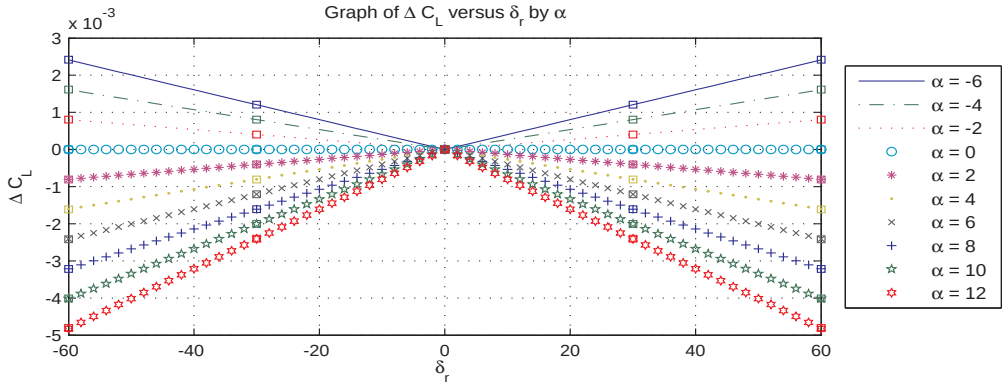

Figure A.11. C_L vs. δ_r.

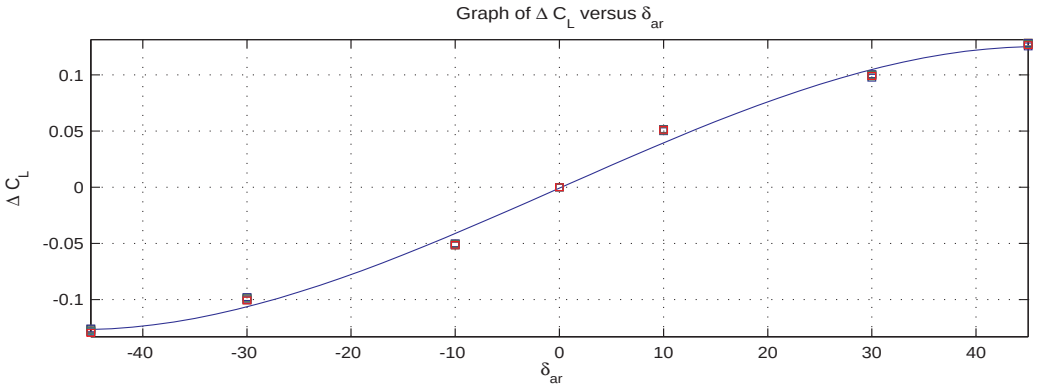

Figure A.12. C_L vs. δ_{ar}.

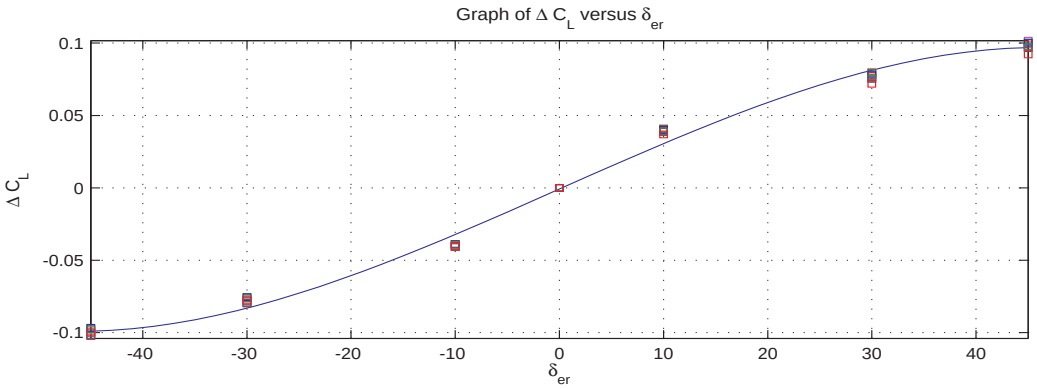

Figure A.13. C_L vs. δ_{er}.

Table A.3. Lift Coefficient Parameters

$C^{\beta 2}_{L_{\alpha 1}}$	-4.2975	$C^{\alpha 1}_{L_{\delta_{r1}}}$	-0.0220
$C^{\beta 1}_{L_{\alpha 1}}$	-0.0000	$C^{\alpha 0}_{L_{\delta_{r1}}}$	1.31e-6
$C^{\beta 0}_{L_{\alpha 1}}$	4.4955	$C_{L_{\delta_{a3}}}$	-0.1208
$C^{\beta 2}_{L_{\alpha 0}}$	0.0004	$C_{L_{\delta_{a2}}}$	0.0001
$C^{\beta 1}_{L_{\alpha 0}}$	0.0000	$C_{L_{\delta_{a1}}}$	0.2348
$C^{\beta 0}_{L_{\alpha 0}}$	-0.0008	$C_{L_{\delta_{e3}}}$	-0.0940
$C^{\alpha 2}_{L_q}$	-2.0900	$C_{L_{\delta_{e2}}}$	-0.0005
$C^{\alpha 1}_{L_q}$	1.0147	$C_{L_{\delta_{e1}}}$	0.1827
$C^{\alpha 1}_{L_q}$	3.6508	–	–

A.4 Rolling Moment Coefficient

A graphical representation of the relationships depicted in Eq. (2.48) is shown in Figs. *A*.14 - *A*.20. $C_{\mathcal{L}}$ is independent of δ_b and q. Table A.4 gives the values of the rolling moment coefficients in Section 2.1.1.4.

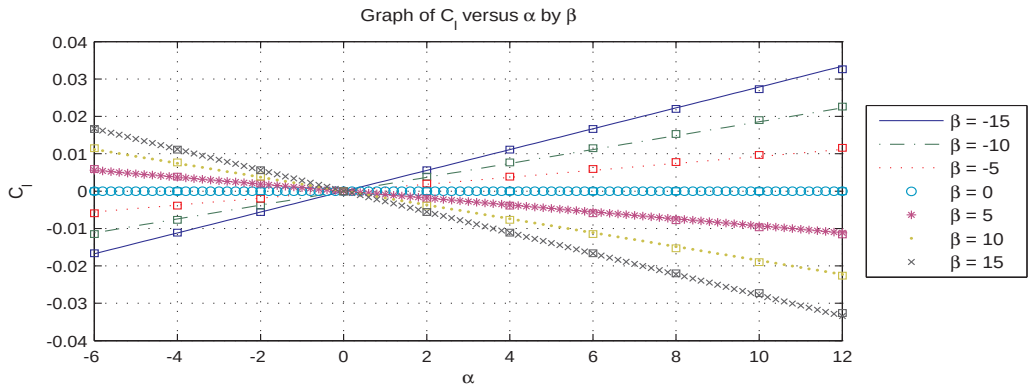

Figure A.14. $C_{\mathcal{L}}$ vs. α.

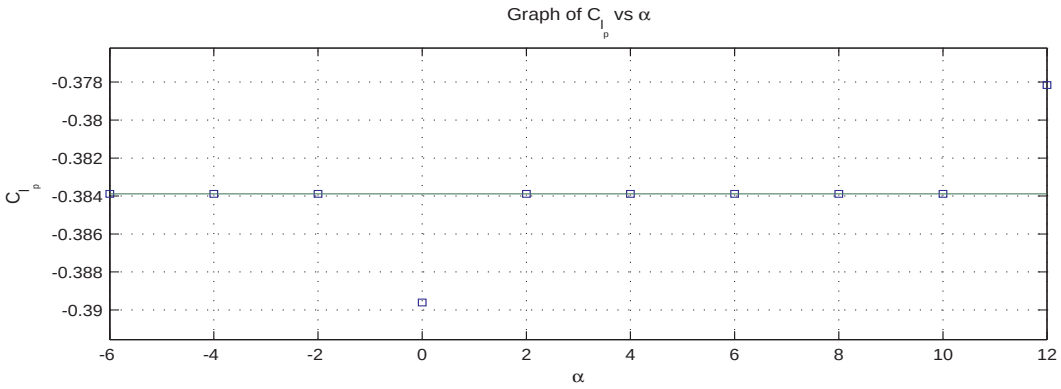

Figure A.15. $C_{\mathcal{L}}$ (Rolling Moment) vs. α.

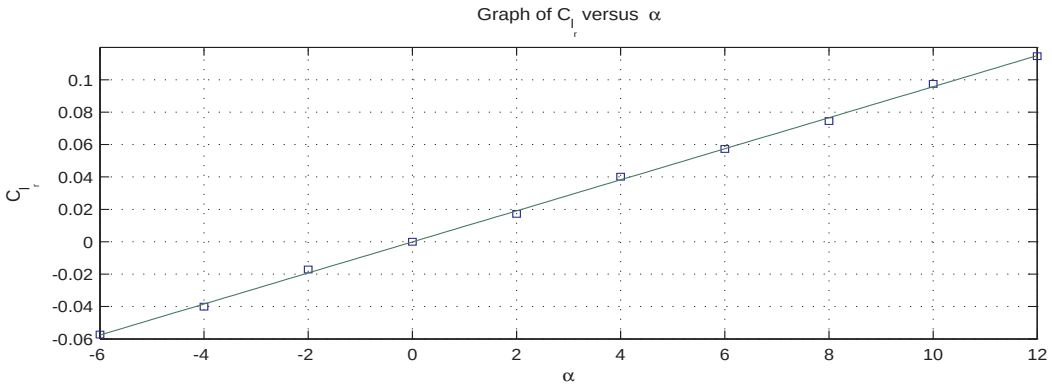

Figure A.16. $C_{\mathcal{L}}$ (Yawing Moment) vs. α.

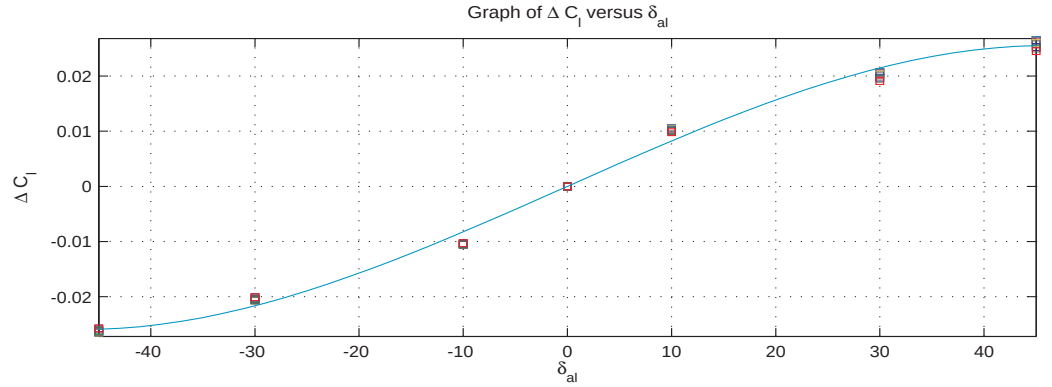

Figure A.17. $C_{\mathcal{L}}$ vs. δ_{al}.

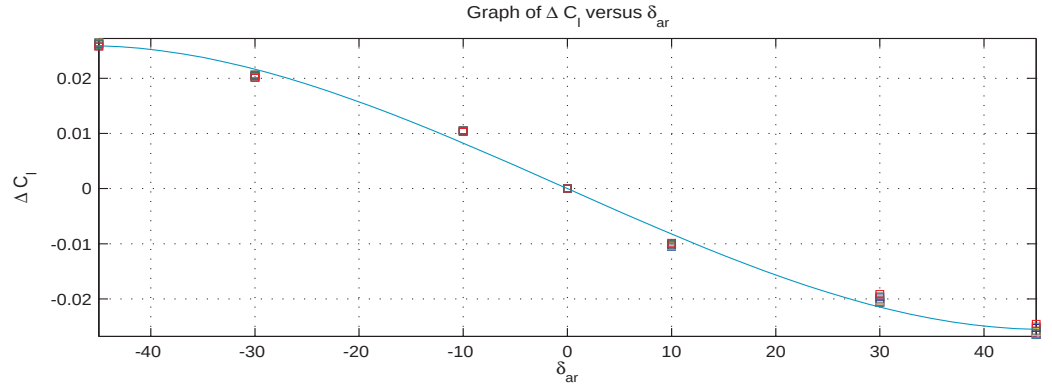

Figure A.18. $C_{\mathcal{L}}$ vs. δ_{ar}.

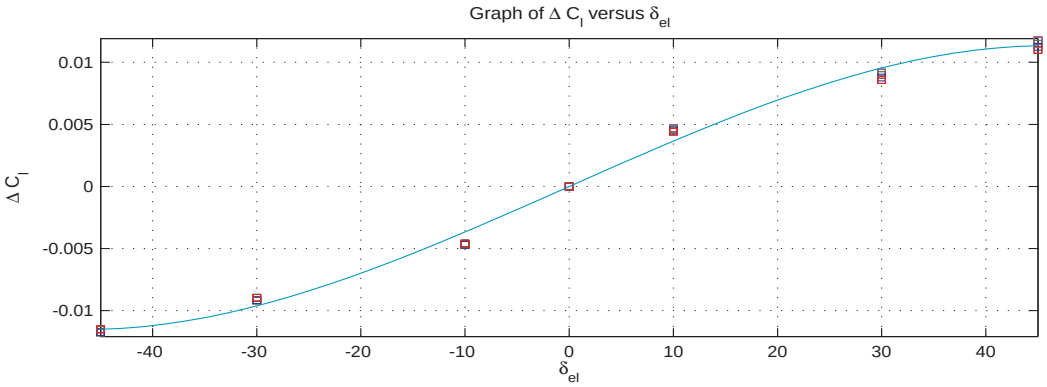

Figure A.19. $C_{\mathcal{L}}$ vs. δ_{el}.

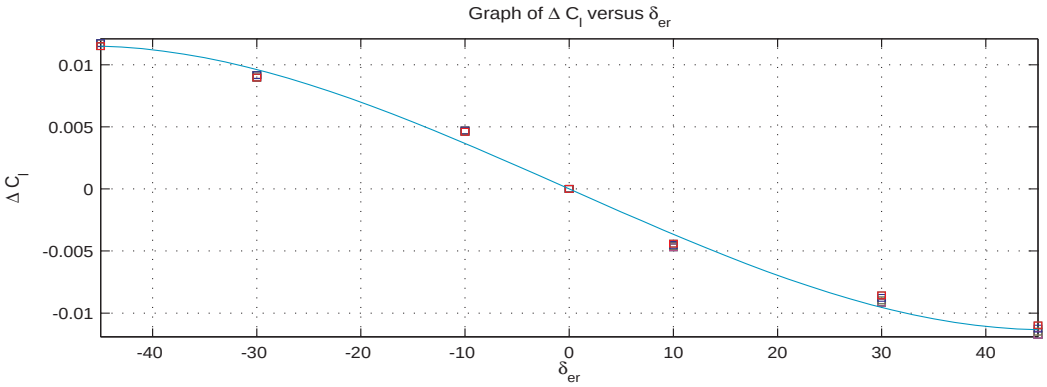

Figure A.20. $C_{\mathcal{L}}$ vs. δ_{er}.

Table A.4. Rolling Moment Coefficient Parameters

$C^{\beta 1}_{\mathcal{L}_{\alpha 1}}$	-0.6100
$C^{\beta 0}_{\mathcal{L}_{\alpha 1}}$	-0.0000
$C^{\beta 1}_{\mathcal{L}_{\alpha 0}}$	0.0001
$C^{\beta 0}_{\mathcal{L}_{\alpha 0}}$	0.0000
$C^{\alpha 1}_{\mathcal{L}_p}$	0.0000
$C^{\alpha 0}_{\mathcal{L}_p}$	-0.3839
$C^{\alpha 1}_{\mathcal{L}_r}$	0.5491
$C^{\alpha 0}_{\mathcal{L}_r}$	-0.0001
$C_{\mathcal{L}_{\delta_{a3}}}$	-0.0247
$C_{\mathcal{L}_{\delta_{a2}}}$	-0.0003
$C_{\mathcal{L}_{\delta_{a1}}}$	0.0479
$C_{\mathcal{L}_{\delta_{e3}}}$	-0.0110
$C_{\mathcal{L}_{\delta_{e2}}}$	-0.0001
$C_{\mathcal{L}_{\delta_{e1}}}$	0.0213

A.5 Pitching Moment Coefficient

A graphical representation of the relationships depicted in Eq. (2.53) is shown in Figures: $A.21$ - $A.26$. Table A.5 gives the values of the pitching moment coefficients in Section 2.1.1.4.

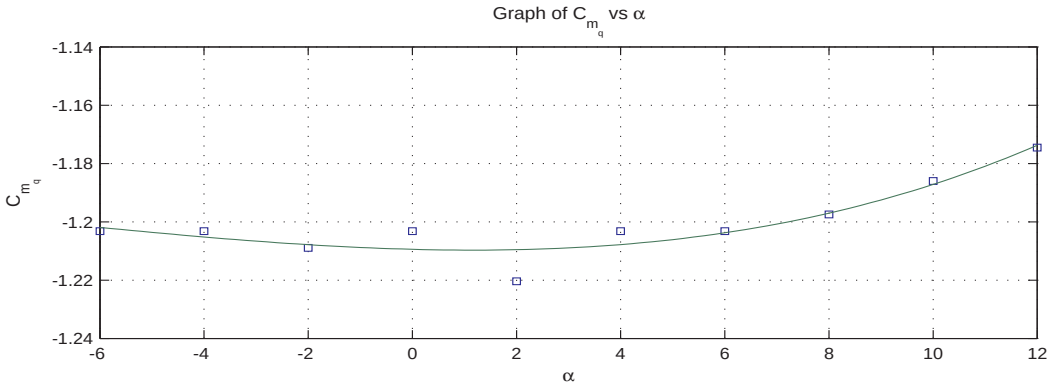

Figure A.21. $C_{\mathcal{M}}$ (Pitching Moment) vs. α.

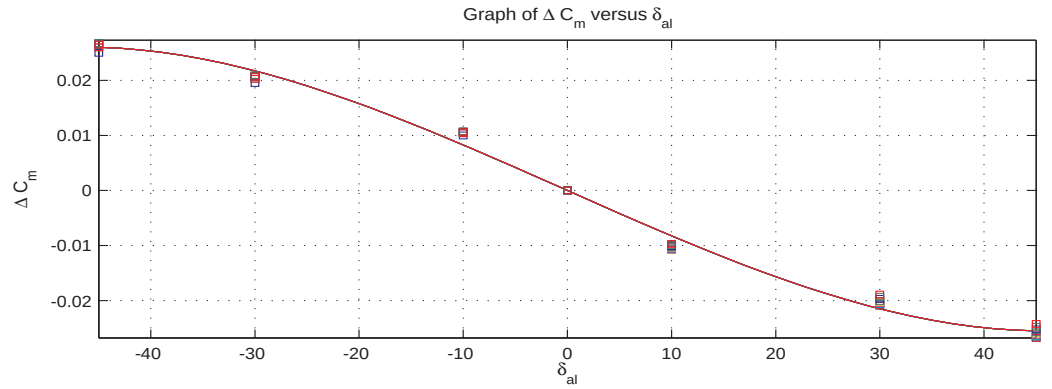

Figure A.22. $C_{\mathcal{M}}$ vs. δ_{al}.

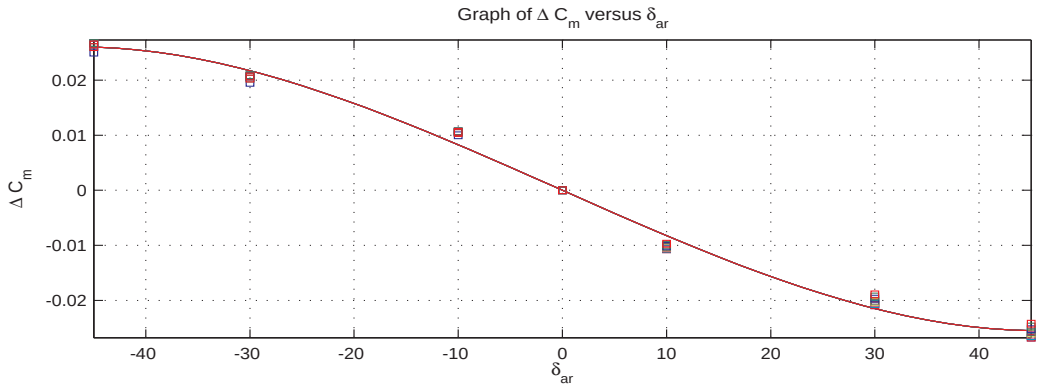

Figure A.23. $C_{\mathcal{M}}$ vs. δ_{ar}.

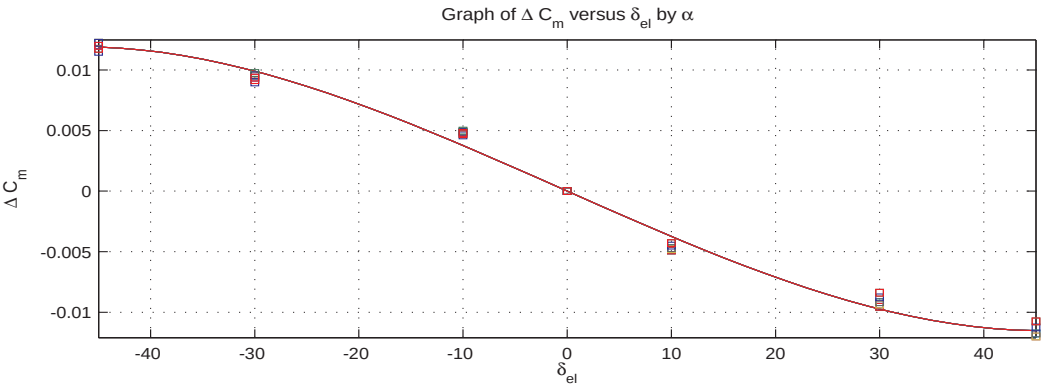

Figure A.24. $C_{\mathcal{M}}$ vs. δ_{el}.

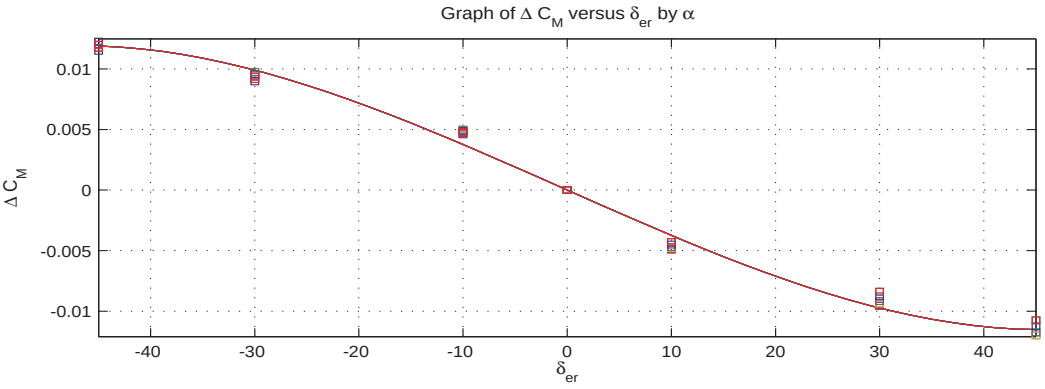

Figure A.25. $C_{\mathcal{M}}$ vs. δ_{er}.

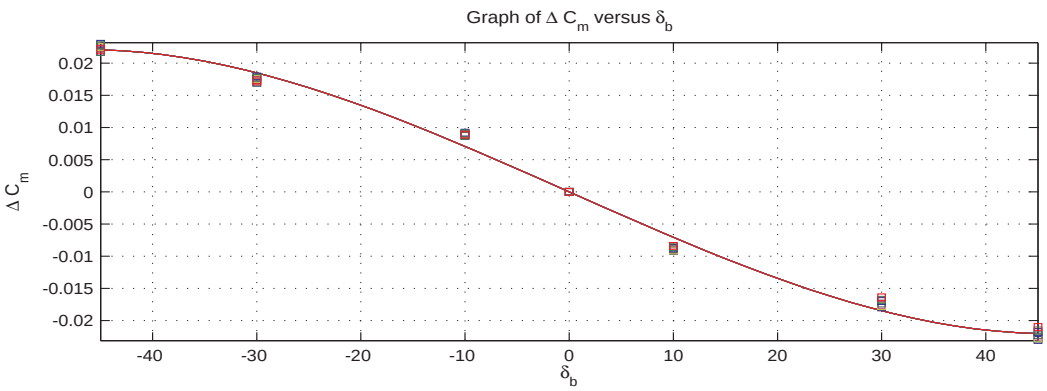

Figure A.26. $C_{\mathcal{M}}$ vs. δ_b.

Table A.5. Pitching Moment Coefficient Parameters

$C_{\mathcal{M}_{\delta_{a3}}}$	0.0247
$C_{\mathcal{M}_{\delta_{a2}}}$	0.0004
$C_{\mathcal{M}_{\delta_{a1}}}$	-0.0480
$C_{\mathcal{M}_{\delta_{e3}}}$	0.0112
$C_{\mathcal{M}_{\delta_{e2}}}$	0.0003
$C_{\mathcal{M}_{\delta_{e1}}}$	-0.0218
$C^{\alpha 3}_{\mathcal{M}_q}$	1.6224
$C^{\alpha 2}_{\mathcal{M}_q}$	0.6001
$C^{\alpha 1}_{\mathcal{M}_q}$	-0.0266
$C^{\alpha 0}_{\mathcal{M}_q}$	-1.2094
$C_{\mathcal{M}_{\alpha 1}}$	-0.0969
$C_{\mathcal{M}_{\alpha 0}}$	-0.0000

A.6 Yawing Moment Coefficient

A graphical representation of some of the relationships depicted in Eq. (2.54) is shown in Figs. *A*.27 - *A*.31. Table B.6 gives the values of the yawing moment coefficients in Section 2.1.1.4.

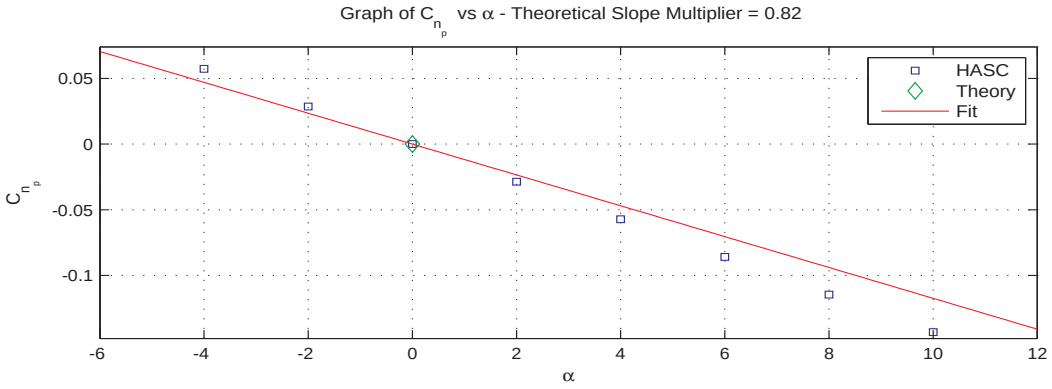

Figure A.27. $C_{\mathcal{N}}$ (Rolling Moment) vs. α.

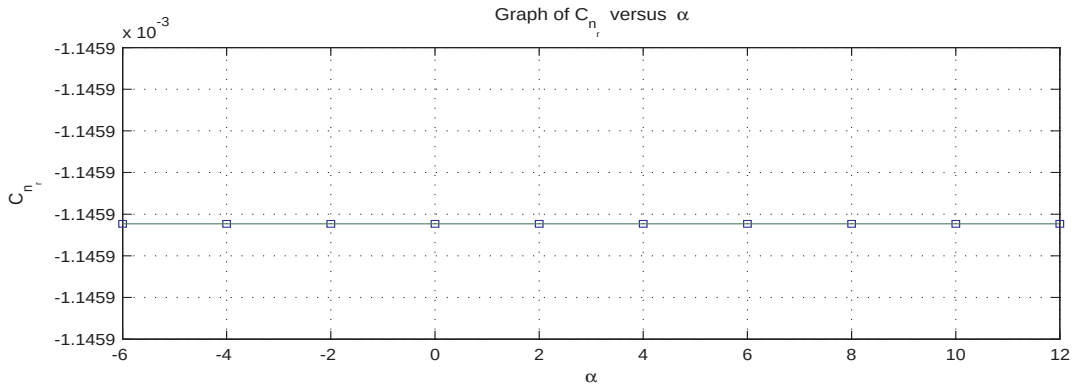

Figure A.28. $C_{\mathcal{N}}$ (Yawing Moment) vs. α.

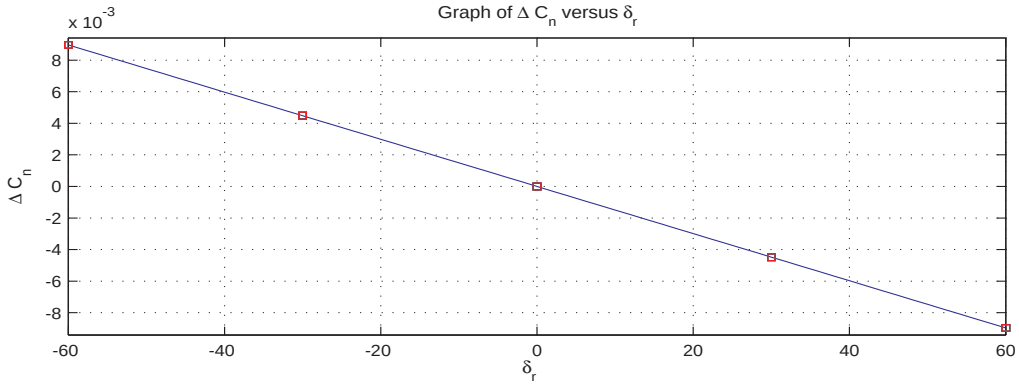

Figure A.29. $C_{\mathcal{N}}$ vs. δ_r.

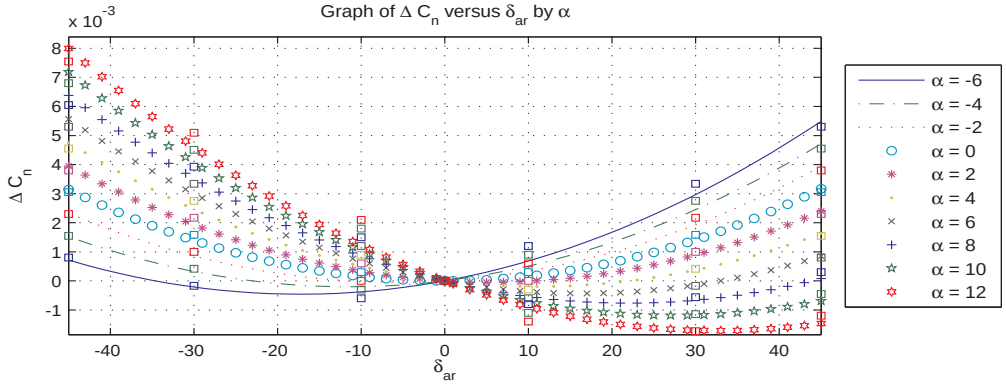

Figure A.30. $C_{\mathcal{N}}$ vs. δ_{ar}.

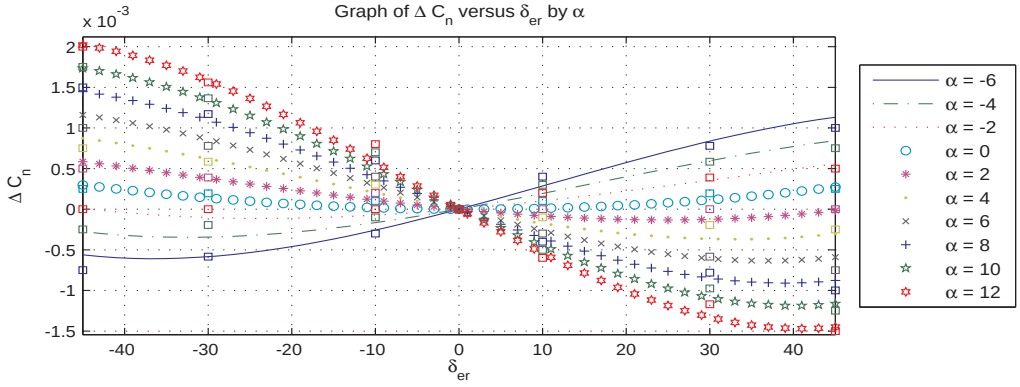

Figure A.31. $C_{\mathcal{N}}$ vs. δ_{er}.

Table A.6. Yawing Moment Coefficient Parameters

$C^{\alpha 1}_{\mathcal{N}_p}$	-0.6730
$C^{\alpha 0}_{\mathcal{N}_p}$	-0.0000
$C^{\alpha 1}_{\mathcal{N}_r}$	-0.0000
$C^{\alpha 0}_{\mathcal{N}_r}$	-0.0011
$C_{\mathcal{N}_{\delta_{r1}}}$	-0.0086
$C^{\alpha 1}_{\mathcal{N}_{\delta_{a2}}}$	-0.0008
$C^{\alpha 0}_{\mathcal{N}_{\delta_{a2}}}$	-0.0051
$C^{\alpha 1}_{\mathcal{N}_{\delta_{a1}}}$	0.0288
$C^{\alpha 0}_{\mathcal{N}_{\delta_{a1}}}$	-0.0000
$C^{\alpha 1}_{\mathcal{N}_{\delta_{e3}}}$	-0.0079
$C^{\alpha 0}_{\mathcal{N}_{\delta_{e3}}}$	-0.0000
$C^{\alpha 1}_{\mathcal{N}_{\delta_{e2}}}$	-0.0000
$C^{\alpha 0}_{\mathcal{N}_{\delta_{e2}}}$	-0.0005
$C^{\alpha 1}_{\mathcal{N}_{\delta_{e1}}}$	0.0153
$C^{\alpha 0}_{\mathcal{N}_{\delta_{e1}}}$	0.0000

APPENDIX B

KC-135R AERODYNAMIC MODEL DATA

This appendix contains additional plots aerodynamic force and moment coefficients of the KC-135R aircraft. In addition, the values for all coefficients and stability derivatives are given in this appendix.

B.1 Drag Coefficient

Figures B.1 to B.3 depict the dependence of the drag coefficient on the elevator, aileron, and rudder deflections respectively.

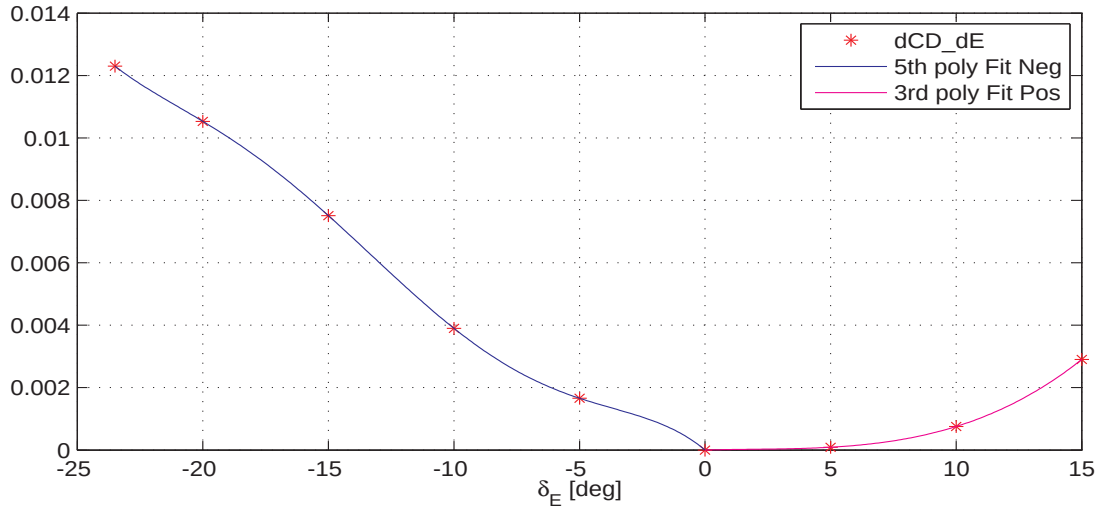

Figure B.1. $\boldsymbol{f}_{C_{D_{\delta_e}}}$ (Drag Coefficient Increment) versus δ_e (elevator deflection).

B.2 Lift Coefficient

The lift coefficient dependency on the rate of change of angle of attack and elevator deflection is depicted in Figs. B.4 and B.5.

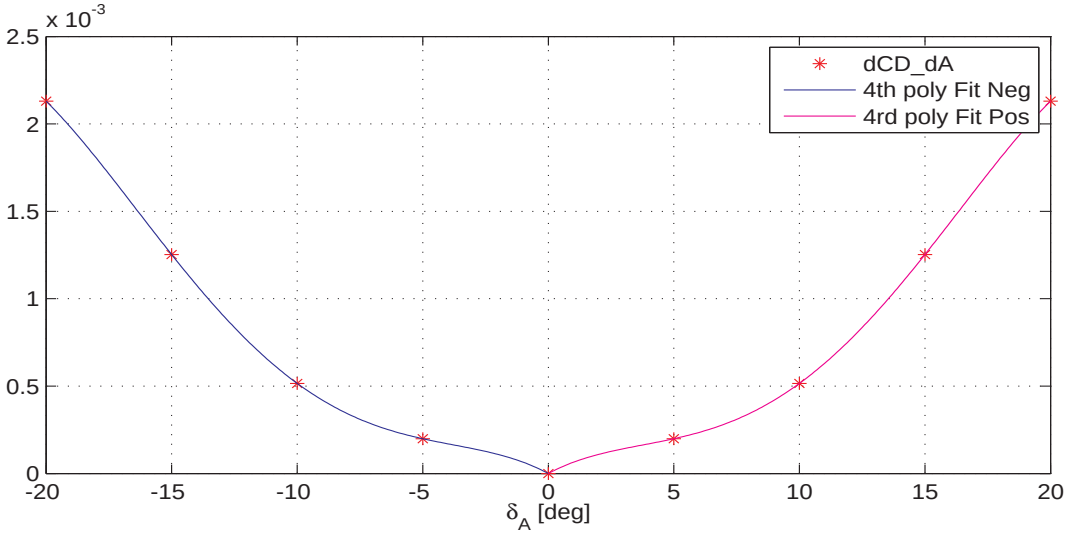

Figure B.2. $\boldsymbol{f}_{C_{D_{\delta_a}}}$ (Drag Coefficient Increment) versus δ_a (aileron deflection).

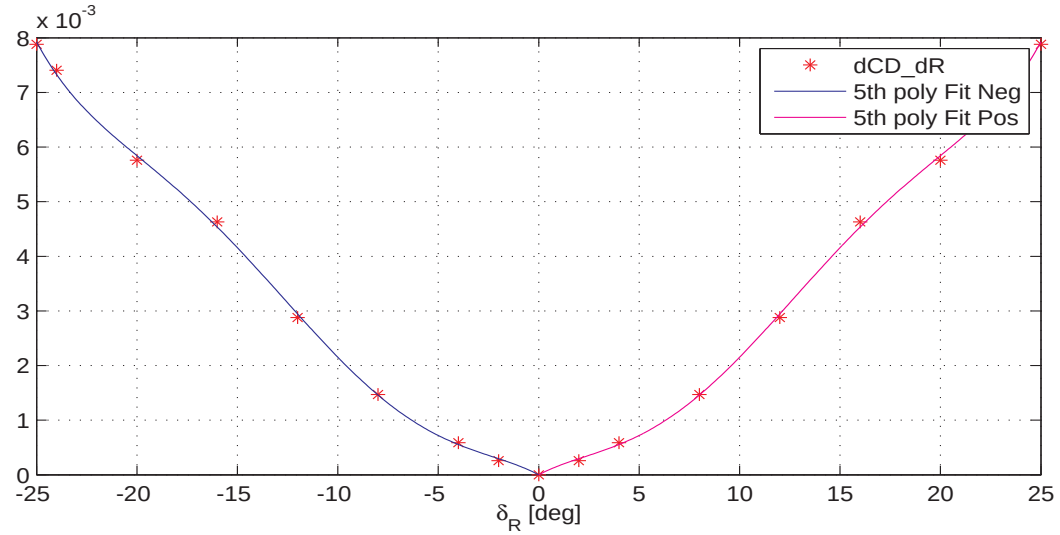

Figure B.3. $\boldsymbol{f}_{C_{D_{\delta_r}}}$ (Drag Coefficient Increment) versus δ_r (rudder deflection).

B.3 Side Force Coefficient

Figure B.6 shows the side force coefficient dependency on the roll rate versus angle of attack while Fig. B.7 shows the side force increment relationship with the rudder deflection.

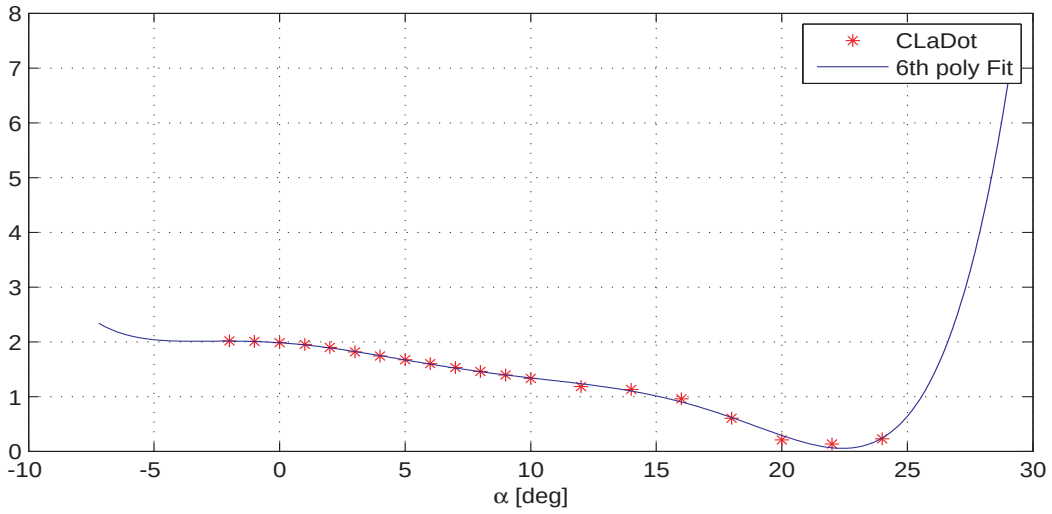

Figure B.4. $\boldsymbol{C}_{L_{\dot{\alpha}}}$ (Lift Coefficient dependency on $\dot{\alpha}$) versus α (angle-of-attack).

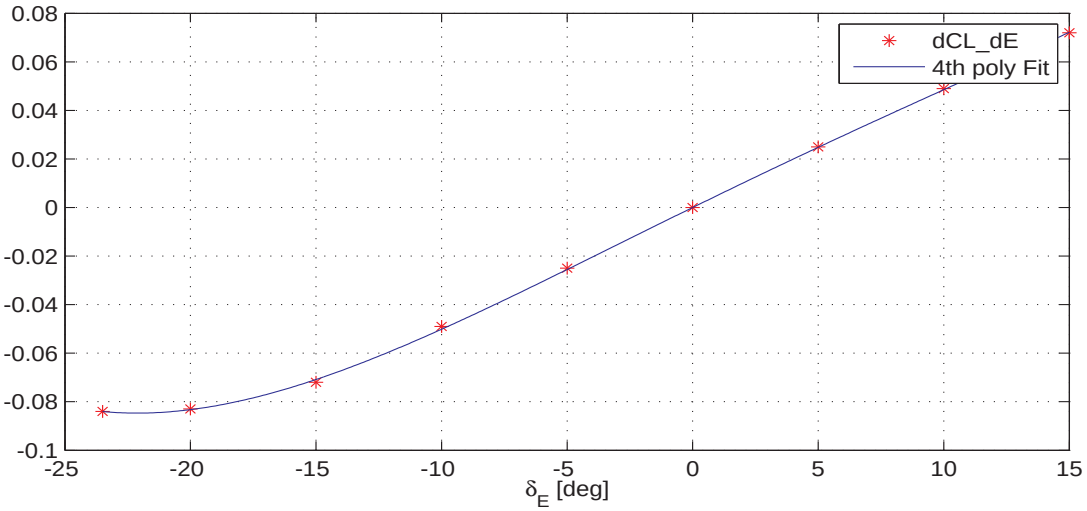

Figure B.5. $\boldsymbol{f}_{\boldsymbol{C}_{L_{\delta_e}}}$ (Lift Coefficient Increment) versus δ_e (elevator deflection).

B.4 Rolling Moment Coefficient

Figs. B.8 through B.12 depict rolling moment dependencies on angle of attack and sideslip, euler angle rates, and control effector deflections.

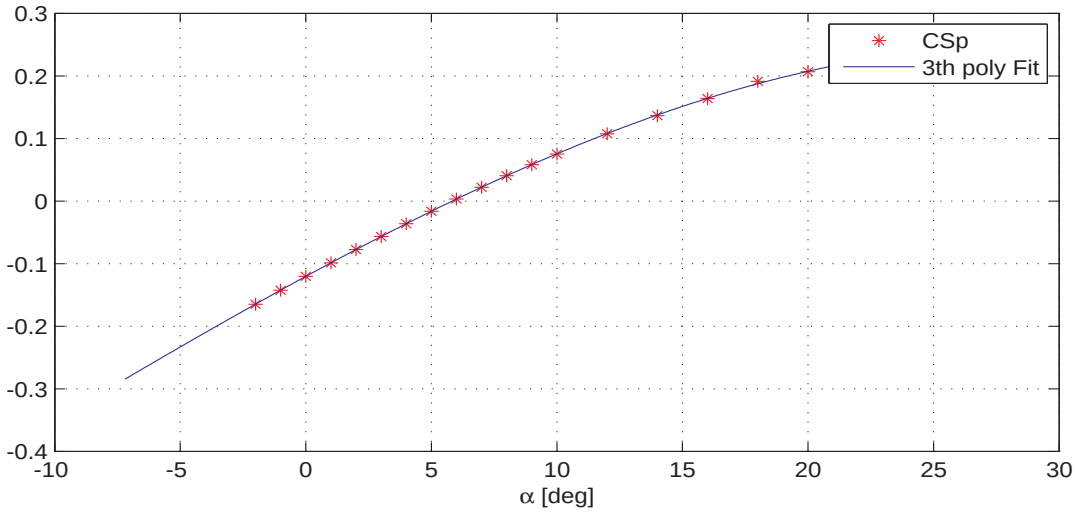

Figure B.6. $\boldsymbol{C}_{S_{p1}}$ (Side Force Coefficient Dependency on Rolling Rate) versus α (angle-of-attack).

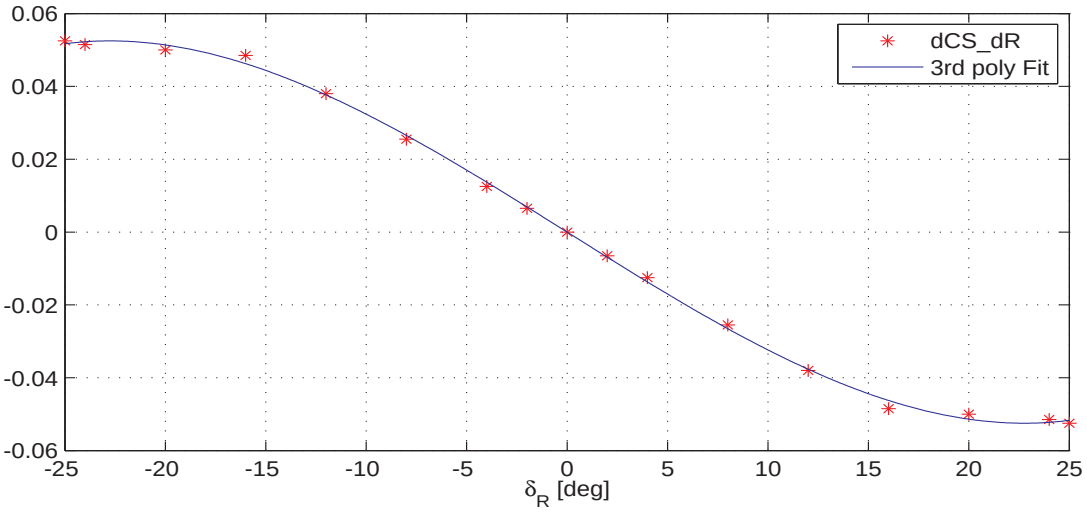

Figure B.7. $\boldsymbol{f}_{\boldsymbol{C}_{S_{\delta_r}}}$ (Side Force Coefficient Increment) versus δ_r (rudder deflection).

B.5 Pitching Moment Coefficient

Figs. B.13 and B.14 depict pitching moment coefficient dependencies on angle of attack elevator deflections.

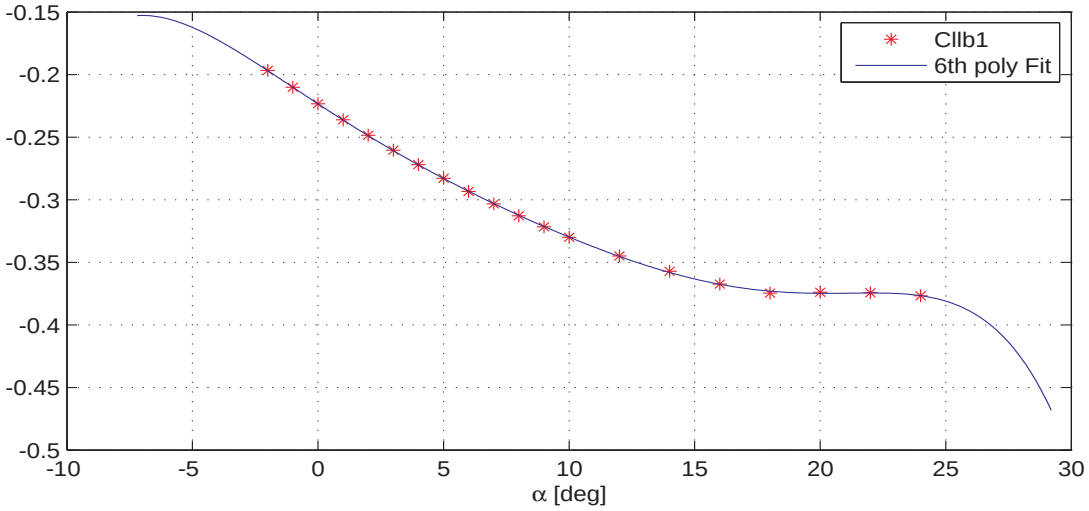

Figure B.8. $\boldsymbol{C}_{\mathcal{L}_{\beta 1}}$ (Rolling Moment Coefficient Dependency on Side Slip Angle) versus α (angle-of-attack).

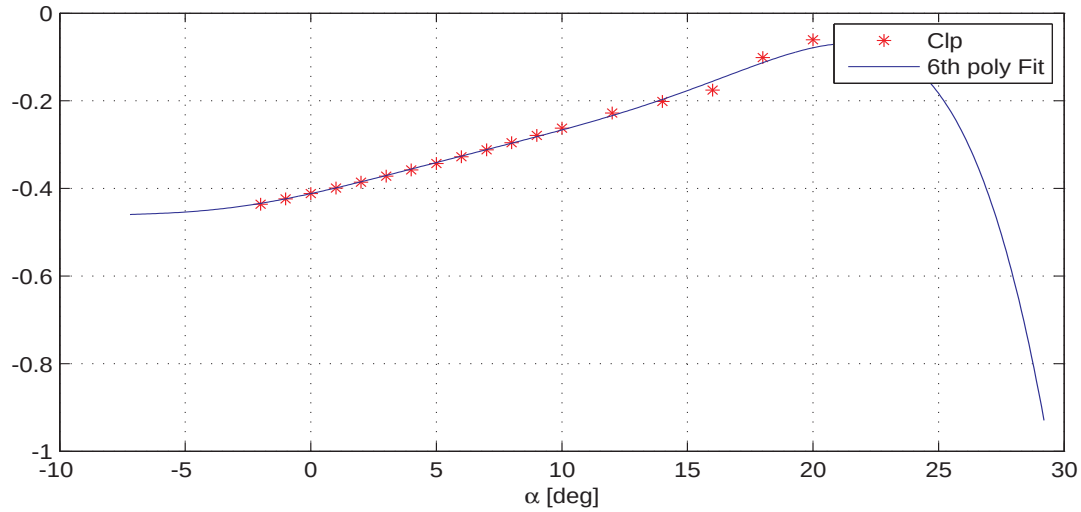

Figure B.9. $\boldsymbol{C}_{\mathcal{L}_{p1}}$ (Rolling Moment Coefficient Dependency on Rolling Rate) versus α (angle-of-attack).

Table B.1. Drag Coefficient Parameters

$C_{D_{\alpha 6}}$	759.1819	$C_{D_{\delta_{a4_n}}}$	-0.4189	$C_{D_{\delta_{e5_n}}}$	-8.5537	$C_{D_{\delta_{r5_n}}}$	-3.8819
$C_{D_{\alpha 5}}$	-857.8747	$C_{D_{\delta_{a3_n}}}$	-0.2953	$C_{D_{\delta_{e4_n}}}$	-9.4403	$C_{D_{\delta_{r4_n}}}$	-3.9268
$C_{D_{\alpha 4}}$	350.5271	$C_{D_{\delta_{a2_n}}}$	-0.0473	$C_{D_{\delta_{e3_n}}}$	-3.5125	$C_{D_{\delta_{r3_n}}}$	-1.2818
$C_{D_{\alpha 3}}$	-63.1476	$C_{D_{\delta_{a1_n}}}$	-0.0044	$C_{D_{\delta_{e2_n}}}$	-0.4635	$C_{D_{\delta_{r2_n}}}$	-0.1182
$C_{D_{\alpha 2}}$	5.1159	$C_{D_{\delta_{a0_n}}}$	0	$C_{D_{\delta_{e1_n}}}$	-0.0385	$C_{D_{\delta_{r1_n}}}$	-0.0112
$C_{D_{\alpha 1}}$	0.1582	$C_{D_{\delta_{a4_p}}}$	-0.4189	$C_{D_{\delta_{e0_n}}}$	0	$C_{D_{\delta_{r0_n}}}$	0
$C_{D_{\alpha 0}}$	0.0136	$C_{D_{\delta_{a3_p}}}$	0.2953	$C_{D_{\delta_{e3_p}}}$	0.2280	$C_{D_{\delta_{r5_p}}}$	3.8819
$C_{D_{\beta 2}}$	0.6621	$C_{D_{\delta_{a2_p}}}$	-0.0473	$C_{D_{\delta_{e2_p}}}$	-0.0221	$C_{D_{\delta_{r4_p}}}$	3.9268
$C_{D_{\beta 1}}$	0	$C_{D_{\delta_{a1_p}}}$	0.0044	$C_{D_{\delta_{e1_p}}}$	0.0012	$C_{D_{\delta_{r3_p}}}$	1.2818
$C_{D_{\beta 0}}$	0	$C_{D_{\delta_{a0_p}}}$	0	$C_{D_{\delta_{e0_p}}}$	0	$C_{D_{\delta_{r2_p}}}$	-0.1182
–	–	–	–	–	–	$C_{D_{\delta_{1_p}}}$	0.0112
–	–	–	–	–	–	$C_{D_{\delta_{r0_p}}}$	0

Table B.2. Lift Coefficient Parameters

$C^{\alpha 6}_{L_{\dot{\alpha}1}}$	7.6905E3	$C_{L_{\alpha 2}}$	-7.1271
$C^{\alpha 5}_{L_{\dot{\alpha}1}}$	-6.3346E3	$C_{L_{\alpha 1}}$	6.5688
$C^{\alpha 4}_{L_{\dot{\alpha}1}}$	1.4279E3	$C_{L_{\alpha 0}}$	0.2765
$C^{\alpha 3}_{L_{\dot{\alpha}1}}$	0.0021E3	$C_{L_{\delta_{e4}}}$	0.9651
$C^{\alpha 2}_{L_{\dot{\alpha}1}}$	-0.0283E3	$C_{L_{\delta_{e3}}}$	-0.2488
$C^{\alpha 1}_{L_{\dot{\alpha}1}}$	-0.0018E3	$C_{L_{\delta_{e2}}}$	-0.0563
$C^{\alpha 0}_{L_{\dot{\alpha}1}}$	0.0020E3	$C_{L_{\delta_{e1}}}$	0.2902
$C_{L_{q1}}$	8.3910	$C_{L_{\delta_{e0}}}$	0

Table B.3. Side Force Coefficient Parameters

$C^{\alpha 3}_{S_{p1}}$	-0.9171	$C_{S_{\delta_{r3}}}$	0.4189
$C^{\alpha 2}_{S_{p1}}$	-0.5690	$C_{S_{\delta_{r2}}}$	0
$C^{\alpha 1}_{S_{p1}}$	1.2493	$C_{S_{\delta_{r1}}}$	-0.1983
$C^{\alpha 0}_{S_{p1}}$	-0.1204	$C_{S_{\delta_{r0}}}$	0
$C_{S_{\beta 1}}$	0.6620	–	–

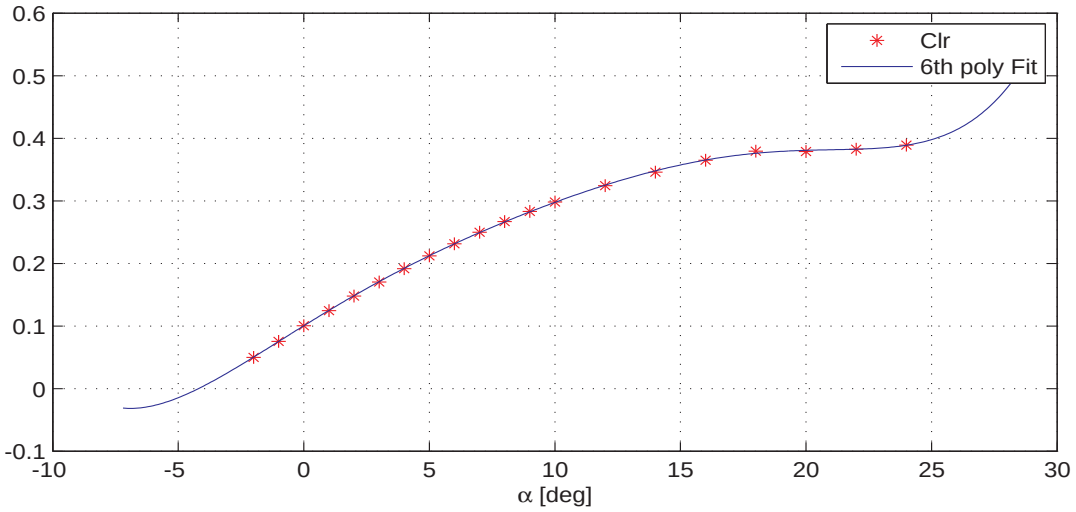

Figure B.10. $\boldsymbol{C}_{\mathcal{L}_{r1}}$ (Rolling Moment Coefficient Dependency on Yawing Rate) versus α (angle-of-attack).

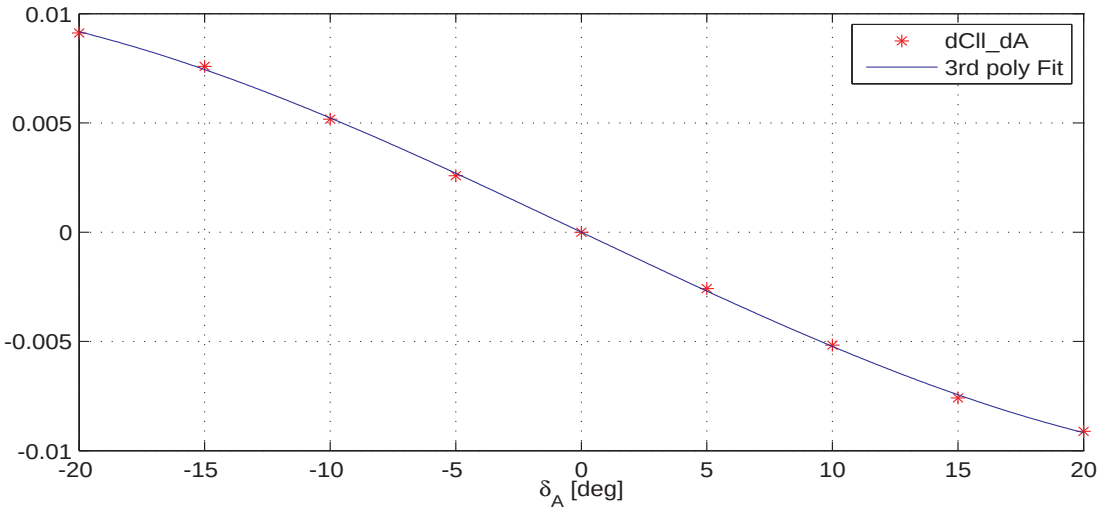

Figure B.11. $\boldsymbol{f}_{\boldsymbol{C}_{\mathcal{L}_{\delta_a}}}$ (Rolling Moment Coefficient Increment) versus δ_a (aileron deflection).

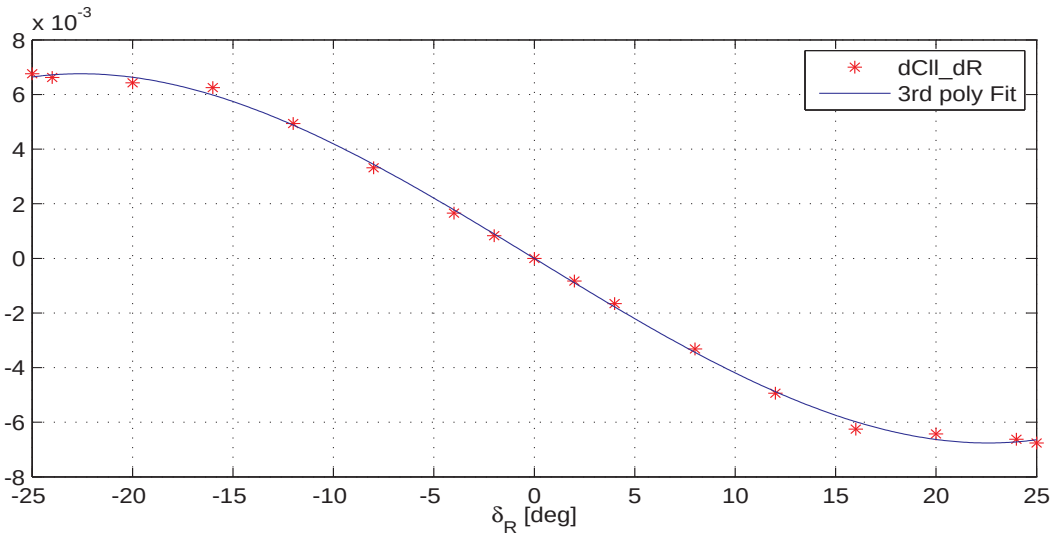

Figure B.12. $\boldsymbol{f}_{\boldsymbol{C}_{\mathcal{L}_{\delta_r}}}$ (Rolling Moment Coefficient Increment) versus δ_r (rudder deflection).

Table B.4. Rolling Moment Coefficient Parameters

$C^{\alpha 6}_{\mathcal{L}_{\beta 1}}$	-160.7288	$C^{\alpha 6}_{\mathcal{L}_{p1}}$	-395.0633	$C^{\alpha 6}_{\mathcal{L}_{r1}}$	282.2997	$C_{\mathcal{L}_{\delta_{a3}}}$	0.0403
$C^{\alpha 5}_{\mathcal{L}_{\beta 1}}$	156.2232	$C^{\alpha 5}_{\mathcal{L}_{p1}}$	216.2781	$C^{\alpha 5}_{\mathcal{L}_{r1}}$	-282.2450	$C_{\mathcal{L}_{\delta_{a2}}}$	0
$C^{\alpha 4}_{\mathcal{L}_{\beta 1}}$	-51.2088	$C^{\alpha 4}_{\mathcal{L}_{p1}}$	-7.2540	$C^{\alpha 4}_{\mathcal{L}_{r1}}$	97.9450	$C_{\mathcal{L}_{\delta_{a1}}}$	-0.0312
$C^{\alpha 3}_{\mathcal{L}_{\beta 1}}$	6.8714	$C^{\alpha 3}_{\mathcal{L}_{p1}}$	-10.7373	$C^{\alpha 3}_{\mathcal{L}_{r1}}$	-14.1518	$C_{\mathcal{L}_{\delta_{a0}}}$	0
$C^{\alpha 2}_{\mathcal{L}_{\beta 1}}$	0.4965	$C^{\alpha 2}_{\mathcal{L}_{p1}}$	1.9803	$C^{\alpha 2}_{\mathcal{L}_{r1}}$	-0.9597	$C_{\mathcal{L}_{\delta_{r3}}}$	0.0551
$C^{\alpha 1}_{\mathcal{L}_{\beta 1}}$	-0.7527	$C^{\alpha 1}_{\mathcal{L}_{p1}}$	0.7162	$C^{\alpha 1}_{\mathcal{L}_{r1}}$	1.4240	$C_{\mathcal{L}_{\delta_{r2}}}$	0
$C^{\alpha 0}_{\mathcal{L}_{\beta 1}}$	-0.2234	$C^{\alpha 0}_{\mathcal{L}_{p1}}$	-0.4119	$C^{\alpha 0}_{\mathcal{L}_{r1}}$	0.1004	$C_{\mathcal{L}_{\delta_{r1}}}$	-0.0257
–	—	–	–	–	–	$C_{\mathcal{L}_{\delta_{r0}}}$	0

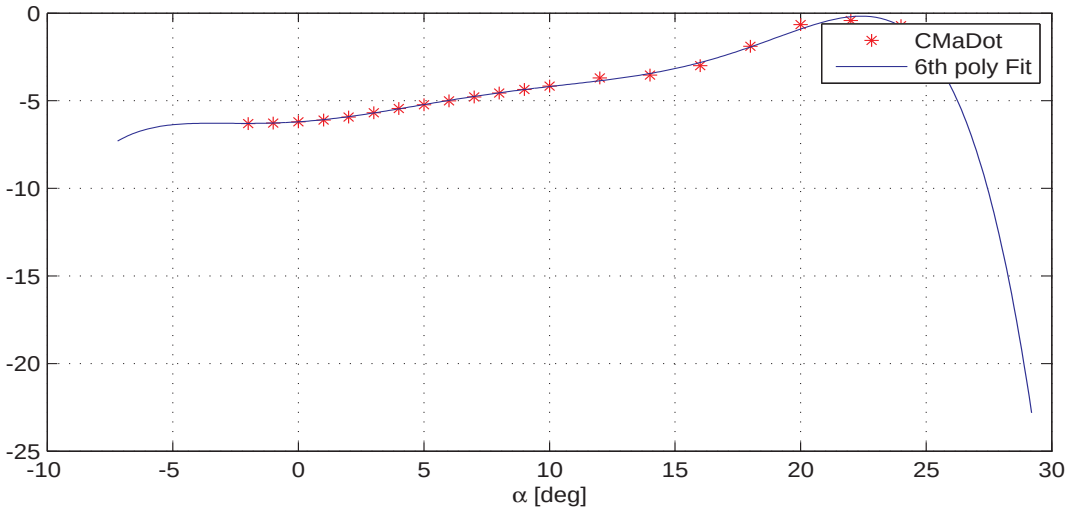

Figure B.13. $\boldsymbol{C}_{\mathcal{M}_{\dot{\alpha}}}$ (Pitching Moment Coefficient dependency on $\dot{\alpha}$) versus α (angle-of-attack).

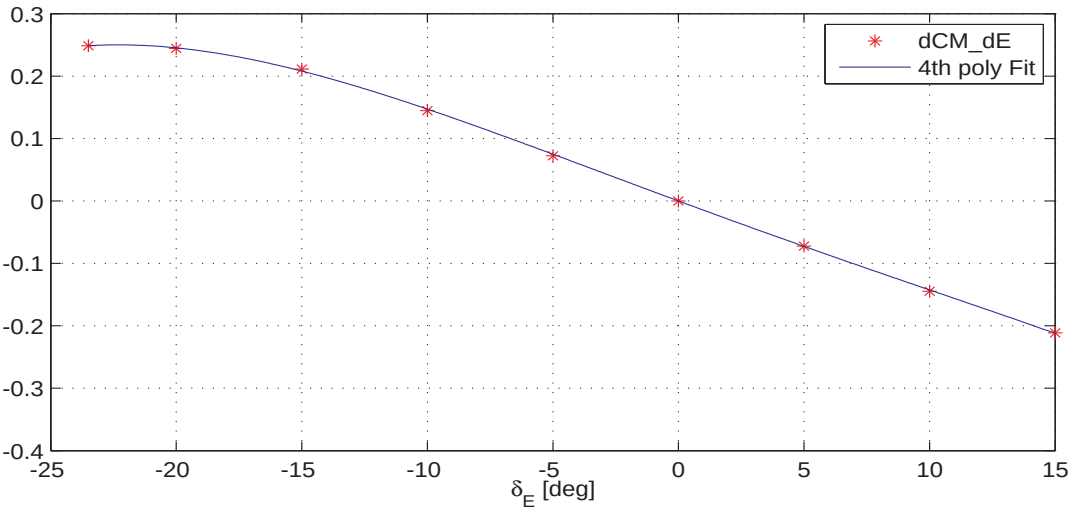

Figure B.14. $\boldsymbol{f}_{\boldsymbol{C}_{\mathcal{M}_{\delta_e}}}$ (Pitching Moment Coefficient Increment) versus δ_e (elevator deflection).

Table B.5. Pitching Moment Coefficient Parameters

$C_{\mathcal{M}_{\dot{\alpha}1}}^{\alpha 6}$	-2.4045E4	$C_{\mathcal{M}_{\alpha 3}}$	1.2914
$C_{\mathcal{M}_{\dot{\alpha}1}}^{\alpha 5}$	1.9807E4	$C_{\mathcal{M}_{\alpha 2}}$	-1.1556
$C_{\mathcal{M}_{\dot{\alpha}1}}^{\alpha 4}$	-0.4464E4	$C_{\mathcal{M}_{\alpha 1}}$	-0.7804
$C_{\mathcal{M}_{\dot{\alpha}1}}^{\alpha 3}$	-0.0008E4	$C_{\mathcal{M}_{\alpha 0}}$	-0.0146
$C_{\mathcal{M}_{\dot{\alpha}1}}^{\alpha 2}$	0.0089E4	$C_{\mathcal{M}_{\delta_{e}4}}$	-2.7520
$C_{\mathcal{M}_{\dot{\alpha}1}}^{\alpha 1}$	0.0005E4	$C_{\mathcal{M}_{\delta_{e}3}}$	0.7192
$C_{\mathcal{M}_{\dot{\alpha}1}}^{\alpha 0}$	-0.0006E4	$C_{\mathcal{M}_{\delta_{e}2}}$	0.1595
$C_{\mathcal{M}_{q1}}$	-17.2300	$C_{\mathcal{M}_{\delta_{e}1}}$	-0.8516
–	–	$C_{\mathcal{M}_{\delta_{e}0}}$	0

B.6 Yawing Moment Coefficient

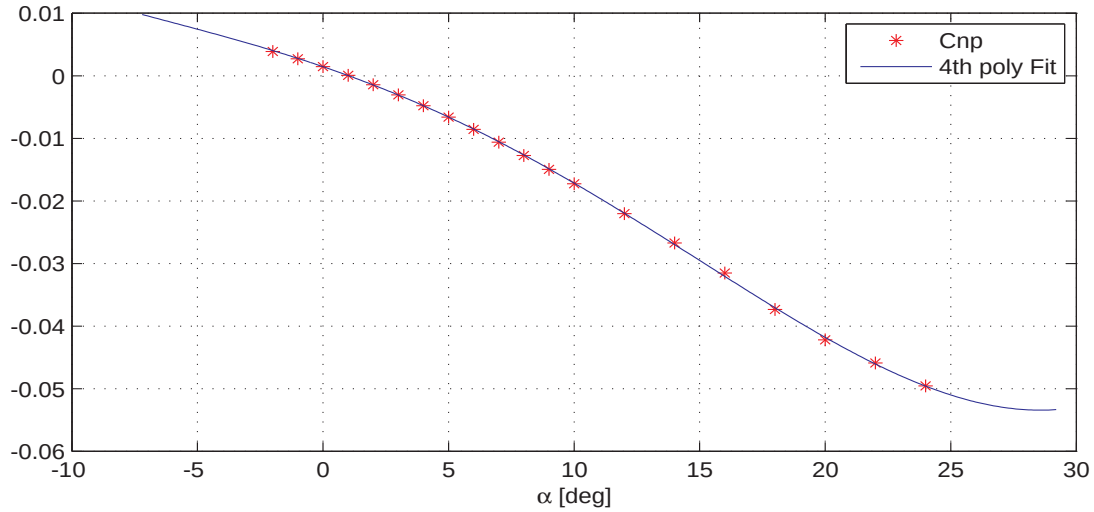

Figure B.15. $\boldsymbol{C}_{\mathcal{N}_{p1}}$ (Yawing Moment Coefficient Dependency on Rolling Rate) versus α (angle-of-attack).

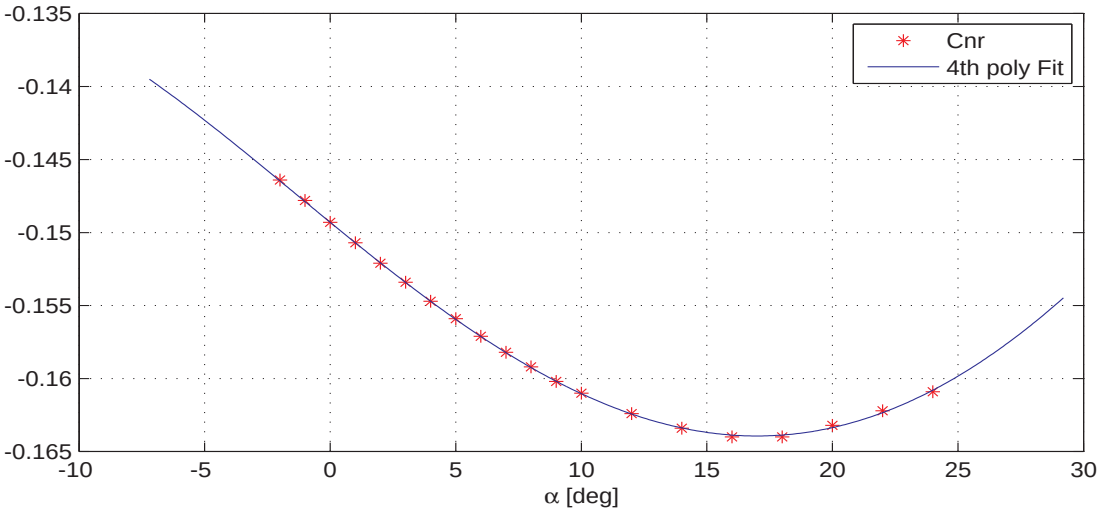

Figure B.16. $\boldsymbol{C}_{\mathcal{N}_{r1}}$ (Yawing Moment Coefficient Dependency on Yawing Rate) versus α (angle-of-attack).

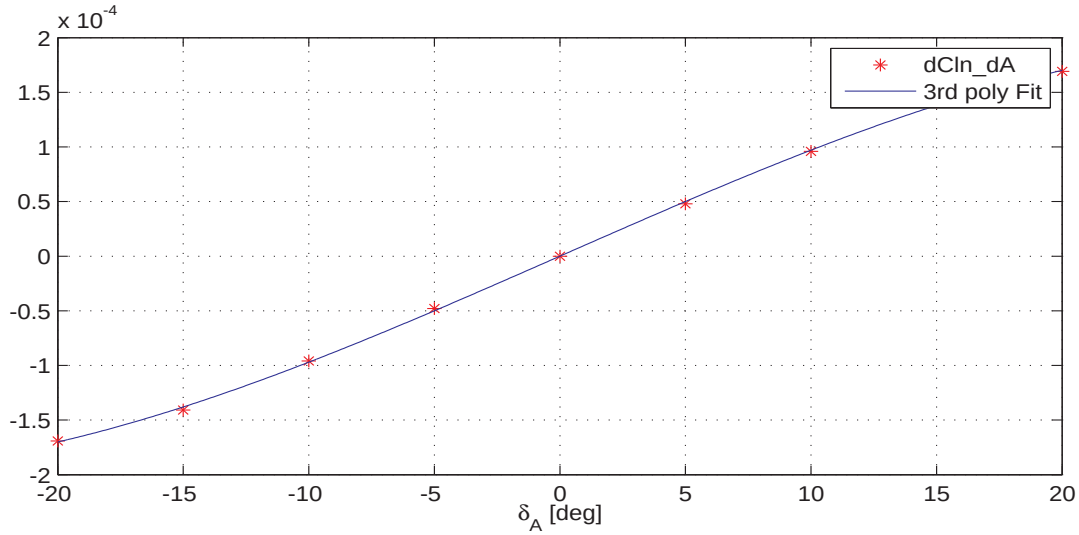

Figure B.17. $\boldsymbol{f}_{\boldsymbol{C}_{\mathcal{N}_{\delta_a}}}$ (Yawing Moment Coefficient Increment) versus δ_a (aileron deflection).

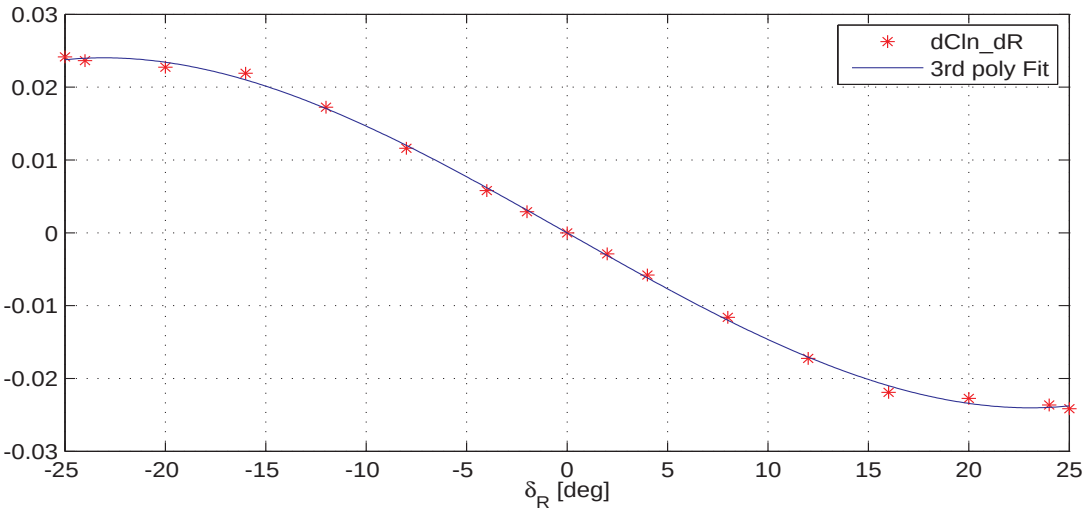

Figure B.18. $\boldsymbol{f}_{\boldsymbol{C}_{\mathcal{N}_{\delta_r}}}$ (Yawing Moment Coefficient Increment) versus δ_r (rudder deflection).

Table B.6. Yawing Moment Coefficient Parameters

$C_{\mathcal{N}_{p1}}^{\alpha 4}$	0.8287	$C_{\mathcal{N}_{r1}}^{\alpha 4}$	-0.2370	$C_{\mathcal{N}_{\delta_{a3}}}$	-7.5064E-4	$C_{\mathcal{N}_{\delta_{r3}}}$	0.1843
$C_{\mathcal{N}_{p1}}^{\alpha 3}$	-0.2560	$C_{\mathcal{N}_{r1}}^{\alpha 3}$	0.3441	$C_{\mathcal{N}_{\delta_{a2}}}$	0	$C_{\mathcal{N}_{\delta_{r2}}}$	0
$C_{\mathcal{N}_{p1}}^{\alpha 2}$	-0.1418	$C_{\mathcal{N}_{r1}}^{\alpha 2}$	0.0247	$C_{\mathcal{N}_{\delta_{a1}}}$	5.7874E-4	$C_{\mathcal{N}_{\delta_{r1}}}$	-0.0896
$C_{\mathcal{N}_{p1}}^{\alpha 1}$	-0.0785	$C_{\mathcal{N}_{r1}}^{\alpha 1}$	-0.0808	$C_{\mathcal{N}_{\delta_{a0}}}$	0	$C_{\mathcal{N}_{\delta_{r0}}}$	0
$C_{\mathcal{N}_{p1}}^{\alpha 0}$	0.0015	$C_{\mathcal{N}_{r1}}^{\alpha 0}$	-0.1493	–	–	–	–
$C_{\mathcal{N}_{\beta 1}}$	-0.1318	–	–	–		–	–

REFERENCES

[1] P. Lissaman and C. Shollenberger, "Formation flight of birds," in *Science*, vol. 168, 1970, pp. 1003–1005.

[2] S. J. Cutts, C., "Energy savings in formation flight of pink-footed geese," *Journal of Experimental Biology*, vol. 189, pp. 251–261, 1994.

[3] C. Y. A. P. J. S. Weimerskirch H., Martin J., "Energy savings in flight formation," *Nature*, vol. 413, no. 697-698, 2001.

[4] W. Blake and D. Multhopp, "Design, performance and modeling considerations for close formation flight," Jul. 1998, aIAA Paper 1998-4343.

[5] S. Venkataramanan and A. Dogan, "Modeling of aerodynamic coupling between aircraft in close proximities," in *Proceedings of the AIAA Atmospheric Flight Mechanics Conference and Exhibit*, Providence, RI, August 2004, aIAA paper 2004-5172.

[6] A. Dogan, S. Venkataramanan, and W. Blake, "Modeling of aerodynamic coupling between aircraft in close proximity," *Journal of Aircraft*, vol. 42, no. 4, pp. 941–955.
doi: 10.2514/1.7579, 2005.

[7] A. Dogan and S. Venkataramanan, "Nonlinear control for reconfiguration of unmanned–aerial–vehicle formation," *Journal of Guidance, Control and Dynamics*, vol. 28, no. 4, pp. 667–678.
doi:10.2514/1.8760, 2005.

[8] D. Hummel, "The use of aircraft wakes to achieve power reductions in formation flight," in *AGARD Conference Proceedings 584*, Trondeim, Norway, November 1996, pp. 36.1–36.13.

[9] J. Hansen and B. Cobleigh, "Induced moment effects of formation flight using two f/a-18 aircraft," in *AIAA Atmospheric Flight Mechanics Conference and Exhibit*. Monterey, CA: AIAA, August 2002, aIAA paper 2002-4489.

[10] W. Okolo, A. Dogan, and W. Blake, "Application of sweet spot determination to a conventional pair of aircraft," in *Proceedings of the AIAA Atmospheric Flight Mechanics Conference and Exhibit*, Minneapolis, MN, August 2012, aIAA Paper 2012-4402.

[11] G. Wagner, D. Jacques, W. Blake, and M. Pachter, "An analytical study of drag reduction in tight formation flight," in *AIAA Atmospheric Flight Mechanics Conference, Montreal Canada*, vol. 2001-4075, August 2001, aIAA paper 2001-4075.

[12] R. Drinnon, *Chief scientist: Airmen's innovative spirit vital to future*. http://www.af.mil/news/story.asp?id=123147709: Air Mobility Command Public Affairs, 5 May 2009.

[13] J. V. C. S. J. Ronald Ray, Brent Cobleigh, "Flight test techniques used to evaluate performance benefits during formation flight," in *AIAA Atmospheric Flight Mechanics Conference and Exhibit*. Monterey, CA: AIAA, August 2002.

[14] K. Ariyur and M. Krstic, "Real-time optimization by extremum-seeking control," in *Real-Time Optimization by Extremum-Seeking Control*. John Wiley & Sons, Inc., 2003.

[15] D. Chichka, J. Speyer, F. Claudio, and C. Park, "Peak-seeking control for drag reduction in formation flight," *Journal of Guidance, Control, and Dynamics*,

vol. 29, no. 5, pp. 1221–1230.
doi: 10.2514/1.15 424, 2006.

[16] P. Binetti, K. Ariyur, K. Miroslav, and F. Bernelli, "Formation flight optimization using extremum seeking feedback," *Journal of Guidance, Control, and Dynamics*, vol. 26, no. 1, pp. 132–142.
doi: 10.2514/2.5024, 2003.

[17] J. Ryan and J. Speyer, "Peak-seeking control using gradient and hessian estimates," in *American Control Conference*, Baltimore, MD, July 2010, weA17.5.

[18] W. Okolo, A. Dogan, and W. Blake, "Modified study of trail aircraft trim effect on sweet spot in formation flight," in *Proceedings of the AIAA SciTech Conference*, National Harbor, MD, January 2014, aIAA paper 2014-0541.

[19] J. Rosser, R. Newton, and G. Gross, "Motion during burning," in *Mathematical Theory of Rocket Flight*. McGraw–Hill Book Company, Inc., 1947, pp. 78–183.

[20] K. Jarmolow, "Dynamics of a spinning rocket with varying inertia and applied moment," *Journal of Applied Physics*, vol. 28, no. 3, pp. 308–313, 1957.

[21] J. Ellis and C. McArthur, "Applicability of euler's dynamical equations to rocket motion," *American Rocket Society Journal*, vol. 29, no. 11, pp. 863–864.
doi: 10.2514/8.4931, 1959.

[22] W. T. Thomson, *Introduction to Space Dynamics*. Dover Publication, Inc., 1986.

[23] F. O. Eke, T. C. Mao, and M. J. Morris, "Free attitude motions of a spinning body with substantial mass loss," *Journal of Applied Mechanics*, vol. 71, no. 2, pp. 190–194.
doi:10.1115/1.1 653 738, 2004.

[24] J. D. Schierman, D. Ward, J. Monaco, J. Hull, and T. Lawrence, "On-line identification and nonlinear control of rotorcraft/external-load systems," in *Proceedings*

of AIAA Guidance, Navigation, and Control Conference and Exhibit, Denver, CO, 14-17 August 2000, aIAA paper 2000-4042.

[25] J. Shen and N. H. McClamroch, "Translational and rotational spacecraft maneuvers via shape change actuators," in *Proceedings of the American Control Conference*, Arlington, VA, June 25-27, 2001.
doi: 10.1109/ACC.2001.946284.

[26] C. Woolsey and N. Leonard, "Moving mass control for underwater vehicles," in *Proceedings of the American Control Conference*, Anchorage, AK, May 8-10 2002.
doi: 10.1109/ACC.2002.1025217.

[27] C. Schultz and C. Woolsey, "An experimental platform for validating internal actuator control strategies," in *IFAC Workshop on Guidance and Control of Underwater Vehicles*, Newport, South Wales, U.K., April 2003, pp. 209–214.

[28] D. Collard, "Future supersonic transport studies at aerospatiale," *SAE (Society of Automotive Engineers) Transactions*, vol. 99, pp. 1700–1708, 1990.

[29] ——, "Concorde airframe design and development," *SAE (Society of Automotive Engineers) Transactions*, vol. 100, pp. 2620–2641, 1991.

[30] C. Orlebar, "Taking shape," in *The Concorde Story*. London, United Kingdom: The Hamlyn Publishing Group Limited, 1994, p. 39.

[31] G. B. Gilyard, J. L. Conley, J. Le, and F. W. Burcham Jr, *A Simulation Evaluation of a Four-Engine Jet Transport Using Engine Thrust Modulation for Flightpath Control*. National Aeronautics and Space Administration, Office of Management, Scientific and Technical Information Program, September 1991, vol. 4324, nASA TM-4324.

[32] F. W. Burcham, J. Burken, T. A. Maine, and J. Bull, *Emergency flight control using only engine thrust and lateral center-of-gravity offset: A first look*. Na-

tional Aeronautics and Space Administration, Office of Management, Scientific and Technical Information Division, July 1997, nASA TM-4798.

[33] G. Bramesfeld, M. D. Maughmer, and S. M. Willits, "Piloting strategies for controlling a transport aircraft after vertical-tail loss," *Journal of aircraft*, vol. 43, no. 1, pp. 216–225.
doi: 10.2514/1.13 357, 2006.

[34] "Aircraft accident report: United airlines flight 232," National Transportation Safety Board, US Government Printing Office, Washington, D.C. 20594, Tech. Rep. NTSB/AAR-90/06, 1990.

[35] A. Brindisi and A. Concilio, "Passengers' comfort modeling inside aircraft," *Journal of aircraft*, vol. 45, no. 6, pp. 2001–2008, 2008.

[36] I. D. Jacobson, A. R. Kuhlthau, L. G. Richards, and D. W. Conner, "Passenger ride quality in transport aircraft," *Journal of Aircraft*, vol. 15, no. 11, pp. 724–730, 1978.

[37] S. S. Stevens, "On the psychophysical law." *Psychological review*, vol. 64, no. 3, p. 153, 1957.

[38] ISO, *Mechanical vibration and shock-Evaluation of human exposure to whole-body vibration-Part 1: General requirements*. International Organization for Standardization, 1997.

[39] H. E. Von Gierke, "On noise and vibration exposure criteria," *Archives of Environmental Health: An International Journal*, vol. 11, no. 3, pp. 327–339, 1965.

[40] H. Von Gierke and R. Coermann, "The biodynamics of human response to vibration and impact." *Industrial medicine & surgery*, vol. 32, p. 30, 1963.

[41] P. R. Payne and I. A. M. PAYNE, *On quantizing ride comfort and allowable accelerations*. Defense Technical Information Center, 1976.

[42] J. Pahle, D. Berger, M. Venti, C. Duggan, J. Faber, and K. Cardinal, "An initial flight investigation of formation flight for drag reduction on the c-17 aircraft," in *AIAA Atmospheric Flight Mechanics Conference*, 2012.

[43] R. Drinnon, "Air mobility command scientist: Nature was model for innovative c-17 flight tests to save air force millions," News Release, Air Mobility Command Public Affairs, Scott Air Force Base, 15 August 2013.

[44] M. J. Allen, J. Ryan, C. E. Hanson, and J. F. Parle, *String stability of a linear formation flight control system.* National Aeronautics and Space Administration, Dryden Flight Research Center, 2002.

[45] N. Bizinos, "Passenger comfort during formation flight within atmospheric turbulence (masters thesis)," 2012.

[46] H. M. H.P. Thien, M.A. Moelyadi, "Effects of leader's position and shape on aerodynamic performances of v flight formation," in *International Conference on Intelligent Unmanned Systems*, Bali, Indonesia, October 2007.

[47] J. Waishek, A. Dogan, and W. Blake, "Derivation of the dynamics equations of receiver aircraft in aerial refueling," *AIAA Journal of Guidance, Control and Dynamics*, vol. 32, no. 2, pp. 585–597.
doi: 10.2514/1.35 892, 2009.

[48] B. Nguyen and W. Blake, "Automated aerial refueling (aar) equivalent model-iii specification," AFRL, Tech. Rep. AFRL-RB-WP-TR-2011-0079, June 2012.

[49] A. Dogan, C. Elliott, F. Riley, and W. Blake, "Effects of mass and size on control of large receiver in aerial refueling," in *AIAA Atmospheric Flight Mechanics Conference.* AIAA, 2009, aIAA paper 2009-5927.

[50] A. Barfield and J. Hinchman, "An equivalent model for uav automated aerial refueling research," vol. AIAA paper 2005-6006. San Francisco, CA: Proceedings

of the AIAA Modeling and Simulation Technologies Conference and Exhibit, August 2005.

[51] D. C. Albright, A.E. and M. Heggedus, "Modification and validation of conceptual design aerodynamic prediction method hasc95 with vtxchn," NASA, CR 4712, March 1996.

[52] J. Stevens, V.I. and G. McCormack, "Power-off tests of the northrop n9m-2 tailless airplane in the 40- by 80-foot wind tunnel," NACA, Tech. Rep. MR A4L14, December 1944.

[53] I. Ashkenas and D. Klyde, "Tailless aircraft performance improvements with relaxed static stability," NASA, Tech. Rep. CR 181806, March 1989.

[54] e. a. Hoak, D.E., "Usaf stability and control datcom," AFWAL TR 83-3048, Tech. Rep., October 1960 (revised 1978).

[55] W. Blake and C. Clark, "Technology assessment and simulation of advanced concepts: Sensorcraft flight and ground dynamics," AFRL, Tech. Rep. AFRL-VA-WP-TR-2006-3093, 2006.

[56] "Automated aerial refueling Equivalent Model-II specification (large variant)," Tech. Rep. AFRL/RBCC 937-255-3047, 27 March 2008, version 3.0.

[57] "Automated aerial refueling Equivalent Model-II specification (small variant)," Tech. Rep. AFRL/RBCC 937-255-3047, 28 March 2008, version 2.0.

[58] A. Dogan, "Center of mass formulation for fuel in eq-ii inner fuel tank," Air Force Research Laboratory, Wright Patterson AFB OH, Tech. Rep., 2011.

[59] J. E. Williams and S. R. Vukelich, "The usaf stability and control digital datcom," Tech. Rep. AFFDL-TR-79-3032, April 1979.

[60] W. E. McNeill, "Calculated and flight-measured handling qualities factors of three subsonic jet transports," Tech. Rep. NASA TN D-4832, November 1968.

[61] K. R. Crenshaw, "Stability and control of the winglet configured kc-135a," Master's thesis, Air Force Institute of Technology, December 1976, thesis GAE/MC/76D-5.

[62] J. G. Richard Johnson, "Aircraft fuel tank inerting system," AiResearch Manufacturing Company, Torrance California, 90509, Tech. Rep. AFWAL-TR-82-2115, July 1983.

[63] E. Kim, "Control and simulation of relative motion for aerial refueling in racetrack maneuver," Master's thesis, The University of Texas at Arlington, Arlington, TX, May 2007.

[64] J. Waishek, "Derivation of the dynamics equations for receiver aircraft in aerial refueling," Master's thesis, The University of Texas at Arlington, Arlington, TX, December 2007.

[65] A. Dogan, T. Lewis, and W. Blake, "Flight data analysis and simulation of wind effects during aerial refueling," *AIAA Journal of Aircraft*, vol. 45, no. 6, pp. 2036–2048.
doi: 10.2514/1.36 797, 2008.

[66] W. Okolo, A. Dogan, and W. Blake, "Formation flight analysis of two kc-135r aircraft," Air Force Research Laboratory, Wright Patterson AFB OH, Tech. Rep., 2011.

[67] A. Dogan, F. Riley, and W. Blake, "Control and simulation of relative motion for aerial refueling in racetrack maneuver," Air Force Research Laboratory, Wright Patterson AFB OH, Tech. Rep., June 2008.

[68] A. Dogan, E. Kim, and W. Blake, "Control and simulation of relative motion for aerial refueling in racetrack maneuvers," *Journal of Guidance, Control and Dynamics*, vol. 30, no. 5, pp. 1551–1557, 2007.

[69] A. Dogan, S. Sato, and W. Blake, "Flight control and simulation for aerial refueling," in *Proceedings of AIAA Guidance, Navigation, and Control Conference*, San Francisco, CA, August 2005, aIAA paper 2005-6264.

[70] C. Elliot and A. Dogan, "Investigating nonlinear control architecture options for aerial refueling," Proceedings of the AIAA Atmospheric Flight Mechanics Conference, Toronto, Ontario, Canada, Conference 2010-7927, August 2010.

[71] J. Kampoon and A. Dogan, "Guidance of receiver aircraft to rendezvous with tanker in the presence of wind," Proceedings of the AIAA Guidance, Navigation, and Control Conference, Toronto, Ontario, Canada, Conference 2010-8226, August 2010.

[72] T. A. Lewis, "Flight data analysis and simulation of wind effects during aerial refueling," Master's thesis, The University of Texas at Arlington, Arlington, TX, May 2008.

[73] A. Dogan and W. Blake, "Modeling of bow wave effect in aerial refueling," Proceedings of the AIAA Atmospheric Flight Mechanics Conference, Toronto, Ontario, Canada, Conference 2010-7926, August 2010.

[74] A. Dogan, T. Lewis, and W. Blake, "Wake-vortex induced wind with turbulence in aerial refueling - part B: Model and simulation validation," in *Proceedings of the AIAA Atmospheric Flight Mechanics Conference and Exhibit*, Honolulu, Hawaii, August 2008, aIAA-2008-6697.

[75] S. M. Haag, C. and W. Blake, "Computational analysis of the bow wave effect in air-to-air refueling," Proceedings of the AIAA Atmospheric Flight Mechanics Conference, Toronto, Ontario, Canada, Conference 2010-7925, August 2010.

[76] A. A. Z. A. Bangash, R.P. Sanchez, "Aerodynamics of formation flight," in *AIAA Aerospace Sciences Meeting and Exhibit*, no. 42, 2004.

[77] S. Venkataramanan, A. Dogan, and W. Blake, "Vortex effect modelling in aircraft formation flight," in *Proceedings of the AIAA Atmospheric Flight Mechanics Conference and Exhibit*, Austin, TX, August 2003, aIAA paper 2003-5385.

[78] M. Munk, "The minimum induced drag of aerofoils," NACA, Tech. Rep. NACA TR-121, 1979.

[79] D. G. William Blake, Edward Dickes, "Uav aerial refueling – wind tunnel results and comparison with analytical predictions," in *AIAA Atmospheric Flight Mechanics Conference and Exhibit*, no. AIAA 2004-4820. AIAA, August 16 - 19 2004.

[80] R. R. W. K. Vachon, M.J. and K. Ennix, "F/a-18 aircraft performance benefits measured during the autonomous formation flight project," in *Proceedings of AIAA Atmospheric Flight Mechanics Conference*, vol. 4491. Monterey, CA: AIAA, August 2002.

[81] R. Drinnon, "'vortex surfing' could be revolutionary," News Release, Air Mobility Command Public Affairs, Scott Air Force Base, 10 October 2012.

[82] H. Jordan, "Air force research laboratory utilizes experimental 'surfing' formation flight to reduce fuel cost," News Release, 88th Air Base Wing Office of Public Affairs, Air Force Materiel Command, Wright-Patterson Air Force Base, 11 October 2012.

[83] S. Sumner. (2014, October) Kc-135 fuel tank locations and quantities. Aviation Stack Exchange. [Online]. Available: http://aviation.stackexchange.com/questions/9001/do-tanker-aircraft-distribute-their-own-fuel

[84] P. Stoica and R. Moses, *Introduction to Spectral Analysis*. Upper Saddle River, NJ: Prentice Hall, 1997, ch. 1–2.

[85] P. Stoica and R. L. Moses, *Spectral Analysis of Signals*. Upper Saddle River, NJ: Pearson Education, Inc., 2005, ch. 2.7.2.

BIOGRAPHICAL STATEMENT

Wendy A. Okolo had her elementary and secondary education in St. Mary's Private School and Queen's College (QC) Yaba, respectively, in Lagos, Nigeria. She enrolled at the University of Texas at Arlington (UTA) in 2006 for her undergraduate studies in aerospace engineering. As an undergraduate, she interned with Lockheed Martin Information Systems and Global Services, working on the Orion spacecraft for NASA.

After graduating with her B.S. in 2010, she began the B.S. to Ph.D. program in the Computer Aided Controls Systems Design (CASCD) Laboratory. She accompanied her advisor as a graduate student researcher to the Air Force Research Laboratory (AFRL) at Wright-Patterson Air Force Base in the summers of 2010 to 2012. At the time of conferral of her doctorate degree, her research efforts have culminated in a total of ten publications.

Her graduate studies were funded by the UTA Honors College, the Mechanical and Aerospace Engineering Department, and the College of Engineering (COE). Her research was also recognized and funded by the Department of Defense through the National Defense Science and Engineering Graduate Fellowship, Zonta International through the Amelia Earhart Fellowship, the American Institute for Aeronautics and Astronautics through the John Leland Atwood Graduate Fellowship, and the Texas Space Grant Consortium. Other research awards include a resolution of commendation from the Tarrant County Court of Texas and an award for excellence in research by the Women Of Color in STEM.

During years at the university, she was a resident assistant in the engineering learning Community at Kalpana Chawla Hall at UTA, she was involved with the Graduate Student Senate as the representative to the COE, she was a mentor for freshmen through the University HOSTS (Helping Other Students To Succeed) Program, and she was also a president for the Society of Women Engineers, UTA Chapter.